Evaluation of Solder Joints on Aluminum Surfaces for the Interconnection of Silicon Solar Cells

Dissertation zur Erlangung des akademischen Grades
Doktor-Ingenieur (Dr.-Ing.)
der Fakultät für Informatik und Elektrotechnik
der Universität Rostock

Vorgelegt von
Angela De Rose, M. Sc.

April 2021

https://doi.org/10.18453/rosdok_id00003383

Dekan
Prof. Dr.-Ing. habil. Mathias Nowottnick

Gutachter
Prof. Dr.-Ing. habil. Mathias Nowottnick
Institut für Gerätesysteme und Schaltungstechnik, Universität Rostock

Prof. Dr. rer. nat. Stefan W. Glunz
Institut für Nachhaltige Technische Systeme, Albert-Ludwigs-Universität Freiburg

Datum der mündlichen Prüfung
29. September 2021

Abstract

In this thesis, direct soldering of aluminum is investigated, with a special focus on application in the photovoltaic industry. The native Al_2O_3 layer impedes the solderability of Al components. However, strong solder joints can be formed when suitable surface coatings are used. The formation of solder joints and the relevant fundamental properties of these joints and coatings are evaluated.

For silicon solar cells, the rear electrode is typically made from Al, and expensive Ag rear pads are used for soldering instead of coatings. The established high-throughput interconnection equipment and the processes of the photovoltaic industry are used as a baseline in this work. With this, reliable soldering of Al at ambient air using temperatures of around 250 °C and no-clean flux is demonstrated.

A systematic evaluation of solder joints is presented to determine essential properties of the joints. The findings are correlated to the different coating materials to identify suitable material combinations. Solderable layers are deposited on Al by three different coating techniques. First, mechanical joining of Al and a solderable layer is done by roll cladding. Also, a wet-chemical coating by a zincate treatment and electroless plating is used. Lastly, thin solderable layers are deposited on Al by magnetron sputtering. Several material combinations of different layer thicknesses are tested. The wettability of the coatings with solder is characterized by means of the optical contact angle, as a simple method to assess the solderability. A systematic comparison of different coating thicknesses reveals a minimum required layer thickness for good wettability, strongly depending on the deposition method.

After soldering of the differently coated Al, an in-depth analysis of SnPb-based solder joints is performed, using several characterization techniques. The mechanical strength of the solder joints is investigated by a 90° peel force measurement, yielding a good correlation with the initial wetting tests. Solder joints on 200 µm thick coated Al foils show high peel forces of $3\,\mathrm{N\,mm^{-1}}$ to $8\,\mathrm{N\,mm^{-1}}$ for all three coating approaches. The electrical properties of the solder joints on all coatings have shown to be uncritical for the solar cell with $< 20\,\mu\Omega\,\mathrm{cm}^2$. Isothermal aging at 85 °C and 125 °C is performed and several stable coatings are identified.

Using electron microscopy (SEM, TEM), the interfaces of the solder joints are analyzed with high resolution, regarding homogeneity and defects. In combination with EDX spectroscopy it is shown that diffusion zones and/or phase formation in the interfacial regions support adhesion of the material systems.

The most promising material combinations are tested on the Al rear side of Si solar cells. For wet-chemically and sputter-coated Al, a successful interconnection process is realized by infrared soldering on an industrial stringer with fast soldering times $< 2\,\mathrm{s}$. The implementation on Si solar cells is tested for FoilMet® solar cells with Al foil rear side and modified passivated emitter and rear cells (PERC) with PVD Al rear side.

I-V measurements and electroluminescence imaging of 1-cell-modules prove a successful module integration. A loss in module power of less than 2 % is achieved after 200 thermal cycles in a climate chamber, on the same level as the current state-of-the-art PERC technology. Possible failure mechanisms of the solder joints are analyzed in detail on solar cell and module level. The overall results of the solder joint evaluation show the high potential of direct contacting Al for Si solar cells, by suitable coatings, in which established processes and tools of the photovoltaic industry can be used.

Kurzfassung

Im Rahmen dieser Dissertation wird die direkte Lötbarkeit von Aluminium, mit dem Ziel der Anwendung in der Photovoltaik Industrie, untersucht. Die natürliche Al_2O_3 Oxidschicht erschwert das Weichlöten von Aluminiumbauteilen. Dennoch ist es möglich, unter der Verwendung einer geeigneten Oberflächenbeschichtung, starke Lötverbindungen auszubilden. Die Lötstellen, deren relevante Eigenschaften, sowie die der Beschichtungen, werden in der vorliegenden Arbeit evaluiert.

Die Rückseitenelektrode von Siliciumsolarzellen wird typischerweise aus Al hergestellt, wobei statt Beschichtungen zusätzliche teure Silberflächen als Lötkontakte genutzt werden. Als Grundlage für die Verschaltung in dieser Arbeit werden die in der Photovoltaik etablierten Hochdurchsatzanlagen und -prozesse verwendet. Unter diesen Bedingungen wird zuverlässiges Weichlöten von Al an Umgebungsluft bei Temperaturen um 250 °C mit no-clean Flussmittel demonstriert.

Um grundlegende Eigenschaften der Lötstellen zu bestimmen, wird eine systematische Bewertung der Lötstellen durchgeführt. Die Erkenntnisse werden mit den verschiedenen Beschichtungsmaterialien korreliert, um geeignete Materialkombinationen zu identifizieren. Es werden drei Beschichtungstechnologien verwendet, um lötbare Schichten auf Al abzuscheiden. Zum einen wird mechanisches Fügen von Al und einer lötbaren Schicht mittels Walzplattierung realisiert. Außerdem erfolgt die nasschemische Behandlung von Al mit Zinkatbeize und Nickelplating. Zuletzt wird die Abscheidung dünner Schichten mittels Sputterverfahren genutzt. Es wird eine Vielzahl von Materialkombinationen und -dicken untersucht. Ihre Benetzbarkeit mit flüssigem Weichlot wird mittels optischer Kontaktwinkelmessung bewertet, einer einfachen Methode um die Lötbarkeit zu testen. Ein systematischer Vergleich verschiedener Beschichtungsdicken zeigt, abhängig von der jeweiligen Beschichtungsmethode, eine benötigte minimale Dicke für gute Benetzbarkeit.

Nach dem Weichlöten des beschichteten Al wird eine eingehende Analyse von Zinn-Blei-Lötstellen mittels diverser Charakterisierungsverfahren durchgeführt. Die mechanische Festigkeit der Lötstellen wird mit einem 90° Abzugstest untersucht, wobei eine gute Korrelation der Ergebnisse mit den Benetzungstests beobachtet wird. Lötstellen auf 200 µm dicker beschichteter Aluminiumfolie erzielen hohe Haftkräfte zwischen $3\,\mathrm{N\,mm^{-1}}$ und $8\,\mathrm{N\,mm^{-1}}$. Die elektrischen Eigenschaften der Lötstellen für alle Beschichtungen liegen im für die Solarzelle unkritischen Bereich $< 20\,\mu\Omega\,\mathrm{cm}^2$. Durch isotherme Alterung bei 85 °C und 125 °C werden mehrere temperaturstabile Kombinationen identifiziert.

Mittels Elektronenmikroskopie (REM, TEM) werden die Grenzflächen der Lötstellen bei hoher Auflösung hinsichtlich Homogenität und Defekten analysiert. Durch Kombinaton mit EDX Spektroskopie wird gezeigt, dass Diffusion und/oder Phasenbildungen an den Grenzflächen zur Verbesserung der Verbundhaftung führen.

Die vielversprechendsten Materialkombinationen werden auf der Aluminiumrückseite von Siliciumsolarzellen getestet. Für nasschemisch und sputterbeschichtetes Al wird ei-

ne erfolgreiche Verschaltung mittels Infrarotlöten auf einem Industriestringer mit Lötzeiten $< 2\,\mathrm{s}$ realisiert. Die Umsetzung auf Siliciumsolarzellen wird für FoilMet®- und PERC-Solarzellen mit PVD Aluminiumrückseite getestet. Die Charakterisierung von 1-Zell-Modulen mittels I-V und EL Messungen weist eine erfolgreiche Modulintegration nach. Nach 200 Zyklen termischer Wechsellast in Klimakammertests wird ein Leistungsverlust von weniger als $2\,\%$ demonstriert. Dies entspricht dem Stand aktuell etablierter PERC Technologie. Mögliche Fehlermechanismen der Lötstellen werden im Detail auf Zell- und Modulebene analysiert. Mithilfe der umfassenden Analyse der Lötstellen, kann das hohe Potential dieses Ansatzes zur direkten Lötbarkeit von Aluminium für Siliciumsolarzellen gezeigt werden, wobei bereits etablierte Prozesse und Anlagen aus der Photovoltaikindustrie genutzt werden können.

Contents

1. Introduction

1.1. Motivation

Our global energy system has changed drastically within the past decade: Within the last ten years (2009 - 2019), the annual worldwide demand for electricity has increased by 21 % to 580 EJ [1]. As coal, oil and natural gas have been the worlds main energy sources (> 80 %) [2], the combustion of these fossil fuels caused carbon dioxide emissions, provoking a global climate change. The need for carbon-free energy sources is higher than ever before [3].

One renewable energy source is **p**hoto**v**oltaics (PV), the direct conversion of sunlight into electrical energy. For a carbon-free energy supply, PV is of major significance and offers several advantages: 1.5×10^{12} TWh radiant power provided by the sun every year, the potential for decentralized energy supply and a cost-efficient energy generation.[1]

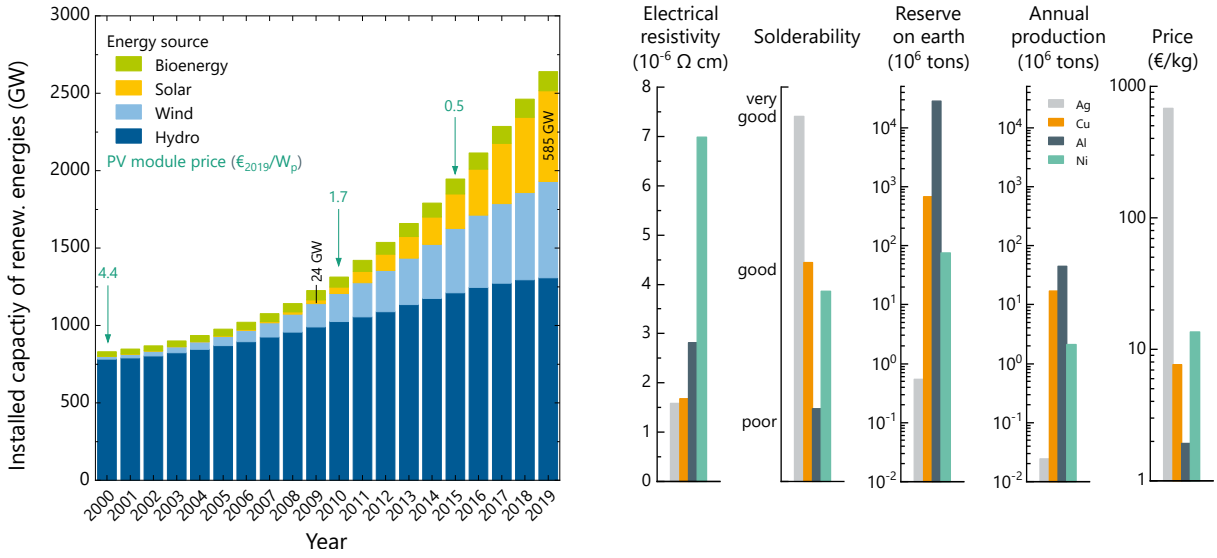

Figure 1.1.: Left: Worldwide installed capacity of renewable energies [5]. Taken from the Fraunhofer ISE Photovoltaics Report 2020 [4]. Module prices (all commercially available PV technologies) that demonstrate the PV learning rate, are listed for 2000, 2010 and 2015 (*cf.* Figure A.1). Right: Comparison of different properties of Ag (grey), Cu (orange), Al (dark grey) and Ni (green). Data taken from [6–8].

The left graph in Figure 1.1 shows the worldwide increasing installed energy production capacity of renewable sources over the past twenty years [5]. In 2019, the installed capacity

[1] The energy payback time of PV systems depends on the geographical location, the installed technology and grid efficiency. It is calculated to be 1-2 years for modules located in Europe [4].

for solar energy increased to 585 GW (thereof 141 GW in Europe, 49 GW in Germany).

Simultaneously, the market price for PV modules decreased constantly [4], as also indicated in Figure 1.1 left by the module prices for 2000, 2010 and 2015. Both trends imply a significant growth of the PV market, which is necessary to counter the climate crisis, as the currently installed capacity (*e.g.* 52 GW in Germany, 2020 [4, 9]) is far too little.[2]

Ag is the most expensive material in PV module production [11] and used for the electrodes of Si solar cells. Therefore, the price curve in Si PV is strongly driven by the Ag price. The worldwide Ag reserves are limited and tends to be depleted within the next 20 years [6]. Three very important targets are therefore to increase the installed PV capacity, further boost the solar cell energy conversion efficiency[3] and replace Ag by more cost-efficient metals with a higher availability.

As illustrated by the bar charts in Figure 1.1 on the right, the best choices for Ag replacement are Cu and Al. They have an electrical conductivity in the same order of magnitude, which is important to allow for low ohmic losses in PV modules. The reserves of Cu are also rather low, whereas Al is highly available [6]. Currently, the estimated reserve for Al is $\sim 25\,000 \times 10^6$ t and the annual production is $< 0.2\,\%$. Since Ag is still one of the most used metals in our industrialized world, the annual production makes up $\sim 4.5\,\%$ of the already low reserve. The depletion of Ag will increase the PV module price drastically (*cf.* [14, 15]), if no alternatives will be found.

While Al looks like a very promising candidate, its main challenge is found during PV module assembly, when several cells are electrically interconnected in a string. With the currently established technologies and processes described in the next section, interconnection of Al electrodes is not feasible.

Replacing the Ag pads on the solar cell rear side by Al with a solderable coating would simplify solar cell manufacturing and save costs due to reduced Ag consumption. This new approach for solar cell interconnection of Al is evaluated within this work.

[2] Only 5 % of the global primary energy production are generated from renewable sources [10]. See also Figure A.1 in the appendix.

[3] For crystalline Si solar cells, the current world record is at 26.7 % for monocrystalline Si and 23.3 % for multicrystalline Si solar cells [12]. The history of the worldwide best energy conversion efficiencies of different cell types is collected in a chart by the National Renewable Energy Laboratory [13].

1.2. State of the Art

With over 90 %, soldering is the dominant interconnection technology for Si solar cells [11]. The front electrode of one solar cell is connected in series with the rear electrode of the next solar cell to increase the voltage of the PV module by manufacturing "strings" of solar cells (s. Figure 1.2 right). For a full-size module, consisting of 60 solar cells, six strings with ten solar cells each are interconnected, resulting in a power output of about 290 W to 320 W.[4]

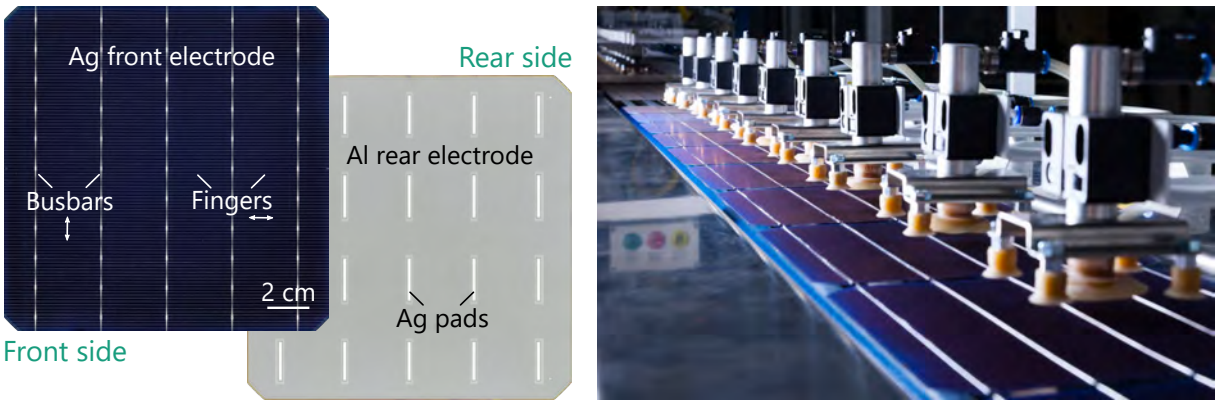

Figure 1.2.: Left: Monofacial five busbar (5BB) passivated emitter and rear solar cell (PERC), which is currently the state-of-the-art Si solar cell concept in industry. For soldering, the Ag busbars on the front and the Ag pads on the rear are contacted by IR soldering using solder-coated Cu interconnectors. Right: Series interconnection of ten solar cells on industrial stringer. © Fraunhofer ISE

The electrodes of a Si solar cell mostly consists of a screen-printed Ag grid on the front side and a full-area electrode of screen-printed Al on the rear side (for monofacial cell concepts, s. Figure 1.2 left). At ambient air, soldering of Al surfaces is hampered due to the native Al_2O_3 [7, 16] and requires *e.g.* high temperatures $\sim 600\,°C$, special solders, aggressive flux or adapted processes [17]. To overcome this problem, additional local Ag pads are currently screen-printed on the solar cell rear side to allow for contacting by soldering (s. Figure 1.2 left).

Beside others, infrared soldering is implemented in industrial stringer machines (s. Figure 1.2 right), realizing an inline soldering process at ambient air with a high throughput of $< 2\,s$ per solar cell. Not yet restricted by the RoHS regulations [18], tin-lead solder alloys with melting points at $\sim 180\,°C$ and no-clean flux are used for soldering Si solar cells. Most of the cells are sensitive to high temperatures, handling (cell breakage) and impurities, which can be induced by different metals. Therefore, the interconnection process has to be adapted precisely for each type of solar cell.

[4] PERC solar cells with 5 busbar (BB) of Cz-Si, monofacial cells and module setup, cell power $\sim 5\,W$ (*cf.* Section 2.1).

1.3. Approach of this Thesis

In this thesis, direct contacting of Al surfaces by soldering within the frame of Si photovoltaics is investigated. While several approaches are discussed in literature, as reviewed in Chapter 2, this work focuses on solderable coatings on Al substrates.

Three coating methods and different material combinations are analyzed, as sketched in Figure 1.3: roll-cladding of Al foil with a solderable layer, wet-chemical treatment followed by electroless plating and magnetron sputter deposition.

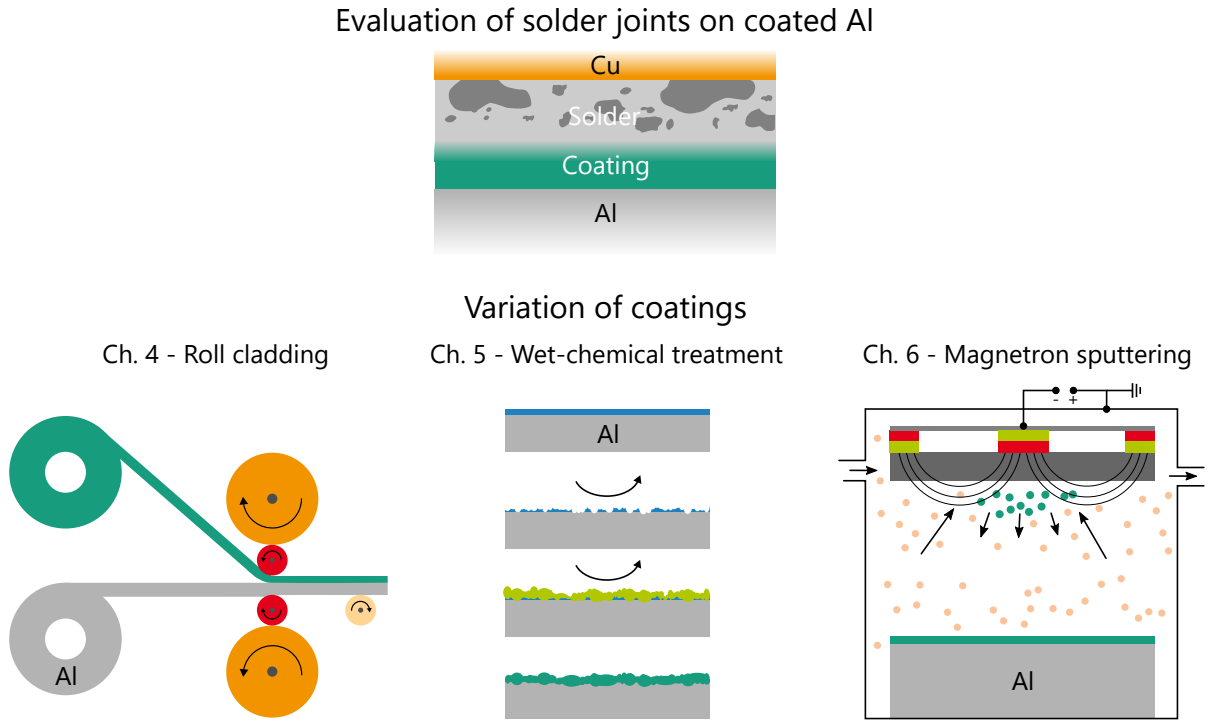

Figure 1.3.: Sketch of deposition techniques, used within this work to coat Al with a solderable layer. Left: Quarto roll stand for cladding of two metal foils. Middle: Wet-chemical pre-treatment of Al and electroless plating. Right: Magnetron sputter deposition.

The evaluation, performed throughout this thesis, addresses the following aspects, from fundamentals to practical applications:

- Investigation of coatings on Al regarding solderability
- Analysis of solder joints on coated Al and their long-term stability
- Process transfer to industrial infrared soldering

In the context of this thesis, "solderability" refers to the requirements given by Si PV technology. The evaluation of solder joints includes stability and failure analysis. The industrial equipment used for process transfer is established for Si PV module manufacturing.

The details of these requirement are presented in **Chapter 2** (p. 7 *ff.*), along the relevant physics of Si solar cells and modules. In addition, the fundamentals of soldering and the state of the art for soldering in PV, the industrial implementation and the challenges of soldering on Al surfaces are explained. In **Chapter 3** (p. 37 *ff.*), the three coating methods, the sample preparation of 200 µm thick coated Al foil and the used characterization methods are introduced. The remaining chapters present the experimental work and analysis.

The variations of the three coatings are presented in **Chapter 4** (p. 61 *ff.*), **Chapter 5** (p. 87 *ff.*) and **Chapter 6** (p. 125 *ff.*), as indicated in Figure 1.3. In each chapter, the suitability is first analyzed by initial assessment of the coating and wettability with SnPb solder. Afterwards, solder joints are manufactured on 200 µm thick Al foils and peel force, microstructure and contact resistance are evaluated. Based on the initial characterization, further analysis have been performed addressing relevant characteristics of the solder joints (*e.g.* fracture analysis, isothermal aging, TEM). At the end of each chapter, the most promising material combination of each coating method is tested on the Al rear side of solar cells. For this, the soldering process is transferred to industrial interconnection equipment, followed by module integration. Where successful, module testing and solder joint failure analysis is performed.

Finally, **Chapter 7** (p. 175 *ff.*) discusses general findings and compares the suitability of the different approaches. A conclusion of this thesis and outlook for future work is given in **Chapter 8** (p. 185 *ff.*).

2. Theory of Solar Modules and Fundamentals of Soldering

This chapter reviews the basic theoretical background for this thesis. This work combines investigations of the soldering process on Al surfaces from a materials science perspective with the application for the interconnection of solar cell rear sides. Therefore, both topics will be addressed.

In ***Section 2.1****, an introduction into the working principle of silicon solar cells and modules is given. The scope is on the PERC solar cell concept, its interconnection and module integration. In addition, special emphasis is put on the FoilMet® solar cell as profitable alternative by using a 10 µm thin Al foil as rear side electrode.* ***Section 2.2*** *introduces the general soldering process and the involved materials. The theory of phase diagrams of metal alloys and solid state diffusion is addressed. The last two subsections highlight the challenge of this work, to combine ultrafast soldering on Al surfaces and the industrial implementation of the soldering process in high-throughput inline stringers in the photovoltaic industry.*

2.1. Silicon Photovoltaic Cells and Modules

Photo**v**oltaics (PV) is the direct conversion of sun light into electrical energy. Photovoltaic devices are usually called "solar cells" and can be made from semiconductor materials. Semiconductors absorb sun light and realize a separation of the generated charge carriers. The induced potential difference can be used to enable a current flow. The most common solar cells are made from silicon (Si). The first silicon solar cell was presented by Chapin, Fuller and Pearson in 1954 with a photo conversion efficiency of $\eta = 6\,\%$ [19]. Today, a variety of solar cell concepts exist, *e.g.* homo- and heterojunction Si solar cells, III-V semiconductor solar cells, thin film, perovskite or organic solar cells and tandem solar cells, combining different technologies for enhanced light absorption. The best research cell efficiencies are collected and presented annually in a chart by the **N**ational **R**enewable **E**nergy **L**aboratory (NREL) [13]. For Si single junction solar cells, the best efficiencies are achieved with **S**i **h**etero**j**unction (SHJ) solar cells of 26.7 % and for two-terminal two-junction tandem solar cells with 32.9 %, reported in April 2020 [12, 13].

The PV market is dominated by Si photovoltaics with a share of >90 % [11]. In industry, the current state-of-the-art Si solar cell concept is the **p**assivated **e**mitter and **r**ear **c**ell (PERC). The following sections will briefly introduce this cell concept and the general working principle of a Si solar cell. More detailed descriptions and fundamental introductions are available in several textbooks treating fundamentals of PV (*e.g.* [20–23]).

In the following sections, the focus is on industrial Si solar cells and modules. Sections 2.1.2 and 2.1.3 present the working principle of PERC solar cells with special em-

phasis on their metal electrodes as the relevant part for the interconnection. Section 2.1.4 reviews the typical interconnection of solar cells and the fabrication of PV modules.

2.1.1. Working Principle of Semiconductor Solar Cells

Semiconductor materials use the photoelectric effect [24,25] to absorb sun light (photons): if the photon energy exceeds the energy of the semiconductor band gab, electrons can be transferred to the conduction band, where they contribute to current transport [20].

Si is a highly available material and an indirect semiconductor with a band gap at $E_G = 1.1\,\text{eV}$ (1.13 µm). The band gap energy limits the photo conversion efficiency, according to the Shockley-Queisser limit [26]. For Si, this ideal limit is around $\eta \approx 33.5\,\%$, whereas the practical limit, taking the Auger recombination into account, is even lower $\eta < 29.6\,\%$ [27].

To extract the charge carriers from the device, a positive and a negative contact are used. The junction between these two regions is called the *pn*-junction and can be created by doping of the silicon wafer. For standard PERC solar cells, the *pn*-junction is located inside the silicon substrate close to the front surface. The negative contacts are placed at the front, while the positive contacts are placed at the rear side.

In principle, a solar cell is similar to a *pn*-diode. Therefore, it is common to describe the solar cell *I*-*V* characteristic by a "diode model" [20]. Here, only the simplest form of the 1-diode model should be reviewed and the interested reader is referred to the literature for more complex models [20, 22].

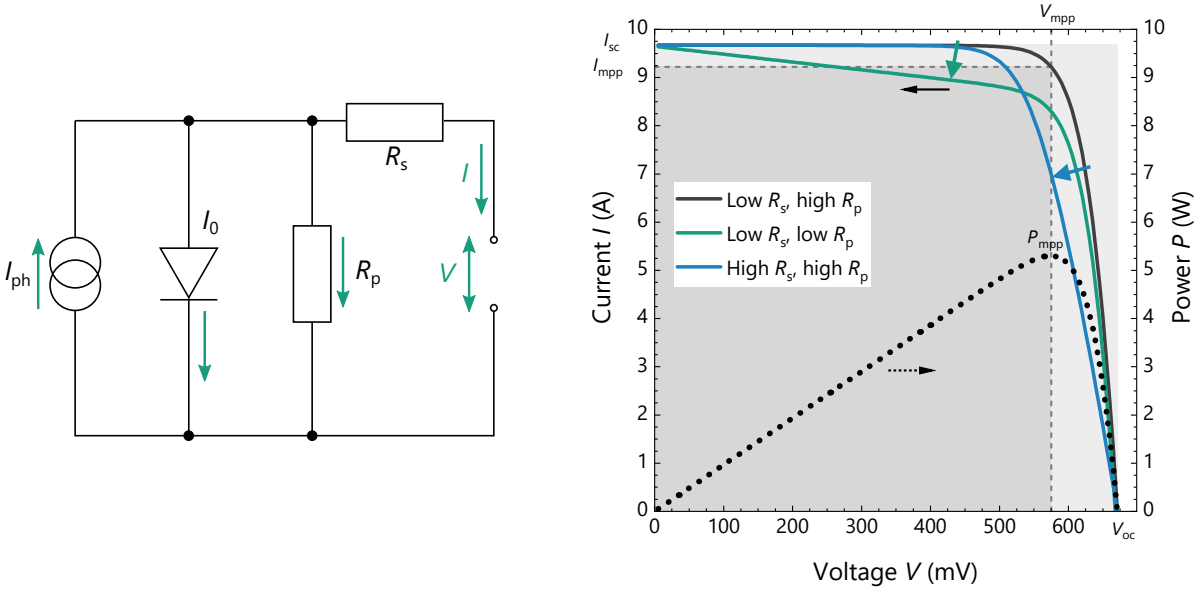

Figure 2.1.: Schematic of equivalent circuit of the 1-diode model and resulting *I*-*V* characteristics for different resistances.

The schematic drawing in Figure 2.1 shows the equivalent circuit of the 1-diode model for solar cells. While a typical diode has an exponential current increase after the threshold

voltage is exceeded, the solar cell has an opposing current flow I_{ph}, due to the light-induced charge carriers. It is common to plot the *I-V* characteristic in the first quadrant as shown in Figure 2.1: the positive current ($I > 0$) is the extracted current from the solar cell. When the voltage is increased, the current is reduced by the exponential diode current, with the dark saturation prefactor I_0. In practice, the resistances of the device have to be considered as well, either in series (R_{s}) or parallel (R_{p}) to the intended current flow. Their influence is demonstrated in the *I-V* graph in green and blue.[1]

The implicit equation for this is [22]:

$$I(V) = I_{\mathrm{ph}} - I_0 \left[\exp\left(\frac{V + IR_{\mathrm{s}}}{nkT}\right) - 1\right] - \frac{V + IR_{\mathrm{s}}}{R_{\mathrm{p}}}. \tag{2.1}$$

For any solar cell, two extreme cases can be examined. The short circuit state, where no voltage is applied, which leads to a maximum current flow $I(V = 0) \equiv I_{\mathrm{sc}}$. And the open circuit state, where no external current flows and the maximum voltage $V(I = 0) \equiv V_{\mathrm{oc}}$ is found.

As a solar cell is used to generate energy, the output power $P = V \cdot I$ is highly relevant. For the *I-V* curve (black) in Figure 2.1, the *P-V* curve is given by the dotted line on the right axis. There is a single **m**aximum **p**ower **p**oint (mpp), with $max(P) = P_{\mathrm{mpp}} = V_{\mathrm{mpp}} \cdot I_{\mathrm{mpp}}$.

For short and open circuit conditions, no power is generated, yet $I \leq I_{\mathrm{sc}}$ and $V \leq V_{\mathrm{oc}}$ and therefore $I_{\mathrm{sc}} \cdot V_{\mathrm{oc}}$ is an upper limit to P_{mpp}. Under practical operating conditions, the device is influenced by the diode and resistance losses. The ratio

$$\frac{P_{\mathrm{mpp}}}{V_{\mathrm{oc}} \cdot I_{\mathrm{sc}}} = \frac{V_{\mathrm{mpp}} \cdot I_{\mathrm{mpp}}}{V_{\mathrm{oc}} \cdot I_{\mathrm{sc}}} = FF \tag{2.2}$$

is called the **f**ill **f**actor *FF*. While I_{sc} and V_{oc} can be used to assess the potential of the device, the *FF* can be used as a figure of merit for the practical losses found. This is also illustrated by considering the photo conversion efficiency η. This is defined as the ratio of the output power to the input power P_0. Therefore, the highest η is found at mpp with

$$\eta = \frac{P_{\mathrm{mpp}}}{P_0} = \frac{FF \cdot V_{\mathrm{oc}} \cdot I_{\mathrm{sc}}}{P_0}. \tag{2.3}$$

Typically, these four parameters (I_{sc}, V_{oc}, *FF*, η) are derived from the measured *I-V* characteristics to compare different solar cells, without having to consider the full diagram. However, these parameters are not only used to describe single solar cells, but are also derived for solar modules, where several cells are interconnected, as described later.

[1] Parameters taken from a typical PERC cell with $\eta = 21.7\,\%$. Green curve: $5 \cdot R_{\mathrm{s}}$. Blue curve: $R_{\mathrm{p}}/100$.

2.1.2. Structure of Industrial Silicon Solar Cells

For industrial PERC cells, wafer sizes of 156.75 mm × 156.75 mm and larger with a thickness of 160 µm to 180 µm of mono- or multi-crystalline Si are used. A sketch of the cross section of a PERC structure is shown in Figure 2.2 on the left. For a *p*-doped base, the *pn*-junction is on the cell front side. The absorption of sun light is enhanced by a textured front side (typically "random pyramids" [28, 29]) and an **a**nti-**r**eflection **c**oating (ARC). The ARC is typically a dielectric (*e.g.* silicon nitride), therefore small contacts to the silicon substrate are formed by different metals for current extraction. On the solar cell front side, thin lines ("fingers") are in direct contact with the Si wafer (not shown) to collect the current and lead it to the "**b**us**b**ars" (BB), printed perpendicular. Depending on the process, the busbar can also be in contact to the substrate or "floating" as shown here. On the rear side, a full area electrode of Al paste is printed to form the positive contact. In the PERC concept, the rear side is protected by a surface passivating dielectric, to reduce the surface recombination and enhance the device performance. The direct contact with the Si is typically realized by **l**aser **c**ontact **o**penings (LCOs) of the passivation before Al deposition.

For the interconnection, the perpendicular busbars on the solar cell front side are used and therefore highlighted in Figure 2.2. On the rear side, additional local Ag "pads" serve as solderable areas to extract the current. Busbars on the front side and pads on the rear side are soldered to copper interconnectors for series connection. This interconnection step is described in Section 2.1.4.

More details on the design and fabrication of (PERC) solar cells can be found in textbooks and literature [20, 30–33].

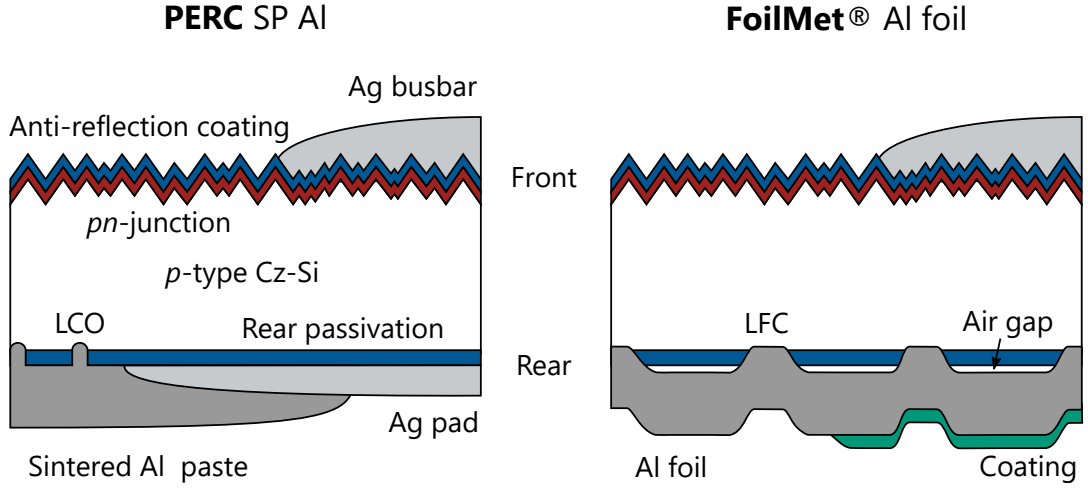

Figure 2.2.: Sketch of cross section of PERC solar cells. Not to scale. Left: State-of-the-art PERC structure with screen-printed (SP) Al rear electrode and Ag pads. Right: FoilMet® solar cell with LFCs and coated Al foil at the rear side.

2.1.3. Metallization of Silicon Solar Cells

The electrodes on cell front and rear side are conventionally fabricated by **s**creen **p**rinting (SP). This process is very simple and fast and has a market share over 95 % for front and rear side metallization in PV [11]. For the front side, Ag-based pastes and for the rear side Al-based pastes are used. After SP, the solar cell is heated up to about 850 °C for a couple of seconds ("firing") in an inline furnace.

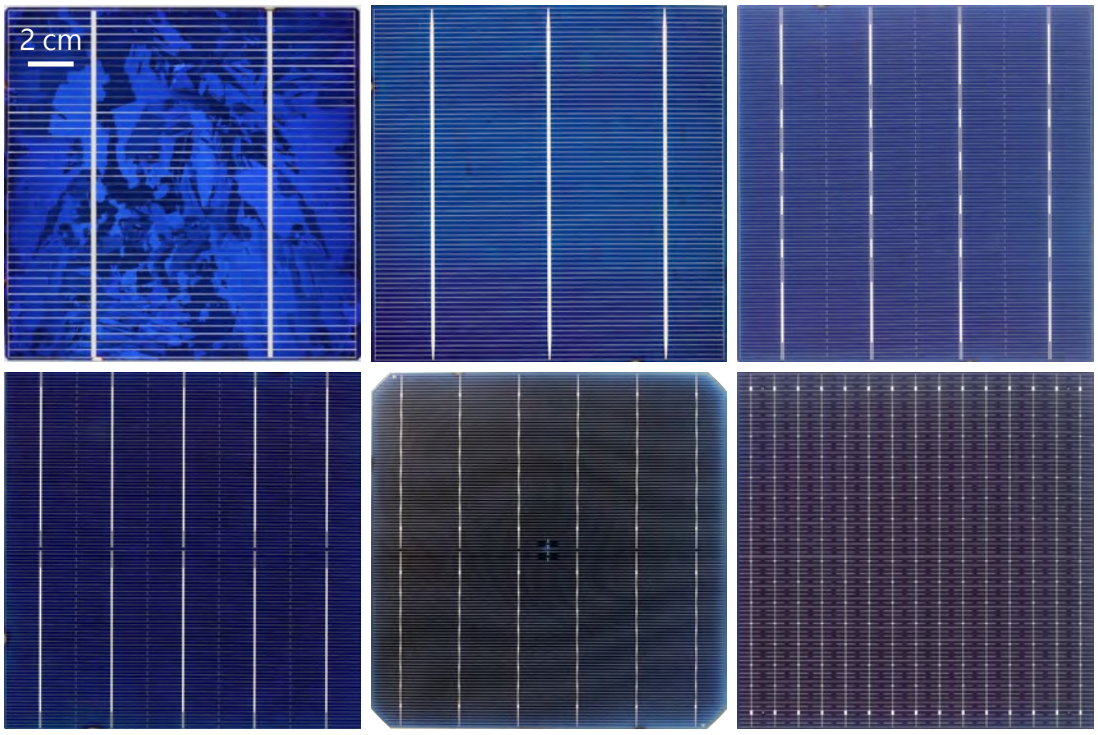

Figure 2.3.: Photographs of industrial silicon homojunction solar cell front sides of the last years. The industrially dominant market share changed from 2BB (2010) to 5BB (2020). Within the next years, 5BB cells will be displaced by 6+BB and busbarless cells as MBB [11]. The development of the front electrode shows the trend to finer and more complex structures to improve cell efficiency.

The pastes consist of Ag or Al particles with a diameter between 1 µm to 10 µm, organic binders and solvents. Optionally, a glass frit for the front side is used to locally etch the ARC under the fingers during the firing step. Where the ARC is removed, metal-semiconductor contacts are formed, to enable good current extraction. The Ag and Al particles are sintered during firing to enable a good lateral conductivity of the printed structures. In addition, Al can alloy into the Si, which creates a local doping during cooldown, called **b**ack **s**urface **f**ield (BSF), enhancing the contact [34, 35].

The solar cell metallization is typically different for the illuminated front side and the non-illuminated rear side (*cf.* Figure 1.2).[2] On the illuminated side, the metal electrodes reflect the light, which can be reduced by using smaller fingers. These have a lower conductivity, so that the number of collecting busbars is increased. The fabrication of smaller fingers has been improved in the past years [36]. Figure 2.3 shows a compilation of solar cell front sides over the past years, incorporating these advances, going from two busbars (2BB) up to recent "**m**ulti **b**us**b**ar" layouts (MBB). The **I**nternational **T**echnology **R**oadmap for **PV** (ITRPV) predicts "6+BB" or "busbarless" (including MBB) to be the dominant market share in 2024 [11].

As alternative metallization techniques to SP, electro plating [37], inkjet [38] and dispensing [39] are evaluated for solar cell fabrication. The current silver consumption represents 13 % of the cell processing cost and is therefore one of the most expensive components of the solar cell, beside the high costs of the silicon wafer [11]. To substitute Ag by cheaper metals like Al, it is therefore tried to enable different concepts with similar cell performances [17, 40].

FoilMet® Solar Cells

The PERC-based FoilMet® solar cell combines an improved photo conversion efficiency of the PERC technology with material cost savings for the rear side metallization. This concept was introduced by Nekarda *et al.* in 2007 [41] and has then been further improved by several researchers [40, 42–48].

A 10 µm thin Al foil was shown to work as replacement for the standard screen-printed and sintered Al in combination with **l**aser **f**ired **c**ontacts (LFC) to create a rear side metallization for high-efficiency PERC solar cells [41, 49]. A sketch of the cell concept is given in Figure 2.2 on the right. The LFC laser process is used to attach the aluminum foil to the rear side of the solar cell, creating the mechanical and electrical contact in one process step. With a laser processing time of $t_{\mathrm{pro}} \sim 0.8\,\mathrm{s}$ for industrial wafers, the throughput is comparable to the **l**aser **c**ontact **o**pening (LCO) reference process in common PERC production lines [45].

Figure 2.4 shows images of the contacts on the FoilMet® solar cell rear side. In a), an LFC contact is shown in an SEM cross section. Alloying of Al and Si at the LFCs leads to a mechanical and electrical contact, whereas an air gap between Al foil and Si wafer remains in between the LFCs. This leads to higher internal reflection and therefore a current gain of $0.4\,\mathrm{mA/cm^2}$ (average of a batch of 24 FoilMet® solar cells compared to 39 LCO reference solar cells [43]). Additionally, the replacement of screen-printed Al by Al foil offers a significant material cost-saving potential of 75 % predominantly due to reduced Al consumption [40].

In the past years, it has been shown that an adapted laser process is more suitable for attaching the Al foil on the cell rear side. The LFC process causes a reduction of the solar cell voltage V_{oc} due to laser damage and thus higher recombination at the contact

[2] A special case are so-called "bifacial" solar cells, which can be used to absorb light from both sides. These also feature fingers and busbars on the rear side.

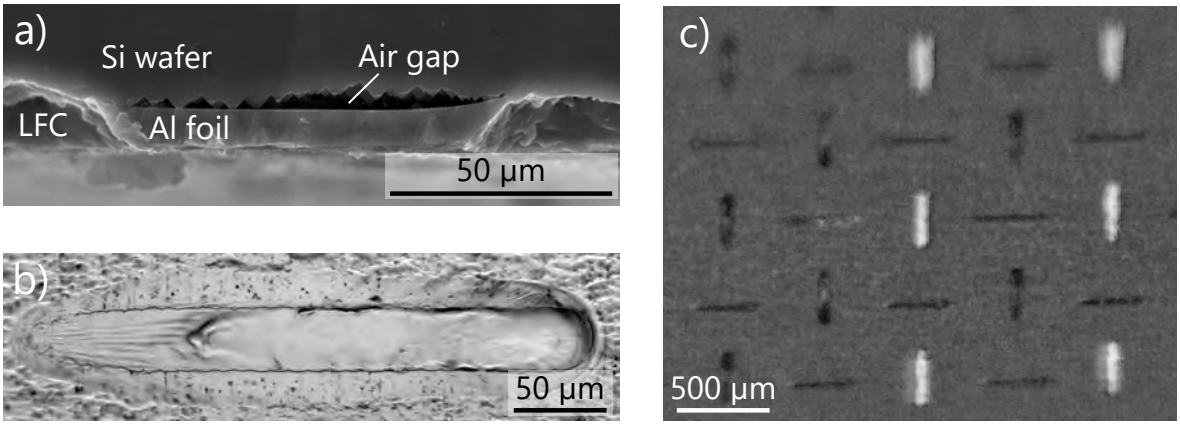

Figure 2.4.: The FoilMet® solar cell concept. a) SEM cross section of LFC contact on the cell rear side. Taken from [40]. b) Optical microscope image of contact created by LMB. Taken from [46]. c) *In-situ* photograph of the CW LMB process creating a cross dash pattern. Taken from [46].

points [50]. Therefore, a process called "**l**aser **m**etal **b**onding" (LMB) was introduced by John *et al.* in 2020 [46]. This new approach combines a gentle processing with an improved adhesion of the Al foil on the solar cell rear side. In Figure 2.4 b), a top view image made by optical microscopy of an LMB line contact is presented and in c) the corresponding laser process for the cross dash pattern is imaged *in-situ*.

2.1.4. Interconnection and Module Integration

Series Interconnection of Solar Cells

To increase the voltage for the PV module, several solar cells are connected in series. A principle sketch is shown in Figure 2.5 for the example of three solar cells. In the classical busbar front-to-rear interconnection, solder-coated Cu ribbons are soldered to front busbars and rear pads of each solar cell. To generate the series connection, the front electrode of one cell is connected with the rear electrode of the next cell and so on (*cf.* Figure 2.5 a) and c)). This leads to the summation of the voltage of each solar cell, increasing the power output of the string (*cf.* Figure 2.5 b)).

The most commonly used technique for interconnecting Si solar cells is soldering with SnPb-based solder alloys at temperatures around 250 °C. This process is realized on industrial inline tools (stringer), allowing for cycle times of less than 2 s per solar cell. The interconnection process by soldering is explained in Section 2.2.4 in detail.

Due to the increasing complexity of the front side metallization, the interconnection for high-efficiency solar cells is challenging and has to be adapted constantly. For a higher number of smaller busbars per solar cell (*cf.* Figure 2.3), the cross section of the ribbons becomes smaller. This increases the requirements for the alignment precision and process control during the industrial interconnection process. A continuative technological

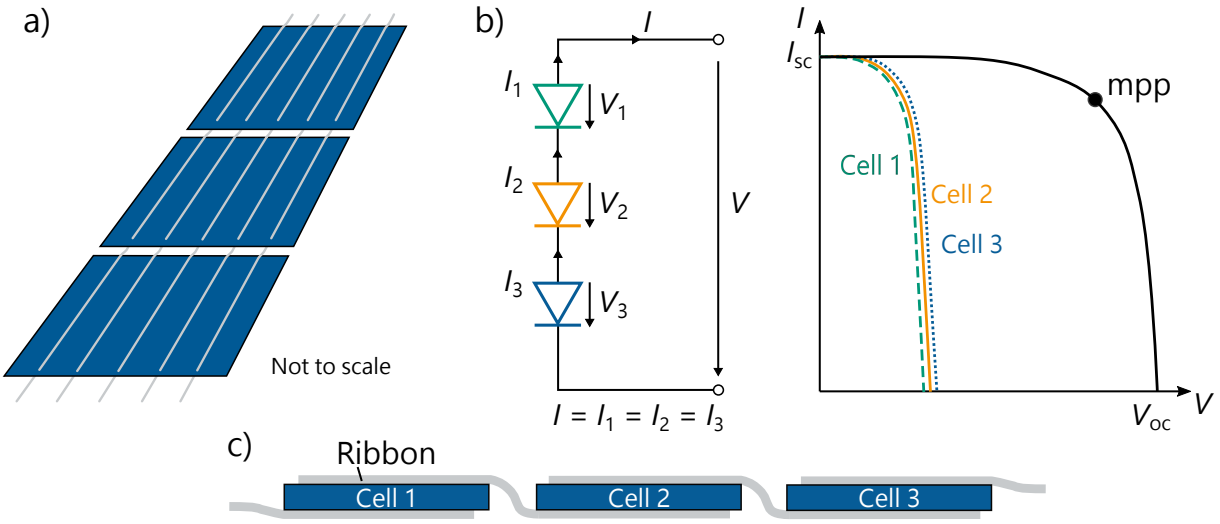

Figure 2.5.: Series interconnection of three solar cells. a) Sketch in tilted view. b) Simplified circuit diagram of three diodes with corresponding *I*-*V* graph. c) Sketch of side view of interconnected solar cells. Not to scale.

trend is the use of round wires for soldering [51–56], to reduce the shading losses of the interconnectors and to interconnect temperature-sensitive high-efficiency solar cells (*e.g.* SHJ or tandem cells).

There exist several other alternatives to the classical busbar interconnection by soldering *e.g.* soldering at reduced temperatures (using alternative solder alloys) [57–60] or the interconnection with **e**lectrically **c**onductive **a**dhesives (ECAs) [61–65]. Additionally, the shingle interconnection, using ECAs, realizes the series interconnection by direct overlap of the cells without additional interconnectors [66–70]. All approaches have their inherent advantages and disadvantages, depending on the solar cells and the desired module layout. The following section briefly describes the typical integration of cell strings into solar modules.

Conventional Design of Solar Modules

Due to their mechanical and chemical instability, solar cell strings have to be encapsulated into a solar module to ensure a reliable operation for > 20 years [71]. To maximize the output voltage of the module, six solar cell strings are connected in series ("cross connection") for a conventional 60-cell module [22]. To avoid huge losses in case of local shadings or hot spots, normally three bypass diodes are included. The classical module setup is visualized in Figure 2.6. For stability of the module, a 2 mm to 3 mm thick front glass of tempered low-iron soda-lime glass is used [72]. To improve transparency, the glass is textured, coated or could be reduced in thickness [73–75].

The matrix of interconnected solar cells is embedded into a (polymer) encapsulant by lamination. This ensures mechanical stability of the solar cells, electrical isolation of the components and physical isolation from the environmental exposure [76]. For state-of-the-art PERC modules, commonly **e**thylene-**v**inyl **a**cetate (EVA) is used as encapsulation

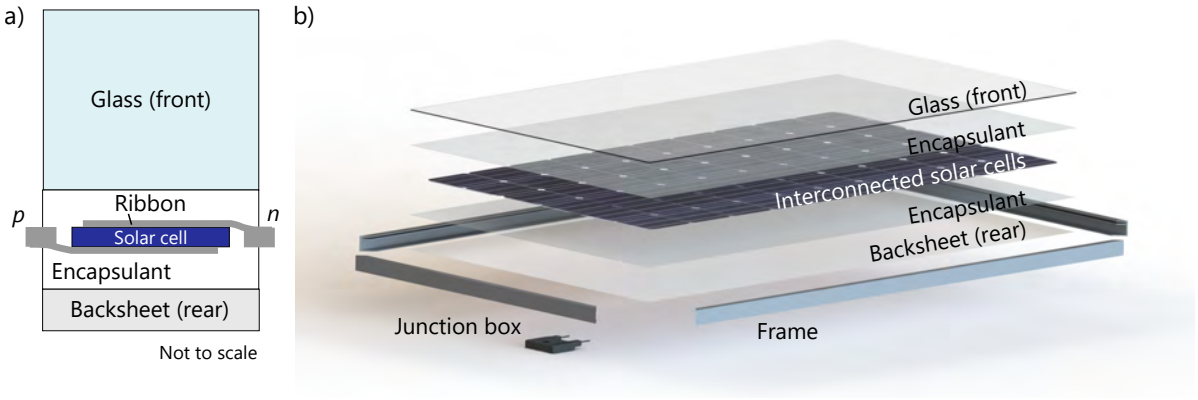

Figure 2.6.: Conventional PV module setup with commonly used materials. a) Sketch of side view (without module frame). Not to scale. b) Rendering of a 60-cell solar module. © Fraunhofer ISE

material since it is cheap and fulfills the requirements regarding transparency and processability. The choice of encapsulant influences lamination temperature and time, the optical properties of the module (and therefore the power output) and, during operation, the mechanical and chemical reliability [77, 78].

To protect the solar cells from the rear side, a multilayer backsheet, mostly consisting of **t**edlar-**p**olyester-**t**edlar (TPT), is used.

Industrial laminators consist of a hotplate, vacuum chambers and an elastic membrane. First, the module stack, sketched in Figure 2.6 on the right, is heated up so that the encapsulant melts and cross links. Typical lamination temperatures for EVA are 150 °C, held for 10 min. During this time, the chamber is evacuated, removing air and other volatiles to avoid bubbles inside the module. In addition, a pressure is applied to ensure safe bonding of all components. Therefore, a solar module is laminated with the front side (glass) facing down. After cooling, the Al frame and the junction box can be installed.

A conventional 60-cell-module consists of six strings with ten solar cells each interconnected in series. It measures approximately 1.6 m in height, 1 m in width and about 5 cm in thickness (with frame). Conventional modules are glass-backsheet modules, whereas the more robust glass-glass modules are widely used in combination with bifacial solar cells.

PV Module Testing

During operation of a PV module in the field, different influences affect the device performance. To certify the quality of a PV module, several test procedures are defined in IEC 61215 [79]. These are designed to simulate different stresses on the module components to reveal failure potentials of the final product. To quantify the effects, typically the I-V characteristics are compared before and after the test. According to the standard, the loss of power has to be less than 5 % after each test and less than 8 % after each test sequence, to make them "suitable for long-term operation in general open-air climates" [79]. Today, typical warranties for commercial PV modules are about 25 years,

including a guaranteed performance of 80 % nominal power output.

In addition to the *I-V* testing, visual inspection and **e**lectro**l**uminescence (EL) imaging can reveal local defects. Effects observed in testing can typically be correlated to different components of the module. The most relevant test for interconnection-related effects is **t**hermal **c**ycling (TC). In addition, **d**amp **h**eat (DH) and **h**umidity **f**reeze (HF) tests can also be performed to gain additional insights. Detailed descriptions of the tests performed in the context of this thesis are given in Chapter 3.4.4.

2.2. Joining of Metals by Soldering

Joining is a manufacturing process in which two or more solid components are connected together, *e.g.* by soldering, gluing, brazing, welding, bonding, forming or filling [80]. Depending on the component and its intended application, each of the above mentioned techniques has its advantages and disadvantages. As described in Section 2.1.4, the most common joining technique in PV is soldering. This process is described in the following.

According to ISO 857-2, soldering is a "joining process in which a molten filler material is used that has a lower liquidus temperature than the solidus temperature of the partent material(s), which wets the surfaces of the heated parent material(s) and which, during or after heating, is drawn into (or, if pre-placed, is retained in) the narrow gap between the components being joined." [81].[3] Soldering (German: "Weichlöten") and brazing (German: "Hartlöten") involve essentially the same bonding mechanism [7]. The main difference between soldering and brazing is the melting temperature, $T_\mathrm{m}(\text{solder}) \leq 450\,^\circ\mathrm{C} < T_\mathrm{m}(\text{braze})$ (and therefore the process temperature) and the material combination within the joint. Soldering is more suitable for PV manufacturing, as discussed later (Section 2.2.2). For soldering, a solder alloy with a defined melting point or range is used to form the joint. The two base materials stay solid at the used process temperature. In contrast to soldering, during welding (German: "Schweißen") no filler material is needed: at least the interfacial regions of the solid partners get liquid and form the joint at the interface.

In the following sections, the fundamental basics of soldering are explained. General introductions and further reading can be found in the textbooks of *e.g.* Klein Wassink [16] or Humpston [7]. The scope of the following sections is to introduce soldering with a special focus on the context of PV manufacturing and the restrictions and requirements found there. The general soldering process and the involved materials during soldering are presented in Sections 2.2.1 and 2.2.2. To provide a rough understanding of solder joint formation, phase diagrams of metal alloys and diffusion in solids are introduced in Section 2.2.3. The industrial implementation of the soldering process in Si photovoltaics is addressed in Section 2.2.4. For a better classification and evaluation of the performed

[3] German definition of **soldering** given in DIN ISO 857-2: "Fügeprozess, bei dem ein geschmolzenes Lot genutzt wird, das eine Liquidustemperatur besitzt, die tiefer ist als die Solidustemperatur der/des Grundwerkstoffe(s). Das geschmolzene Lot benetzt die Oberflächen der/des Grundwerkstoffe(s) und wird während oder bei Ende des Aufheizens in einen engen, zwischen den zu fügenden Teilen befindlichen Spalt hineingezogen (oder, falls vorab eingelegt, dort gehalten).", in Sec. 3.1 of [81].

experiments within this thesis, the requirements for solder joints in Si solar cells and modules are summarized in Section 2.2.5. The last Section 2.2.6 briefly summarizes the challenges of soldering aluminum surfaces.

2.2.1. The Soldering Process

Several different soldering processes can be used to join two metal components. Depending on the assembly (*i.e.* the thermal mass, temperature sensitivity, thermal conductivity, geometry) and the required process speed, one soldering technique may be better suited than others. For "reflow soldering" by contact, hot air, induction, ultrasonic, laser and **i**nfra**r**ed (IR) soldering, the solder is pre-placed between the base materials and gets liquid within the soldering process [7,16,82–86]. In contrast, the assembly is contacted by already molten solder during so-called "flow soldering" as wave or dip soldering [16, 82]. Within this work, manual contact soldering with a soldering iron (*cf.* Section 3.2.2) and IR soldering on an industrial stringer (*cf.* Section 2.2.4) are used. In the following, the soldering process is explained in general.

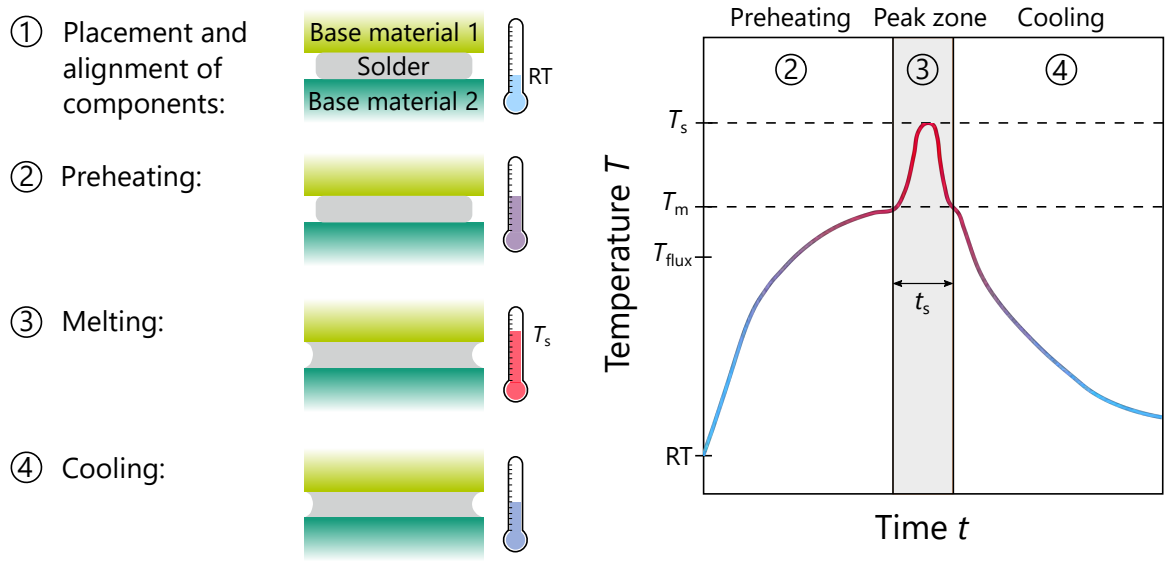

Figure 2.7.: Principle of soldering two components. Left: Sketch of general process steps for soldering two base materials. Right: Sketched soldering profile to explain the basic process parameters: activation temperature of the flux T_{flux}, melting temperature of the solder T_{m}, soldering temperature T_{s} and soldering time t_{s}.

Figure 2.7 illustrates the process steps for joining two base materials by a soldering process. The components are aligned and the solder is placed into the solder gap ①. The correct alloy and amount of solder has to be selected. Additionally, a well-chosen fluxing agent ("flux") influences the quality of the soldering result. Details on the involved materials will be given in the following section. After the alignment, the solder has to be heated up by one of the above mentioned soldering techniques ②. For some of them, this implies heating of the whole assembly. The temperature profile is sketched on the right

in Figure 2.7. When the activation temperature of the flux T_{flux} is reached, the flux has time to react with present oxide layers of the base materials and the solder and cleans the surfaces to ensure good wetting. After reaching the melting temperature T_{m} of the solder alloy, the alloy starts melting and wets the two base materials. The temperature reaches its maximum peak which is generally referred to as the soldering temperature T_{s} ($T_{\text{s}} > T_{\text{m}}$) ③. In the subsequent cooling phase, the solder solidifies and the whole assembly cools down to **r**oom **t**emperature (RT) at a controlled speed ④. The actual profile differs for each soldering technique and the soldering environment (*e.g.* ambient air, inert gas, vacuum). The period where $T > T_{\text{m}}$ is referred to as the soldering time t_{s}. If t_{s} is too short, this may lead to incomplete wetting and to thermomechanical stress due to rapid heating and cooling. If the soldering time is too long, the components are exposed to high temperatures for a longer period which can cause damage within the device.

Si photovoltaics is a very cost-driven and rapidly evolving industry. Given this, IR soldering in ambient air with very short soldering times has been established as the dominant soldering technique in the past years [87]. Yet, the interconnection process has to be adapted regularly while considering the various requirements and limits for soldering high-efficiency solar cells. The next section will first present the materials needed for solder joint formation before addressing the aforementioned requirements to define the boundary conditions for the soldering process within this thesis.

2.2.2. Materials and Requirements

A general overview on solder alloys for all temperature ranges can be found in textbooks, *e.g.* [7,16]. This section focuses on solder alloys and fluxes for the temperature range relevant for solder joints in a PV module. The boundary conditions, limits and requirements are discussed in the following.

Solder

The main component during soldering is the solder, which is a fusible metal alloy. It is used to join two work pieces together and create a permanent bond. A solder alloy consists of two or more metal components with a defined composition, normally given in weight percent ($\%_{\text{wt.}}$). There exist several solder alloy families which are arranged in Figure 2.8 left according to their base metal (x-axis) and melting temperatures (y-axis). In principle, a 6^{th} family, based on Au, could be listed. However, Au-based alloys are not of importance for PV due to their high costs and mostly very high melting temperatures.

To put these solder alloy families into the context of this thesis, the major requirements for the selection of a solder alloy for Si PV applications should be considered. Table 2.1 summarizes these requirements, sorted by their necessity. To not melt the base materials or remelt the solder alloy during operation of the PV module, the melting temperature of the alloy T_{m} should be lower than the melting temperature of the base materials (Cu interconnector and Ag metallization) and higher than the temperature of the solar cells

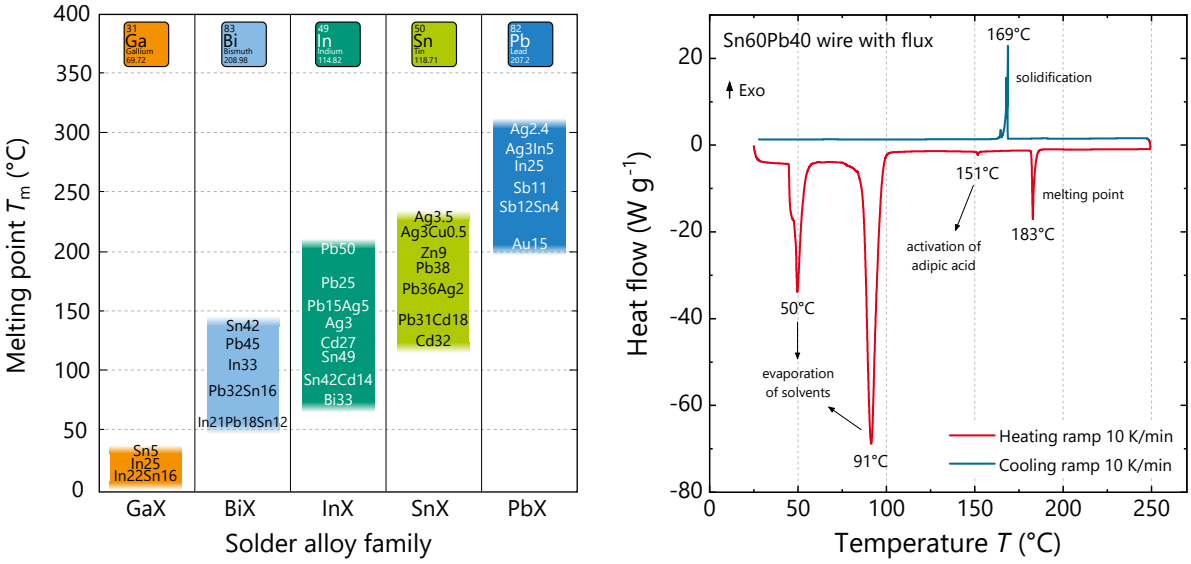

Figure 2.8.: Left: Solder alloy families and its (near-)eutectic combinations within 0 °C to 400 °C. The elements on the x-axis state the base metal, whereas X indicates an alloy with the above mentioned compositions. Redrawn after [7]. Right: DSC curves of Sn60Pb40 solder wire with flux. © Fraunhofer ISE

during operation of the PV module.[4] Additionally, the alloy can not be toxic or brittle and must be compatible with the solar cell. In particular, this means that neither the soldering temperature, nor the metals of the alloy will damage the solar cell. For good solder joint formation, good wettability of the base materials is essential. In addition to these requirements, it is advantageous to use no-clean flux since typical post-cleaning sequences are harmful to solar cells, time-consuming and therefore too expensive for PV module production. The alloy should be (near-)eutectic to allow for a very short soldering process (as discussed later) and all components of the alloy should be as cheap as possible and highly available to "fulfill" the existing cost pressure for PV module production (*cf.* Figure A.1).

Based on these frame conditions, Ga- and In-based alloys can not fulfill all requirements and are avoided for soldering in PV. Cd as additional component is as well not used due to its toxicity. The most promising solder alloy family is based on tin ($T_m^{Sn} = 232\,°C$) due to some significant advantages of Sn. Beside low costs and high availability, it provides good electrical and thermal properties required for joining of metals. Additionally, Sn forms a good metallic bonding to other metals and features a good flow behavior when liquid. For alloying with Sn, there exist a variety of other metals like Ag, Au, Bi, Cu, In, Pb, Sb and Zn. To solder Ag-dominant surfaces as present on common Si solar cells, it is advantageous to add Ag to the solder alloy to reduce Ag leaching within the joint by changing the concentration gradient for diffusion processes [16, 91].

[4] The module temperature during operation strongly depends on the module materials and setup (glass-glass, glass-foil), the type of solar cells, the size of cells and module and the module location of installation, tilt and orientation. Mostly T_{max} stays between 30 °C and 80 °C during module operation [88–90].

Table 2.1.: Requirements for the choice of solder alloy for the interconnection of Si solar cells.

Essential requirements	T_m alloy $< T_\mathrm{m}$ base materials and $> T_\mathrm{service}$ PV module
	Alloy is not toxic or brittle
	Alloy is compatible with solar cell: T-impact, materials
	Inherent wetting of base materials by liquid alloy
Additional requirements	Process compatibility of the alloy with no-clean flux
	Alloy is (near)-eutectic
	Alloy components are cheap and highly available

In the European Union, the RoHS (**R**estriction **o**f **H**azardous **S**ubstances) entered into force as of July 2006, restricting the usage of lead in electric and electronic components to a maximum concentration of 0.1 $\%_\mathrm{wt.}$ [18]. This caused an intensive research on lead-free alternatives and drastically influences the choice of solder alloys in many areas of application [92–97]. Subject to the regulations in Art. 2(4)(i) in the current RoHS 2011/65/EU, the usage of Pb in PV is excluded, whereas lead-containing solder alloys have still the highest marked share in Si PV.[5]

Within the past years of soldering in PV, the eutectic ternary alloy Sn62Pb36Ag2 has been replaced by the binary eutectic system Sn63Pb37 or the near-eutectic alternative Sn60Pb40 to further reduce costs by eliminating Ag.[6] A combination of Sn and Zn could also be used for the interconnection of Si solar cells, *e.g.* the eutectic alloy Sn91Zn9. However, Zn may lead to corrosion problems within the module and is known to be volatile [99]. The listed alloys in Figure 2.8 show the basic constituents and temperature distribution. In extension, other multicomponent systems have been developed, as found in literature. Table 2.2 presents a list of different alloys, their melting temperatures and the currently dominating application. Within this work, the eutectic alloy Sn62Pb36Ag2 with $T_\mathrm{m}^\mathrm{SnPbAg} = 179\,°\mathrm{C}$ has been widely used for manual soldering tests (contact soldering), whereas the near-eutectic alloy Sn60Pb40 with $T_\mathrm{m}^\mathrm{SnPb} \approx 183\,°\mathrm{C}$ is used for the industrial interconnection on the stringer (IR soldering). The intention is to use the established processes and materials for interconnection, whereas no optimization regarding Pb-free alternatives for soldering have been focused.

For some solar cell concepts, a lower melting point than 183 °C is required. On the one hand, some layers, *e.g.* the amorphous Si layer of SHJ solar cells, do not withstand such high temperatures, on the other hand, thinner Si wafers tend to more breakage, which is supported by a higher temperature difference during cooling after soldering (*cf.* CTE mismatch in Table 2.3). Therefore, Bi-based alloys have also been used as alternatives to Pb-containing alloys. Especially for upcoming interconnections with round wires (*cf.* MBB, SWCT®), SnBi-based alloys find a wide application in PV.

[5] Soldering with Pb-containing alloys: >90 % market share in 2019 in PV manufacturing [11].

[6] It is noteworthy to point out that suppliers of solder alloys typically give a range of $\pm 0.5\,\%_\mathrm{wt.}$ for their products [98].

Table 2.2.: Sn-based solder alloys arranged by their melting points [7, 16, 100, 101]. A general overview on lead-free solder alloys can be found in [102].

Alloy composition ($\%_{wt.}$)	Melting point solidus | liquidus (°C)	Application
Sn99.3Cu0.7	227	Electronics
Sn96.5Ag3.5	221	Automotive
Sn96.5Ag3Cu0.5	217 | 220	Electronics
Sn91.8Bi4.8Ag3.4	211	
Sn60Pb40	**183 | 190**	**Photovoltaics**
Sn62Pb38	183	Electronics*
Sn62Pb36Ag2	179	Photovoltaics**
Sn43Bi57	139	Consumer Electronics
Sn48In52	117	

*Before RoHS restrictions in 2006 **Until 2017

Flux

Beside the solder alloy, the choice of flux drastically influences the quality of the solder joint. If flux is used, cleaning of the surfaces prior to soldering can be omitted in many cases. This depends on the flux itself and the state of the surface to be soldered [7].

According to ISO 857-2, a flux is a non-metallic material which major task is to remove present oxide layers and avoid oxidation prior to solder joint formation [81]. There exist three main classes of fluxes: resin-based (organic), rosin-based and anorganic fluxes. The choice of flux strongly depends on the surface to be soldered and the used solder alloy. One of the main challenges with fluxes are the residues left behind after soldering. They are often corrosive and difficult to remove on the assembly. To avoid corrosion in the PV module, less aggressive solutions have been developed, which are often called "no-clean fluxes". They consist of a wide range of chemical ingredients, all only leaving "benign" residuals which can be left on the assembly. Due to the sensitivity of many solar cells and the potential for corrosion within the PV module, no-clean fluxes are the best option to use during soldering in PV. Those fluxes have a low solid content of $\sim 2\,\%$, are based on solvents *e.g.* isopropanol and acids as the organic adipic acid and only provide low to medium activity.

To activate the flux, a certain temperature has to be reached, depending on the flux ingredients. It is recommended to use a flux activating around 50 K below the liquidus temperature of the solder alloy. This allows the flux to have enough time to remove most of the oxides, prevent oxidation and support wetting. The exact behavior of the flux strongly depends on its chemical ingredients. It is known that the chloride content in rosin reduces the surface tension of Sn60Pb40, supporting spreading [16].

The reaction of Sn60Pb40 solder and a no-clean flux during heating and cooling are presented in Figure 2.8 on the right. **D**ifferential **s**canning **c**alorimetry (DSC) is used to measure the melting and solidification characteristics of a solder wire with flux core [103].

The heat flow, plotted on the y-axis, is measured with 10 K/min during heating (red curve) and subsequent cooling (blue curve). The two peaks at 50 °C and 91 °C represent the evaporation of the solvents of the flux. The small endothermic peak at 151 °C marks the activation of the adipic acid HOOC−$(CH_2)_4$−COOH of the used flux [16]. The heating rate during soldering influences the time span where the flux can react with the surface before melting of the solder starts. The melting point of the solder at 183 °C is given by an endothermic peak. During cooling, solidification of the solder sets in at 169 °C, given by the exothermic peak in blue. The lower the difference between melting and solidification of the solder, the better the nucleation of solidified phases, resulting in a finer microstructure. This temperature difference of about 14 K is called undercooling [104].

The melting of the solder is a phase transition from solid to liquid state. The melting temperatures of different solder alloys, can be deducted from the phase diagrams, among other information. On the other hand, phase diagrams offer valuable insight into possible stable compounds of different metal combinations. Therefore isobaric phase diagrams are briefly reviewed in the following section.

2.2.3. Phase Diagrams of Alloys and Solid State Diffusion

Each homogeneous region in a system is defined as a *phase*. Several phases can coexist within one system. The transitions between phases can be studied in phase diagrams. General introductions into (alloy) phase diagrams can be found in various textbooks [7, 16, 100, 105].

In most soldering applications, all processing is done at ambient pressure. Therefore isobaric phase diagrams are used, with the temperature T as the independent variable on the y-axis. For two-component systems of metals (*i.e.* an alloy), the ratio between the components is highly important. This concentration c of an alloy is usually displayed on the x-axis.

Phase Transitions in Binary Systems

In Figure 2.9, the binary phase diagram of lead and tin is given on the left. On the y-axis, the temperature T is given, on the x-axis the concentration of Sn in $\%_{\text{wt.}}$ (bottom) and $\%_{\text{at.}}$ (top).

The intersection with the y-axis at $x = 0$ and $x = 100$ state the melting points of pure Pb and Sn, respectively (black dots). They are connected by the liquidus line (light green). Above this line, the alloy is fully liquid (L). On the left and right α and β represent the Pb-rich and Sn-rich regions existing as solid solutions. This means that for the given concentration Sn is fully dissolved in Pb and vice versa. In the region $\alpha + \beta$, both phases exist (miscibility gap). For the case of SnPb, these can be easily detected by the contrast in optical and electron microscopy. The transition towards the $\alpha + \beta$ region, crosses a line called the solvus line. This can be used to determine the solubility of one metal in the other. The dark green line depicts the solidus line, confining the solid states of the alloy. The intersection of solidus and liquidus line is called eutectic point (Greek *eu tēxis* for "well melting", white dot), for PbSn at 183 °C and a composition of $c_{\text{Sn}} = 61.9\,\%_{\text{wt.}}$

and $c_{\mathrm{Pb}} = 38.1\,\%_{\mathrm{wt.}}$ (Sn61.9Pb38.1). Only for an eutectic solder alloy, a direct transition from liquid into solid upon rapid cooling is possible. A near-eutectic alloy, as Sn60Pb40, has a melting range between solidus and liquidus line.

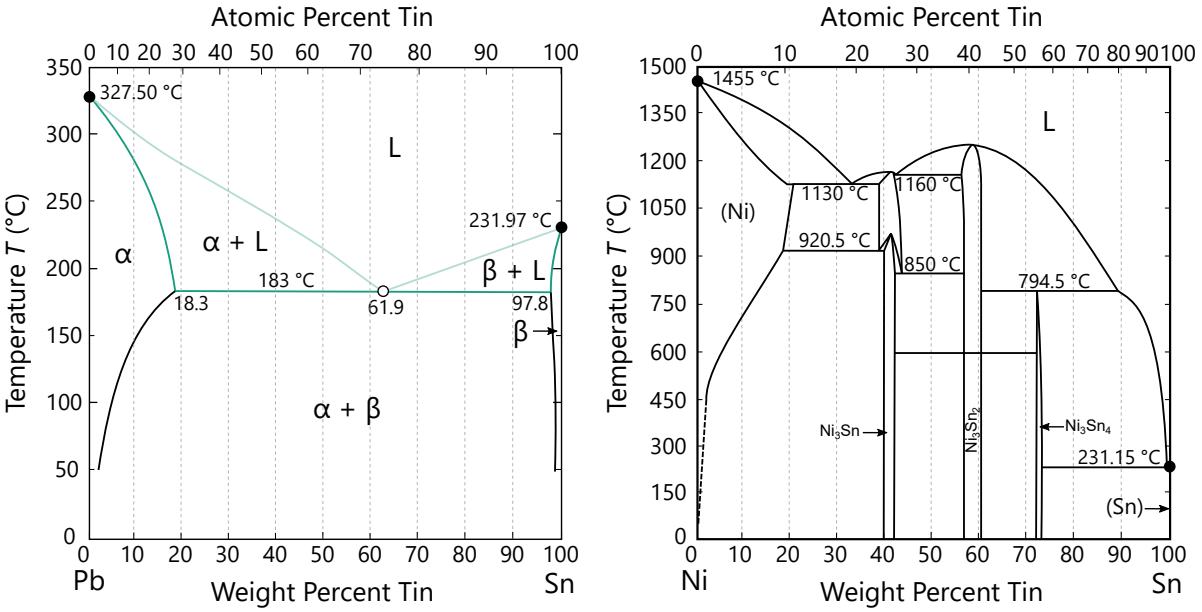

Figure 2.9.: Left: Binary phase diagram of Pb and Sn. Right: Binary phase diagram of Ni and Sn. Both diagrams adopted from [100].

In general, phase diagrams of metallic alloys can contain further phases in the intermediate region between the pure elements. They are called intermetallic phases or **inter**m**e**tallic **c**ompounds (IMCs). Their presence in binary and ternary systems is of relevance for this work.[7] One the one hand, IMCs are a good indicator for a metallurgical reaction between the solder and the base material. On the other hand, IMCs are known to be brittle and may cause failure within the joint if they get too thick [92, 106]. Figure 2.9 shows the NiSn phase diagram on the right. In this system, three IMCs can be found: Ni_3Sn, Ni_3Sn_2 and Ni_3Sn_4, all stable at RT. An IMC can either appear for a defined range of composition or with fix stoichiometric composition (*cf.* Al_3Ni in Figure A.4) but all within a finite region. Additional phase diagrams of binary alloys, relevant for this thesis, can be found in the Appendix A.5.

[7] The reasons for their formation is not focus of this work and can be further studied in one of the textbooks treating the material science for metal alloys [105].

Diffusion in Metal Components

To understand the formation of phases at metallic interfaces, the occurance of solid state diffusion has to be considered. Solid state diffusion is a static phenomenon without the presence of any external forces. It is driven by the concentration gradient Δc between two joined components. This leads to a particle flux j_D in both directions perpendicular to the surface and to particle exchange. The diffusion process can by described by Fick's first law [105]:

$$j_\mathrm{D} = -D\frac{\partial c}{\partial x}. \tag{2.4}$$

In general, the diffusivity D is material-, concentration- and temperature-dependent and follows an Arrhenius law:

$$D = D_0 \cdot \exp\left(\frac{E_\mathrm{a}}{kT}\right). \tag{2.5}$$

Across different metals, the activation energy E_a increases with increasing melting temperature of the element. D_0 is called diffusion constant and a material parameter, independent of temperature but depending on the concentration gradient. The concentration changes over time with the same diffusivity and the second spatial derivative of the concentration (Fick's second law):

$$\frac{\partial c}{\partial t} = D\frac{\partial^2 c}{\partial x^2}. \tag{2.6}$$

Figure 2.10 shows a sketch of the working principle of solid state diffusion at the interface of two metals in contact. Depending on the diffusion constant of metal A with respect to metal B D_0^{AB} and vice versa (D_0^{BA}), the depth of the diffusion zone Δx can be deeper in one metal than in the other.

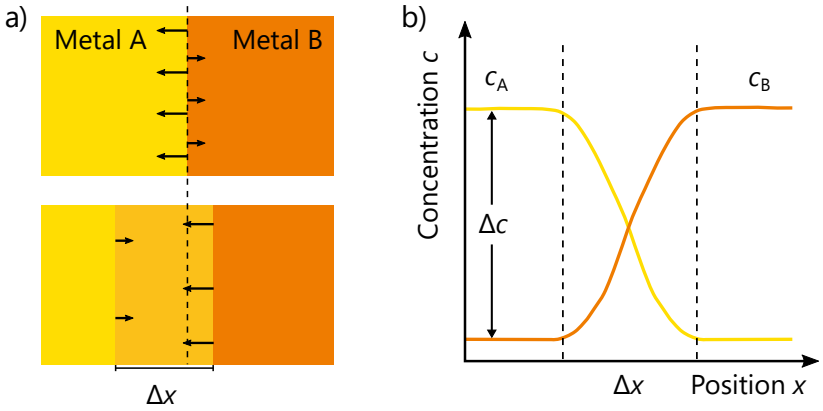

Figure 2.10.: a) Sketch of principle of solid state diffusion of two metal components A and B in contact. b) Simplified concentration profiles for diffusion zone Δx.

Identification of Local Phase Formation

Within this thesis, the solder alloy used for soldering onto coated Al substrates or Ag metallization of solar cells is always Sn60Pb40 or the previous version Sn62Pb36Ag2. To generate a solderable coating for Al, different metals as Ag, Ni or Cu are used wherefore the interfaces after soldering may exhibit different diffusion zones and phase formation. To quantify the interfacial reactions, especially the formation of IMCs, binary or ternary phase diagrams serve as helpful tool. As an example, the system of Ni and Sn (Figure 2.9 on the right) can be used to illustrate the approach applied within this work.

After soldering with Sn-based solder onto a Ni surface, the solubility of Ni within Sn and vice versa lead to diffusion at the interface. To analyze the thickness of the diffusion zone and possible intermetallic layers, *e.g.* line scans with EDX can be performed perpendicular to the interface; the quantification of a line scan reveals a concentration profile $c(x)$ depending on the position x perpendicular to the interface.

The binary phase of Ni_3Sn_4 dominates in an Sn-rich environment. The quantification of the EDX line scan would reveal $\sim 43.5\,\%_{\text{at.}}$ Ni and $\sim 56.5\,\%_{\text{at.}}$ Sn, which matches to the ratio 1.0:1.3 of Ni:Sn at this position in the phase diagram. To make a reliable statement on phase formation at a metallic interface, the stoichiometry of the involved metals has to be determined in atomic percent for comparison with the IMCs given in the phase diagrams. In addition to the two introduced phase diagrams, additional ones of AgSn, CuSn, SnBi, CuNi, AlNi and AlCu can be found in the Appendix A.5.

2.2.4. Industrial Implementation of Soldering in PV Industry

Materials

To realize a series connection of several solar cells, the front electrode of one solar cell is connected with the rear electrode of the next solar cell and so on (see Figure 2.5 as introduced in Section 2.1.4). Figure 2.11 gives a detailed overview on the solder joints formed by both-side contacting a PERC solar cell with Sn60Pb40-coated Cu ribbons after the industrial stringing process. The six images on top and bottom exemplarily show magnifications of the image in the middle, labeled with A-F. The two joining partners are the Ag metallization of the solar cell (*i.e.* front busbar in A-C and rear pad in E+F) and the Cu core of the ribbon. Both metals (Ag and Cu) are known to be easily solderable [16] since they do not form stable oxides. However, the electrodes of the solar cell, front busbars and rear pads, are fabricated by screen printing Ag pastes followed by a firing process (*cf.* Section 2.1.3). Therefore, the wettability of Ag busbars and pads may be different compared to *e.g.* pure evaporated Ag.

The temperature range used for soldering PERC solar cells is about 220 °C to 260 °C peak temperature, depending on the used solder alloy. The near-eutectic alloy Sn60Pb40 with a melting temperature of 183 °C is one of the most suitable ones for solar cell interconnection, ensuring fast melting and solidification. Since the interconnection is done with a high throughput (cycle time $t_{\text{cycle}} < 2\,\text{s}$), the alignment of solar cell and Cu ribbon has to be realized very fast. Therefore, it is advantageous to coat the Cu ribbon with a solder layer prior to cell interconnection. Commonly, manufacturers of solder ribbons

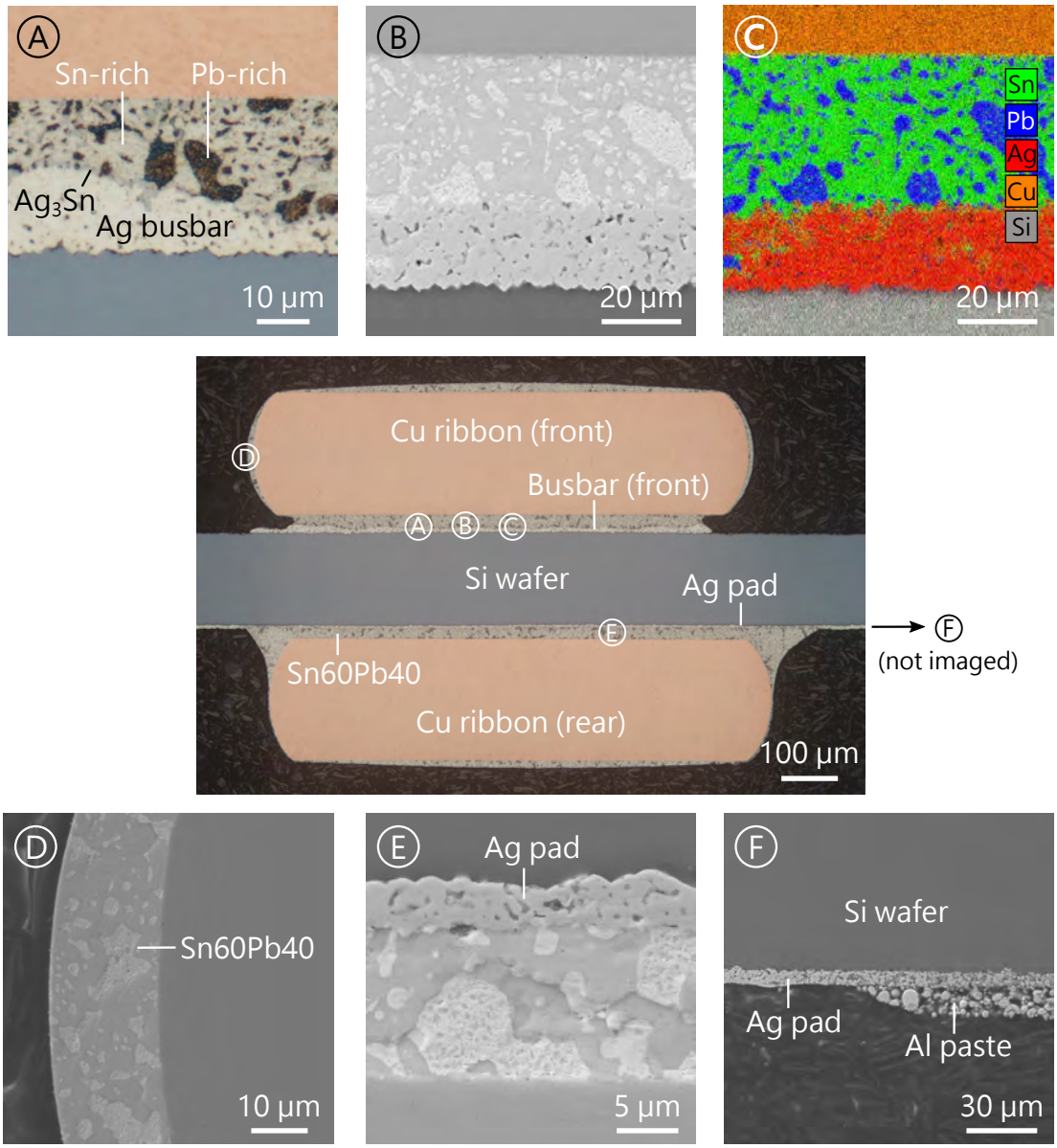

Figure 2.11.: Cross section of a both-side interconnected monofacial Si solar cell (PERC). Optical microscopy (A, middle image), SEM (B, D, E, F, all taken at 20 kV) and EDX (C) are used to show different parts of the interconnected solar cell.

for PV (*e.g.* *Luvata* or *Ulbrich*) use a hot dip tinning process where the Cu ribbon or wire is guided through a liquid solder bath. By variation of the velocity, the thickness of the solder layer can be adjusted in a particular range. The conventional solder-coated Cu ribbon has a solder layer in the range of 10 µm to 25 µm (*cf.* SEM image D in Figure 2.11), whereas wires feature 5 µm to 15 µm solder coating. The solder layer remaining on top of the ribbon, *i.e.* not contributing to the solder joint formation, protects the bare Cu core from oxidation.

The dimension of the Cu core of the ribbon is roughly matched to the current to collect from one solar cell, to reduce the loss in power. A state-of-the-art PERC cell ($P_{mpp} \approx 4.9\,W$) has a current of about $I_{mpp} \approx 9\,A$ at the maximum power point. In a 5BB configuration, each ribbon collects 1.8 A with a loss in power of less than 1 % over approximately 150 mm contact length per ribbon. A more detailed consideration of the power and resistance losses of a solder joint on a Si solar cell can be found in the Appendix A.3. The higher the number of busbars per solar cell, the more ribbons or wires are used with simultaneous reduction of their cross section. On the one hand, this leads to more solder joints per solar cell (increased redundancy) and therefore to a reduced impact of one joint on the fill factor, on the other hand, the designs of the electrodes become smaller,[8] which increases the requirements regarding the alignment precision of the ribbons/wires and the strength of the solder joint.

Industrial Stringer Process

The implementation of the soldering process in industrial PV manufacturing is realized on inline tools ("stringer"). The throughput of these automated machines ranges from 1000 to 5500 solar cells per hour, resulting in less than 2 s process time for each solar cell. The general procedure for interconnecting solar cells is given in Figure 2.12.

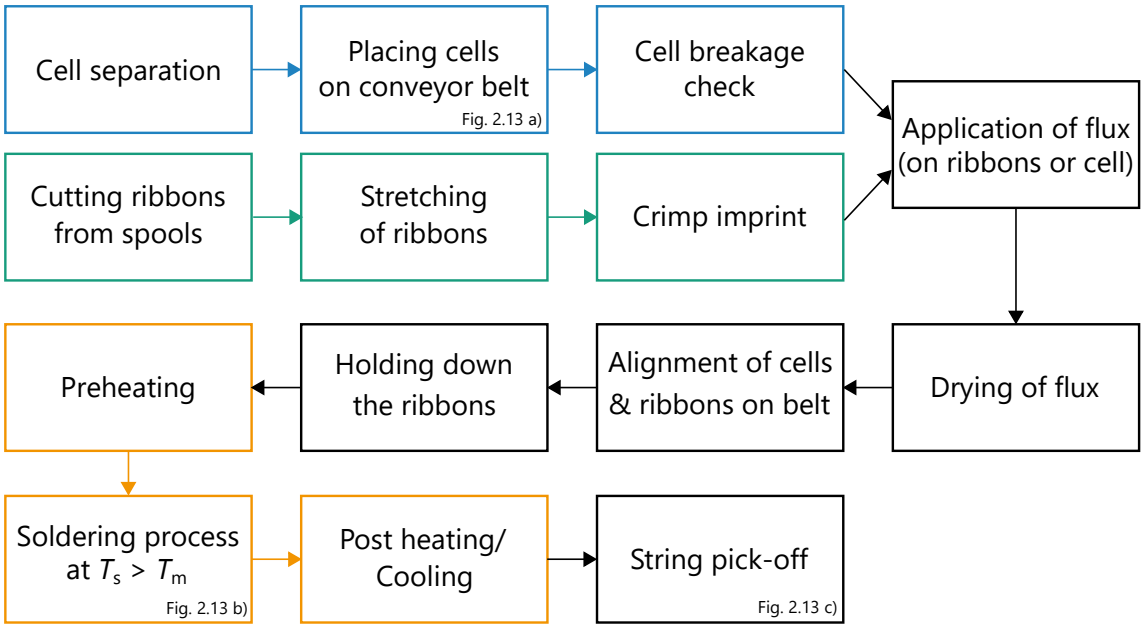

Figure 2.12.: Process steps for industrial interconnection of solar cells within an automated stringer. The main soldering steps are given in the orange boxes.

[8] Typical busbar width are: 0.8 mm on a 5BB solar cell, 0.6 mm on a 6BB cell, 0.1 mm pad width on a 9BB, 0.7 mm pad width on a 12BB solar cell. It has to be considered that most of the cells with more than 6BBs are used as half-cells within a PV module and larger cell dimensions, which affects the current per cell.

The solar cells are fed into the machine out of boxes. After separation *e.g.* by an air stream, the cells are placed onto the conveyor belt of the stringer (s. photo in Figure 2.13 a)). A camera is used to inspect for cell cracks or unintended rotated cells. At the same time, the ribbons are cut from their spools[9] and are stretched for a defined length ($\sim 0.5\,\%$ of initial length) to straighten them and improve their handling. To interconnect two solar cells, a ribbon length of approximately twice of the cell length is required. In the middle of this ribbon (in the cell gap), a crimp is imprinted to avoid cell cracks at the edges (*cf.* Figure 2.5). Prior to soldering, no-clean flux is applied onto the metallization of the solar cells or the ribbons (depending on the stringer). For the alignment, ribbons and solar cells are placed on the belt alternately so that five ribbons are in contact with the cell rear side and five ribbons with the cell front side. Hotplates are used to heat the conveyor belt. A fixation unit is put onto cell and ribbons to prevent the "stack" from shifting ("down holder").

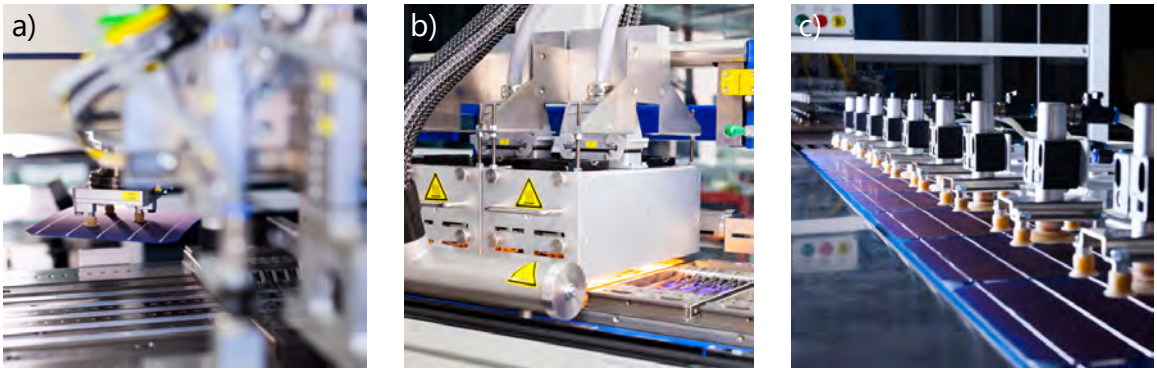

Figure 2.13.: Photographs of the industrial stringer "TT1800" of the company *teamtechnik GmbH*. a) Pick-up of the solar cells out of their boxes and placing them onto the conveyor belt. b) IR lamps during soldering. c) String gripper at the end of the stringer to pick-off the solar cell strings. © Fraunhofer ISE

The orange boxes in Figure 2.12 correspond to the main soldering unit of the stringer. The set temperature profile is given in Figure 2.14 on the left. This example shows the temperature of the hotplates (blue) and IR lamps (yellow) with a cycle time $t_{\mathrm{cycle}} = 2000\,\mathrm{ms}$. The liquidus temperature T_{liq} of Sn60Pb40 is marked with a black dashed line. For preheating, three hotplates (HP 1-3) are used. When reaching 150 °C, the activation temperature of the flux is reached and the reaction starts. Two additional hotplates (HP 4+5) are used to support in the main heating zone. Here, two IR lamps[10] are used (s. photo in Figure 2.13 b)) to heat the solar cell above the liquidus temperature of the solder. The rest of the flux solvents evaporate and the solder wets the Ag metallization and the Cu core of the ribbon. The down holding unit keeps everything in place until the cooling phase starts (HP 6-8) and the solder is completely solidified. Finally, the interconnected string of solar cells is picked off the belt by a string gripper (s. photo in Figure 2.13 c)).

[9] For the interconnection of a 5BB solar cell 10 spools are necessary.
[10] The spectrum of the IR light is near-infrared radiation with a maximum at 1200 nm.

Compared to contact soldering, IR soldering is contactless and therefore very flexible regarding the size and geometry of the assembly to be soldered. Additionally, it can be used to solder through IR-transparent materials. Disadvantages of using IR lamps are the indirect heating of the solder via the solar cell and a strong dependence on the emissivity of the components which leads to inhomogeneous heating. This requires to heat up the whole solar cell and expose it to higher temperatures for some seconds. This can become critical for temperature-sensitive solar cells. To achieve the desired high throughput with the inline tool, the process speed has to be very high, requiring short cycle times. To ensure the full compliance of the process and to reach the desired power per area, practically two IR lamps are used in series in the stringer presented in this work.

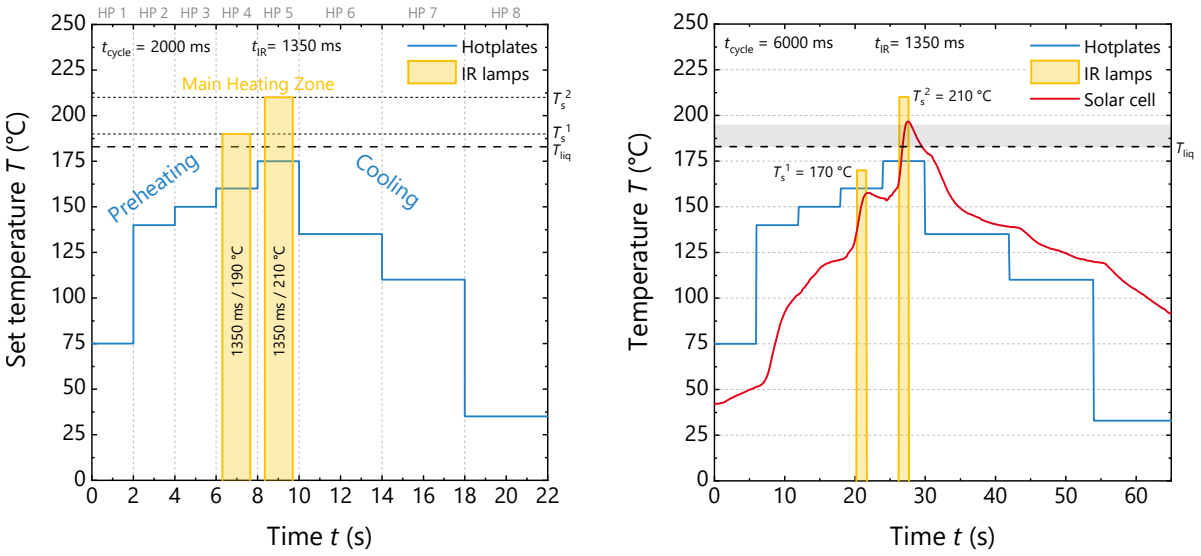

Figure 2.14.: Temperature profiles of IR soldering within the industrial stringer. Left: Set temperature profile of the industrial interconnection of PERC solar cells (1800 cells/h) with Sn60Pb40-coated ribbons and a cycle time of $t_{\mathrm{cycle}} = 2000\,\mathrm{ms}$. The heating and cooling of the cells is supported by hotplates (blue), the main heating is performed by IR radiation of two lamps (yellow). Right: Example for temperature measurement of a monofacial PERC cell within the stringer, measured at a cycle time of $t_{\mathrm{cycle}} = 6000\,\mathrm{ms}$.

The right graph in Figure 2.14 shows an example of a temperature measurement with a thermocouple on the front side of one monofacial PERC solar cell during its way through the industrial stringer. The cycle time has been extended by a factor of 3 ($t_{\mathrm{cycle}} = 6000\,\mathrm{ms}$) compared to the industrial process, as the automated inline machine could not handle the solar cell contacted with six thermocouples and down holder. Nevertheless, the active time of the IR lamps was kept at $t_{\mathrm{IR}} = 1350\,\mathrm{ms}$ as for the industrial profile on the left. The strong heating effect of the IR light on the solar cell temperature becomes clearly visible. The temperature drop between lamp 1 and 2 (at $t \approx 23\,\mathrm{s}$) is assumed to be negligible if the cycle time is reduced. This measurements only shows one possible example. The set parameters could be further adjusted to reach the desired soldering profile.

The process described above is a classical busbar interconnection of solar cells, dominating the market for PV manufacturing ($> 90\,\%$), since most of the cell technologies currently feature 4, 5 or 6 busbars ($\sim 95\,\%$) [11]. Beside IR soldering, other manufacturer use induction, contact or hot air soldering within their stringer [87]. The right choice of soldering profile strongly influences the solder joint formation and especially the thermomechanical stresses induced during cooling. This topic is shortly introduced in the following.

Coefficient of Thermal Expansion

In general, all materials expand and contract with different rates upon temperature changes. As different materials are firmly connected during soldering, thermomechanical stress can be induced during cooling of the assembly. As an example, Table 2.3 gives the **c**oefficients of **t**hermal **e**xpansion (CTE) for all relevant parts during the interconnection process of a Si solar cell. Mainly the difference between the CTE of the Si solar cell ($\sim 2.6 \times 10^6\,\mathrm{K}^{-1}$ at RT) and the Cu core of the ribbon ($\sim 17 \times 10^6\,\mathrm{K}^{-1}$ at RT) support stress induction during heating and cooling of all components.

Table 2.3.: Coefficients of thermal expansion (CTE) of different components. Most of the data is temperature-dependent.

Component	**Material**	**CTE** ($10^6\,\mathrm{K}^{-1}$)	**Reference**
Si solar cell	Silicon	2.3 - 4.7	[107–109]
	Ag metallization	10	[110, 111]
	Al paste	16	[112]
Interconnector	Copper	17	[113]
	Solder (Sn60Pb40)	25.2	[114, 115]
	Solder (Sn42Bi58)	15	[116]
Other	Aluminum	46.4	[117]

As an illustration of the stress induced by the CTE mismatch, a simulation using the **f**inite **e**lement **m**ethod (FEM) is carried out by a colleague at Fraunhofer ISE [118].

Figure 2.15 shows the results of a Si solar cell after the soldering process when cooling from 183 °C (stress-free temperature; solidus temperature of Sn60Pb40) to 25 °C. Details of the input parameters (geometry, materials, material properties) are listed in the Appendix A.4. The color code qualitatively states the enhancement of the first principle stress [77, 119], pronounced at the end of the soldered ribbons. In research, such simulations serve to identify critical parameters, *e.g.* to reduce the stress by good matching of the materials, geometries and processes. For the development of a good solder joint on a solar cell, the stress enhancement at the end of the ribbons has to be considered and will be discussed within the results of this work.

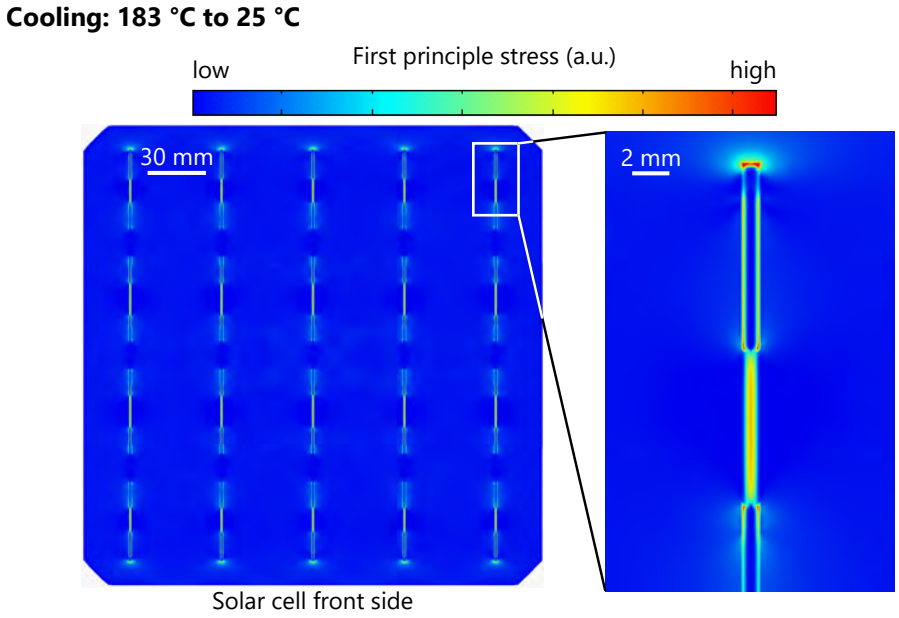

Figure 2.15.: Enhancement of first principle stress in a Si solar cell after soldering. Results of an FEM simulation of an interconnected solar cell for cooling from 183 °C to 25 °C. Further details on the simulation can be found in the Appendix A.4.

There exist several other options to actively reduce these thermomechanical stresses *e.g.* adaptation of the busbar layout at the cell edges [119], controlling the cooling ramp after soldering by hotplates, both-side (symmetrically) interconnected solar cells, interconnection with wave-shaped wires [120] or reducing the yield strength of the Cu ribbon [121,122].

One specific characteristic of solders is their creep behavior. For Sn60Pb40, RT is already $0.65 \cdot T_\mathrm{m}$ (in K), whereas phase coarsening by diffusion, *i.e.* changes of the microstructure, is very likely. Creep leads to a reduction in stiffness resulting in stress relaxation.[11]

2.2.5. Requirements for Solder Joints in Si Solar Cells & Modules

The solder joints in the PV module play a central role for the overall module performance. To utilize the maximum power conversion of the solar cells, losses due to the interconnection process have to be minimized. For each solar cell and module concept, the diligent selection of suitable interconnection materials and processes is of prime importance. For a reasonable process and material development, the requirements for solder joints on a Si solar cell within a PV module have to be considered.

Table 2.4 gives an overview on these requirements for the three "levels" (joint, string, module) of the soldered interconnection. First, an appropriate solder alloy provides a high **conductivity** σ_solder through the joint for current transport from the solar cell into the Cu core of the ribbon. Second, the overall **contact resistance** R_c at the two interfaces of the solder joint has to be as low as possible. Both can be evaluated on simple test

[11] As an example, for Sn60Pb40 halving an uniaxial strain of 20 N/mm^2 at 50 °C takes about 1 h, 10 N/mm^2 nearly 10 h and 5 N/mm^2 nearly 100 h [16].

Table 2.4.: Requirements for solder joints in Si solar cells and modules and corresponding measurement indicators.

	Requirement	**Indicator**
Solder joint	High vertical conductivity	σ_{solder}
	Low contact resistance	R_{c}
	Material compatibility with solar cell	τ
Cell string	Mechanical stress resistance	F
	Equal contacts across cell	I_{EL}
	Material compatibility with solar cells	c_{i}, I_{PL}
PV module	Equal contacts across module	I_{EL}
	Material compatibility with cells and module	$I(V)_{\text{TC,DH,...}}$
	Mechanical stability under thermal changes	$I(V)_{\text{TC}}$
	Chemical resistance	$I(V)_{\text{DH}}$
	Low CTM loss in power	ΔP_{mpp}

structures. Third, the materials used for soldering (alloy, flux) have to be **compatible with the solar cell**, to not influence the operation of the solar cell, *e.g.* by reducing the lifetime τ of the excited charge carriers within the semiconductor. Several information on critical contaminants is available in literature [21] and can be easily reproduced with *e.g.* symmetrical lifetime samples.

After the industrial interconnection process, the solar cell strings have to show a certain **mechanical stress resistance**. To ensure a fast and reliable module integration, they have to withstand the string handling. The 90° peel force F on cell front and rear side can be evaluated as a measure for the mechanical stability of the solder joints. A successful interconnection of a solar cell can be characterized by a homogeneous intensity of the **e**lectro**l**uminescence (EL) signal I_{EL} indicating **equal contacts and a homogeneous current flow** across the solar cell. Again, the **compatibility of the used materials with the solar cells** is of great importance. On the one hand, the process parameters (*i.e.* soldering temperature and time) could negatively affect the solar cells (*cf.* EL image with cell damage in Figure 3.13). On the other hand, a possible diffusion of metal i into the Si wafer can be investigated by measuring the EDX concentration c_{i} along a certain length x of the solder joint into the solar cell. In addition, **p**hoto**l**uminescence (PL) imaging can be used, where a high signal I_{PL} is correlated with dominant radiative recombination within the solar cell (*i.e.* high lifetimes).

The solder joints in a PV module are exposed to further influences which can lead to a power degradation of the module. There exist several requirements for solder joints within the module, to guarantee a long lifetime without interconnection failures. A maximum power output of a large-area module is reached, if a **homogeneous interconnection across the whole module** is realized, yielding a uniform EL signal I_{EL}. For the PV module, the **compatibility of the interconnection materials with the solar cells and the module materials** is essential. On module level, repeated I-V measurements

offer valuable information on potential degradation. To ensure a reliable module performance over years, this has to be evaluated by accelerated aging tests (thermal cycling (TC), damp and heat ingress (DH)) and other environmental impacts, depending on the module location. Regarding the solder joints in the PV module, the **mechanical stability** under thermal cycling and the **chemical resistance** *e.g.* within damp heat testing should be evaluated to ensure a successful interconnection process. The *I-V* measurement of the module reveals global information about the module degradation. In general, losses caused by the interconnection can be summarized within the cell-to-module (CTM) loss, influencing the overall loss in power ΔP_{mpp} of a solar module [123].

This list of requirements offers a guideline for material, process and product development for interconnection in PV. If parameters deviate from the established standard process flow described in the previous sections, the impact on the listed requirements can be evaluated starting from simple and going to more complex samples. Examples could be alternative interconnection materials, novel solar cell metallizations or new module encapsulants, among others.

In this thesis, solder joints on coated aluminum electrodes are investigated, targeting an integration into the established PV interconnection process. The experimental work discussed in this thesis, will evaluate suited samples along the presented guidelines on different levels. The following section reviews the overall challenge of soldering aluminum surfaces.

2.2.6. Soldering of Aluminum

Aluminum is much cheaper than Ag or other (precious) metals, provides a good conductivity and is widely available (*cf.* Figure 1.1). It is used in many applications, due to its several advantages [17]. A general overview is given in the appendix in Section A.2. In PERC solar cells, Al is typically used as the rear side electrode, as it allows excellent contact to the *p*-type Cz-Si wafer [35, 124]. In contrast to the front side Ag electrodes, the Al surface brings up challenges for direct contacting for solar cell interconnection. Al surfaces are not directly solderable because of their native Al_2O_3 oxide layer, which is formed within seconds when exposed to air. Al_2O_3 is a very stable insulating layer with a thickness around 3 nm to 5 nm [125]. It prevents wetting of the surface by the liquid solder.

There are well-established approaches to overcome the challenging Al_2O_3 layer in engineering and electronics. Table 2.5 gives an overview on the three most common approaches, which are described in the following.

Adjustment of Soldering Process

To use soldering as joining technique for Al components, the process parameters and/or the involved materials can be adapted. The most commonly implemented process change is soldering under inert gas [126]. After cleaning of the Al surface and removal of the oxide layer, oxidation is prevented due to oxygen exclusion and a firm bonding can be realized by using conventional solder alloys and flux. However, a joining process under

Table 2.5.: Approaches for joining Al surfaces. Due to the native oxide film, it is challenging to use the established soldering process in PV to directly contact Al. In mechanical engineering and electronic industry, several alternatives have been established.

Approaches for soldering of aluminum	Ref.
Adjustment of soldering process	
Soldering under inert gas	[126]
Aggressive flux	[127]
Al solder alloys *e.g.* silumin	[128]
Al cleaners	[127, 128]
Ultrasonic soldering	[129–131]
High process temperatures $T > 400\,°C$	[17, 128]
Alternative joining processes	
(Vacuum) brazing	[132–134]
Inert gas welding	[126, 135]
Fusion welding	[135]
Arc welding	[135, 136]
Laser welding	[137]
Friction stir welding	[138, 139]
Modification of Al surface	
Laser surface treatment	[140]
Ultrasonic surface activation	[141]
Friction stir processing	[142]
Solderable coating/cladding	[143–147]

inert gas is expensive, which is why alternatives for soldering at ambient air have been developed. To remove the stable Al_2O_3 layer prior to soldering, aggressive fluxes, special Al cleaners [127, 128] or ultrasonic soldering [129–131] can be applied. Furthermore, long soldering times $t \geq 15\,\text{min}$ for oven soldering in combination with suitable solder alloys and fluxes can be used to contact Al components by soldering [127, 128]. There exist a variety of solder alloys (*e.g.* silumin) and fluxes on the market, which are developed for soldering of Al components. However, in combination with particular solder alloys and fluxes, increasing the joining temperature is also effective in most cases (depending on involved materials), which makes alternative joining processes feasible for Al surfaces.

Alternative Joining Processes

If the process temperature can be increased without damaging the base materials, brazing and welding provide suitable joining techniques for Al. Depending on the involved components (*i.e.* materials, dimensions) and the requirements for the joints during operation, vacuum brazing [132–134], inert gas welding [126, 135], fusion welding, arc welding, laser welding [135, 137, 148] or friction stir welding [138, 139] can be used. In addition, the application of active brazes supports solder joint formation of high mechanical and

electrical quality, as it is well established for soldering of ceramic components [149, 150].

Most of the approaches presented so far are not compatible with the established processes of solar module production. To provide an industrially feasible approach, the conventional, fast soldering process has to be used as far as possible and further process changes have to be as cheap as possible. Therefore, it is advantageous to realize a solderable Al surface, which would allow to use established interconnection equipment, processes and materials.

Modification of Al Surfaces

A promising solution for this is a pretreatment of Al to provide solderability by a surface modification. Special laser processes can be used to remove oxides and change the surface roughness [140]. Alternatively, activation of the Al surface by ultrasonic processes [141] or friction stir processing [142] are done, immediately before joining.

Another alternative to contact Al is the application of a solderable coating or cladding. Numerous investigations focus on solderable coatings of Al. The most relevant ones are summarized shortly in the following.

A process for coating of Al surfaces was protected by a patent in 1927 by Hewitson [143]. It is based on electrolytic coating and is most widely used for plating onto Al. Since then it has been optimized by various groups. One study with focus on PV was published by Kamp *et al.* who used a zincate process for wet-chemical treatment of the Al surface to force an exchange reaction between Al and zincate [147]. This process allows plating on Al and sufficient adhesion on PVD Al layers was demonstrated. A similar electrochemical process based on zincate was published in 2016 by Nagel *et al.* [146]. Here, the focus was on soldering onto PVD Al and screen-printed Al. In 2012, Jung *et al.* developed a metallization stack based on NiV to allow solderability of evaporated Al for cell interconnection [151]. Similar research was done by Kumm *et al.* where a solderable and long-term temperature stable PVD metallization was characterized to enable soldering on evaporated Al rear sides of PERC cells [145]. Another approach to make Al solderable is the application of tin-based solder in combination with ultrasonic soldering as done by von Campe *et al.* [130] and Schmitt *et al.* [131].

Beside PV applications, there have been other studies on coating of Al, *e.g.* by Zhao *et al.* in 2006 [144]. Within their work, they developed a cold spray process to deposit a braze alloy onto an Al alloy. Due to a high particle velocity during spraying, deformation of the braze alloy takes place, inducing a rupturing of the oxide.

As introduced in Section 2.1.3, the FoilMet® solar cell concept features a rear electrode consisting of a 10 µm thick Al foil, attached by the LMB process. To realize solderability of this cell rear side, three different coating approaches of Al foils are evaluated within this thesis: roll cladding (Chapter 4), wet-chemical coating (Chapter 5) and sputter coating (Chapter 6). The fundamentals of these coating techniques are presented in Section 3.1. They all allow to coat the Al foil prior to the attachment onto the cell rear side. The finished FoilMet® solar cell with solderable Al rear side can then be interconnected by established tools of PV production lines.

3. Experimental Methods and Characterization Techniques

This chapter gives an overview on the experimental methods and introduces the most relevant characterization techniques, applied to obtain the results within this work. The three coating techniques, used to provide a solderable layer on top of Al surfaces, are discussed in ***Section 3.1****: roll cladding (Sec. 3.1.1), as a mechanical bonding technique, wet-chemical coating (Sec. 3.1.2) and magnetron sputter deposition (Sec. 3.1.3). Beside the introduction of the deposition methods, the requirements for the coating, specific for each approach, are listed. The solder joint evaluation on material level is mostly conducted on 200 µm thick Al foil, which is shown in* ***Section 3.2****. Furthermore, the manual contact soldering process, used for sample preparation on Al foils, is described. The last part of this section presents the design of the experiments, conducted within this work.* ***Section 3.3*** *gives an overview on the characterization methods for solder joint evaluation: As initial characterization of the coatings, wetting tests with liquid solder are performed (Sec. 3.3.1). After soldering, the strength of the solder joints is tested by peel force measurements (Sec. 3.3.2). Interfacial reactions are analyzed by microstructural analysis using electron microscopy (Sec. 3.3.3). Finally, the electrical properties are evaluated by contact resistance measurements (Sec. 3.3.4). In the last part of this chapter,* ***Section 3.4*** *addresses the electrical measurements conducted on Si solar cells (I-V, luminescence imaging) and the performed aging tests on material (isothermal aging) and solar module (temperature cycling, damp heat) level.*

3.1. Coating Techniques

In this section, the three coating techniques used to deposit solderable layers onto the Al surface are described: roll cladding, wet-chemical coating and magnetron sputter deposition. Depending on the deposition method, the deposited material (coating) has to fulfill certain requirements to be processable by soldering for solar cell interconnection. In general, these are:

- Provide solderability for SnPb-based alloys in combination with no-clean flux
- Form a firm bond to the Al substrate
- Provide a low contact resistance
- Be resistant to oxidation and corrosion
- Remain long-term stable upon aging
- If possible, prevent Al and oxygen diffusion

Beside the analysis of the solder joints, the evaluation of different coatings regarding these aspects is presented in Chapters 4, 5 and 6 for each coating technique. The working principle of the coating techniques are introduced in the following.

3.1.1. Roll Cladding of Metal Foils

In this thesis, roll cladding is used to coat the Al foil with a solderable layer during the foil fabrication process. Cladding is both a mechanical coating technique as well as a joining technique for two or more metals [152]. It finds application in the automotive sector, in electronic industry but also in thermal engineering and coinage, beside others [152, 153]. Roll cladding is part of the rolling process, used for thinning metal foils. Compared to chemical or physical vapor deposition techniques, this method is based on mechanical joining of two or more metal layers through an externally applied pressure by rolls. Figure 3.1 left shows a sketch of a roll stand with the involved components.

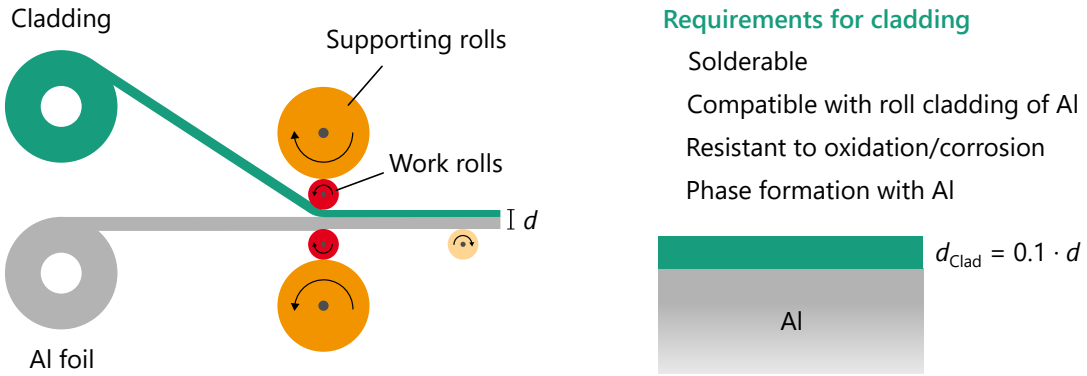

Figure 3.1.: Left: Sketch of a quarto roll stand for cladding of two metal foils. The final composite has the total thickness d. Right: Requirements for cladding.

Typically, two process variations are distinguished by the process temperature: cold and warm roll cladding. Whereas the cold roll process is conducted at RT, during warm rolling the composite is heated to a certain temperature before cladding. This allows for higher degrees of deformation, supports diffusion at the interfaces, but can also lead to unfavorable oxidation.

At the contact point of the rolls to the foil, a high compressive stress in the direction of the sample normal is applied. For cladding of Al foils, this causes cracking of the native Al_2O_3 layer. Plastic deformation leads to a direct mechanical contact between the roll cladded layer and the Al surface which is supported by diffusion processes at the interface. In general, a vertical material deformation of about 50 µm or more is required to realize a compact layer system through a cold roll process [152]. The degree of the required deformation strongly depends on the metal combination [154]. During roll cladding, the vertical material deformation of each layer is influenced by its mechanical properties. Because the integrated layers can only be thinned proportionally, only materials with a similar hardness can be joined together. In order to realize the target thickness for each material layer, the initial layer thicknesses have to be considered. On the right in Figure 3.1, the requirements for the coating are listed in particular for the performed roll cladding process.

Within this thesis, a cold roll process is used to fabricate a material compound of Al foil and a solderable layer. The process is carried out externally on a roll stand of *SCHLENK Metallfolien GmbH & Co. KG* or *Wickeder Westfalenstahl*. Other research studies have shown that there are several parameters influencing the quality of the roll cladded product [152, 154].[1] While different claddings are investigated in this thesis, they have been supplied by the mentioned manufacturers. As the fabrication is therefore not exactly the same, the direct comparability between different claddings is limited.

Due to the used cold roll process, the quality of the initial materials is highly relevant and the surface morphology of the used rolls during rolling and cladding plays a major role. To improve the adhesion between Al foil and coating, an additional heat treatment after cladding is tested for some of the material compounds.

For the process implementation into the FoilMet® solar cell process, this comparably simple approach is of high relevance since it can be done in combination with the standard production process of the Al foil. This potentially results in a very cheap and industrially feasible process.

[1] Parameters of relevance are *e.g.* the process temperature, the surface morphology of the rolls, the speed of the rolls, the curvature of the rolls, the friction during rolling, the thickness ratio of the two metals, the roll gap, the material properties of the initial metals (*e.g.* composition, stiffness), the thickness of the initial metals and the degree of plastic deformation within one rolling pass [152, 154].

3.1.2. Wet-Chemical Coating

There exist several possibilities to realize coatings out of a bath, by spraying, evaporation or other deposition methods, based on a chemical reaction of the material source with the sample to be coated. As an alternative to screen-printed and sintered electrodes of Si solar cells, electroplating of Ni, Cu and Ag can be used as a wet-chemical coating method [11, 155, 156].

A similar method is electroless plating, which is used in this work. To provide a good adhesion and remove the Al_2O_3 layer, a pretreatment of Al, with *e.g.* zincate, is required.[2] Afterwards, an additional coating can be deposited to preserve the interface, *e.g.* by a wet-chemical deposition of Ni on top of Al. Different variations of this process are compared in this thesis to coat Al substrates. They are carried out on lab scale equipment at Fraunhofer ISE and are described in the following.

Zincate Process

The zincate solution is used to remove the native Al_2O_3 layer and to activate the aluminum surface by an exchange reaction. A single zincate (s-Zn) as well as different double zincate (d-Zn) processes are tested to prepare the Al foils before Ni plating. This process is widely known as pre-treatment for Al coatings or surface modification [99, 158–162]. The general procedure for electrochemical coating in this work is sketched in Figure 3.2 on the left.

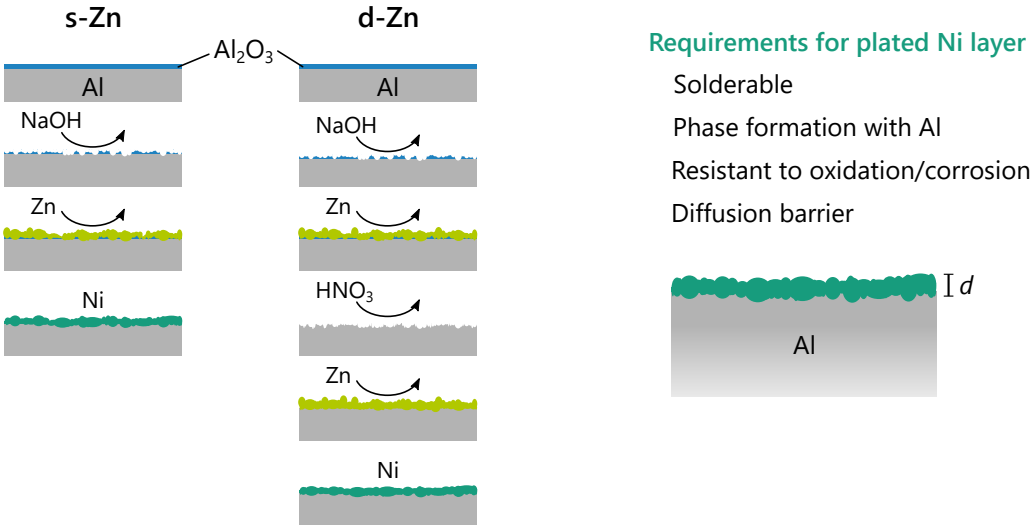

Figure 3.2.: Left: Sketch of process sequence for a single (s-Zn) and double (d-Zn) zincate treatment, followed by electroless Ni plating. Right: Requirements for plated Ni layer.

A commercially available Zn bath of *SurTec* with pH = 14 is used at room temperature [163]. The ingredients of the bath are listed in Table 3.1.

[2] There exist a variety of possible pretreatments for Al surfaces, which have been summarized by Critchlow *et al.* [157].

Table 3.1.: Ingredients of Zn bath used for zincate treatment of Al substrates, taken from the data sheet of *SurTec*.

Amount (%)	**Ingredient**	
10-20	Sodium hydroxide	NaOH
5-10	Zinc sulfate heptahydrate	$ZnSO_4{*}7\,H_2O$
3-7	Nickel(II) sulfate hexahydrate	$NiSO_4{*}6\,H_2O$
<1	Copper(II) sulfate pentahydrate	$CuSO_4{*}5\,H_2O$

This alkaline NaOH based solution reacts with the Al_2O_3 surface layer and leads to its dissolution in the bath [164]:

$$2\,NaOH + Al_2O_3 + 3\,H_2O \longrightarrow 2\,NaAl(OH)_4. \tag{3.1}$$

The Al can then react with the Zn leading to Zn deposition in the form of small seeds. This exchange reaction during Zn treatment is described by:

$$3\,Na_2Zn(OH)_4 + 2\,Al \longrightarrow 2\,NaAl(OH)_4 + 4\,NaOH + 3\,Zn. \tag{3.2}$$

Zn is reduced and Al is oxidized in this reaction. Electrons, released by the anodic reaction, are used within the cathodic reaction resulting in Zn deposition. Within this work, the process time for the s-Zn treatment is kept constant at 30 s bath time. For the d-Zn treatment, the samples are dipped into nitric acid (30 %) after the first Zn step, to remove the deposited Zn layer and to clean the Al:

$$Zn + 2\,HNO_3 + 6\,H_2O \longrightarrow Zn(NO_3)_2 * 6\,H_2O + H_2. \tag{3.3}$$

A second Zn step leads to improved homogeneity of the Zn layer, with more seeds on top of the Al as analyzed in detail in Section 5.1. Since a layer of pure Zn has shown to cause corrosion within a PV module [99], it is preferred to either completely remove Zn or fully cover it with a protection layer as *e.g.* Ag, Sn or Ni. Another disadvantage of Zn is its limited wettability with liquid solder (*cf.* Figure 5.3 in Section 5.1.2). Therefore, Ni plating is chosen as coating technique to provide a solderable and long-term stable layer on top of the Al substrate.

Electroless Nickel Plating

In contrast to electroplating, no external electric current or voltage and no sacrificial Ni anode are required for electroless plating. This allows the formation of dense and homogeneous Ni coatings by the deposition of Ni, chemically available in the solution (reducing agent). A commercially available Ni electrolyte based on Ni sulfate with a low sodium hypophosphite content of about 30 g/l and pH $\approx$ 4.8 is used [165]. The bath is constantly stirred and the temperature is set to $(88 \pm 2)\,°C$ resulting in a deposition rate of about $18\,\mu m\,h^{-1}$ during electroless plating [164]:

$$Ni^{2+} + H_2PO_2^- + H_2O \longrightarrow Ni + H_2PO_3^- + 2\,H^+. \tag{3.4}$$

Hydrated sodium hypophosphite reacts as reducing agent with the Ni ions of the electrolyte. For this study, the plating time was kept constant at 8 min, leading to a Ni layer of about 2.0 µm - 2.5 µm thickness.

In this thesis, Zn treatment in combination with electroless Ni plating is used to coat pure Al foils and the rear side of FoilMet® solar cells as well as PERC cells with PVD Al rear side (*cf.* Chapter 5). In Figure 3.2, the specific requirements for the plated Ni layer are listed on the right. The following table summarizes the process variations, used for the different Al substrates under investigation.

Table 3.2.: Parameter range of the wet-chemical process: (single/double) Zn treatment and electroless Ni plating of Al foils, FoilMet® solar cells and solar cells with PVD Al rear side.

Substrate	Process	Process time	Bath temperature	pH
200 µm thick Al foil	s-Zn	30 s	RT	14
	d-Zn	30 s + (15 - 30) s	RT	14
	Ni	8 min	88 °C	4.8
FoilMet® solar cell	d-Zn	20 s + 20 s	RT	14
	Ni	8 min	88 °C	4.8
PERC with PVD Al	d-Zn	15 s + 15 s	RT	14
	Ni	8 min	88 °C	4.8

3.1.3. Magnetron Sputter Deposition

Sputtering is a vacuum-based coating method and is, as well as electron-beam physical vapor deposition and thermal evaporation, categorized as **p**hysical **v**apor **d**eposition (PVD). The major advantage of sputtering is the possibility to deposit several thin layers of a wide range of different materials with a high reproducibility and homogeneity onto a substrate. The method is established in a broad spectrum of industries including semiconductor manufacturing and commonly used for novel solar cells with *e.g.* transparent conductive oxides [166] and absorber or thin film solar cell production [167].

Magnetron sputtering is a plasma-based coating process where a magnetically confined plasma is created near the surface of a target material. Positively charged ions from the plasma collide with negatively charged target material, and atoms from the target are ejected or "sputtered" onto the substrate. A sketch of a general magnetron sputter process is given in Figure 3.3 on the left.

Within this thesis, the layer deposition is carried out at Fraunhofer ISE on a horizontal inline plasma coater within an argon atmosphere.

The focus in this thesis is on very thin total stack sizes ($d < 100$ nm) of the sputtered layers, which reduces material consumption as well as total production costs and rates. The sputter deposition is performed after the fabrication of the Al foil. To achieve a

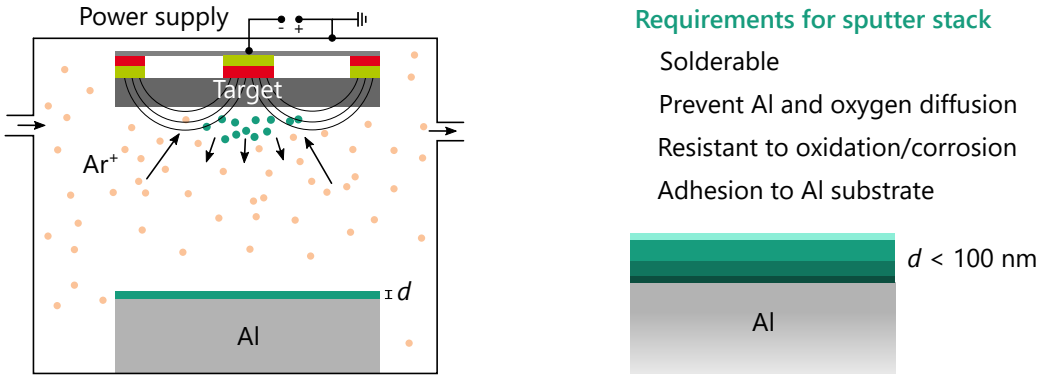

Figure 3.3.: Left: Sketch of magnetron sputter process to deposit very thin layers of thickness d in the nm range. Right: Requirements for sputter stack.

firmly bonded connection to the Al foil, argon plasma surface etching is used prior to the deposition of an adhesion layer (Cr, NiCr). A diffusion barrier (NiCr, Ni) stops Al diffusion towards the surface to prevent the formation of Al_2O_3 layers as well as alloying of Al with the top layers. The top layer (Ag, Cu, AgCu, Ni, AgNi) needs to be able to establish the desired solder connection and should be temperature stable. An additional protection layer (Ag) is evaluated as top layer to prevent the stack from oxidation.

A huge range of material combinations and thicknesses of either two-, three- or four-layer systems is investigated in detail. Material system (composition, thickness) and sputter conditions (*e.g.* pressure, current) are optimized to achieve a suitable functional layer system. In most of the sputter stacks, NiCr plays a central role. If not mentioned otherwise, NiCr is always used with 80 $\%_{\mathrm{wt.}}$ Ni and 20 $\%_{\mathrm{wt.}}$ Cr. The amount of Cr is chosen as low as possible to avoid the target being ferromagnetic, while taking advantage of the functionality of Cr for the stack development.

3.2. Experimental Details

3.2.1. Aluminum Foil

Within this work, roll-milled Al foil with a thickness of 200 µm from monolithic Al sheets (alloy 1200, 99 $\%_{\text{wt.}}$ Al, annealed) manufactured by *Hydro Aluminium* is used for most of the experiments on material level [17]. The exact composition of the alloy is listed in Table 3.3.

Table 3.3.: Al foil (99 % Al, 200 µm thickness) of alloy EN AW-1200 of *Hydro Aluminium*. Chemical composition given in $\%_{\text{wt.}}$ according to DIN EN 573-3 [168].

	Al	Si + Fe	Cu	Mn	Zn	Ti
Al1200	> 99 %	max. 1.0 %	0.05 %	0.05 %	0.10 %	0.05 %

The alloy 1200 is a very pure alloy with at least 99 $\%_{\text{wt.}}$ Al. This is advantageous for the implementation to a Si solar cell to not contaminate the semiconductor with metals during the laser process on the solar cell rear side. Al1200 is optimized to be highly resistant to corrosion. One possibility to positively influence the mechanical and chemical properties of the Al is the specific addition of small amounts of other elements. Fe reduces the oxidation of Al. Si is used in the alloy 1200 to reduce the melting point and provide a higher resistivity against corrosion. Also the other elements, listed in Table 3.3 have a positive impact on the alloy [17]. Depending on the application, the choice of Al alloy should be well selected.

For the evaluation of solder joints on coated Al foils within this thesis, a foil thickness of 200 µm has shown to be suitable. It is thick enough to withstand rupture during the peel force measurement of strong solder joints, it is soft and flexible and can be easily cut.

For the rear side of the FoilMet® solar cell, an Al foil of ~ 10 µm thickness is required (*cf.* Section 2.1.3). Soldering pretests on FoilMet® solar cells have shown that the Al foil is too thin for the intended mechanical characterization of the solder joints. Figure 3.4 shows top view images of the FoilMet® rear side after the peel force measurement of a soldered ribbon.

The Al foil rips exactly along the laser contacts. Therefore, the measured force describes the mechanical strength between Al foil and the laser contacts to the Si wafer. This force is only $F/w \approx 0.2$ N/mm to 0.5 N/mm, strongly depending on the laser contacts [46]. The peel force measured for the solder joints within this work, is much higher ($F/w \approx 1$ N/mm to 8 N/mm). The experiments are therefore performed on the 200 µm thick Al foil of the same alloy (and manufacturer *Hydro Aluminium*). The transfer of the developed process and knowledge is addressed at the end of Chapter 5 and 6 with the implementation in solar cells and modules (Sec. 5.4 and 6.5).

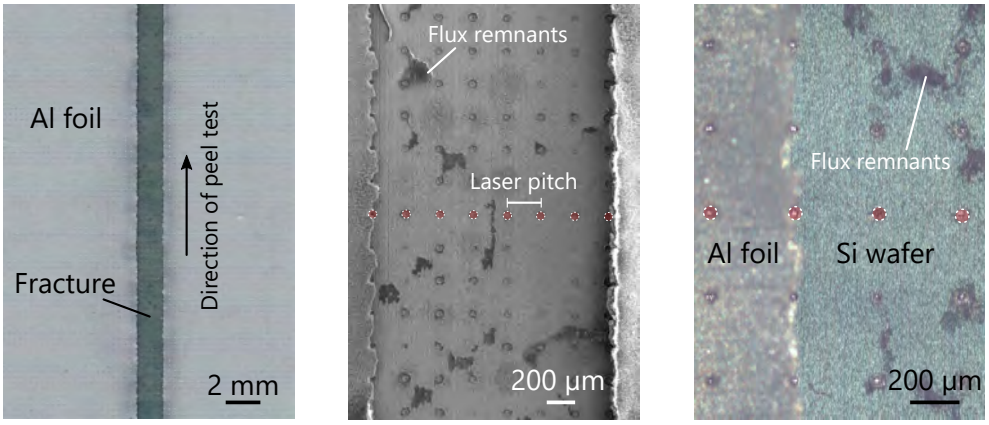

Figure 3.4.: Top view images (from left to right: photo, SEM, optical microscopy) of peel force measurement after soldering on the FoilMet® solar cell rear side, featuring a 10 µm thick Al foil attached with a special laser process to the Si wafer. No quantitative statement on the strength of the solder joint can be made due to rupture of the thin Al foil in the direction of the ribbon peeled off.

3.2.2. Soldering Process

The manual contact soldering process is shown in the photo on the left in Figure 3.5.[3] A hotplate with $T_{\mathrm{HP}} = (120 \pm 5)\,°\mathrm{C}$ is used as preheating, to reduce the temperature difference between Al foil and soldering iron and the induced stress. The temperature of the soldering iron (s. Figure 3.5 right) is set to $T_{\mathrm{s}} = 280\,°\mathrm{C}$, whereas the actual temperature within the joint can vary by up to $\pm 20\,°\mathrm{C}$.

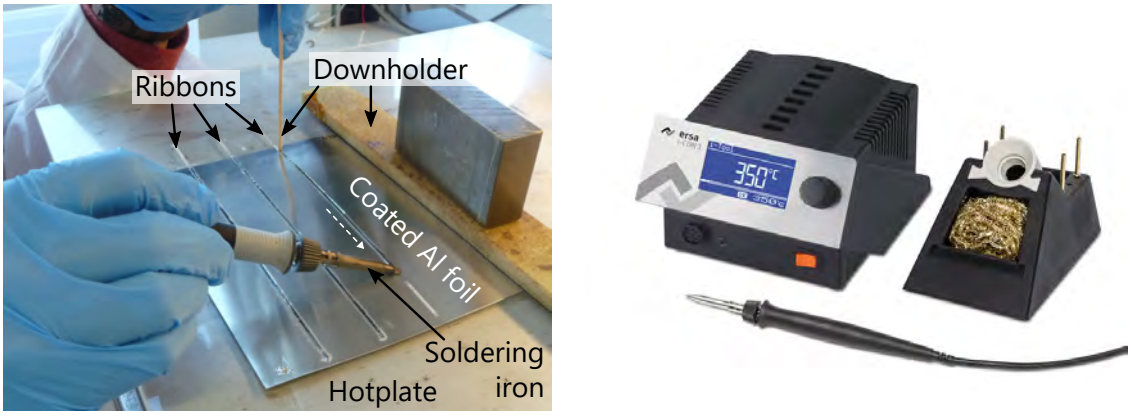

Figure 3.5.: Left: Photo of manual contact soldering of solder-coated Cu ribbons to a 200 µm thick coated Al foil. The dashed white arrow indicates the direction of soldering. Right: Soldering iron i-CON 1 of *kurtz ersa* for manual soldering (© *kurtz ersa*).

[3] It is not possible to solder the Al foils with IR light as used in the stringer, since most of the radiance is reflected by the foils [45, 169].

After preheating of the Al foil on the hotplate at T_{HP} and ambient air, the ribbons are soldered one after the other by moving the soldering iron at an angle of $\sim 45°$ along the ribbon with a constant speed of approximately $(0.8 \pm 0.2)\,\mathrm{cm\,s^{-1}}$.[4] The direction of soldering is marked with a dashed white arrow in Figure 3.5.

For soldering tests on Si solar cells, the industrial stringer and IR soldering is used. The equipment, materials and soldering process are introduced in Section 2.2.4.

If not mentioned otherwise, Cu ribbons with Sn62Pb36Ag2 coating (cross section: $0.20\,\mathrm{mm} \times 1.50\,\mathrm{mm}$, $R_{p02} = 85\,\mathrm{MPa}$) are used for manual soldering. For the experiments with solar cells, interconnected on an industrial stringer, Sn60Pb40-coated ribbons (cross section: $0.22\,\mathrm{mm} \times 0.90\,\mathrm{mm}$, $R_{p02} = 70\,\mathrm{MPa}$) are used.[5] Prior to soldering, all ribbons are stretched by $\sim 0.5\,\%$ of their initial length and fluxed with a no-clean flux of *kester*.

In the following, the different sample types, fabricated by manual and automated soldering, are introduced.

3.2.3. Experimental Procedure

Figure 3.6 gives an overview on the main characterization methods and involved sample types, used within this thesis.

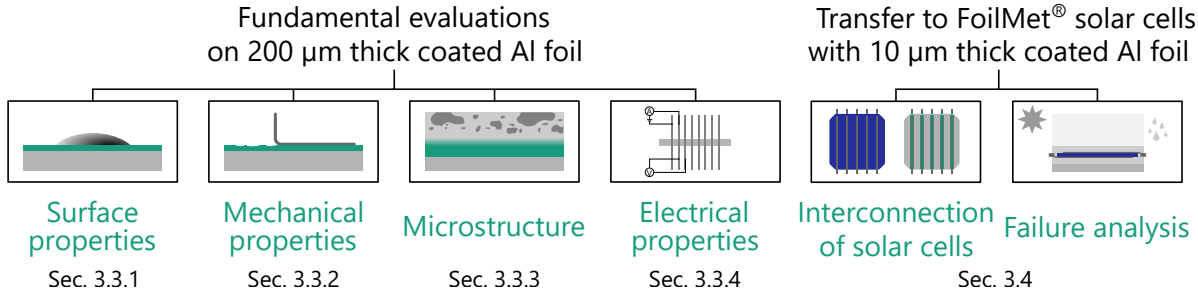

Figure 3.6.: Schematic of experimental characterization within this work, split in evaluation on material level (200 µm thick Al foil) and on solar cell and module level (FoilMet® solar cell with 10 µm thick Al foil rear side).

The characterization is split into two main parts: the evaluation on material level on the coated 200 µm thick Al foil and the evaluation of the component "solar cell" with the thin coated Al foil on the FoilMet® rear side.

As far as possible, solder joints on each of the three coatings are characterized along the procedure in Figure 3.6, which is why the results in Chapter 4, 5 and 6 are structured in the same order. The mentioned measurement techniques are introduced in detail in the following.

[4] Within the time period of this work, the speed is measured regularly to keep the sample preparation as identical as possible.

[5] During the development of this thesis, the alloy of the common PV ribbon changed from Sn62Pb36Ag2 to alloy Sn60Pb40 to save costs [87]. In addition, the ribbon width became smaller for more busbars/ribbons per solar cell [11].

3.3. Solder Joint Characterization

The characterization of solder joints is conducted on different levels: on the base material (Al foil), on solar cells, and after PV module integration. Evaluation is performed with common characterization tools available at Fraunhofer ISE **Module-T**echnology **E**valuation **C**enter (Module-TEC). Exceptions are **T**ransmission **E**lectron **M**icroscopy (TEM), performed in collaboration with **K**arlsruhe **I**nstitute of **T**echnology (KIT) and wetting balance tests in collaboration with University of Rostock. The following sections give an overview on the important characterization methods, the used tools and the relevant parameters for the evaluation of solder joints with the background of PV applications. The characterization tools are presented in the same order as the derived results, presented in Chapters 4, 5 and 6.

3.3.1. Surface Properties

The quality of a solderable surface is essential for the formation of a proper solder joint. Wetting with liquid solder is improved, if oxides are removed before solder joint formation. Practical (qualitative) wetting tests or quantitative contact angle measurement can be used to characterize the wettability of a surface. In the following subsection, the focus is on wetting a metal surface with a liquid solder alloy.

Optical Contact Angle Measurement

The ability of a liquid droplet to spread over a solid surface is called wetting. Three media are involved: The vapor (V) around the droplet, the liquid (L) of the droplet itself and the solid (S) interface, on which the droplet is placed. In the equilibrium state, this situation is described by the tensions γ_{ij} and Young's equation:

$$\gamma_{SL} = \gamma_{SV} - \gamma_{LV} \cos(\alpha), \tag{3.5}$$

which is sketched in Figure 3.7 b). Surface and interfacial tension γ_{ij}, indicated by the arrows, strongly depend on the involved materials and the quality of the interface liquid (L) to solid (S).

The contact angle α provides a measure for the quality of wetting. The geometric shape with the smallest surface-to-volume ratio is a perfect sphere. Any droplet tends towards this state with the lowest energy. During a static contact angle measurement, the involved materials are in balance.

The area of spreading will increase with decreasing contact angle. For $90° < \alpha < 180°$, wetting is hampered and the droplet will not spread on the surface. This is called dewetting. Figure 3.7 c) shows an example of dewetting in the upper image ($\alpha > 90°$) and very good wetting in the bottom ($\alpha < 30°$). The images are the results of an **o**ptical **c**ontact **a**ngle (OCA) measurement, which is performed within this work to evaluate the wettability of the solderable Al surfaces. Wetting can be improved by cleaning and providing an oxide-free surface, *i.e.* by using flux.

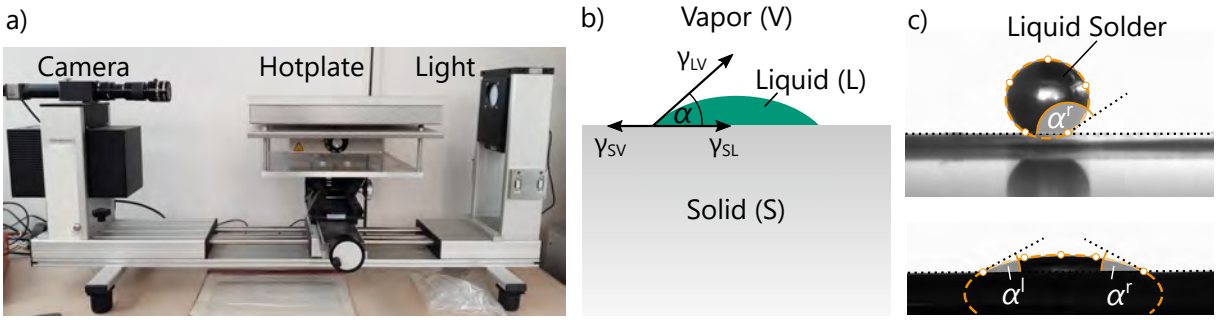

Figure 3.7.: a) Optical contact angle (OCA) measurement device of *dataphysics*. b) Surface tension forces γ_i when a liquid droplet (L) wets a solid surface (S). The determination of the contact angle α is described by Young's equation. c) Examples for a contact angle measurement with dewetting ($\alpha > 90°$, top) and very good wetting ($\alpha < 30°$, bottom). For the evaluation, an elliptical fit, consisting of 5 contact points, is used. In this equilibrium, left contact angle α^l and right contact angle α^r are determined by fitting a tangent line to the droplet shape.

A common simplification during the static contact angle measurement is to assume that the solid/liquid interface does not change significantly within the measurement time, *i.e.* any reaction at the interface is neglected.[6] Additionally, gravity, temperature gradients and local surface inhomogeneities are neglected.

In a solder joint, there are always two facing solid surfaces. If both provide good wetting, a positive capillary force will act to fill the joint with the liquid solder. For solder joint analysis as performed in this work, one component (Al foil or solar cell metallization) serves as substrate, whereas the other component (Cu ribbon) is pressed on during the soldering process. The liquid solder is inherently within the solder gap, as the ribbons are coated with the solder (*i.e.* reflow soldering).

For the measurements within this work, a device of the OCA series of *dataphysics* is used, which is extended by a hotplate to heat the samples above the liquidus temperature of the solder alloy (s. Figure 3.7 a)). Small pieces of Al foils are cut ($\sim 2\,\text{cm} \times 2\,\text{cm}$) and cleaned with ethanol. The hotplate temperature is set to 250 °C. Small solder droplets of $(11 \pm 1)\,\text{mg}$ of Sn60Pb40 are coated with no-clean flux (*kester* 952s) so that oxides are removed when the droplet is put onto the heated sample. When exceeding its liquidus temperature of $T_{\text{liq}}(\text{Sn60Pb40}) = 183\,°\text{C}$, the solder starts melting and spreading.

To determine the static contact angle α, the sessile drop method is applied by fitting a tangent line along the droplet profile (s. Figure 3.7 c)) [170]. The droplet profile itself is reproduced by an elliptical fit within the contrast image after full liquidation of the solder droplet. Each surface is characterized by at least $N = 10$ measurements on individual samples to get a statistical uncertainty. To estimate the systematic uncertainty of the measurement procedure, one droplet is measured five times by fitting the ellipse and

[6] The solubility of the liquid in the solid is less than 0.1 % [7].

calculating the mean of left α_i^l and right contact angle α_i^r. The optical contact angle α is then given as:

$$\alpha = \frac{1}{N}\sum_{i=1}^{N}\frac{1}{2}\cdot(\alpha_i^l + \alpha_i^r). \tag{3.6}$$

The measurements show that the most dominating factor is the surface itself, especially inhomogeneities in roughness or cleanness.

Determination of Contact Angle by Wetting Balance Test

In addition to optical contact angle measurements, a wetting balance is used to quantify the wetting behavior of sputter-coated Al foils (*cf.* Section 6.1). The measurement principle is given in Figure 3.8. The sample is mounted to a vertical force sensor above a solder bath on a height-adjustable table. After leveling of the force sensor (*i.e.* correction to zero by the sample's weight) and heating up the solder bath above T_{liq}, the bath is moved upwards by a defined speed ($2\,\mathrm{mm\,s^{-1}}$) until the sample is dipped into the bath for a depth of $x = (0.5 \pm 0.1)\,\mathrm{mm}$. The signal of the force sensor is recorded for at least 5 s dwell time. The sample is removed with the same speed and can be visually inspected.

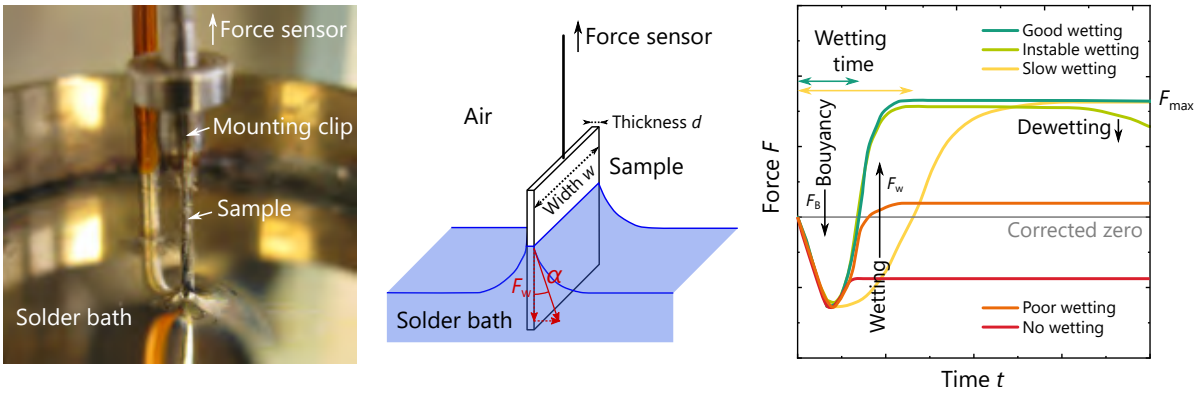

Figure 3.8.: Wettability tests of a metallic sample by a wetting balance. Left: Photo of the test setup of the Malcom SP-2 of *Malcom Tech*. With permission of University of Rostock. Middle: Sketch of Wilhelmy plate method. Right: Resulting force-time-diagrams for different states of wetting.

In this work, a wetting balance Malcom SP-2 of *Malcom Tech* is used. For each sample type, at least 12 measurements with a total measurement time of 10 s are carried out. The samples under investigation are 200 µm thick Al foils coated by sputtering on both sides, as described in Chapter 6. The foils are cut into $w = (3.0 \pm 0.2)\,\mathrm{mm}$ wide stripes. For the solder bath, the eutectic alloy of Sn63Pb37, heated up to 230 °C, is used. After fluxing[7], the samples are dipped in upright orientation which can be described by the Wilhelmy plate method [171]. The geometry is sketched in Figure 3.8 in the middle. The sample

[7]The nonhalogen flux ACTIEC LF-A of Stannol with a low resin content of 1.5 % and a solid content of (6.0 ± 0.1) % is used.

geometry resembles a thin plate which is wetted when contacting the liquid solder. At the three-phase contact line ($U = 2 \cdot w + 2 \cdot d$), a tensile force acts tangentially to the liquid surface (red line). The resulting wetting force F_w can be expressed by

$$F_\mathrm{w} = \gamma_\mathrm{LV} \cdot U \cdot \cos(\alpha). \tag{3.7}$$

This force component is recorded by the sensor. Additionally, the buoyancy of the sample has to be considered. It is given by

$$F_\mathrm{B} = g \cdot \rho_\mathrm{solder} \cdot V \tag{3.8}$$

with the acceleration of gravity g, the density $\rho_\mathrm{SnPb} \approx 8.4\,\mathrm{g\,cm^{-3}}$ of liquid Sn63Pb37 at 230 °C [172] and the displaced volume $V = w \cdot d \cdot x = 3.0\,\mathrm{mm} \cdot 0.2\,\mathrm{mm} \cdot 0.5\,\mathrm{mm} = 0.3\,\mathrm{mm^3}$. This leads to a buoyancy force of the investigated samples of $F_\mathrm{B} = 0.025\,\mathrm{mN}$.

The development of the measured force during the measurement time t is sketched in Figure 3.8 on the right for different cases. After overcoming the buoyancy of the sample, the solder wets the sample and a maximum force F_max is measured. Dewetting is characterized by a decrease in F with time. The time until the corrected zero line is crossed is called wetting time t_w. The shorter t_w and the higher F_max, the better the sample is wettable.

To quantify the wetting behavior of the sample, the contact angle α can be evaluated (*cf.* Equation 3.7). In equilibrium, the maximum recorded force F_max is given by

$$F_\mathrm{max} = F_\mathrm{w} - F_\mathrm{B} \tag{3.9}$$

$$\Leftrightarrow \alpha = \arccos\left(\frac{F_\mathrm{max} + F_\mathrm{B}}{\gamma_\mathrm{SnPb} \cdot U}\right). \tag{3.10}$$

This simplified equation gives a measure for the contact angle. Beside the assumptions mentioned above, *e.g.* the meniscus of the liquid solder is neglected when stating the immersion depth of the sample. A detailed description on the influence of the assumptions can be found in [173].

3.3.2. Mechanical Properties

Solder joints on front and rear side of Si solar cells have to withstand the string handling during module manufacturing. Additionally, the induced lateral stress caused by temperature changes during the operation of the PV module acts on the solder joints. Beside a shear test [63], the mechanical strength of the solder joints can be qualified by a peel force measurement, which is described in the following.

Peel Force Measurement

The peel force is a measure for the minimum mechanical strength of a solder joint between two components.[8] It is a destructive test method, executable for different peel angles and peel speeds.

[8] Except for the case, where the inner strength of a material is lower than the solder joint. This is commonly the case for highly reliable solder joints on silicon solar cells, where the silicon breaks during the peel force measurement.

The peel force measurements in this thesis are performed according to DIN EN 50461 [174], which refers to Test 2M05 in § 9.5 of IEC 61189-2 [175]. The strength of solder joints is measured between a metallic surface (*e.g.* coated Al substrates, Ag electrodes on solar cells) and a Cu ribbon. The ribbons are peeled off under an angle of 90° at a fixed rate of $(50 \pm 2)\,\mathrm{mm\,min^{-1}}$. The tests are conducted on a zwicki Z0.5 TN peel testing machine of *Zwick Roell* with a 50 N force sensor. Figure 3.9 shows the used setup and illustrates the measurement principle.

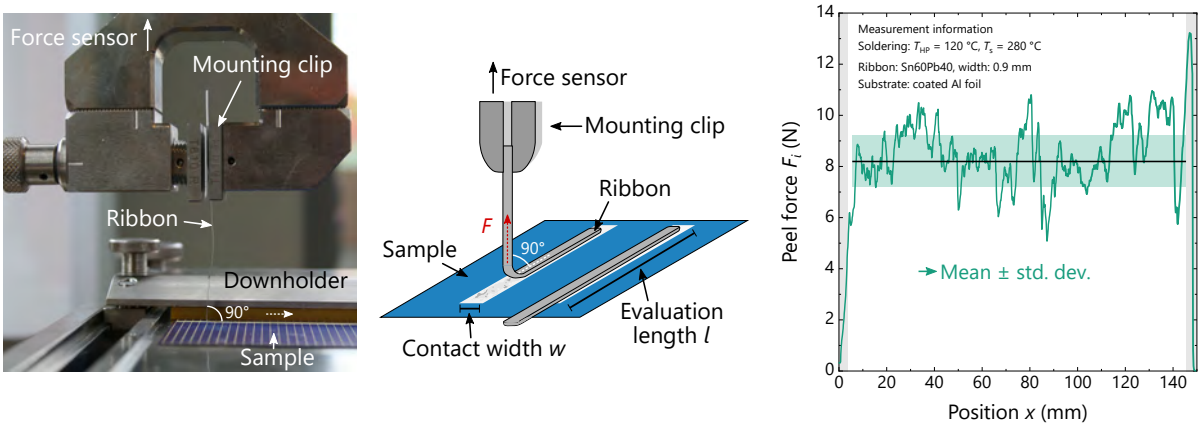

Figure 3.9.: Principle of the 90° peel force measurement for mechanical characterization of the solder joints. The graph on the right shows an example of the data evaluation after soldering on a homogeneous surface (continuous peel force). © Fraunhofer ISE

The sample is fixed on a tray and the loose end of the ribbon is mounted into the clip of the force sensor. When the force sensor moves upwards, the peeling angle is preserved by a corresponding movement of the sample tray. The force component normal to the sample surface ("peel force F_i") of the sample is recorded by the force sensor upon the traverse path ("position x").[9] The force-path-diagram, exemplarily given on the right in Figure 3.9, shows the relevant measurement quantities and the data evaluation. To determine the mean peel force, the arithmetic mean is calculated, excluding first and last part of the test.[10] The recorded force values F_i per position x are normalized to a defined contact width w of the joint. To take inhomogeneities both of the coating and the solder joints into account, each test is carried out for a length of $l \approx 150\,\mathrm{mm}$ and repeated with at least $N = 5$ samples.

The standard DIN EN 50461 states a minimum required (90°) peel force of $1\,\mathrm{N\,mm^{-1}}$ for joints on Si solar cells [174]. For the evaluation of the solder joints on coated Al substrates, this value is given in the graphs as lower limit.

[9] Systematic uncertainty: 0.1 mN, 1 µm

[10] In the first and last part of the peel force measurement, bending of the ribbon and solder accumulation due to manual soldering both influence the result.

Fracture Pattern

After conducting the peel force measurement, the fracture pattern can be analyzed by optical inspection and microscopy. This gives information about the failure mechanism, which is essential for the development of the soldering process and the formation of a reliable solder joint. An adhesive failure at the interfaces mostly leads to lower peel forces. A cohesive failure can occur within the solder alloy or the screen-printed Ag metallization. An ideal failure mode, resulting in high peel forces, consists of a mixed fracture, including cohesive and adhesive failures, since this indicates no dominating weak interface or material in the joint.

3.3.3. Microstructure

The microstructure of a component correlates with its physical properties. The analysis of the microstructure using microscopy and/or other sample preparation and characterization techniques, can reveal information about the crystal structure, grain boundaries, the overall grain distribution, interfacial reactions *e.g.* (intermetallic) phases or diffusion, micro cracks, voids and other defects [105].

Two different approaches are chosen: top view images (esp. fracture pattern after peel force measurement) and cross section images (interfacial reactions of solder and coatings). Especially, the preparation of cross sections (metallography, *cf.* Section A.6 in the appendix), provides a deeper insight into the inner part of the soldered components, the composition of the joint, as well as the involved interfaces. They can be analyzed by different microscopic methods, which are presented in the following.

Scanning Electron Microscopy

To gain an overview on the whole sample area of the cross sections, optical microscopy is used. For microstructural analysis and reliable statements on the interfacial reactions, higher magnifications are advantageous. Therefore, **s**canning **e**lectron **m**icroscopy (SEM) is conducted, providing insight into sub-micrometer structures. Electron microscopy is performed in high vacuum ($\sim 10^{-6}$ mbar) to avoid scattering of the electron beam with air molecules. Figure 3.10 illustrates the interactions of a high-energy focused electron beam with a sample and the resulting signals that can be analyzed.

In SEM, the integrated intensity of **s**econdary **e**lectrons (SE), generated in a depth from the sample surface of 10 Å to 100 Å, can be measured. They feature a characteristic energy in the range of 1 eV to 50 eV. For materials with large atomic number Z, the probability to measure a SE is higher than for materials with small Z. This higher intensity leads to a brighter SEM image. An example is given in Figure 3.11 on the left. For the analysis of the involved materials in solder joints, high acceleration voltages (15 kV to 20 kV) are used, to generate and release SE of Sn ($Z = 50$) and Pb ($Z = 82$). The SEM image is generated by point-wise scanning a defined region with the electron beam. In case only one scaling bar is given within the SEM images, all images of one figure are scaled equally.

In this work, the Auriga 60 setup of *Carl Zeiss Microscopy* with a crossbeam workstation is used for high resolution imaging. All samples (top view samples and cross section

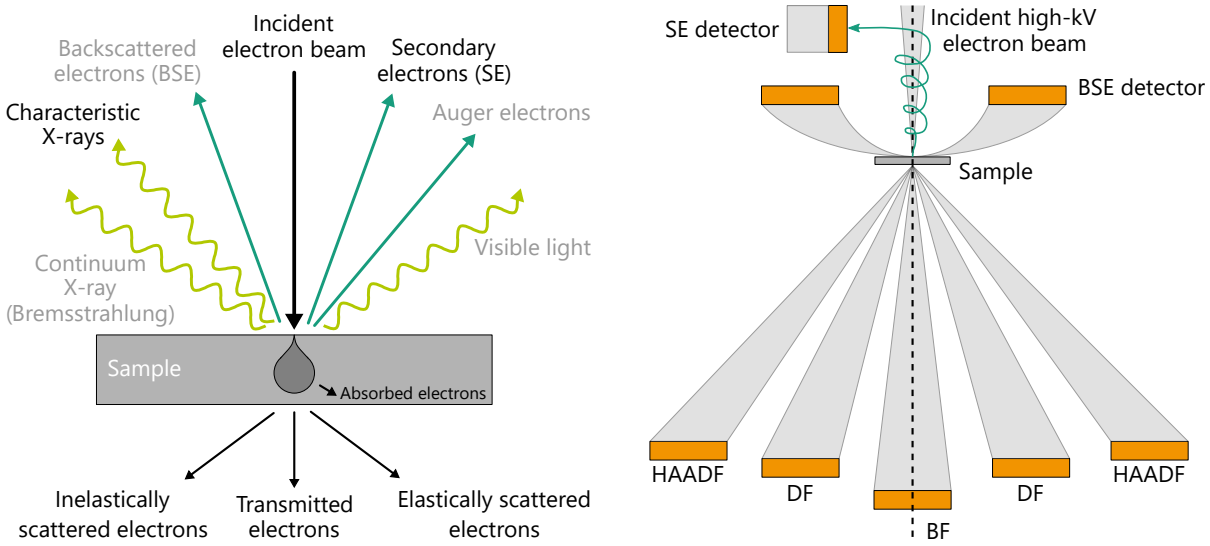

Figure 3.10.: Left: Schematic of electron beam interaction with sample. Relevant signals for this work are given in black. Right: Schematic of different detectors in STEM mode (adapted from [176]).

samples) analyzed within this thesis mostly consist of metals or semiconductors, whereas the electrical conductivity of the samples is guaranteed. In addition, by using an epoxy with conductive particles, charging of the cross section sample surface can be largely avoided. The working distance is set to 4.9 mm to 5.1 mm, to allow for simultaneous EDX analysis, performed in the same setup. The procedure is described later in this section.

Transmission Electron Microscopy

Another method to get even higher magnification of metallic samples is **t**ransmission **e**lectron **m**icroscopy (TEM). It applies for studies where the resolution of an optical light microscope or even a conventional SEM is limited. TEM samples are called "lamella" and feature a thickness of < 100 nm so that most of the incoming high-electron beam is transmitted through the sample.

If an high-energy electron beam passes through a thin specimen, the electrons are scattered. The reflection (*i.e.* elastic scattering) of electrons at a crystal lattice is described by Bragg's law [105]:

$$n\lambda = 2d\sin(\theta) \tag{3.11}$$

whereas λ is the wavelength of the incoming wave, d the interplanar distance, θ the angle of incidence and n a positive integer. When two scattered waves interfere constructively, they remain in phase since the difference between the path length is equal to an integer multiple of λ.

In a TEM, the crystal orientation of the spot of interest of the sample is aligned parallel to the electron beam. An aperture is used to select electrons of a certain scattering angle and to guide them to one of the detectors [176]. Figure 3.10 on the right shows a sketch of the arrangement of different detectors within a TEM. In **b**right **f**ield (BF) mode,

unscattered electrons are analyzed (orientation contrast), whereas in **d**ark **f**ield (DF) mode, scattered electrons reach the detector (material contrast: Z contrast). Additionally, **h**igh-**a**nnular **a**ngle **d**ark **f**ield (HAADF) mode is used in combination with **s**canning **t**ransmission **e**lectron **m**icroscopy (STEM) to detect incoherently scattered electrons (as opposed to Bragg's scattering) to yield a high material contrast (high Z contrast) [176].

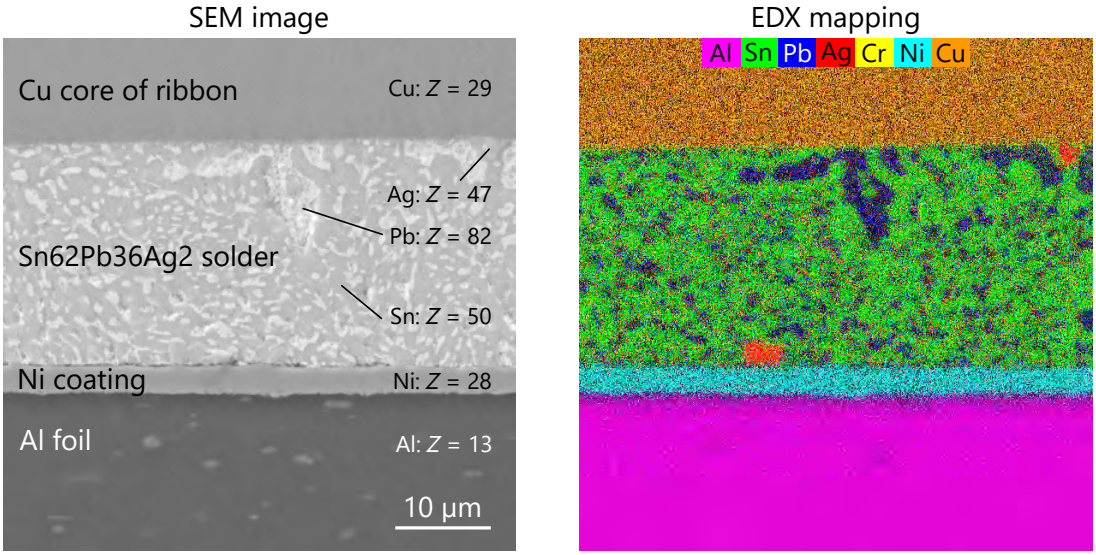

Figure 3.11.: Example for SEM image (SE detector, 20 kV) and corresponding EDX mapping of a solder joint on coated Al foil (cross section view). The contrast of the secondary electrons (SE) in the SEM image is given by the atomic number of the elements. The color code for the elements in the EDX mapping is kept throughout this thesis.

For TEM analysis of solder joints on sputter-coated Al foils, two cross section samples are prepared using metallography. After intensive SEM analysis of the interface of the solder joints, the points of interest are marked and the samples are sent to Karlsruhe Institute of Technology for FIB preparation and analysis with TEM. Preparation of the thin lamellas is done by a **f**ocused-**i**on **b**eam (FIB) using gallium ions. The samples are mounted on a sample holder of molybdenum and covered with platinum to protect the surface. The final thickness of the lamellas is less than 70 nm. Between FIB preparation and TEM, the lamellas are stored oxygen-free at room temperature. For (S)TEM analysis, a Tecnai Osiris™ by *FEI Company* with a maximum voltage of 200 kV and a resolution limit of 0.24 nm is used.

Energy-Dispersive X-ray Spectroscopy

A quantitative classification of the elements within the solder joints is performed for the investigation of interfacial reactions. Therefore, **e**nergy **d**ispersive **X**-ray (EDX) **s**pectroscopy (EDXS) is used. The analysis is conducted within the SEM setup, introduced before. The incident focused electron beam also leads to emission of characteristic

X-rays of the sample (s Figure 3.10 left): The incoming electrons of the beam lead to ejection of electrons from the inner shells (lower energy levels). When the vacant energy states are filled with electrons from higher energy levels, characteristic X-rays are emitted. This specific energy is characteristic for the detected element.

Within this thesis, the analysis is carried out with a Quantax XFlash 6|60 detector of *Bruker*. Either EDX mappings or quantification with EDXS is performed. While the mappings provide information on the global element distribution, spectroscopy allows for quantitative analysis of specific points or lines, provided by analysis of the composition c_i. Figure 3.11 right shows an example for an EDX mapping and the color code for the involved elements, kept throughout this thesis.

EDX can also be performed in combination with TEM. Within the TEM setup, a 4-quadrant detector is installed to avoid shaded areas within the EDX maps. Due to the much higher acceleration voltage within the TEM, higher count rates for EDX are achieved, leading to higher resolutions for the EDX analysis.

3.3.4. Electrical Properties

The solder joints in a PV module should be highly conductive to minimize ohmic losses which would reduce the module output power. On solar cell level, the series resistance and the fill factor are the most prevalent measures for the quality of the solder joints. To evaluate the electrical properties of solder joints on coated Al foils already on material level, the contact resistance is measured with a dedicated sample geometry, presented in the following.

Contact Resistance Measurement

To determine the contact resistance, (mostly 200 µm thick) Al foils are cut to a defined width $z = 5\,\mathrm{mm}$ and n ribbons are soldered perpendicular to the strip with a constant pitch $x = 5\,\mathrm{mm}$. Figure 3.12 schematically shows geometry and measurement principle of the samples.

A Nanovoltmeter of the Model 2182A of *Keithley* is used in combination with a reversing current source of Model 6220.[11] The conducted procedure is called contact end resistance measurement [177,178].[12] An electric current of $I = 100\,\mathrm{mA}$ is applied at two neighboring contacts i and $i+1$ and the voltage is measured in parallel between contact $i+1$ and $i+2$. With the given geometry and material parameters of the sample, the contact resistance R_meas can be derived [177]. This measurement is repeated for all contacts of one sample and for a minimum of two samples per variation. The resistance $R_\mathrm{meas} = \frac{U}{I}$ is multiplied by the contact area $A = w \cdot z$ to obtain the specific contact resistance R_c.

For all samples of one group, the calculated values for R_c are averaged. The investigated joints are metallic contacts, providing small values of mostly $R_\mathrm{c} < 10\,\mu\Omega\,\mathrm{cm}^2$. The

[11] The sensitivity of the device is stated as 1 nV.

[12] The **t**ransfer-**l**ength **m**ethod (TLM), as commonly used to characterize contact resistances on Si solar cells, is not used in this work. The reason for this are significantly lower values for R_c than for a metal-semiconductor contact [179], which often prohibits the determination of R_c of the y-axis intercept due to negative values.

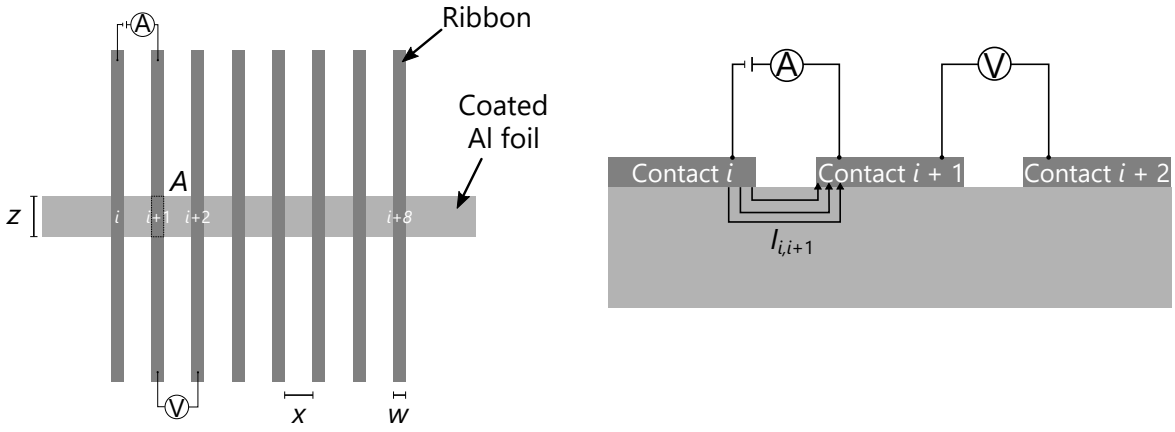

Figure 3.12.: Measurement of contact resistance of solder joints on coated Al foils according to the contact end resistance method [177]. Schematically sketched in top view (left) and detailed side view (right).

electrical properties of a solder joint is affected by elevated temperatures, resulting in *i.e.* formation of IMCs or oxidation, by humidity causing corrosion or other chemical impacts on the joints.

For the investigated metal contacts, the measurement values are in the range of the resolution limit of the measurement device, whereas large systematic errors occur.

According to Zemen *et al.*, a specific contact resistance smaller than $500\,\mu\Omega\,cm^2$ does not influence the fill factor of a Si solar cell [180]. Therefore, this value is also presented as a reference value in the result chapters. The flexibility of the presented sample geometry also allows to laminate them into common module materials (glass, encapsulant, backsheet, *cf.* Section 2.1.4) to perform aging *i.e.* in a climate chamber under the same conditions as a PV module would be stressed.

3.4. Solar Cell & Module Characterization and Climate Chamber Tests

Within Chapter 5 and 6, solar cells with coated Al rear sides are fabricated. In addition to the fundamental characterization of the solder joints as presented above, these solar cells are investigated. This gives additional insight into the performance and interactions of the solder joints. Therefore, established methods of PV are applied: luminescence imaging and *I-V* measurements. As common for PV modules, their long-term stability under thermal stress is characterized after accelerated aging tests: isothermal aging, thermal cycling and damp heat testing [79] are conducted.

3.4.1. *I-V* Measurement

The current-voltage characteristic of solar cells and modules is measured with an automated cell tester of *h.a.l.m. elektronik* in the **P**hoto**v**oltaic **T**echnology **E**valuation **C**enter (PV-TEC) laboratory at Fraunhofer ISE.

The intensity of the flash is calibrated to STC (standard test conditions[13]) using a reference cell, calibrated at Fraunhofer ISE CalLab PV Cells. For the measurement of solar cells, both polarities are contacted with contact bars holding several pins for independent current and voltage measurement. On each solar cell side, five bars are aligned with the five busbar positions along the cell. For contacting the electrodes of the modules, a four-wire measurement is used, with the soldered cross connectors.

The measurement of current and voltage is done under illumination, while a variable load is connected to the terminals. As introduced in the fundamentals in Section 2.1.1, the short-circuit current I_{sc}, the open-circuit voltage V_{oc} and the maximum output power P_{mpp} are the most important measurement quantities. The fill factor FF, as well as the energy conversion efficiency η can be derived by using Equations 2.2 and 2.3. The pseudo fill factor pFF is measured in the same setup (Suns-V_{oc} method, [182]) and can be used to estimate an upper limit for the FF, as is it not influenced by series resistances. Table 3.4 gives the measurement uncertainty of these quantities, used within the graphs of this thesis.

Table 3.4.: Systematic uncertainties (2σ) for *I-V* measurement of solar cells and modules, performed within this thesis.

	V_{oc} (mV)	I_{sc} (A)	FF (%)	pFF (%)	P_{mpp} (W)	η (%)
2σ	±0.09 %	±0.15 %	±0.17 %	±0.12 %	±1.62 %	±0.28 %

The measurement uncertainty (2σ) of the flasher is routinely derived from sets of reference Si solar cells and used to estimate the systematical uncertainty of the measurement results. To evaluate the cell and module performance, several samples are processed, from which a statistical mean and standard deviation can be derived. To compare the impact of different fabrication and durability tests, the relative changes in these parameters are analyzed in this thesis. As an example, the relative change ΔV_{oc} after thermal cycling (TC) is calculated as:

$$\Delta V_{\mathrm{oc}} = \frac{V_{\mathrm{oc}}^{\mathrm{TC}} - V_{\mathrm{oc}}^{\mathrm{ini}}}{V_{\mathrm{oc}}^{\mathrm{ini}}} \cdot 100, \tag{3.12}$$

whereas $V_{\mathrm{oc}}^{\mathrm{ini}} \pm \sigma_{\mathrm{ini}}$ is the initial value before TC and ΔV_{oc} is given as a percentage. The uncertainty on ΔV_{oc} is calculated by error propagation:

$$\sigma_{\Delta V_{\mathrm{oc}}} = \sqrt{\left(\frac{V_{\mathrm{oc}}^{\mathrm{TC}}}{V_{\mathrm{oc}}^{\mathrm{ini}} \cdot V_{\mathrm{oc}}^{\mathrm{ini}}}\sigma_{\mathrm{ini}}\right)^2 + \left(\frac{1}{V_{\mathrm{oc}}^{\mathrm{ini}}}\sigma_{\mathrm{TC}}\right)^2} \cdot 100 \tag{3.13}$$

[13] Intensity of incoming light: $1000\,\mathrm{W\,m^{-2}}$, "Air Mass 1.5" solar spectrum, cell temperature: $(25 \pm 2)\,^{\circ}\mathrm{C}$ [181].

The *I-V* parameters of solar cells and modules are used to value the global performance, *e.g.* to improve manufacturing by deducing failures and defects.

3.4.2. Luminescence Imaging

To receive local information on the solar cell performance, luminescence imaging can be used as non-destructive and fast measurement technique. Within this thesis, two techniques are applied: First, **e**lectro**l**uminescence (EL) by injection of charge carriers to the solar cell by an external current. Secondly, **p**hoto**l**uminescence (PL) with charge carrier injection by light, *e.g.* a laser source. Both yield contrast images, which can be generated on solar cell as well as on module level.

EL imaging is an established method as quality control after the interconnection of solar cells and after module fabrication. In this thesis, EL is done in the same setup as the *I-V* measurements. The cells and modules are measured at a current of 10 A, which is close to the maximum current (I_{sc}). This leads to excited charge carriers within the Si semiconductor. They release their energy in form of radiative recombination of electrons and holes. For Si, this radiation is in the IR range and can be measured with a CCD camera.

Figure 3.13 shows four examples for EL images of Cz-Si solar cells, showing different defects which can be identified by EL imaging. The image on the right is defect-free, indicated by the homogeneous and bright EL signal.[14]

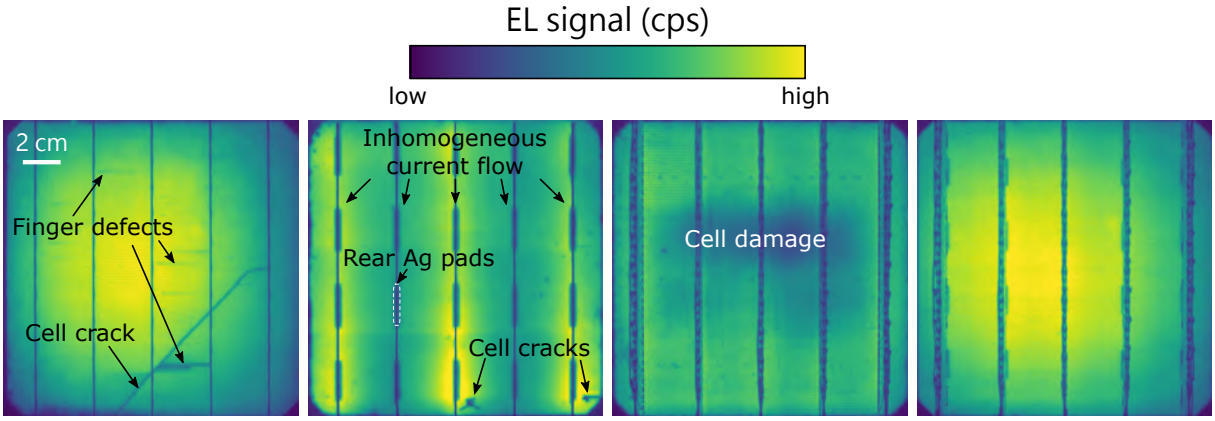

Figure 3.13.: Examples for EL images of Cz-Si solar cells, showing possible defects, visualized by EL measurement. Two images on the left: solar cells after soldering ("strings"), *i.e.* current flow from top and bottom cross connectors. Two images on the right: solar cells contacted by 5BB pin contact bars from top and bottom, *i.e.* homogeneous current flow through solar cell.

To compare different samples, the exposure time of the camera and the applied current have to be considered during evaluation. Within this thesis, the EL images are normalized to the same scaling. However, if samples show strong systematic deviations, a scaling

[14] The increase of brightness to the inner part of the solar cell occurs from a vignetting effect of the CCD camera, mounted nearly 64 cm above the solar cell [183, 184].

factor is applied to visually compare different samples on similar levels. The color code gives the measured EL signal on a linear scale.

3.4.3. Isothermal Aging

For temperature stability tests, samples are stored in ambient air at a constant temperature of $(85 \pm 5)\,°C$ or $(125 \pm 5)\,°C$ to focus on aging effects within the coatings and at the interface to the solder joint. The aging conditions are selected according to standard IEC 60068 [185]. This test is conducted on material level on Al foils as a pretest for accelerated aging tests with solar modules. By exposure to higher temperatures, the solder joint resistance can increase due to corrosion of the interfaces, which is tested in combination with contact resistance measurements (s. Section 3.3.4). Additionally, diffusion processes can lead to (intermetallic) phase formation, mostly influencing the mechanical stability of the joints. This is tested by peel force measurements (s. Section 3.3.2) after isothermal aging of the joints. Contact resistance as well as peel force measurements are carried out after the samples have cooled down to RT.

3.4.4. Climate Chamber Tests for PV Modules

The ability of a PV module to perform without failure for a given time interval under given conditions is refereed to as "reliability" in PV industry [186]. To assess the long-term performance of a PV module, accelerated aging tests are performed in climate chambers of Fraunhofer ISE.[15] For crystalline Si solar modules, the tests are specified in standard IEC 61215 [79]. The most relevant tests for the experiments presented within this thesis are the thermal cycling (TC) and damp heat (DH) test.[16] A maximum power degradation of $-5\,\%$ relative loss (ΔP_{mpp}) is given as criterion for a PV module at the end of each test sequence. Therefore, the power output of each module is set off against its initial power output, as given by Equation 3.12.

Temperature Cycling

The temperature profile for thermal cycling is stated in § 4.11 (Module Quality Test 11) in IEC 61215-2:2016 [79] and sketched in Figure 3.14. One temperature cycle is defined as the temperature change from RT to $(-40 \pm 2)\,°C$ up to $(85 \pm 2)\,°C$ and back to RT. The heating and cooling rate should not exceed $100\,K/h$. A dwell time of at least $10\,min$ at the lowest and highest temperature is required. The module temperature is recorded and the air circulation within the climate chamber can be adjusted, depending on the thermal load within the chamber to assure a homogeneous temperature distribution. In addition, a continuous current flow ($\sim I_{\mathrm{mpp}}$) during heating is applied to the PV module. For 1-cell-modules, as examined within this thesis, this is of minor importance.

[15] IEC 61215 specifies: "The actual lifetime expectancy of modules so qualified will depend on their design, their environment and the conditions under which they are operated." [79].

[16] Beside these two, other tests given in IEC 61215 are *e.g.* humidity freeze, UV preconditioning, hot-spot endurance test, wet leakage current test, insulation test or mechanical load. Mostly, several are combined in test sequences and a specific number of full-size solar modules has to be tested [79].

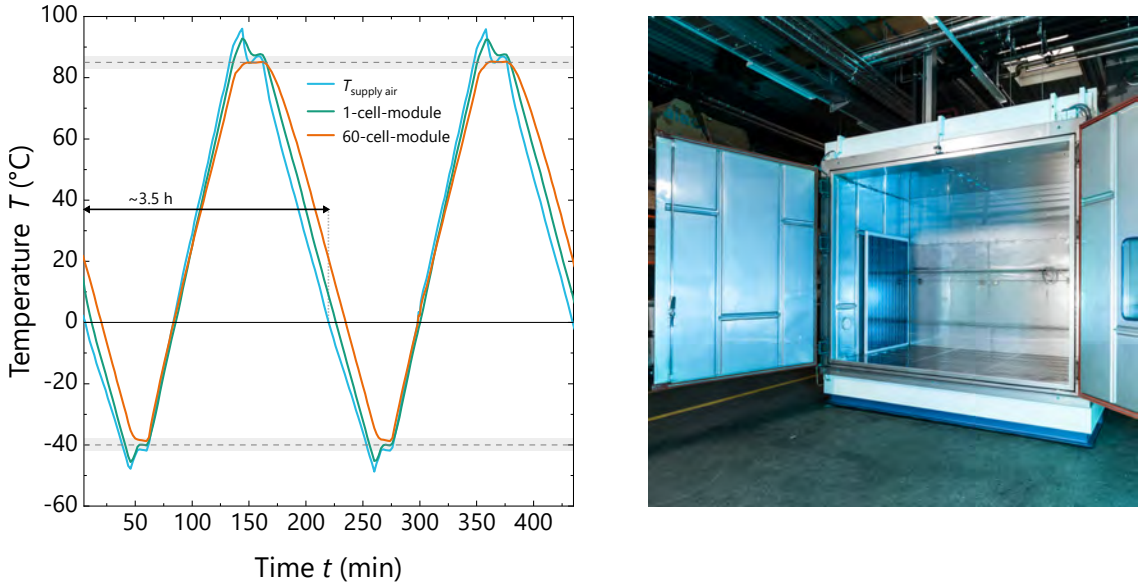

Figure 3.14.: Left: Temperature profile for TC test (two cycles) from RT to (-40 ± 2) °C up to (85 ± 2) °C and back to RT. The green curve shows a measurement on one of the 1-cell-modules, tested in this work. Right: Photo of climate chamber for testing of full-size PV modules. © Fraunhofer ISE

A TC test is performed to characterize the module regarding mechanical fatigue of the components due to thermal mismatch. Module components which are prone to temperature changes are interconnectors, cross connectors and solder joints between components. In this thesis, 1-cell-modules with coated Al rear electrodes are tested in TC to analyze the solder joint stability on the coated Al within a small format PV module.

Damp Heat

Another common test for PV modules is the damp heat (DH) test, specified in IEC 61215-2:2016 [79]. In § 4.13 (Module Quality Test 13), the required damp heat conditions are listed as (85 ± 2) °C and (85 ± 5) % relative humidity within the climate chamber. The test should be carried out at least for 1000 h to value a possible degradation of the PV module.

Beside the exposure to elevated temperature, the long-term penetration of humidity could cause delamination, corrosion, discoloration of the encapsulant or solder joint failure [187]. To assess the stability of the coating on the Al electrode of the solar cells and the influence on the solder joints within this thesis, DH testing is carried out with 1-cell-modules with a transparent backsheet to allow for a visual inspection of the cell rear side.

4. Roll-Cladded Aluminum Foils

This chapter presents the analysis of solder joints on aluminum foils coated with a solderable layer by roll cladding. A main goal is to identify critical parameters, influencing the adhesion and electrical resistance of the solder joints. Three different solderable composites are investigated: Al/Sn62Pb36Ag2, Al/Sn99Cu1 and Al/Ni. They are fabricated externally by SCHLENK Metallfolien GmbH & Co. KG and Wickeder Westfalenstahl. The results have been partly published by the author in 2017 [188] and 2018 [189].

In the first ***Section 4.1****, the quality of the rolled surfaces after delivery to Fraunhofer ISE is analyzed by top view SEM images. In addition, the temperature stability of the material compounds is qualified by heat treatment on a hotplate. In* ***Section 4.2****, the mechanical stability after soldering is evaluated by 90° peel force measurements. The fracture pattern is analyzed afterwards, to yield information about the interaction of the different layers. Isothermal aging of solder joints is used to evaluate the long-term stability of the joints and the material compound regarding their mechanical properties. The microstructure of solder joints on the different roll claddings is investigated in* ***Section 4.3*** *by SEM and EDX. The electrical characterization of solder joints on roll-cladded Al foils is presented in* ***Section 4.4*** *by contact resistance measurements after isothermal aging. All characterizations on material level are performed with foils of about 200 µm total thickness. In the last part of this chapter, first tests for the implementation to Si solar cell rear sides are shown in* ***Section 4.5****. The transition to very thin Al foils (10 µm) induces challenges for the interconnection, as well as for the processing of FoilMet® solar cells, both of which are addressed.*

In this work, current state-of-the-art processes for the coating of Al surfaces are tested for the applicability to solar cell manufacturing and interconnection. Roll cladding of thin Al foils is known to be challenging, as discussed in the next section. The **scope of this chapter** is to evaluate different material compounds, fabricated by roll cladding, regarding solder joint formation. The material compounds are provided by different manufacturers. Therefore comparability between compounds is limited, yet qualitative indications can be derived. Critical aspects, which are relevant to provide good solderability on Al, are presented in the following. The focus hereby is on the specific interconnection process used in PV (220 °C to 250 °C, $\sim$ 2 s, SnPb solder alloy, no-clean flux, ambient air), as discussed in the introduction.

This first chapter with experimental results also establishes several methods and approaches as continued in the following chapters, focusing on other coating methods.

Challenges for Roll-Cladding Al and Choice of Material

The roll cladding process is widely used in industry to fabricate metal foils of several composite materials, *e.g.* for packaging technology, automotive industry, electronics, in heat engineering or as surface finish against corrosion [152]. "Roll cladding" in principle refers only to the first pass of the two metals through the rolls. Further passes are carried out to reach the final product geometry while maintaining the bonding ("rolling") [190]. The overall goal is to create a permanent bond through plastic deformation of the two layers. Bonding by roll cladding has been extensively studied by researchers of *e.g.* TU Bergakademie Freiberg and RWTH Aachen University [153, 154, 190–193]. Several factors haven been identified, influencing the quality of the final product.[1]

For the investigations of solder joints in this thesis, two general aspects have to be pointed out: First, it is challenging to manufacture a (very) thin composition by using a roll process at RT ("cold roll process").[2] On the one hand, this is due to general handling problems of thin metal foils, leading to *e.g.* tearing of the foil during rolling. On the other hand, the bond strength between the two cladded materials is reduced due to microstructural changes (*i.e.* grain size, diffusion, recrystallization) by further thinning through several passes [190].

The second aspect is the cladding of Al in general. The choice of materials is limited since a material pairing with similar mechanical properties (elastic and plastic deformation, microstructure, heat expansion coefficients [153]) is required. In addition, the native Al_2O_3 layer has to be removed to allow for a firm metal-metal contact. Removal prior to roll cladding is costly. Therefore the actual roll cladding process is used to "destroy" the oxide layer: the enlargement of the surface during material deformation leads to fracturing of this layer [152, 194] and to an adhesive bond at the interface of the two highly "active" metal foils [195].

As introduced in Section 3.1.1, the requirements for the cladding used in this work are: solderability, material compatibility for roll cladding with Al, resistance to oxidation and corrosion as well as phase formation with Al at the interface (s. Figure 3.1).

The most popular cladded material combination with Al is Cu, used for batteries, as interconnectors, cable shielding or in cooling systems. Beside this, steel is also often used with Al for *e.g.* dry air cooling condenser, heat shielding or punching parts [196]. Both, Cu as well as steel, are not suitable for the FoilMet® approach. They could induce impurities into the semiconductor since the laser process melts the coated Al foil during foil attachment [21, 46]. Furthermore, both will oxidize within the PV module and lead to solder joint degradation. A third option, to provide a solderable layer on cladded Al is pure Sn. However, in combination with Al, no strong bonding can be achieved at the

[1] These are *e.g.* type of metals to be joined (*i.e.* their elastic and plastic material properties, microstructure, thickness ratio, heat expansion coefficients), the surface state prior to bonding, the degree of plastic deformation within one rolling pass, roll gap geometry, pass reduction, process temperature, friction during rolling, the surface morphology of the rolls, the speed of the rolls, the curvature of the rolls [152–154].

[2] Roll cladding of very thin metal foils is no common process and manufacturer of these products mostly state a lower limit of ∼0.2 mm total thickness (0.02 mm coating) in their portfolios.

Al/Sn interface, since no diffusion or phase formation occurs.

Due to the high technical (*i.e.* for roll cladding) and material specific (*i.e.* for PV) demands for the choice of cladding and due to the limited options fulfilling the mentioned requirements, three different composites are chosen within this work to evaluate their basic suitability: Al/Sn62Pb36Ag2, Al/Sn99Cu1, Al/Ni. Sn62Pb36Ag2 is a common solder alloy for the interconnection of Si solar cells and therefore has a good compatibility with the targeted processes. Sn99Cu1 is a binary eutectic alloy and can promote the formation of AlCu phases at the interface (*cf.* Figure A.4). Ni can form several binary phases with Al and can still be contacted by soldering.

To gain a general material understanding, the evaluation is first done for ∼200 µm thick composites. Later in this chapter, in Section 4.5, the focus is set on thinner composites and the implementation for Si solar cells. The material is provided either by *SCHLENK Metallfolien GmbH & Co. KG* or *Wickeder Westfalenstahl*, whereas the production process itself could not be influenced by the author of this thesis. Due to its large influence on the quality of the product, the direct comparability between different claddings is limited.

4.1. Surface Properties

The quality of the solderable surface after the roll cladding process is essential and strongly influences the solder joint formation. Beside the material of the solderable layer, also the surface morphology, micro cracks as well as dirt and organic remnants influence the wettability with liquid solder. To adapt the soldering process appropriately (temperature, time, choice of flux and solder alloy, s. Section 2.2.2), an initial assessment is performed on the ∼200 µm thick composites, both by wetting tests and on microscopic level by SEM, as presented in the following. Afterwards, the temperature stability of the roll clads is evaluated since this influences the preheating as well as the soldering temperature.

4.1.1. Initial Characterization of Roll-Cladded Al Foil

To provide a high magnification and also detect micro impurities, the three material compounds Al/SnPbAg, Al/SnCu and Al/Ni are investigated by SEM in top view mode. Figure 4.1 shows three SEM images taken at 10 kV.

Figure 4.1.: SEM top view images (10 kV) of three different roll-cladded Al foils of $d \approx 200$ µm total thickness. Left: Al foil with solderable top layer of Sn62Pb36Ag2. Middle: Al foil coated with Sn99Cu1. Right: Al/Ni composite.

The surfaces of the Al/SnCu and Al/Ni composites appear homogeneous and only feature grooves of the rolling process (here horizontally), which is promising to assure homogeneous solder joint formation. In contrast, for the Al/SnPbAg composite (left), several bumps of different size are observed. They are circular with diameters between 50 µm to 180 µm. During fabrication of the Al/SnPbAg and Al/SnCu composites, no heat treatment was applied. Therefore, the appearance of this effect is astonishing. The material composition of these bumps will be addressed later in Section 4.1.2.

Figure 4.2 gives a detailed insight into the SnPbAg surface of the Al/SnPbAg composite by SEM. The Sn-rich phases ($Z_{\mathrm{Sn}} = 50$) of the coating appear darker, whereas the Pb-rich phases ($Z_{\mathrm{Pb}} = 82$) are brighter for the detected secondary electron signal. Two surface defects have been identified: the images on the left side show cavities found over a large

area of the surface. The inspection with EDX excludes other elements (organic or oil residues, oxides, dirt) to be present here. On the right side, an example for micro cracks, found at the grain boundaries, is shown. Compounds produced by cold roll cladding without additional annealing can feature material defects and cracks due to local exceeding of the plasticity of the material during rolling [197]. The observed surface defects will support oxidation of the Al surface at the interface to the cladding and potentially lead to a loss in adhesion between the two components. An additional thermal treatment after roll cladding could lead to a more compact grain structure due to recrystallization [197].

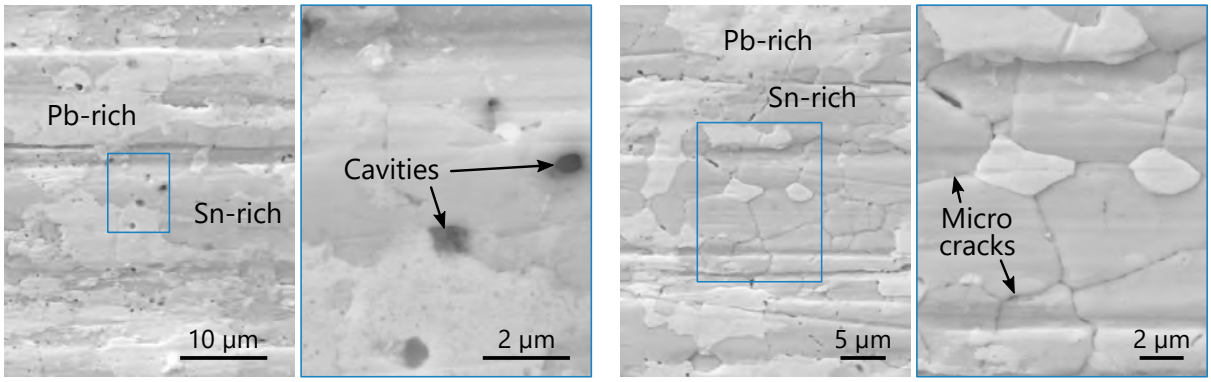

Figure 4.2.: SEM top view images (10 kV) of the surface of the Al/SnPbAg composite after fabrication.

4.1.2. Temperature Stability of Coating

To conduct a qualitative wetting test with liquid solder and to evaluate the temperature stability of the coatings, the coated Al foils are cut to small pieces (3 cm × 3 cm) and placed on a hotplate at a set temperature of $T_{\mathrm{HP}} = (120 \pm 5)\,^{\circ}\mathrm{C}$. In a first test, T_{HP} is increased stepwise and any optical changes of the samples are monitored. Figure 4.3 shows the results of the observations for the three different composites. The temperatures on the x-axis are measured by a sensor touching the hotplate surface, providing a rough indication of the actual sample temperature. Five different observations have been recorded, as given on the y-axis.

Whereas homogeneous surfaces as-rolled are observed at RT for Al/SnCu and Al/Ni (observation 1), the Al/SnPbAg surface features small bumps, as presented before (observation 2). With increasing temperature, the appearance of the coating does not change until the liquidus temperature of Sn62Pb36Ag2 $T_{\mathrm{liq}} = 179\,^{\circ}\mathrm{C}$ is reached. The surface of the Al/SnPbAg composite (blue in Fig. 4.3) starts melting (3) and gets a shiny appearance. The small balls get liquid, decrease (4) and form one melted layer with the rest of the coating (5). Above 200 °C no further changes of the SnPbAg coating are observed. The melted layer of SnPbAg is not homogeneously closed but features small holes. An SEM image of the observed structure (after cooling) is presented in the top right in Figure 4.3. The coating relocates and partly dewets from the Al substrate below. This behavior is also observed in the regions where a qualitative wetting test with SnPb

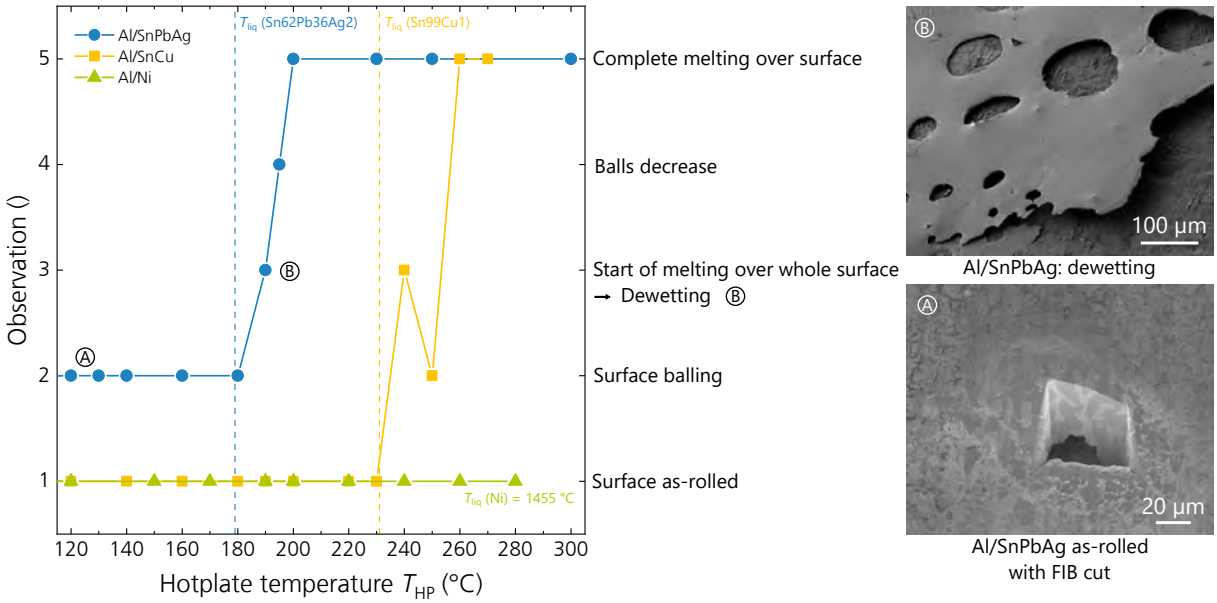

Figure 4.3.: Results of qualitative tests on a hotplate for temperature stability of the three composites. Right: SEM images (10 kV) of Al/SnPbAg.

solder is performed. The solder wets the coating (both SnPb alloy) very well, but both form small solder balls within seconds and dewet from the Al foil. These results are not surprising, since the SnPbAg coating changes its state from solid to liquid when exceeding the liquidus temperature. This limits the use of this composite to process and operation temperatures to below 179 °C.

The SEM image in the bottom right in Figure 4.3 shows one of the small bumps, observed on the initial Al/SnPbAg composite (s. Figure 4.1 left). By using **f**ocused **i**on **b**eam (FIB) milling, material is removed so that the inner structure of this feature is visible. These "bumps" or "balls" consist of SnPbAg (of the coating) and mostly feature a cavity below. This could be due to outgassing of any solvents used during rolling (*e.g.* rolling oil).[3]

A similar behavior of the composite on the hotplate is observed for Al/SnCu when exceeding the liquidus temperature of Sn99Cu1 of $T_{\mathrm{liq}} = 231\,°\mathrm{C}$. The surface starts melting and small balls of SnCu are formed until the whole surface gets liquid at about 260 °C. Inspection of the surface reveals partial dewetting of the SnCu alloy from the Al substrate.

Since the liquidus temperatures of pure Ni and pure Al are much higher (Al: $T_{\mathrm{liq}} = 660\,°\mathrm{C}$, Ni: $T_{\mathrm{liq}} = 1455\,°\mathrm{C}$), no optical changes of the Al/Ni composite are observed within the tested temperature range of up to $T_{\mathrm{HP}} = 280\,°\mathrm{C}$.

The optical contact angle α is measured for the Al/Ni composite as a measure for the degree of wetting. The measurement procedure is described in Section 3.3.1. For the test, liquid Sn60Pb40 and no-clean flux are used with a hotplate temperature of 250 °C. A

[3]Further discussion with the manufacturer of this cladding could not yield alternative explanations.

mean contact angle of $\alpha = (33.3 \pm 5.2)°$ is determined across ten measurements. In case of oxidation of Ni, no measurable impact within 60 min at 250 °C is found; the contact angle stays stable at around 25° to 35°.

The wettability is evaluated qualitatively for the Al/SnPbAg and Al/SnCu composites. For both, small samples of 2 cm × 2 cm are placed on a hotplate at 220 °C after fluxing. With a soldering iron, Sn60Pb40 is placed onto the surfaces. The liquid solder perfectly wets the Al/SnCu composite. For the other samples of Al/SnPbAg, immediate dewetting of the cladding is observed, resulting in the formation of solder balls.

The results show fundamentally different initial surface qualities of the three composites, mainly resulting from different manufacturing processes. Additionally, they behave different upon heating, as expected due to the different choice of material. For the interconnection with Sn60Pb40 in the photovoltaic industry, typically a soldering temperature of 220 °C to 250 °C is used for very short times (< 2 s). This will be too high for the coating of the Al/SnPbAg and Al/SnCu composites and could affect the soldering results. In the following section, this is further investigated among other experiments.

4.2. Mechanical Properties

The mechanical stability of the solder joints is of major importance for their long-term stability during typical operation conditions. Handling of the components during module production as well as temperature changes, wind and snow loads induce mechanical stress to the solder joints in PV modules [198], which may lead to failure. The standard DIN EN 50461 for Si photovoltaic solar cells [174] provides a 90° peel force measurement for the mechanical characterization of solder joints on front and rear side of solar cells. This method is explained in detail in Section 3.3.2.

The following sections focus on the peel force of soldered joints on the three different 200 µm thick roll-cladded Al foils. The fracture mechanism is analyzed by microscopy to reveal the interface(s) of failure. In addition, the stability of the joints upon aging is evaluated by peel force measurements after isothermal exposure.

4.2.1. Dependence of Adhesion on Material Compound

Cu ribbons of width $w = 1.5$ mm with Sn62Pb36Ag2 coating are soldered manually onto the coated Al foils over a length of at least 150 mm. To ensure the solder alloy to fully become liquid, the soldering temperature of the soldering iron is set to 280 °C and a hotplate with a set temperature of 120 °C is used to preheat the samples and to reduce the temperature difference which results in a faster soldering process and reduced thermomechanical stress. The peel force measurement is performed by peeling off the ribbons (five per sample) under an angle of 90° at a fixed speed of 50 mm min^{-1}. Mean and standard deviation of the measured force are plotted in Figure 4.4 for Al/SnPbAg (blue), Al/SnCu (yellow), Al/Ni (green).

The measured peel force is normalized to the contact width $w = 1.5$ mm. All three material compounds clearly exceed the required peel force of 1 N/mm, stated in DIN

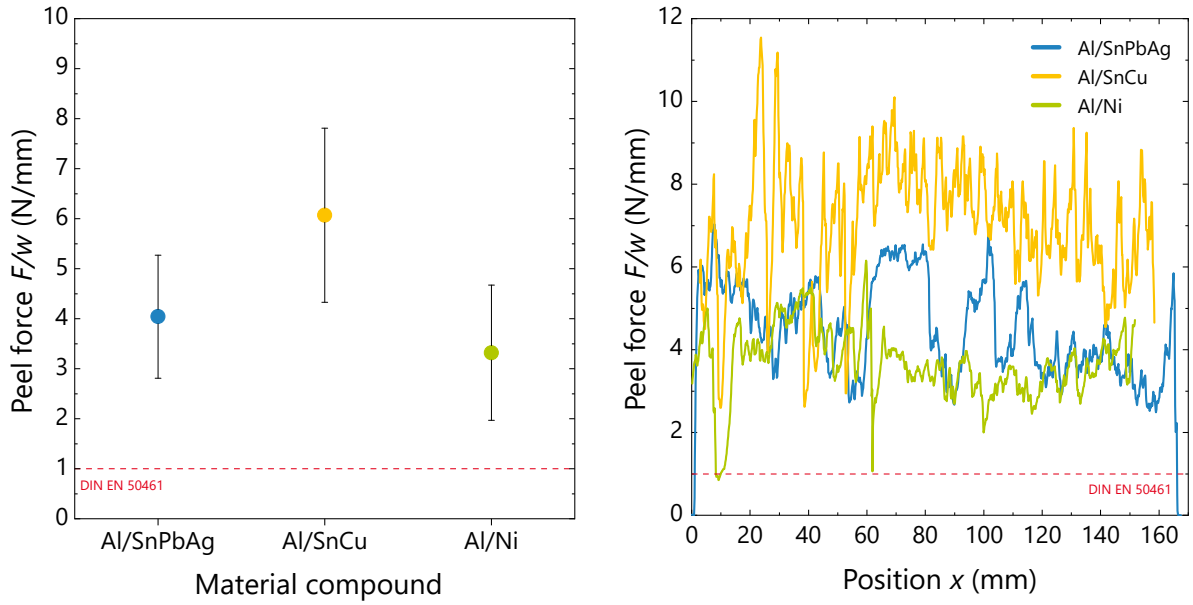

Figure 4.4.: Peel force measurement (90°) after manual soldering on 200 µm thick Al foil coated by roll cladding. Three different material compounds are tested: Al/Sn62Pb36Ag2, Al/Sn99Cu1, Al/Ni. Left: Mean and standard deviation of five measurements each. Right: Examples of one force-path-diagram each.

EN 50461 [174]. As mentioned in the introduction of this chapter, the comparability of the three materials is limited. Nevertheless, the applicability of the composites for *e.g.* the application on a FoilMet® solar cell rear side, can be qualitatively derived from these measurements.

The graph on the right in Figure 4.4 shows three examples for a force-path-diagram, obtained after peeling off one of the ribbons. All three material compounds show large fluctuations of ±1.5 N/mm to 2.5 N/mm, presumably due to the manual soldering procedure. Only for the Al/Ni composite, force values down to 1 N/mm are measured. The Al/SnCu composite even reaches peak values of nearly 12 N/mm. For Al/SnPbAg and Al/SnCu it is assumed that the soldering time of < 3 s is so short that no dewetting from the Al substrate can occur, although both coatings (SnPbAg and SnCu) get liquid in the temperature range used for soldering.

All three roll-cladded Al foils of 200 µm thickness provide strong solder joints which is an ideal condition for a reliable and highly conductive component. This opens the possibility for a successful solar cell implementation. The fracture mechanism of the solder joints after the peel force measurement is investigated in the following, to gain a deeper understanding of the material interactions.

4.2.2. Fracture Mechanism of Solder Joints

Figure 4.5 shows SEM top view images taken at 20 kV of the fracture patterns of solder joints on the Al/SnPbAg (left) and the Al/SnCu (right) composite. In the first row, a part of the sample with a lower peel force is shown next to a part yielding higher peel forces. The enlargements in the bottom show details of the fracture resulting in high peel forces.

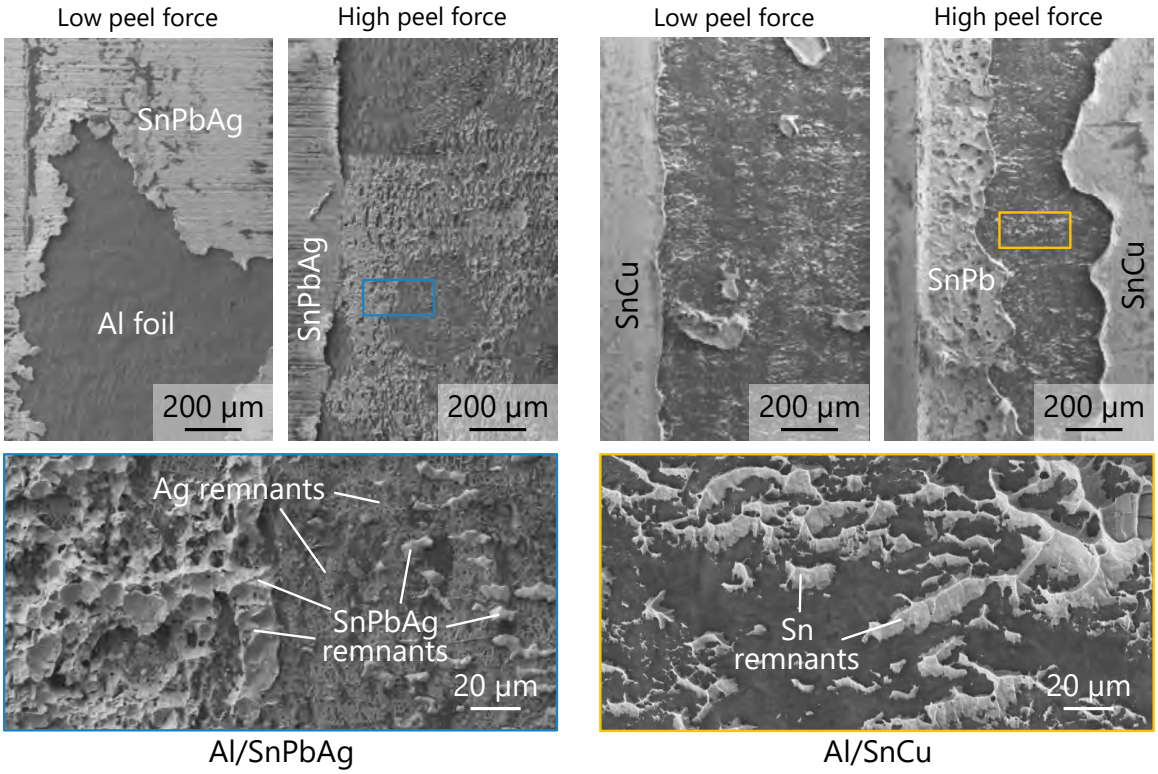

Figure 4.5.: SEM top view images (20 kV) of fracture after 90° peel force measurement of solder joints on roll-cladded Al foils. Left: Al/SnPbAg cladding. Right: Al/SnCu cladding.

Although all composites yield strong solder joints on a high peel force level, most of the observed fracture is adhesive between Al foil and coating. At some parts, a mixed fracture is observed, with remnants of the coating on the Al foil. Their structure looks different for the two composites shown. Only Ag can form a binary phase with Al, stable at RT. However, in all of these phases, Ag is dominant ($c_{\mathrm{Ag}} > 60\,\%_{\mathrm{at.}}$) [100]. EDX spectroscopy is used to quantify the remnants on the Al surface (not shown here). They mostly consist of pure Sn or even SnPb. At some positions of the Al/SnPbAg composite, a thin Ag film is found, but its exact composition could not be quantified by top view SEM and EDX.

Also Cu can form a binary phase with Al. In this case, Cu dominates with $c_{\mathrm{Cu}} > 50\,\%_{\mathrm{at.}}$ (*cf.* Figure A.4). However, no Cu remnants are measurable on the Al foil within the fracture. It should be noted that this may be due to the chosen measurement technique and the sample quality at hand. The fundamental aspect is the bonding mechanism between Al foil and cladding. For the cold roll process, this might be only due to van

der Waals linkage and the mechanical contact, resulting in rather weak bonding. In literature it is reported that the rate of deformation during the cladding step is the most important factor for bonding, *i.e.* the increase of the surface area [190]. Below a certain threshold, depending on the material combination, no bonding can be obtained by roll cladding [154]. Therefore, high normal pressures are required, leading to approximation of the two joining partner on atomic level and allow for cohesive and adhesive forces at the interface [152, 154, 196]. To even enhance the bonding at the interface, solid state diffusion is essential, which is promoted by additional heat treatment.

The fracture of the Al/Ni composite (not shown here) is very similar to the Al/SnCu fracture. The failure is mostly adhesive between Al/Ni, revealing this interface to be the weakest in this material combination.

Further insight into diffusion processes and possible phase formation at the interface can be gained from cross sections. Such investigations are presented in Section 4.3, after the following discussion on the results of isothermal aging of solder joints.

4.2.3. Solder Joint Adhesion after Isothermal Aging

Isothermal aging is performed to stress the solder joints and provoke mechanical failure. These can occur due to corrosion, oxidation or changes in the microstructure. Several "identical" samples are prepared of each material compound. Each sample consists of five soldered ribbons for peel force measurements. All samples are put into an oven at 85 °C at ambient air. After distinct time steps, one sample of each group is taken out and the peel force measurement is conducted. Figure 4.6 shows the results, using the same color code for the composites as introduced before.

The material compound Al/SnPbAg shows a significant loss in adhesion in the first fifty hours of aging. After 100 h, the force is nearly zero for all soldered ribbons. The failure is adhesive between Al and SnPbAg coating. These results support the assumption of oxidation of the Al surface, possibly due to the cavities and micro cracks, already present in the initial state (s. Figure 4.2).

The other two composites Al/SnCu (yellow) and Al/Ni (green) stay constant at around 2 N/mm and 4 N/mm, respectively. The observed fluctuations between the measurements are due to manual sample preparation. Both claddings are suitable to provide a solderable coating on a 200 µm thick Al foil, yielding strong and temperature-stable solder joints, under the tested conditions.

Within a PV module, the solder joints are not directly exposed to elevated temperatures since they are protected by the encapsulant. Typical maximum operation temperatures of a PV module are in the range of 30 °C to 80 °C, depending on the module materials [88–90]. Insufficient (initial) bonding between Al and cladding could also lead to failure of the solder joints on the solar cell. The solder joints on the rear side of the FoilMet® solar cell face the backsheet, which also features a certain permeability for humidity. This supports corrosion and could also lead to solder joint failure.

The graph on the right in Figure 4.6 shows the Al/SnCu composite, in yellow as presented on the left and in orange a tempered version. After the fabrication process, a thermal treatment for 12 h at 165 °C was conducted by the producer to improve the ad-

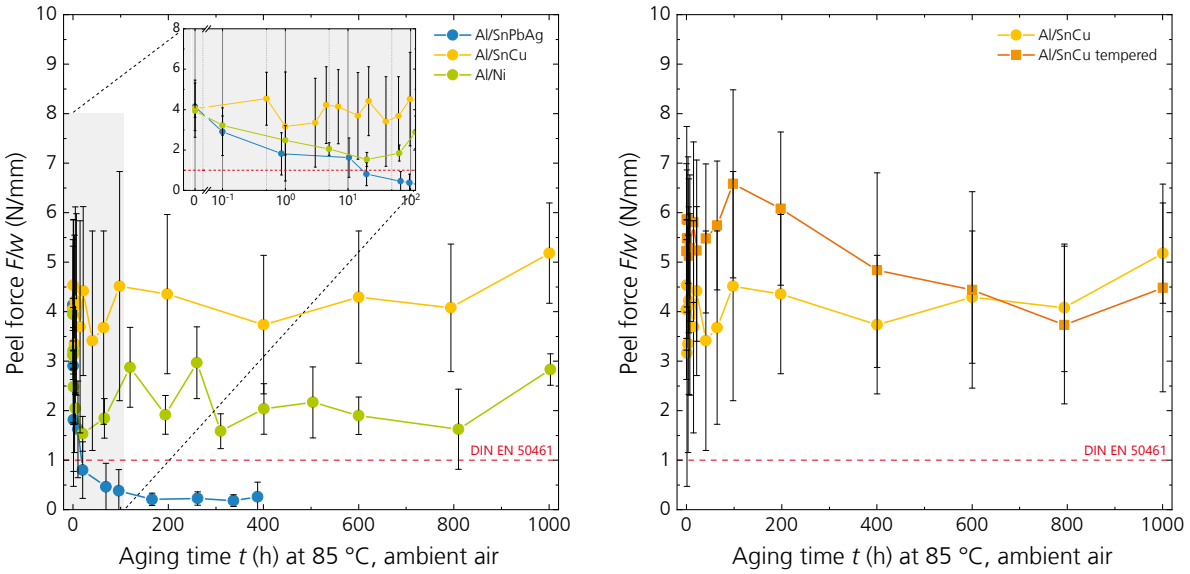

Figure 4.6.: Peel force measurement after isothermal aging (85 °C, ambient air) of solder joints on 200 µm thick roll-cladded Al foils. Each data point includes five peel force measurements. Left: Peel force F/w for three different composites: Al/SnPbAg, Al/SnCu, Al/Ni. Right: Influence of additional heat treatment of composite Al/SnCu on peel force upon aging.

hesion of Al and SnCu (*cf.* Section 3.1.1). In the initial state, this leads to an increase in peel force from 4 N/mm to 6 N/mm compared to the untempered composite. Most likely, a larger diffusion zone promotes the strong adhesion. After about 500 h aging at 85 °C at ambient air, the same force level of the untempered composite of 4 N/mm is reached. Both composites stay stable on this level. The temperature used in the heat treatment is below the liquidus temperature of SnCu, but above its recrystallization temperature. This leads to a reorganization of the microstructure of SnCu and promotes diffusion at the interfaces. After recrystallization of a material, its hardness is usually reduced while its ductility increases [152, 196]. Such changes of the mechanical properties of SnCu and the Al/SnCu composite may lead to a stronger solder joint. However, the cold-rolled Al/SnCu composite is already on a comparably high level, which is a promising baseline for reliable solder joints in a PV module.

4.3. Microstructure of Cross Sections

By the preparation of metallographic cross sections (*cf.* Section A.6), the interfaces of the solder joints can be analyzed in more detail. Although one cross section can always only show a specific location within the joint, it is a very strong and helpful tool to explore the interfacial reactions and identify the interacting parameters. For solder joints on roll-cladded Al foils, two interfaces are of high interest: First, the interface between solder and coating. Secondly, the interface of the Al substrate and the cladding itself. Both interfaces will be analyzed in the following.

4.3.1. Solder Joints on Roll-Cladded Al Foil

After manual contact soldering of solder-coated Cu ribbons, small pieces of each sample are embedded into epoxy and polished (*cf.* Figure A.5) for subsequent analysis by SEM and EDX. Figure 4.7 gives an overview of solder joints on each of the investigated composites.

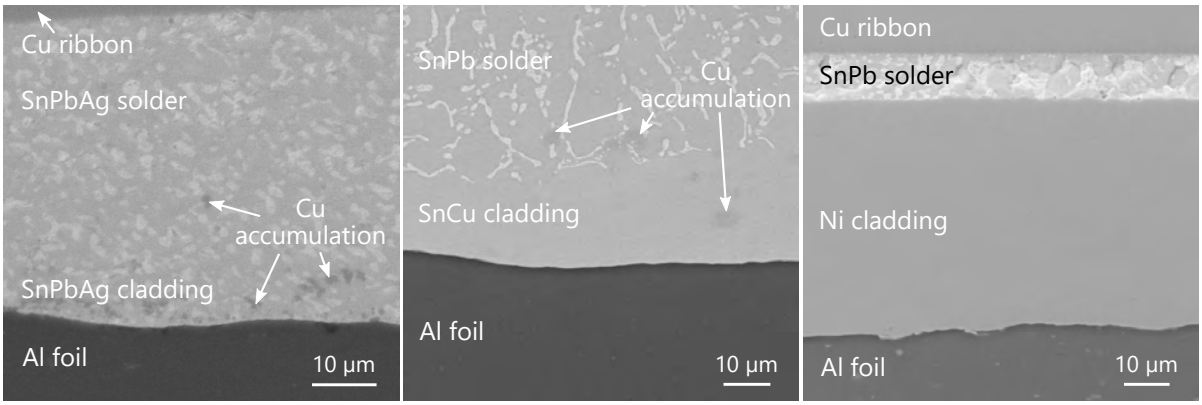

Figure 4.7.: SEM images (20 kV) of cross sections of solder joints on three different roll-cladded Al foils. Left: Al/Sn62Pb36Ag2, contacted with Sn62Pb36Ag2 solder. Middle: Al/Sn99Cu1, contacted with Sn60Pb40 solder. Right: Al/Ni, contacted with Sn60Pb40 solder.

For all three material compounds, a void-free solder joint at the interface solder/cladding is formed during soldering. The system Al/SnPbAg is a special case: During soldering, the cladding gets liquid and is mixed with the solder of the ribbon, which is also Sn62Pb36Ag2. Therefore, the interface cladding/Al foil is even more relevant. In some cases, inhomogeneities at this interface are found (not shown here). No firm bonding could be reached in these cases and small gaps between SnPbAg and Al foil are observed. Nevertheless, this state is only rarely present in the investigated joints; the dominant microstructure is presented in Figure 4.7 on the left.

In the interfacial region of the solder to the Al foil, darker grains of Cu occur. These stem from Cu dissolution and diffusion, originating from the ribbon core towards the Al interface. The elemental distribution is analyzed in the next section.

For the Al/SnCu system, very homogeneous solder joints between Sn60Pb40 and Sn99Cu1 are found. One of them is presented in Figure 4.7 in the SEM image in the middle. Again, the darker grains correspond to Cu agglomerations, which appear locally within solder and cladding and are not distributed equally.

The image on the right shows the Al/Ni system. The joint consists of a comparably thin solder layer of Sn60Pb40 on a thick Ni coating. All three composites feature a microscopically "wavy" surface at the Al/cladding interface. This results from the cladding process and the contact formation by mechanical pressure. The Al/Ni system was fabricated by a different manufacturer and is the only system of these three where the fabrication ended with the cladding process. For the others, two additional steps of rolling were conducted after cladding. Therefore, the Al/Ni interface appears rougher with local unevenness.

In the following, each composite is analyzed in detail using EDX to understand the material distribution, especially in the interfacial regions.

4.3.2. Element distribution at the Interfaces of Al/Sn62Pb36Ag2/Solder

As discussed above, the interface of Al foil and SnPbAg cladding is of special interest for further understanding. This interface is shown in Figure 4.8 at two different positions in cross sections analyzed by SEM and EDX.

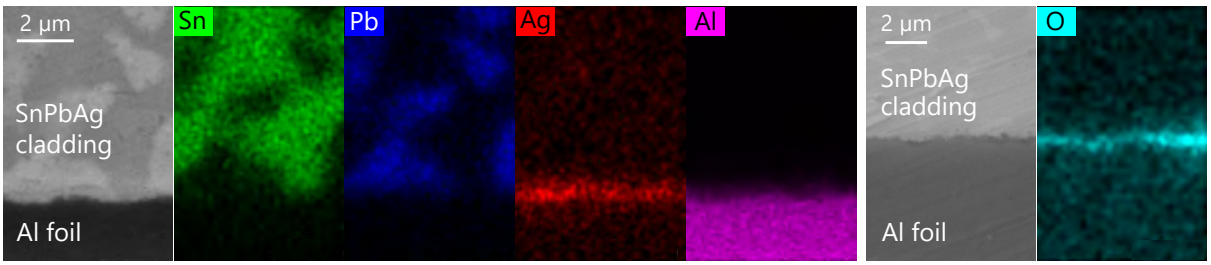

Figure 4.8.: SEM and EDX analysis of cross sections of roll-cladded Al foil with SnPbAg cladding and solder. Two different positions along the interface are shown.

The solder alloy as well as the cladding contain 2 $\%_{wt.}$ of Ag; no other sources of Ag contribute to this metallic contact. The EDX mappings show an agglomeration of Ag at the interface to the Al foil. This is observed along the majority of the Al/SnPbAg interface. The thickness of this layer is measured to be up to $\sim 1\,\mu m$ thick. This finding is in agreement with the Ag remnants found within the fracture after the peel force measurement (*cf.* Figure 4.5). Furthermore, this is reason to assume that the interface between Ag and SnPb is often the weakest in this joint. The formation of this Ag layer could be correlated to the crystallization kinetics of SnPbAg, which crystallizes from the outer surface in its eutectic phase and therefore "pushes" Ag towards the Al interface (*cf.* precipitation of Ag) [16]. Possibly due to the limited amount of Ag, no distinct binary phase formation with Al is measured.

The SEM image on the right in Figure 4.8 shows another position at the same interface. Here, a small gap between cladding and Al foil is found and the EDX map shows an increased portion of oxygen. Such an oxygen layer with a gap in a cross section sample could also be promoted by oxidation of the cross section after polishing from the sides. The samples were stored in nitrogen in the time period after polishing before SEM. The oxygen layer could be formed before soldering by oxygen diffusion into the cladding by the cavities and micro cracks found in the initial assessment of the surface (*cf.* Figure 4.2). It could also be a remnant of the initial Al_2O_3 layer that was broken up during rolling [195]. This layer degrades the interface and could lead to a mechanical failure of the joints, as it is found for the adhesion after isothermal aging.

4.3.3. Element distribution at the Interfaces of Al/Sn99Cu1/Solder

Figure 4.9 presents EDX measurements at the interface of the Al foil to the Sn99Cu1 cladding. On the right, a 6 µm line scan perpendicular to the interface is shown.

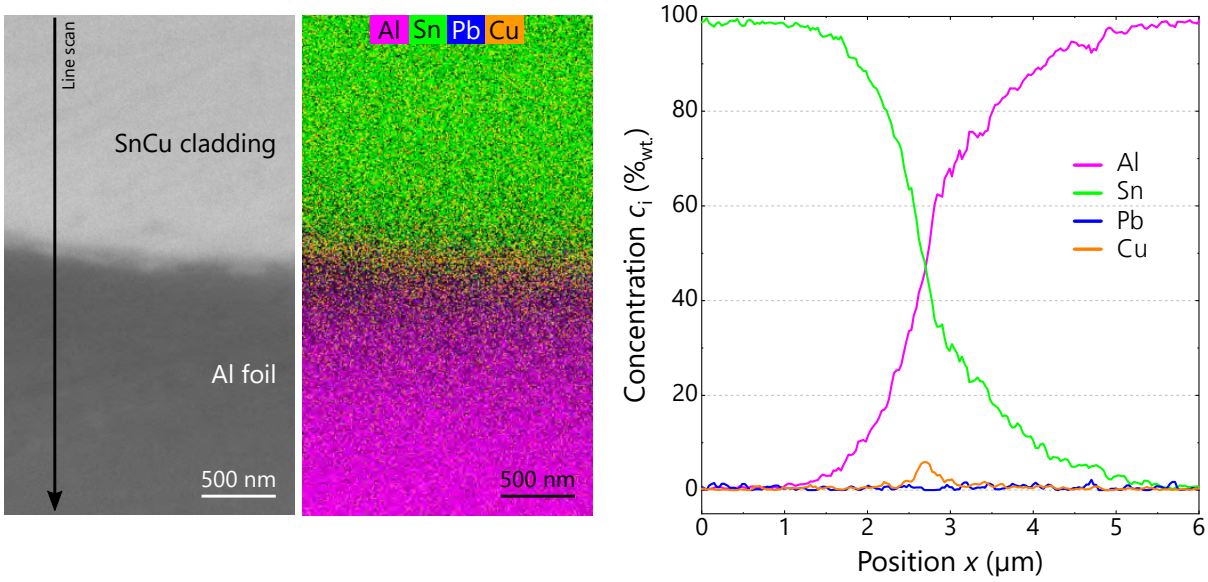

Figure 4.9.: SEM and EDX analysis of the interface Al/SnCu on cross section samples. Left: SEM image (20 kV) and EDX mapping. Right: Indicated line scan perpendicular to the interface.

For this system, a distinct layer of Cu is found at the interface to the Al foil. By dissolution of Cu from the ribbon into the liquid solder, Cu is already distributed within the Sn60Pb40 matrix. Afterwards, diffusion of Cu towards the interface of the cladding could lead to an increase of the Cu content in the Sn99Cu1 cladding. This in turn leads to saturation and Cu diffusion towards the Al interface. This layer can contribute to the relatively higher adhesion of this interface since Al and Cu can form several binary phases at RT (*cf.* Figure A.5). For most of them, Cu is dominating. Due to the reduced signal within the presented results, no quantification of a possible phase formation can be made. However, the fracture pattern, given in Figure 4.5, does not show a measurable amount of Cu after the peel force measurement. Either the Cu is not measurable due to the high signal of the surrounding in the top view mode or the weakest interface is between Cu and Al. It has to be mentioned that this Cu layer is not homogeneously present over the whole solder joint, but rather for about 80 % of the length of the cross section. Initial inspection of the composite by EDX also shows a slight accumulation of Cu at this interface, but considerably less than after soldering.

4.3.4. Element distribution at the Interfaces of Al/Ni/Solder

As expected from the very small contact angle of $\alpha = (33.3 \pm 5.2)°$ for liquid Sn60Pb40 on the Ni cladding, solder joint formation is successful and very homogeneous firmly bonded contacts can be soldered. One example of a cross section is shown in Figure 4.10.

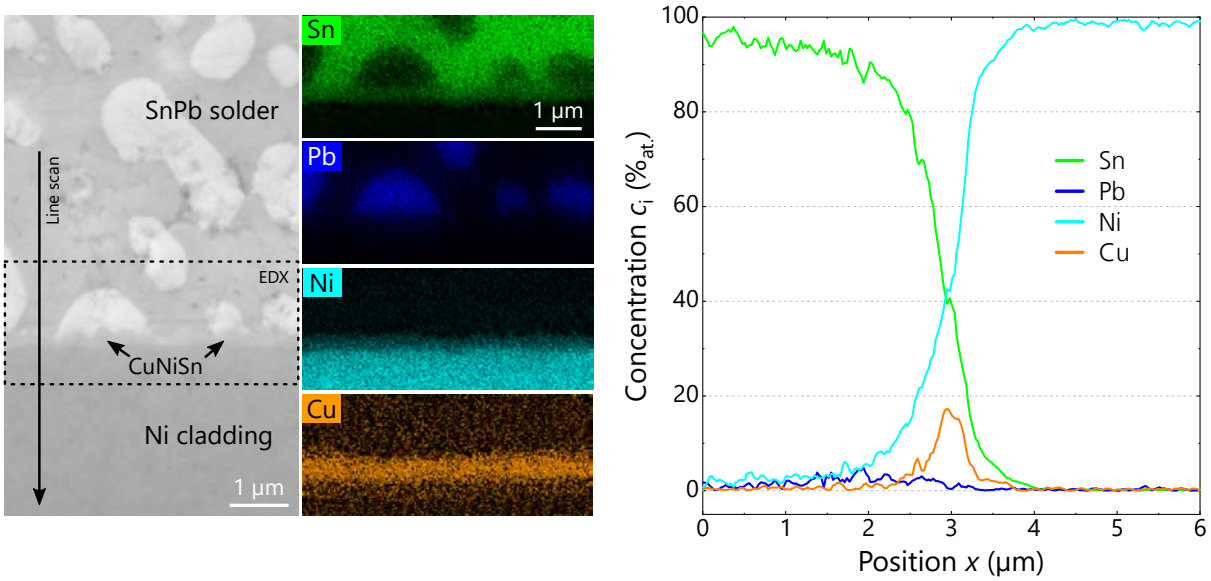

Figure 4.10.: SEM and EDX analysis of cross sections of solder joints on the Al/Ni composite. Left: SEM image (20 kV) with corresponding EDX mappings of the interfacial region. Right: Line scan perpendicular to the interface.

On the left, an SEM image, presenting the interface Ni/Sn60Pb40, is given. The interfacial region is scanned by EDX, to provide the spatial distribution of the elements. Again, a remarkably large amount of Cu is found on top of the Ni layer, although no Cu is present in the initial solder alloy and could only originate from the Cu core of the ribbon. The EDX maps of Sn and Ni reveal that these two elements are also present in the Cu-rich layer. In case of phase formation, most probably, the ternary phase η-$(Cu, Ni)_6Sn_5$ could be built, which is stable at RT [199]. The phase $(Ni, Cu)_3Sn_4$ is less likely due to the high amount of Cu of $\sim 18\,\%_{at.}$ at this position. The presence of this phase proves diffusion within the joint and at the interface. The bonding between Sn solder and Ni surfaces is known to be strong and reliable [7, 200], consequently high peel forces for this material compound are measured.

The other interface, influencing the adhesion of solder joints on the Al/Ni composite, is the interface of cladding. An SEM image of this interface is shown in Figure 4.11.

The line scan shows a small diffusion zone on the side of the Al foil. This indicates Ni diffusion and could lead to binary phase formation. The phase diagram of Al-Ni is given in the appendix in Figure A.4. There exist several stable phases at RT as Al_3Ni, Al_3Ni_2, Al_3Ni_5, $AlNi_3$ and AlNi. For the present sample system, most likely Al is dominating, so that the Al_3Ni phase with $75\,\%_{at.}$ Al and $25\,\%_{at.}$ Ni could be assumed. The dominating

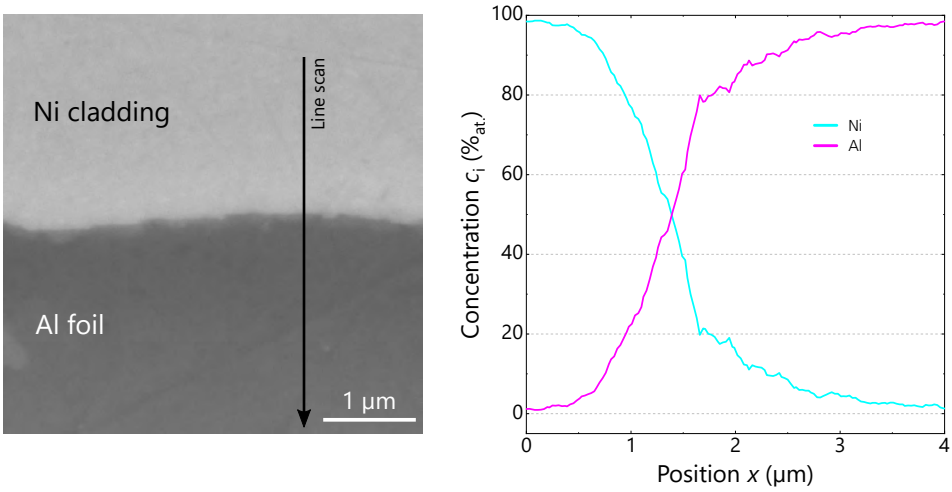

Figure 4.11.: SEM image (20 kV) and EDX line scan of Al/Ni interface in cross section mode.

driving factor for the Ni diffusion is the annealing at 300 °C for 3 h after the fabrication of the composite. Solid state diffusion at RT is very low for Ni in Al [201] and plays a minor role here.

The microstructure of all three composites reveals interfacial reactions, presumably promoting the adhesion of the systems after soldering. By the choice of the cladding material, a good wettable metal or alloy can be chosen. Therefore, the challenge of this approach is the bonding at the interface to the Al foil. The cladding process provides initial solderability of Al. However, the analysis on microstructural level has shown that a reliable bonding to the Al foil is essential to prevent a loss in adhesion, directly after soldering and even after isothermal aging. Present oxide layers at the Al interface reduce the adhesion, as observed for the Al/SnPbAg composite. If such a layer has a measurable impact on the contact resistance of the solder joints, will be analyzed in the following section.

4.4. Electrical Properties

For the implementation of solder joints on roll-cladded Al foil in Si solar cells, the contact resistance has to be low and stable within the PV module during operation (*cf.* Section 3.4.4). To evaluate the electrical resistance on material level, samples for contact resistance measurements are fabricated out of ~ 200 µm thick roll-cladded Al foils.

4.4.1. Solder Joint Resistance after Isothermal Aging

The sample preparation is described in Section 3.3.4 in detail. As solder alloy, Sn62Pb36Ag2 is used. The resistance is extracted for a current flow of 100 mA by using the contact end resistance method. The values are normalized to the contact area to obtain the specific

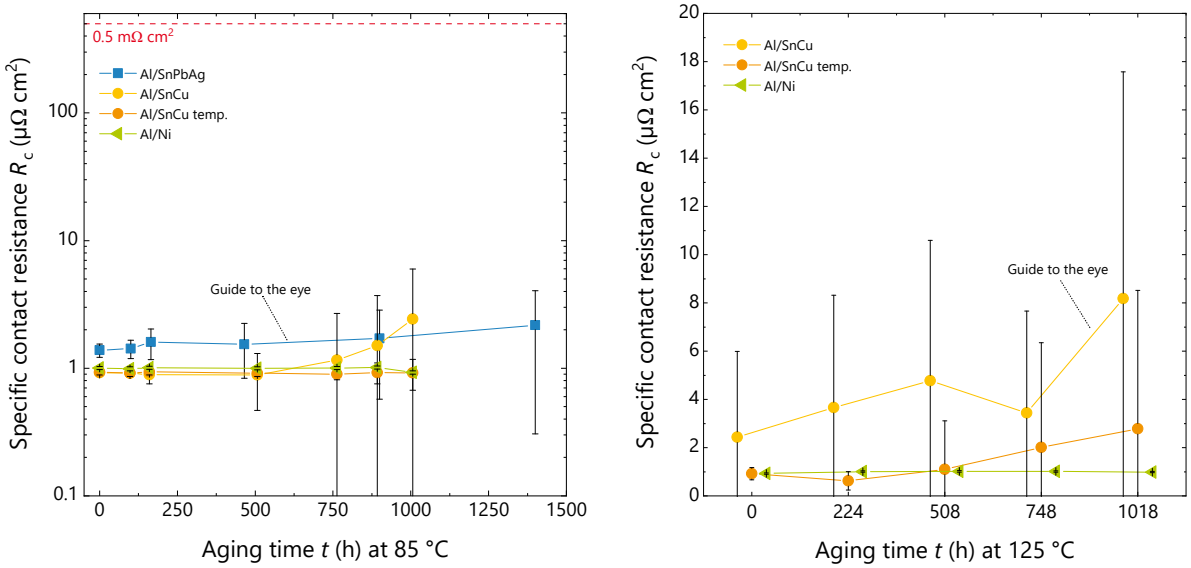

Figure 4.12.: Specific contact resistance R_c of solder joints on different roll-cladded Al foils. Left: Aging under isothermal conditions at 85 °C at ambient air. Note the logarithmic y-axis. Right: Additional aging of some of the samples of the left graph for additional 1000 h at 125 °C.

contact resistance R_c. Figure 4.12 presents the results for the different material compounds, fabricated by roll cladding.

On the left, R_c is plotted against the aging time t. The samples are placed into an oven at ambient air and 85 °C and measured after distinct time steps. For the measurement, the samples are taken out of the oven, let cool down, measured and placed into the heated oven again. Each data point includes mean and standard deviation over five identical samples, each featuring seven solder joints.

For the Al/SnCu composite (yellow), the tempered version (orange) is investigated as well. The solder joints on all four composites show specific contact resistances around 0.9 µΩ cm² to 1.4 µΩ cm². According to Zemen *et al.*, resistances smaller than 500 µΩ cm² have a negligible influence on the cell-to-module (CTM) loss and do not affect the fill factor of the solar cell [180]. The lower the contact resistance of the solder joints on a Si solar cell, the lower the CTM loss due to soldering. All values measured within the plotted aging time are very low and in the uncritical range for the solar cell and module due to good metallic contacts.

Some samples feature single solder joints which start to degrade slightly and lead to an increase of the mean R_c and the corresponding statistical error. In the given measurement range, which is near the resolution limit of the measurement device, the statistic errors are mostly in the same order of magnitude as the mean values (note the logarithmic y-axis).

The graph on the right in Figure 4.12 shows the same samples for three of the composites, aged additional 1018 h at 125 °C after completing the 1000 h at 85 °C (left). Note the different scaling of the y-axis (linear) and the categorical x-axis for better visualization

of the data. A slight increase of R_c from $(2.4 \pm 3.6)\,\mu\Omega\,cm^2$ to $(8.2 \pm 9.4)\,\mu\Omega\,cm^2$ for the solder joints on Al/SnCu (yellow) is measured within 1018 h. The strong increase of the statistical standard deviation, seen by the error bars, indicate that individual solder joints dominate the averaged results, which is confirmed by diligent analysis of the measurements (not shown here). Nevertheless, all values are still in the uncritical range. For all three composites, one reference sample which is not aged (but storage at RT and ambient air) is measured. For the Al/SnCu composite, this reference sample yields $R_{c,ref} = (0.9 \pm 0.1)\,\mu\Omega\,cm^2$ for the measurement at 1018 h, which is still on the same level as for the initial state. This clearly shows that the elevated temperature is the dominant parameter causing the increase in R_c.

To exclude the temperature shock from RT to 125 °C (loading of oven) and back to RT (unloading of oven) as the reason for the increase in R_c, the oven is heated up and cooled down with approximately ±5 K/min in the loaded state for the last measurement at 1018 h. No clear influence on the measurement results is found; the trend for the Al/SnCu composites continues.

The results of the contact resistance measurement show only a slight increase of R_c for the Al/SnPbAg system. This is remarkable since the micro cracks in the SnPbAg cladding, found in the SEM top view images (*cf.* Figure 4.2), should support oxidation of the Al surface, accelerated at elevated temperatures. The presence of an Al_2O_3 layer would lead to an increase in R_c due to its isolating properties [169]. The contact area of each solder joint of this sample type measures $A = 0.05\,cm^2$, whereas the micro cracks are only in the order of $\mathcal{O}(10\,\mu m)$. If oxidation occurs, it does not negatively influence the specific contact resistance of the solder joints on Al/SnPbAg, most likely due to the large contact area.

The best electrical performance is measured for the Al/Ni composite. All solder joints are stable, even at 125 °C, indicated by the small resistances and statistical errors.

The measured data indicate a slight advantage of the tempering step (Al/SnCu temp., orange). This is similar to the finding for the peel force measurements after isothermal aging. Nevertheless, the overall variation is very small and the absolute values of R_c are two orders of magnitude below the critical value. Even the increase of the Al/SnCu system is uncritical, the measurement time of 1000 h is already chosen very long. The conditions for the solder joints in a PV module would be much less severe, depending on the module location. Therefore, no further investigations have been performed within the scope of this thesis.

4.4.2. Solder Joint Resistance after Damp Heat Test

For the material compound Al/SnPbAg, similar samples are used to evaluate the electrical stability of the solder joints under **d**amp **h**eat (DH) conditions (85 °C, 85 % relative humidity). 200 µm thick roll-cladded foil is used to prepare ten contact resistance samples, as described in Section 3.3.4. They are laminated into the classical module setup, consisting of 4 mm thick front glass (10 cm × 10 cm), two layers of EVA and a white PET backsheet. The coated side of the samples, contacted with Sn62Pb36Ag2-coated Cu rib-

bons, is placed into the laminate facing the backsheet, as it would be positioned in the original module setup with a FoilMet® solar cell. Figure 4.13 shows a sketch of the sample geometry (cross section of composite) and the data of the contact resistance measurement, performed with the same procedure as introduced before.

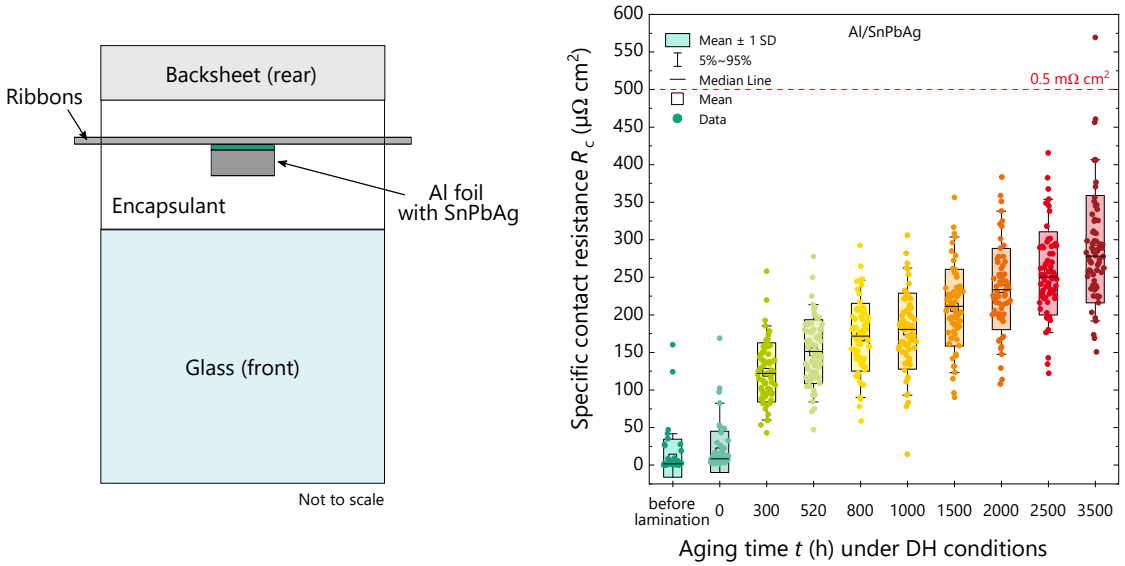

Figure 4.13.: Left: Sketch of the cross section of a laminate for contact resistance measurements after DH aging. The Al foil strip is oriented into the plane of projection, as well as several other ribbons. Right: Specific contact resistance R_c of laminates with solder joints on roll-cladded Al foils. The samples are aged under DH conditions.

Note that the x-axis in Figure 4.13 right is categorical in t. In the appendix (Figure A.6), the mean R_c is plotted as a function of t, for a better visualization of the trend. The lamination process does not influence the overall specific contact resistance. The values, measured for all ten samples (with seven solder joints each), mostly are in the range of $1\,\mu\Omega\,cm^2$ to $10\,\mu\Omega\,cm^2$, in agreement with the values presented before. After the first 300 h of aging under DH conditions, the mean specific contact resistance increases to $R_c = (123 \pm 39)\,\mu\Omega\,cm^2$. This trend continues, but saturates. The increase is driven by an overall increase across all measured solder joints, instead of deviations of single joints, as seen for isothermal aging for other composites. It could be assumed that this homogeneous degradation is caused by an overall effect on all solder joints, *e.g.* the degradation of the coating from the sample rear side (backsheet). Assuming $R_c \propto t^{1/3}$, the critical value of $R_c = 500\,\mu\Omega cm^2$ is reached at around $t \approx 19\,700$ h (2.2 a), exceeding the expected time a PV module would be faced with DH conditions in most applications.

Due to limited amount of samples, this analysis could not be performed for the other two claddings. Especially for the Al/SnCu composite, this would be of interest to evaluate the influence of Cu on the electrical properties. Considering the dimension of the solder joints on the rear side of a solar cell (5BB layout: $5\times$ 150 mm×0.9 mm), they are much

larger than the contact area of 0.15 mm^2 evaluated on material level. Therefore, no critical influence of humidity at elevated temperatures is assumed for the FoilMet® module and a failure could most likely be excluded.

4.5. Implementation in Si Solar Cells

The results on material level, presented in the previous Sections 4.1 to 4.4, show the general suitability of roll-cladded Al foil for the intended application as Si solar cell rear electrode. The Al/SnCu, as well as the Al/Ni composite provide strong and reliable solder joints (under the tested conditions), with a low resistance at the contact. For the implementation of a cladded Al foil to the FoilMet® production route, the Al foil has to be much thinner than the ones tested in previous sections, namely about 10 µm. This is the main challenge for a firm metallic bonding between foil and cladding fabricated by a cold roll process. The following section focuses on the evaluation of solder joints on thin **Al/SnCu composites**, regarding wettability and mechanical strength of the joints. Afterwards, in Section 4.5.2, the challenges for the integration into the FoilMet® solar cell production route are discussed.

4.5.1. Thickness Reduction of SnCu Composite

In Figure 4.14, four optical microscopy images of ribbons, soldered onto the SnCu cladding are shown. The Cu ribbon (Sn60Pb40, cross section: 0.90 mm × 0.22 mm, fluxed with no-clean flux) and the soldering parameters (manual contact soldering, hotplate: 120 °C, soldering iron: 280 °C) are kept constant, while the thickness of the composite is reduced. The image on the left shows the ∼ 200 µm thick material compound, characterized in the previous sections. The low contact angle between Sn99Cu1 and Sn60Pb40 solder confirm very good wetting. By reducing the overall thickness of the composite $d = d_{\mathrm{Al}} + d_{\mathrm{SnCu}}$, the contact angle slightly increases. The image on the right shows the composite with $d = 27$ µm, where first indications for dewetting of the SnCu layer are found. The contact angle is larger and the SnCu cladding is no longer fully homogeneous.

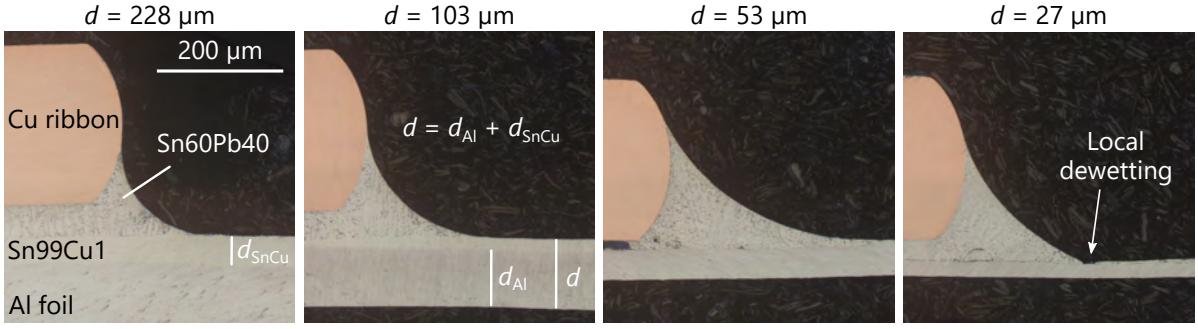

Figure 4.14.: Optical microscopy images of cross sections after soldering. Sn60Pb40 solder joints on Sn99Cu1 coated Al foil for reduced foil thicknesses. From left to right: Decrease of total thickness d of the composites.

The reduction of the composite thickness d implicates several challenges which influence the general foil handling, the characterization methods and further processes for solar cell implementation. Due to the mechanical instability of the 10 µm thick composite,[4] it was not possible to prepare a cross section after soldering. Also peel force measurements after soldering are not reasonable for composites thinner than 50 µm, since the Al foil is too thin and rips during the test.

The results of this restricted characterization of the thinner Al/SnCu composite is summarized in Table 4.1. The cross sections are used to determine the exact thicknesses of Al and SnCu. The thickness is measured at four positions of two samples each, yielding mean and standard deviation of eight measurements per thickness.

Table 4.1.: Characterization results for different thicknesses of the Al/Sn99Cu1 composite. The thickness is determined by optical microscopy of cross sections (*cf.* Figure 4.14). Tape test (90°) is used to evaluate the adhesion of the SnCu layer on the Al foil. Wetting is evaluated by optical inspection of solder droplets. The peel force (90°) is measured after manual soldering of Sn60Pb40 ribbons.

Thickness			**Tape test**	**Wetting**	**Peel force**
d (µm)	d_{Al} (µm)	d_{SnCu} (µm)		(Sn60Pb40)	F/w (N/mm)
227.7 ± 4.9	182.3 ± 3.8	45.4 ± 3.0	passed	good	6.4 ± 2.1
102.6 ± 3.3	81.8 ± 1.6	20.8 ± 2.9	passed	good	7.1 ± 3.2
52.6 ± 2.2	43.0 ± 1.6	9.6 ± 1.6	passed	good	good
27.4 ± 0.9	22.1 ± 0.7	5.4 ± 0.6	-	good	-
10	9	1	-	good	-

A 90° tape test is performed to qualify the initial adhesion of the SnCu layer on the Al substrate. This test could be performed for three composites of 228 µm, 103 µm and 53 µm thickness, all yielding an adhesive failure between tape and SnCu layer. No breakage of the SnCu cladding is observed.

A qualitative wetting test is done with liquid Sn60Pb40 on a hotplate at 220 °C. The solder ($T_{\mathrm{liq}} = 183\,^{\circ}\mathrm{C}$) is applied with the tip of the soldering iron ($T_{\mathrm{iron}} = 280\,^{\circ}\mathrm{C}$), while the wettability directly after deposition is valued by optical inspection. All foils show good wetting but partial dewetting around the solder droplet. The heat of the tip is transferred to the composite by the liquid solder, which leads to melting of the Sn99Cu1 layer ($T_{\mathrm{liq}} = 231\,^{\circ}\mathrm{C}$). For very short soldering times ($t < 2\,\mathrm{s}$) and for thicker SnCu layer, this is uncritical and the droplets as well as soldered ribbons form a strong contact to the substrate. This is proven by peel force measurements for the thicker foils, also listed in Table 4.1.

[4] This Al foil is even thinner than a classical household Al foil with 15 µm thickness.

4.5.2. Challenges for FoilMet® Solar Cell Integration

To assess the wettability and get a rough feeling for the strength of the solder joints on the 10 µm thin foil, manual soldering tests are performed on several pieces of foil. One example is given in Figure 4.15 on the left. Wettability with liquid Sn60Pb40, as well as solder joint formation is qualitatively as good as for the 27 µm thick version of the composite.

For the mechanical and electrical contact formation of the 10 µm thin Al foil to the rear side of a FoilMet® solar cell, a special laser process has been developed at Fraunhofer ISE [40, 41, 43, 44, 46, 50, 202], as introduced in Section 2.1.3. The formation of the so-called "LMB" contacts between Al foil and Si wafer strongly depends on the optical properties of the Al foil, as well as the heat transfer and thickness of the involved materials. The development of this process has been optimized by John *et al.* for uncoated 10 µm thick Al foils.[5] By adding a coating on top of the Al, the surface of the foil is changed and the process has to be adapted. This process development is not part of this thesis and addressed by other researcher at Fraunhofer ISE [202].

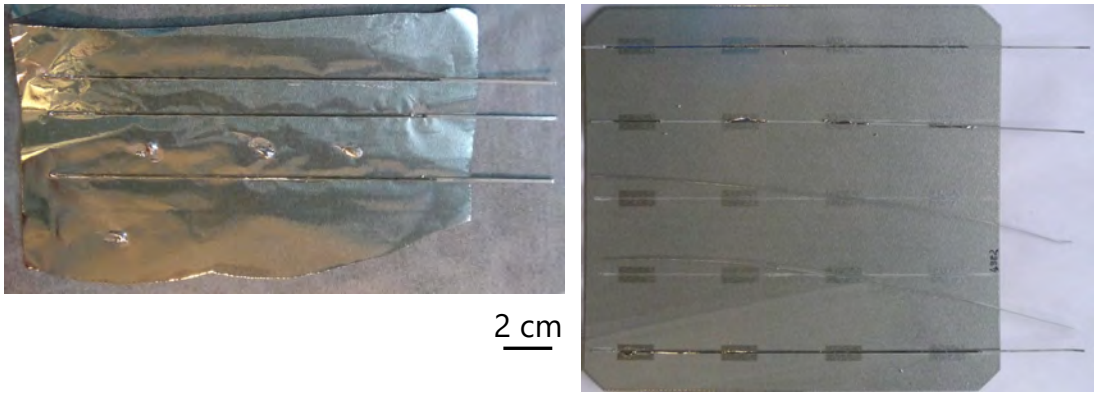

Figure 4.15.: Photos of soldered ribbons onto 10 µm thick roll-cladded Al foil (Al/Sn99Cu1). Left: Pretest on pure foil. Right: Soldering on solar cell rear side with laser-attached Al/SnCu foil. Two of the ribbons are peeled off to investigate the fracture pattern.

Preliminary Soldering Tests

To perform an intermediate feasibility test within the frame of this work, dummy solar cells are prepared. The 10 µm thick Al foil with Sn99Cu1 cladding is attached to the solar cell rear side of a Si solar cell by a preliminary laser process. The intention is to provide a similar rear side regarding the mechanical properties as for the FoilMet® concept to perform wettability and soldering tests. The laser process is selected in a way to ensure

[5] The alloy of the Al foil (1200) is the same as used for the presented studies in this work. All foils are provided by the project partner *Hydro Aluminium*.

a strong bonding of the Al to the Si to allow for manual soldering.[6]

The first soldering tests have shown that no solder joint can be formed at the positions where the laser contacts are placed. This is most probably due to the very high density of laser contacts and induced defects on the surface, leading to a change of the SnCu layer (*e.g.* oxidation or ablation). For the "classical" FoilMet® approach with LMB contacts, this is not a significant problem, since the surface coverage treated with the laser is much lower.

To handle this process-specific influence, areas free of laser contacts are used at the positions of the ribbons. This design is very similar to the Ag pads on the rear side of a state-of-the-art PERC structure. The right photo in Figure 4.15 shows such a solar cell after the interconnection with five ribbons. The soldering process is successful at the 5×4 "pads". Although the ribbons stick to the foil, the adhesion is very weak. By touching one of the ribbons at its end from the side, it can be detached. Anecdotally, the mechanical strength of the ribbons on the unfixed Al foil (*cf.* left photo in Figure 4.15) seems much stronger. A detailed observation of the solder joints shows dewetting of the SnCu layer aside of the ribbons. The fracture of the peeled ribbons is investigated by SEM and EDX for a deeper understanding of the interfacial interactions.

Analysis of Fracture

Figure 4.16 shows three top view SEM images of the fracture on the solar cell rear side, presented on the right in Figure 4.15. All images are taken at 20 kV, while the magnification increases from left to right. In addition, the EDX map of Al is given for the second SEM image.

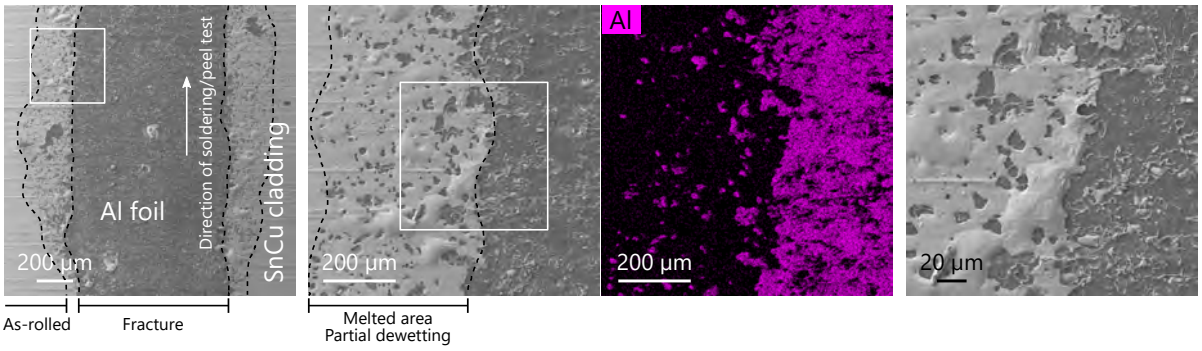

Figure 4.16.: SEM top view images (20 kV) of the fracture pattern after soldering and peeling off a ribbon on 10 µm Al/SnCu on the rear side of a solar cell. For the second image, the EDX map of Al is given.

The darker part in the SEM images corresponds to the area where soldering is done and the ribbon is peeled off. The EDX map of Al clearly reveals a nearly complete removal of the SnCu cladding in this area. Since most of the ~ 1 µm thin SnCu layer remelts below

[6] Preliminary experiments on FoilMet® solar cells have shown that manual soldering of more than 3 ribbons to the solar cell rear side leads to a cell bow after cooling due to asymmetric stress (missing ribbons on the front side). This in turns partly rips off the Al foil.

the ribbon during soldering, it is not surprising that the weakest interface is between Al and SnCu. For thicker SnCu layers, the failure is different since dewetting is not observed for composites with $d > 50\,\mu m$.

The bright part in the SEM image relates to the SnCu cladding. The grooves, arising from the rolling process, are clearly visible in horizontal direction. They confirm no melting of the SnCu layer in this region. However, several "holes" in the SnCu layer are found, uncovering the underlying Al foil. In this region, melting and dewetting occurred in addition to the layer directly below the ribbon. This is a critical issue and a fundamental problem at this stage of the process.

4.6. Chapter Summary

The evaluation of solder joints on roll-cladded Al foil is performed for three different composites: Al/Sn62Pb36Ag2, Al/Sn99Cu1 and Al/Ni. Already the initial as-rolled state of the foils shows a fundamentally different surface, as cavities and micro cracks are found on the SnPbAg layer. All coatings show **good wetting** with liquid SnPb-based solder alloys and therefore successful solder joint formation. The mechanical and electrical characterization of the solder joints yield **high peel forces** ($> 3\,\mathrm{N/mm}$) and **low (specific) contact resistances** ($< 10\,\mu\Omega\,\mathrm{cm}^2$), showing the general suitability of these material combinations on 200 µm thick Al foils. Only the Al/SnPbAg compound shows a loss in adhesion upon isothermal aging within the first 50 h at 85 °C, most likely caused by oxidation of the cladded interface by oxygen diffusion.

The microstructural analysis of all compounds show **homogeneous solder joints**, confirming the good wettability and solderability. The interface to the Al foil is investigated by SEM and EDX. For Al/SnCu and Al/Ni, small **diffusion zones** are found at the interface, **promoting the bond strength** of these two material systems, leading to higher peel forces than the Al/SnPbAg composite.

For the Al/SnCu system, a foil thinning from 200 µm to ∼25 µm is investigated stepwise. **For thinner composites, the interface to the Al becomes of major importance.** Further thinning may cause a loss in adhesion at this interface. Optical microscopy of cross sections and soldering of very thin foils prove partial **dewetting** of the SnCu layer in the region of soldering due to the low melting point of the cladding. This effect and the reduced bond strength to the Al interface dominate the loss in adhesion, achieved on the rear side of FoilMet® solar cells, wherefore no module integration was possible.

Since the melting point of Ni is much higher than for Sn99Cu1 (*cf.* phase diagrams in Figure A.4) and far above the soldering temperature, no dewetting is observed for the Al/Ni composite. This might be advantageous when it comes to thinner composites $< 50\,\mu\mathrm{m}$. In addition, solid Ni acts as diffusion barrier against Cu, preventing Cu diffusion towards the Si solar cell. Within the scope of this work, thin Al/Ni could not be investigated and should be considered in future research.

The results, obtained in this chapter, underline the **great challenge of roll cladding thin Al foils**. The evaluation on material level shows the general suitability of the Al/SnCu and Al/Ni composite for the application on FoilMet® solar cells (in case of a lower soldering temperature $< 220\,^\circ\mathrm{C}$ for the Al/SnCu composite to avoid melting). Further applications are discussed in Chapter 7.

5. Wet-Chemical Modification of Aluminum Surfaces

This chapter focuses on solder joints on wet-chemically coated Al foils and the implementation in Si solar cells and modules. The results on Al foils have been partly published by the author in 2019 [203] and 2020 [204]. After either a single (s-Zn) or double (d-Zn) zincate treatment, electroless Ni plating provides a solderable layer on top of the Al surface. The wet-chemical coating sequence was optimized in cooperation with experts in this field at Fraunhofer ISE. The first ***Section 5.1*** *shows the evaluation of the surface properties before soldering. The quality of the coating process is characterized by SEM top view images, using Zn coverage and the mean Zn particle size as a measure for the formation of the Ni layer. Additionally, the contact angle of liquid solder on the plated Ni surface is characterized to evaluate the wetting behavior.* ***Section 5.2*** *addresses the mechanical stability of solder joints directly after soldering and after isothermal aging. The mechanical strength of the joints is investigated by 90° peel force measurements, comparing the impact of different process variations of the Zn treatment. A detailed SEM and EDX analysis of the fracture mechanism is conducted. Additionally, cross sections are prepared to investigate diffusion at the interfaces and phase formation on microstructural level within the joints. The results are shown in* ***Section 5.3****, also including isothermally aged joints. To complete this chapter,* ***Section 5.4*** *shows the results of the process transformation of this coating approach to solar cells and modules. The solder joint quality on PERC solar cells with different Al rear sides is evaluated after IR soldering on an industrial stringer. After lamination, the electrical performance of 1-cell-modules is analyzed by I-V measurements after TC and DH climate chamber testing. Finally,* ***Section 5.5*** *addresses a detailed failure analysis, revealing the challenges of this implementation. Luminescence (EL & PL) imaging is performed to assess the local electrical changes of the interconnection on cell and module level.*

In contrast to a mechanically cladded component, the wet-chemical coating is applied onto the Al substrates in an additional coating step. Therefore, it is much more flexible regarding the desired application. Another key attractiveness is the simple and low-cost process and the possibility to use batch and inline tools. The **scope of this chapter** is on an insightful characterization of solder joints on wet-chemically coated Al foils. The fundamental scientific understanding of solder joint formation, obtained in sections 5.1-5.3 for Al foils, is transferred to other Al substrates to investigate the practical feasibility for an industrial application in the photovoltaic industry. The implementation of the coating process on PERC solar cells and the detailed analysis of solder joints and the corresponding cell and module performance are used to identify challenges for this new approach.

Challenges for Wet-Chemical Coatings on Al and Choice of Material

Wet-chemical coating can be used to provide solderability on the Al foil rear side of a FoilMet® solar cell (*cf.* Section 3.1.2). One advantage of this approach is the decoupling of the Al coating process from the rest of the solar cell manufacturing. However, this brings up challenges for the conducted coating, since handling of a thin Al foil of 10 µm thickness is difficult. Inappropriate foil handling leads to tearing of the foil, crinkles and contamination. For wet-chemical treatment, the industrial implementation could be challenging. Another option is the coating of the rear side of the finished FoilMet® solar cell, which would allow to use established inline tools. Here, the used chemicals have to be compatible with the solar cell to not induce impurities and reduce lifetime of the charge carriers.

The focus in this chapter is on a pretreatment of Al with Zn, which is very effective and widely used as surface modification for Al components [99, 158–162]. It is used to remove the Al_2O_3 layer and clean the surface. Additionally, it is a fast process with process times of 10 s to 60 s, depending on the Al substrate and the requirements for the final component. The immediate deposition of another metal allows for a direct contact to the Al while providing solderability. In this work, Ni is chosen as the best alternative after Ag (expensive) and Cu (prone to oxidation).

5.1. Surface Properties

To provide a solderable coating on top of the Al foil, a wet-chemical process to deposit Zn either within a single (s-Zn) or double zincate (d-Zn) process is used (*cf.* Section 3.1.2). The previous chapter on roll-cladded Al foils has shown that the quality of the interfaces is essential to yield a good performance of the sample. The time between coating and soldering (and a possible change of the surfaces) has to be considered for the assessment of wet-chemically coated Al substrates. The coating process is very flexible regarding process times and the used chemicals, whereas the deposited layers (Zn, Ni) can vary, which in turn influences wettability and solder joint formation. To assess the quality of the Zn and Ni surfaces, the following sections address the Zn surface coverage after deposition, the resulting Ni layer and their wettability with liquid solder.

5.1.1. Zink Coverage on Al

SEM top view images taken at 10 kV serve for process control after each step, shown in Figure 5.1. The images are compared by a particle detection algorithm, identifying Zn seeds of different particle size a_{Zn}. The minimum particle size is set to 0.2 µm^2, for shapes with a circularity of 0.3 – 1.0. These (arbitrary) thresholds limit the influence of the blurry background and emphasize clearly identifiable particles. This quantitative evaluation will underestimate the Zn coverage to some extend and only serves for comparison between s-Zn and d-Zn. The amount of deposited Zn seeds ζ is quantified by the total area of detected Zn seeds A_{Zn} within the SEM image section $A_{\mathrm{SEM}} = 57.7\,\mu\mathrm{m} \times 43.1\,\mu\mathrm{m}$. The evaluated data is given in Table 5.1.

Table 5.1.: Surface coverage with Zn seeds ζ and mean Zn particle size a_{Zn} (evaluation of SEM top view images in Figure 5.1 b), d)) deposited after single zincate (s-Zn) and a double zincate (d-Zn) process.

	s-Zn (30 s)	**d-Zn** (30 s + 15 s)
Zn coverage ζ (%)	4.0 ± 1.0	10.8 ± 2.0
Mean Zn particle size a_{Zn} (µm^2)	0.44 ± 0.05	0.41 ± 0.05

After 30 s of dipping the 200 µm thick rolled Al foil (Figure 5.1 a)) into the alkaline Zn bath, about $\zeta_{\mathrm{s-Zn}} = (4.0 \pm 1.0)\,\%$ of the Al foil is covered with Zn seeds with a mean particle size of $a_{\mathrm{s-Zn}} = (0.44 \pm 0.05)\,\mu\mathrm{m}^2$ (Figure 5.1 b)). Subsequent electroless Ni plating leads the Zn to dissolve in the bath, whereas a Ni layer is formed in direct contact with the Al surface. After 8 min of plating, a closed Ni layer of about 2 µm thickness is formed (Figure 5.1 c)), which yields a lumpy surface, typical for plated Ni surfaces [159]. A double zincate process (30 s + 15 s, Figure 5.1 d)) results in a more homogeneous Ni layer (Figure 5.1 e)). Due to a larger Zn coverage of $\zeta_{\mathrm{d-Zn}} = (10.8 \pm 2.0)\,\%$, the resulting Ni layer is smoother since more Zn seeds serve as starting points for Ni growth. The mean

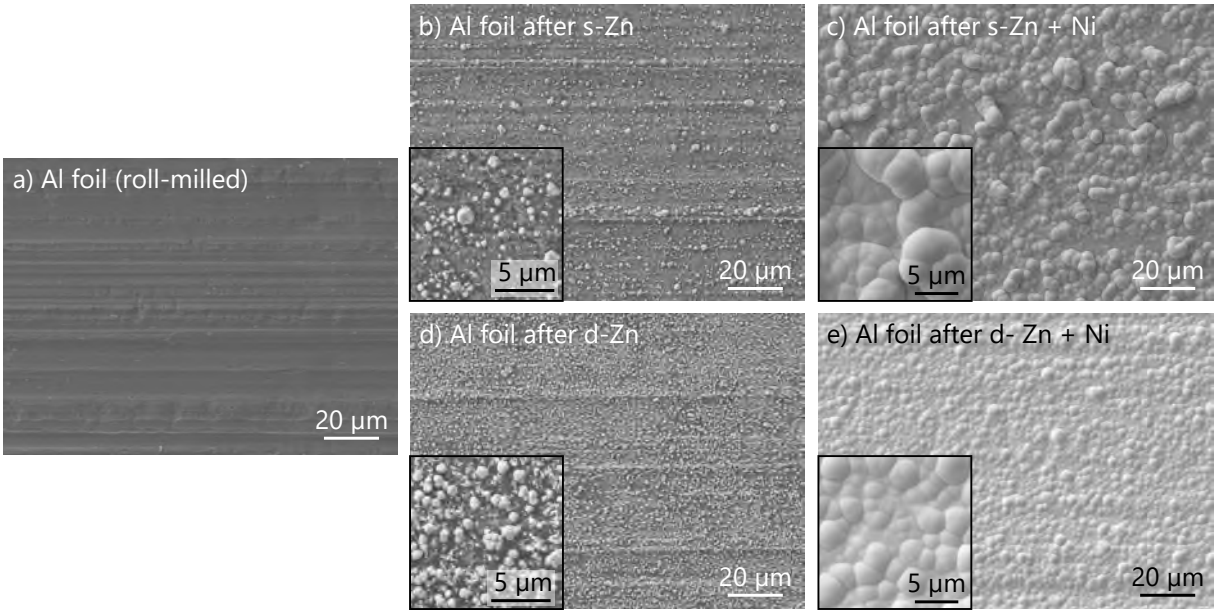

Figure 5.1.: SEM top view images of a) 200 µm thick roll milled Al foil. The coating quality is investigated by SEM showing the Zn deposition after 30 s s-Zn in b) and double Zn treatment 30 s + 15 s in d). The resulting Ni layer after 8 min electroless plating is given in c) and e), respectively. All images are taken at 10 kV.

Zn particle size stays nearly the same ($a_{\mathrm{d-Zn}} = (0.41 \pm 0.05)\,\mu\mathrm{m}^2$), indicating an upper limit of a_{Zn} for the used process conditions for Zn treatment.

5.1.2. Wetting of the Coating

For the reliable formation of a solder joint on a metal surface, a good surface wettability with liquid solder is an important requirement. The static contact angle α between the substrate, liquid Sn60Pb40 solder and air is measured on a hotplate at $(250 \pm 5)\,^{\circ}\mathrm{C}$ (*cf.* Section 3.3.1).

Figure 5.2 left shows the results of the contact angle measurements for Al foil coated with pure Zn, for the Ni surface after s-Zn and Ni plating and for d-Zn and Ni plating. The evaluated d-Zn process (w/o Ni) is optimized to result in a closed Zn surface. Wetting of liquid Sn60Pb40 on pure Zn is poor ($\alpha_{\mathrm{d-Zn}} = (117.0 \pm 15.1)^{\circ}$), as it is expected from the electrochemical potential $E^0_{\mathrm{Zn}} = -0.762\,\mathrm{V}$. The used no-clean flux (*kester* 952s) is not able to remove all native oxides of the Zn surface or reoxidation is too fast. Both Ni-coated Al foils show excellent wetting. Despite the different surface morphology of the Ni surfaces (Figure 5.1 c) and e)), the contact angle is measured to be similar with $\alpha_{\mathrm{s-Zn+Ni}} = (27.7 \pm 9.2)^{\circ}$ and $\alpha_{\mathrm{d-Zn+Ni}} = (32.6 \pm 4.3)^{\circ}$.

For the evaluation of the mean contact angle given in Figure 5.2 left, each surface was measured ten times. The standard deviation is given by the error bars. For good wettable surfaces, a circular or elliptical fit is used for evaluating the shape of the droplet in the contrast image (s. inset in Figure 5.2 right). The systematic error is given by the error bars in Figure 5.2 right. The elliptical fit considers asymmetric droplets and results in

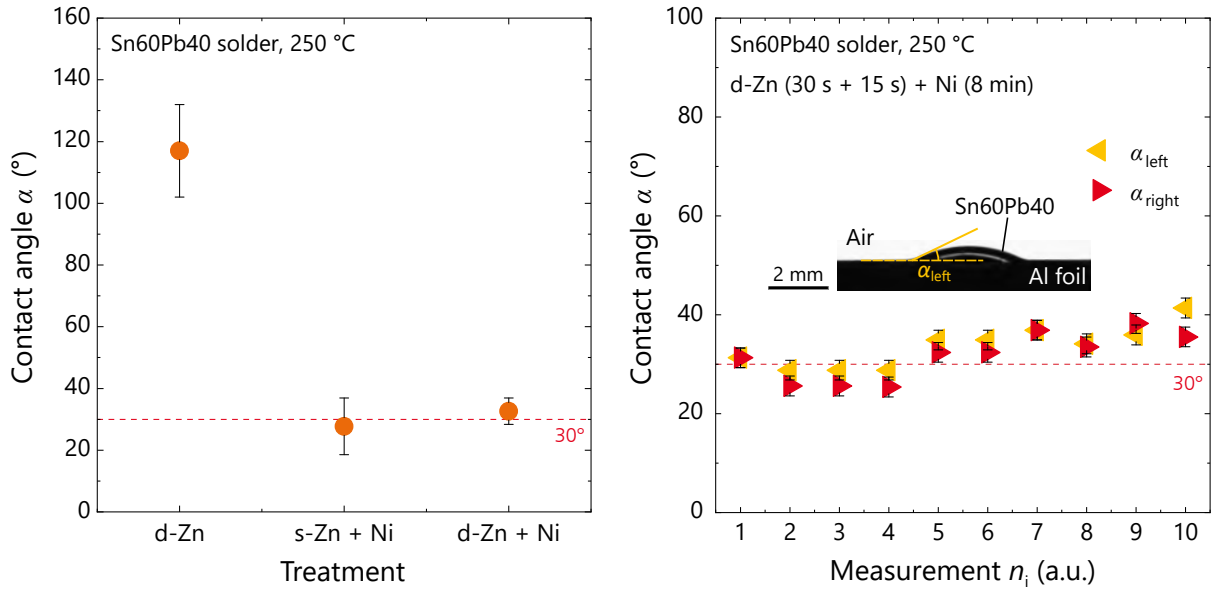

Figure 5.2.: Left: Contact angle measurement on Al foil coated with three different treatments: optimized d-Zn, 30 s s-Zn + 8 min Ni and 30 s + 15 s d-Zn + 8 min Ni. Right: Details of measurements on d-Zn + Ni with example for contrast image of liquid solder droplet.

a difference between left and right contact angle. For the tested Al foils, the standard deviation is very small, indicating a homogeneously coated Al foil.

The fundamental approach of the wet-chemical process sequence can be illustrated by the standard electrode potential E^0. In Figure 5.3 left, this quantity is correlated with the measured values presented before. The bare Al has a negative $E^0_{\mathrm{Al}} = -1.662\,\mathrm{V}$, when measured under standard conditions (298 K, 100 kPa, 1.0 mol dm^{-3}) with respect to the standard hydrogen electrode [205]. Fundamentally, coating of Al with less reactive metals changes E^0 to higher values. This is the case for zinc. When deposited out of an alkaline solution, this can remove the problematic native Al_2O_3 layer. With $E^0_{\mathrm{Zn}} = -0.762\,\mathrm{V}$, Zn is less reactive to oxygen then Al, but reactive enough to build an ZnO layer, which also impedes wetting by solder. Nevertheless, the Zn clusters on top of the Al surface prevent oxidation of the Al underneath and serve as nuclei for subsequent electroless Ni plating. The Ni surface has a standard electrode potential of $E^0_{\mathrm{Ni}} = -0.250\,\mathrm{V}$, closer to those of Sn ($E^0_{\mathrm{Sn}} = -0.138\,\mathrm{V}$), Cu ($E^0_{\mathrm{Cu}} = 0.521\,\mathrm{V}$) and Ag ($E^0_{\mathrm{Ag}} = 0.7996\,\mathrm{V}$) [205]. On these more noble surfaces, wetting with liquid solder is excellent, which enables reliable soldering processes.

After coating, the Al surface may oxidize if the time between coating and soldering is too long. Additionally, the surface quality may change during the soldering process at elevated temperature. To analyze this, *in-situ* contact angle measurements are performed at 250 °C, a typical soldering temperature for Sn-based solder alloys. In Figure 5.3 right, the change of the contact angle α_i/α_0 is plotted against the time t of six identical samples

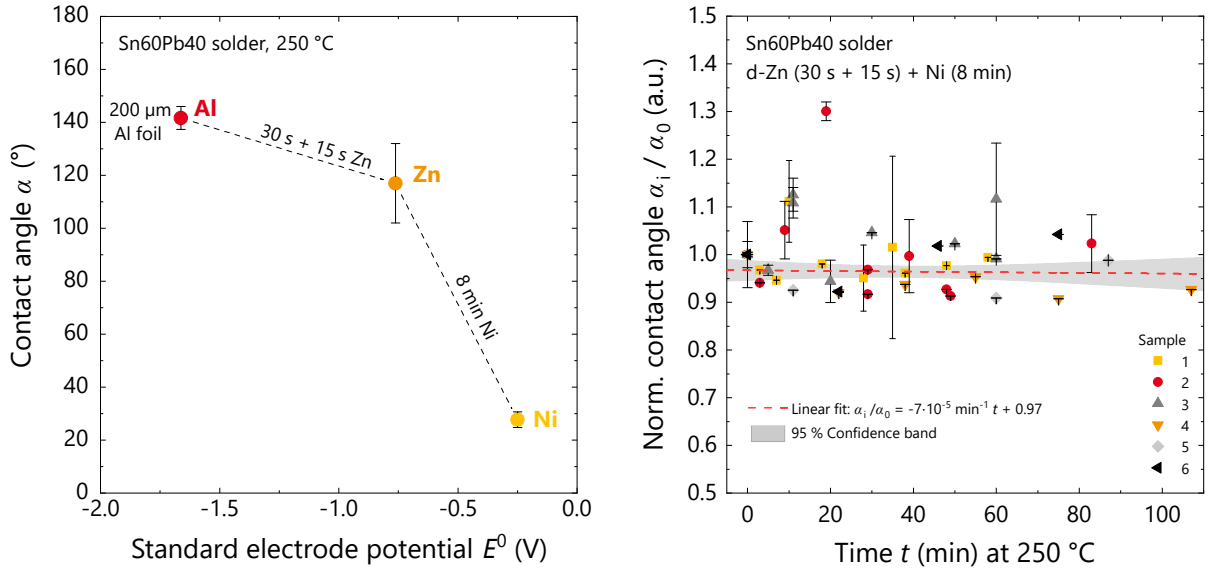

Figure 5.3.: Left: Dependence of the contact angle α of liquid solder (Sn60Pb40) on pure Al foil (red), Zn coated Al foil (orange) and Ni coated Al foil (yellow) of the standard electrode potential E^0. The wet-chemical coating steps represent the sequence of coating used in this work. Right: Change of the contact angle α of liquid Sn60Pb40 solder on d-Zn + Ni coated Al foil, measured at ambient air. Six identical samples (colored symbols) with individual solder droplets of $m_{\mathrm{SnPb}} = (11 \pm 1)\,\mathrm{mg}$ are tested. No dewetting (increase of α_i) was observed within 100 min on a hotplate at 250 °C, as indicated by the linear fit yielding negligible slope.

placed on a hotplate heated up to 250 °C. Each value α_i is normalized to the initial value α_0 of the unaged sample at $t = 0$, to focus on the relative change over time. For each sample 1-6, a different solder droplet with $m_{\mathrm{SnPb}} = (11 \pm 1)\,\mathrm{mg}$ is used. A coated Al foil treated with 30 s + 15 s d-Zn + 8 min Ni is tested.

No dewetting (significant change of $\alpha_\mathrm{i}/\alpha_0$) within the total measurement time t of about 100 min is detected. Since the soldering process for solar cells, processed in an automated stringer, lasts less than 20 s in total at an elevated temperature between $T_{\mathrm{Preheating}} = 50\,^\circ\mathrm{C} - 170\,^\circ\mathrm{C}$ and $T_\mathrm{s} = 190\,^\circ\mathrm{C} - 260\,^\circ\mathrm{C}$ (*cf.* Section 2.2.4), the tested Ni coating should be easily solderable within the stringer for solar module production and similar applications.

5.2. Mechanical Properties

After s-Zn and d-Zn treatment and subsequent Ni plating, both surfaces allow for contact formation by soldering. The mechanical stability of the solder joints is characterized by a 90° peel force measurement. The results are given in Figure 5.4 left.

As expected, a good adhesion (high peel force F/w) is given for good wettable surfaces indicated by a small contact angle α in Figure 5.2 left. For an application on the rear side of a solar cell, the joints have to withstand the string handling after soldering. The measured peel forces for the Ni-coated foils are significantly higher than the required

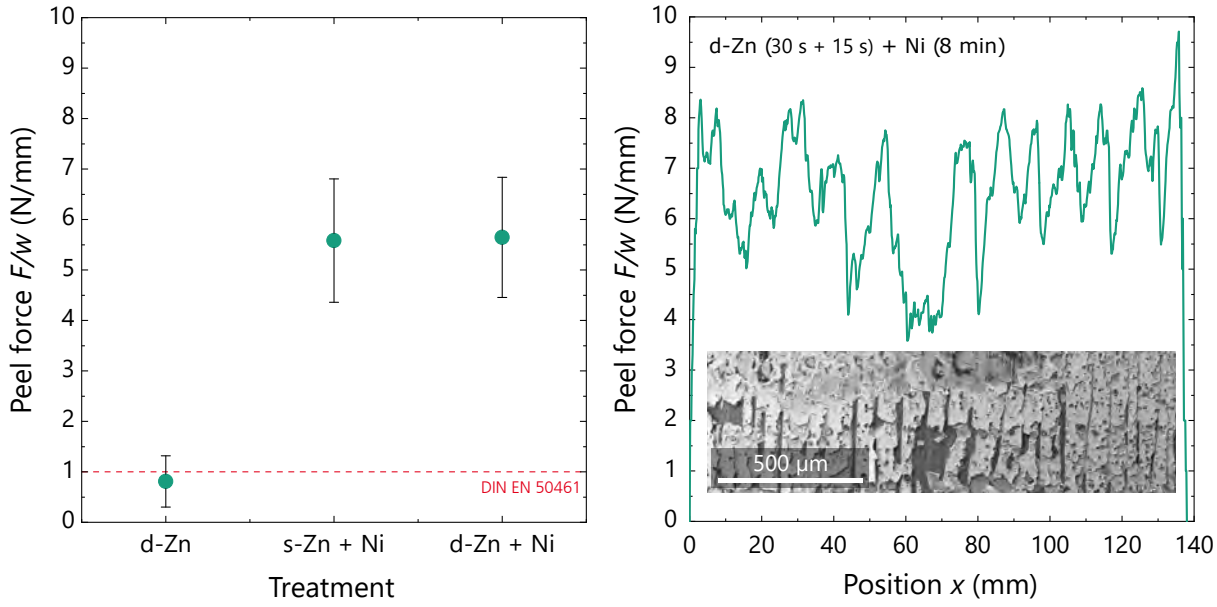

Figure 5.4.: Left: Adhesion for three different treatments: optimized d-Zn, s-Zn + Ni and d-Zn + Ni. Right: Detail of measurements on 30 s + 15 s d-Zn + 8 min Ni with a part of the fracture pattern after the peel force measurement (top view SEM, 20 kV).

value of 1 N/mm, given in the standard DIN EN 50461 [174]. Figure 5.4 right exemplarily presents data of a measurement on a 30 s + 15 s d-Zn + 8 min Ni treated Al foil. Although the force is fluctuating, all values stay above 4 N/mm. A small section of the fracture pattern on the Al foil after the peel force measurement is given by a top view SEM image in the inset. A mixed fracture is observed, showing different failure modes (cohesive as well as adhesive). This indicates no dominant interface to fail, which is an ideal condition for measuring high adhesion of solder joints.

5.2.1. Solder Joint Adhesion after Isothermal Aging

To investigate the long-term stability of the solder joints, isothermal aging at 85 °C is performed [185]. A set of solder joints with Sn62Pb36Ag2-coated Cu ribbons on treated Al foil (30 s + 15 s d-Zn + 8 min Ni) is fabricated and aged for 1000 h at 85 °C in ambient air. After this treatment, the mechanical stability is characterized by 90° peel force measurements. Figure 5.5 shows the results of the peel force measured after distinct time steps of aging. Any data point includes five measurements of 150 mm evaluation length at different positions on the coated Al foils and dedicated standard deviation. The initial value of $F/w_{t=0} = (5.5 \pm 0.8)$ N/mm correlates well with the previous results in Figure 5.4 left, showing a mixed fracture pattern on microstructural level. No significant loss in adhesion within 1000 h at 85 °C is measured; only a slight decrease around 700 h is observed, which however is far below the measurement uncertainty. The mean peel force stays above 4 N/mm without any change of the fracture pattern. This result indicates no detrimental oxidation of the interfaces (Al/Ni and/or Ni/SnPbAg) and no decisive brittle intermetallic phase formation.

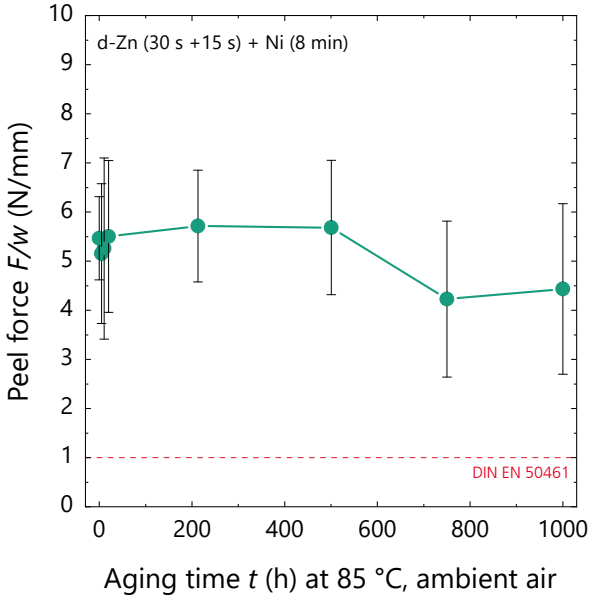

Figure 5.5.: Peel force of solder joints on 200 µm thick Al foil treated with d-Zn (30 s+15 s) + Ni (8 min) plating. Eight sets of samples are aged at 85 °C under ambient air and characterized after distinct time steps t. Each data point represents mean and standard deviation of five 90° peel force measurements.

5.2.2. Fracture Mechanism of Solder Joints

After the peel force measurement, the analysis of the microstructure of the fracture pattern reveals information on the failure mechanism, the quality of the interfaces, voids and phase formation. Since no effect of isothermal aging on the peel force is deducible, the detailed microstructural analysis of the unaged sample, as shown in the inset of Figure 5.4 b), is presented in the following.

An area of 0.8 mm × 0.8 mm of the fracture is scanned by confocal scanning microscopy, resulting in a topography image given in Figure 5.6 a). From this part of the fracture, several investigations are carried out on microstructural level, presented in Figure 5.6 b)-d) and Figure 5.7. All points of interest are labeled within the overview scan in Figure 5.6 a).

Apart from the quality of the Ni coating, the failure could be caused by two main failure mechanisms of the solder itself. The most probable fracture is along intermetallic phases since they are known to be brittle [92, 106]. As already shown in Section 4.3.4, no dominant intermetallic compounds (IMCs) are formed at the interface to the Ni coating. Nevertheless, the binary system of Sn and Cu shows solid state diffusion, already at room temperature (CuSn phase diagram can be found in the appendix in Figure A.4) [100]. At the interface of the Cu ribbon, a thin Cu_6Sn_5 IMC of about 1 µm thickness can lead to an adhesive failure, which is exemplarily shown in Figure 5.6 b). Here, an SEM image (T1), tilted by 30°, shows a close-up with two different failure modes. In the front of the image, the failure is adhesive between Ni coating and Al foil, in the back, the solder layer is intact with a failure at the Cu_6Sn_5 IMC.

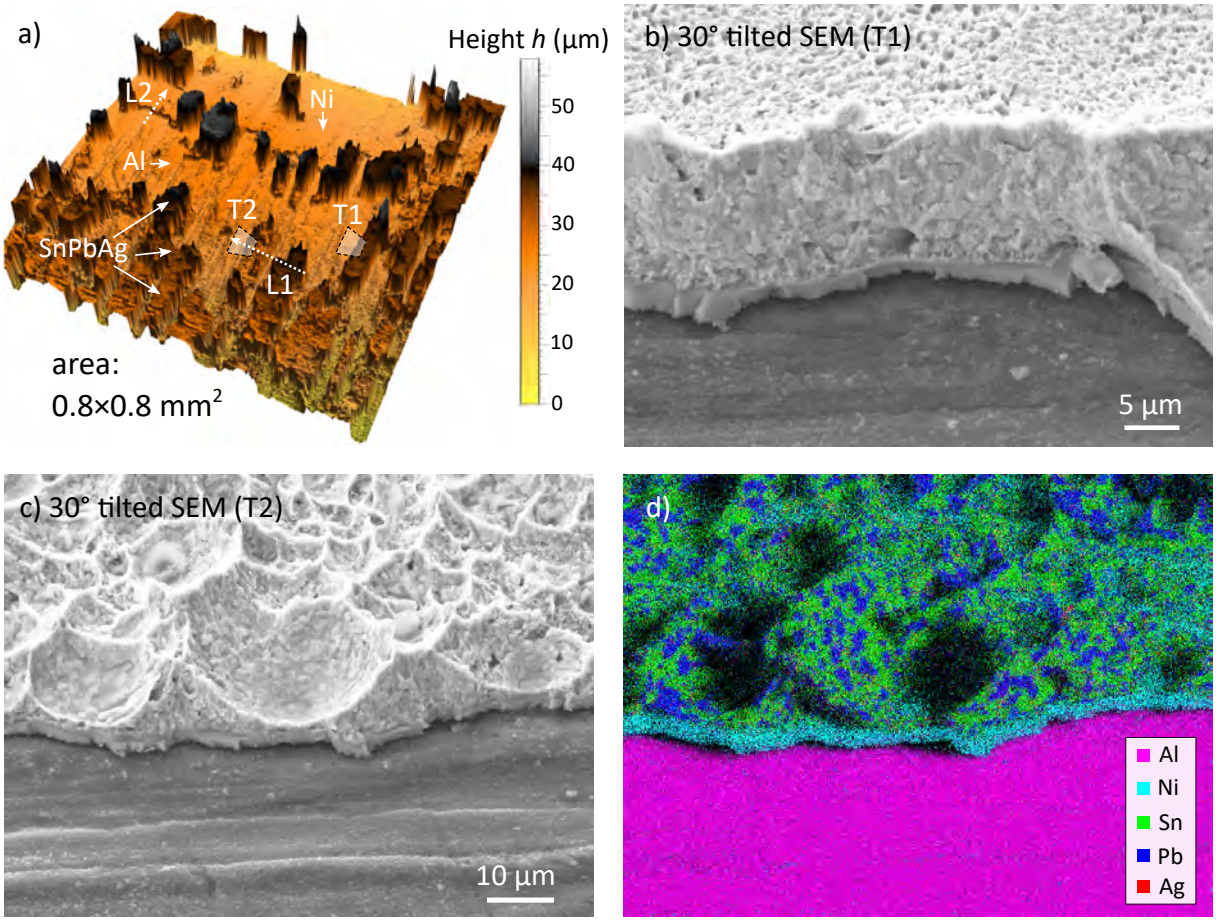

Figure 5.6.: Fracture pattern after a 90° peel force measurement of Sn62Pb36Ag2 solder joint on d-Zn+Ni coated Al foil. a) Topography scan with marked points of interest: Line scans L1 & L2, tilted SEM images T1 & T2. b) 30° tilted SEM image T1. c) 30° tilted SEM image T2. d) Corresponding EDX mapping for SEM image T2 in c).

The second fracture, correlated to the solder, may occur within the solder itself. This cohesive failure is only of minor importance in these samples. An example is shown in Figure 5.6 c) in a 30° tilted SEM image (T2). In the back of the image, the remaining solder layer has a thickness of 5 µm to 20 µm, featuring a rough, grooved surface. This failure is supported by void formation *e.g.* flux remnants inside the solder layer. In general, flux inclusions could cause cavities in the solder [206] and should be avoided as far as possible to not promote failure during operation (*i.e.* loss in adhesion or corrosion). For element correlation, the corresponding EDX mapping is given in Figure 5.6 d). The two solder-related failure modes (adhesive at the interface to the Cu ribbon and cohesive within the solder), can be nicely correlated with height profiles to quantify the measurements.

In Figure 5.7 a), the topography along a part of the fracture of Figure 5.6 a) is shown. For the analysis of the height profile, 21 line scans along the green line L1 are evaluated. The profile is leveled to the Al substrate, which is visible in the marked region 1 in the diagram. The thickness of the solder coating after fabrication of the ribbon can vary

between 10 µm and 20 µm. At the evaluated position of the solder joint, the total solder thickness is nearly 20 µm, shown in region 2. The cohesive failure within the solder, shown in Figure 5.6 c) and d), is located on the right side of this part of the SEM top view image in region 5 and 6, indicated by the area T2. The height is measured to be about 10 µm, also visible in region 3. In the case of an adhesive failure of the coating, the bare Al foil is visible (*cf.* region 1, 4 and 6).

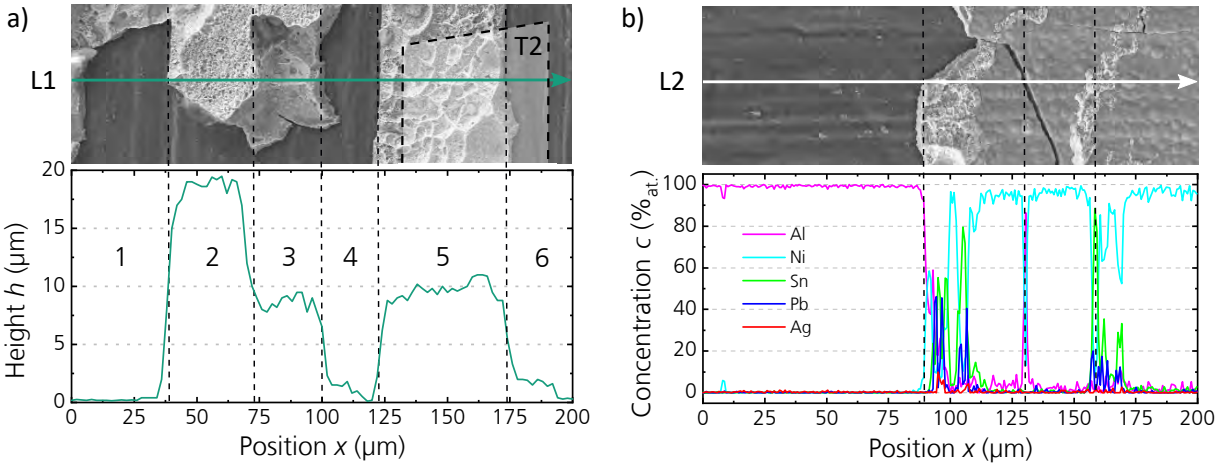

Figure 5.7.: Fracture pattern after a 90° peel force measurement of Sn62Pb36Ag2 solder joint on d-Zn+Ni coated Al foil. a) Topography line scan L1 + SEM top view image. The graph shows the mean height profile of 21 line scans along the green line. b) EDX line scan L2 + SEM top view image.

Figure 5.7 b) shows an EDX line scan (L2) with the corresponding section of the SEM top view image. On the left, the bare Al surface can be seen (magenta in the line scan), where the Al/Ni interface failed during the peel force measurement. This failure may be supported by impurities on top of the Al foil or by oxidation after plating due to oxygen or Al diffusion. On the right, the typical morphology of the Ni layer is observed (cyan, *cf.* Figure 5.1 e)). Remnants of solder (Sn in green, Pb in blue) and a crack within the Ni layer are also visible. The dominant failure mechanism here is along the Ni/Sn interface, presumably due to an inhomogeneous soldering process due to manual contact soldering. The detailed analysis of the fracture pattern shows no dominant failure mechanism for solder joints on Ni-coated Al foils after a 90° peel force measurement. All parts of the solder joints perform similarly; no material weakness is observed. This implies an optimal material combination for joining a Cu ribbon to an Al substrate by a fast soldering process.

From those results, one could conclude that both processes, s-Zn + Ni and d-Zn + Ni, are suitable to provide a solderable coating on Al, which allows to form a mechanical stable joint by soldering. Due to the very high adhesion, the process times for Zn and Ni may be further reduced, while maintaining a well adherent solder joint. This optimization was not focus of this work and could be addressed in future work.

5.3. Microstructure of Cross Sections

For comparison, metallographic cross sections are prepared of solder joints on s-Zn + Ni and d-Zn + Ni coated Al foils, respectively. Figure 5.8 shows SEM images with corresponding EDX mappings. In Figure 5.8 a), a solder joint on s-Zn (30 s) + Ni (8 min) coated Al with Sn62Pb36Ag2 solder is presented. A solder joint on d-Zn (30 s + 15 s) + Ni (8 min) coated Al is given in Figure 5.8 b). Depending on the position of the cross section along the length of the solder joint, the height of the solder layer differs ($\mathcal{O}$(µm)), independent of the coating process. This is basically influenced by the position of the down-holding unit during the soldering process. In the presented examples, the solder layer in 5.8 b) is even twice as thick as in 5.8 a): (43.3 ± 0.6) µm compared to (21.2 ± 0.9) µm. The investigations show that this difference does not affect the performance of the solder joints characterized in this study. All joints are crack- and void-free and very homogeneous over the width of the ribbon $w = 1.5$ mm.

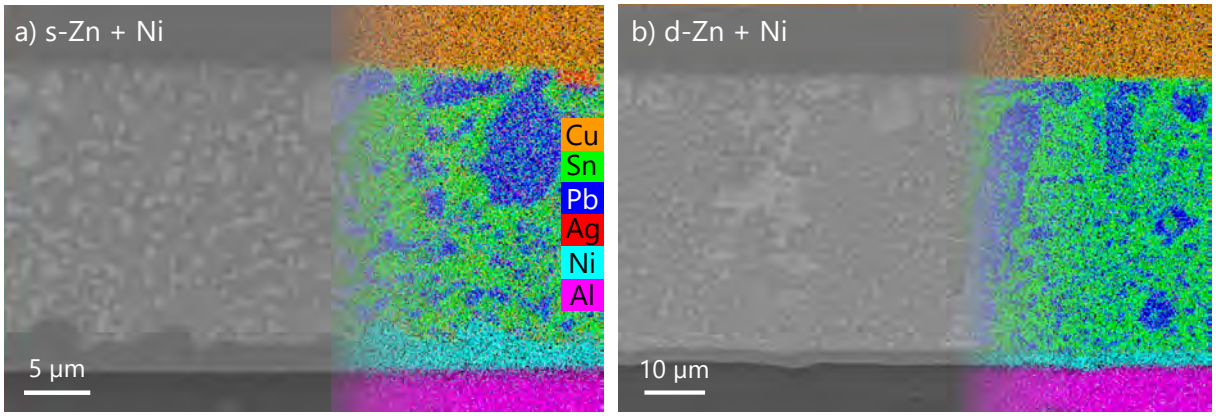

Figure 5.8.: SEM cross section images (20 kV) of solder joints (SnPbAg) on Al foil coated with a) s-Zn (30 s) + Ni (8 min) and b) d-Zn (30 s + 15 s) + Ni (8 min). The corresponding EDX mappings show the element distribution within the joint. Note the different scales of the images.

The comparison of those two images illustrates the different surface morphology of the Ni layer for both processes, similar to the finding from the top view images in Figure 5.1 c) and e). Five cross sections are analyzed, each along the soldered ribbon, covering about 150 mm of coating, tested on several Al foils. For all foils treated with s-Zn + Ni, the resulting Ni layer is rougher, depending on the process time of the Zn treatment. Using EDXS, no Zn remnants are found on the Al foil, which is advantageous for solar applications due to the reported corrosion of Zn in the PV module [99].

Microstructural Changes during Isothermal Aging

Metallographic cross sections of the aged solder joints analyzed in Figure 5.5 are prepared to evaluate possible degradation effects on microstructural level. In the top of Figure 5.9, SEM images at 20 kV of the relevant interfaces are given. Each image from a) to d) shows

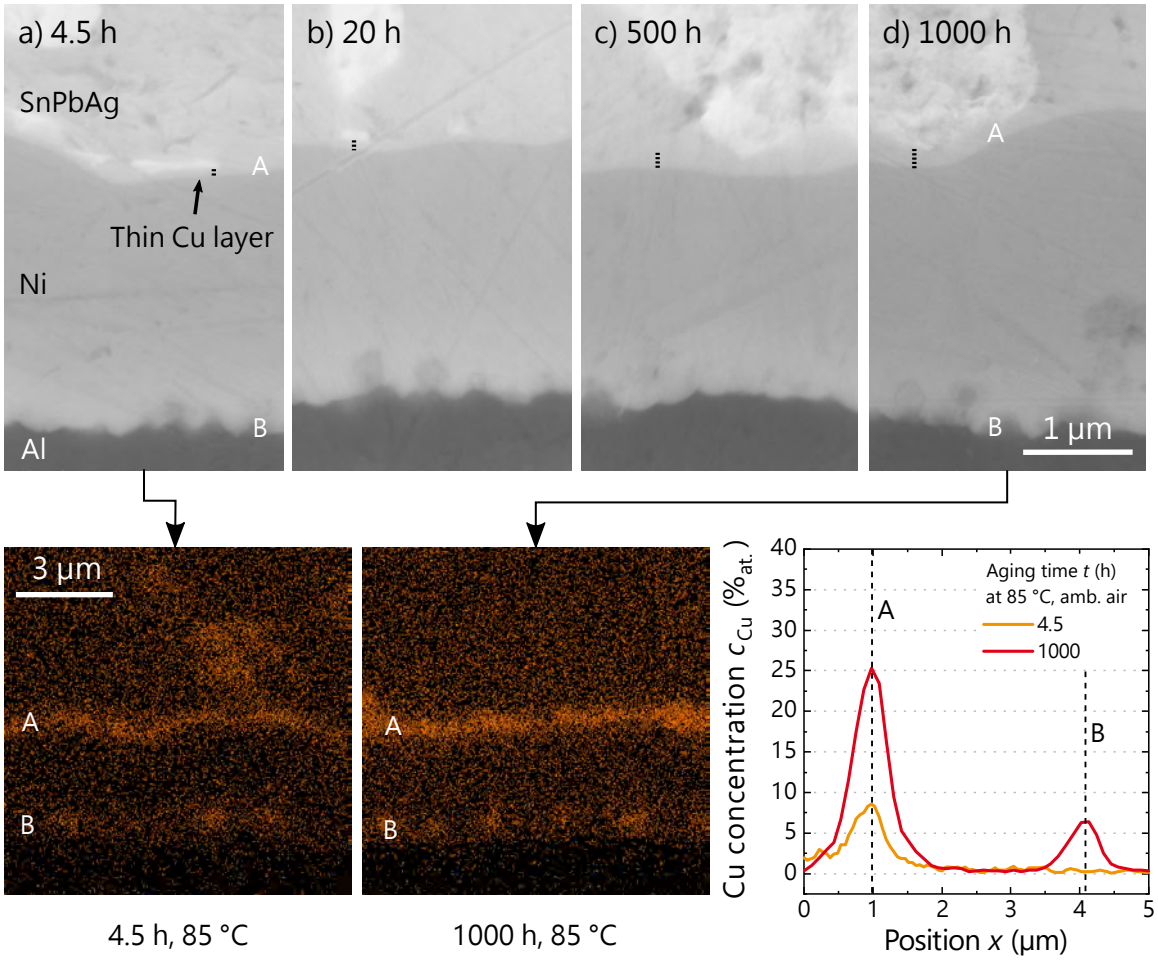

Figure 5.9.: Top: SEM cross section images (20 kV) of solder joints on Al foil coated with d-Zn treatment and 8 min Ni plating, soldered manually with SnPbAg-coated Cu ribbons. a) solder joint after 4.5 h aging at 85 °C at ambient air, b) after 20 h, c) after 500 h and d) after 1000 h aging. Bottom: Cu concentration c_{Cu} within solder joints. EDX mappings of Cu and corresponding line scans (vertically) of aged solder joints of a) and d).

a part of the solder joint in Figure 5.8 b), aged for a certain time t at 85 °C in ambient air and polished again before the SEM measurement.

In accordance with the constant adhesion (*cf.* Figure 5.5), no crack formation or oxidation at the interfaces is found. When solid Al and Ni are in direct contact, they may form several intermetallic phases due to diffusion processes (Al_3Ni, Al_3Ni_2, AlNi, Al_3Ni_5, $AlNi_3$, *cf.* Figure A.4). In this binary system, the Ni-dominant phase $AlNi_3$ is the most prominent phase to be built at temperatures $T < 400$ °C. Within the present joints, no distinct formation of an IMC has been found by EDXS. Nevertheless, a small diffusion zone of several 10 nm is detected at the Al/Ni interface, slightly growing for the aged samples, since the temperature during soldering was comparably low at (260 ± 20) °C. This is a strong hint for a proper metallurgical bond at the Al/Ni interface which is supposed

to be reliable.

Although the core of the ribbon is not imaged in the SEM sections, the presence of Cu should be considered: the dissolved elements from the two different metal species (here Cu and Ni), can quickly diffuse across the molten solder and influence the interfacial reaction on the opposite side [199, 207]. Therefore, the present joints are so-called asymmetric Cu/Sn/Ni solder joints, including a Cu concentration gradient along the Sn-based solder joint. In this study, the exposure temperature of 85 °C is too low to detect a significant amount of Cu within the solder. A thin Cu layer is formed on top of the Ni coating, directly after soldering. In the bottom, Figure 5.9 shows the Cu concentration for the sample after 4.5 h and after 1000 h of aging at 85 °C. The EDX mappings correspond to the SEM images given above in a) and d). At the interface A, the Cu layer slightly growths within 1000 h of aging. No binary Sn-Cu or ternary Sn-Ni-Cu phase has been found. Additionally, Cu diffuses towards the Ni layer and agglomerates at the Al/Ni interface (B). This effect is also visible after 4.5 h. The corresponding line scans on the right show the vertical Cu concentration c_{Cu} within these two mappings. It should be pointed out that it is not possible to state an absolute representative amount of Cu ($\%_{\mathrm{at.}}$) for the solder joints. The concentration c_{Cu} strongly depends on the measurement position along the joint. As can be seen from the EDX mappings, especially the amount of Cu at the Al/Ni interface differs and does not form a closed layer. Several line scans are evaluated and the two, exemplarily given in the graph, show the overall trend of Cu distribution over the solder joints after aging. In general, Ni should act as diffusion barrier for Cu within a solder joint on *e.g.* a plated solar cell metallization [155, 208, 209]. In PV industry, it is not common to solder on a pure Ni metallization. As alternative for screen printing, Ni is used within plated metallization as seed layer for subsequent Cu plating [37]. It is assumed, that the present Cu layers are not disadvantageous for the solar cell performance. Among other aspects, this will be analyzed on module level within the following sections.

5.4. Implementation in Si Solar Cells and Modules

The analysis presented in the previous sections, demonstrate that wet-chemical coating of Al surfaces enables the creation of high-quality SnPb-based solder joints. So far, this has been shown on 10 µm thick Al foils to minimize the influence of the substrate during the evaluation. This allowed to assemble a fundamental understanding of the coating process and important interface properties.

In this section, the scope of the investigation is extended by addressing different substrates as typically used in silicon solar cell manufacturing. For this, the industrial interconnection sequence as presented in Section 2.2.4, is tested on two different solar cell types: The FoilMet® solar cells, where the rear electrode is realized by a thin Al foil and LFC-PERC solar cells, with an evaporated Al layer. The Al interface is first functionalized by the wet-chemical coating and then contacted by Cu ribbons coated with SnPb. The goal is to identify challenges that are introduced by these substrates, when implementing the wet-chemical coating approach, and to evaluate the long-term performance of the realized solder joints in PV modules.

The adaptation of the coating process and critical observations are described first. To achieve high-quality interfaces, the processes are optimized for each substrate, based on the previous results. Different measurements are performed as process control during the fabrication. The solar cells are then embedded in 1-cell-modules and tested with the common climate chamber tests, as described in Section 3.4. The modules are characterized by *I-V* measurements and the data is analyzed to reveal critical parameters.

To further enhance the understanding, the microstucture of the realized contacts is investigated in detail by different methods. The thereby derived differences to the ideal substrates are discussed and possible optimizations are presented.

The results of Sections 5.1-5.3 show comparable performance of solder joints on Ni coated Al foils, either treated with s-Zn or d-Zn, regarding wettability, contact adhesion and long-term stability. In this section, the focus for the implementation in solar cells is set on coating Al with the "d-Zn + Ni" sequence. This way, possible influences from variations of the coating process can be reduced, as the focus is put on the impact of the substrates and interfaces.

5.4.1. Investigated Types of Solar Cells

For the experiment, PERC solar cells are used, which are currently the Si solar cell type in industrial mass fabrication (*cf.* Section 2.1) [11]. Industrial precursors of 156.75 mm × 156.75 mm pseudo-square of mono-crystalline *p*-type Si are used. Within Fraunhofer ISE's PV-TEC back-end laboratory, the cells are metallized on the front side with a 5BB H-pattern by screen printing and subsequent firing for contact formation. Prior to rear side metallization with different Al electrodes, **l**aser **c**ontact **o**pening (LCO) is performed by laser ablation, to enable alloying of Al and Si during the furnace firing step and the formation of the Al-BSF [31, 34].

Solar cells with Al foil and PVD Al on the rear side are processed to test the wet-chemical coating. Figure 5.10 illustrates the experimental process flow of the two groups until the interconnection process. As a reference, PERC solar cells with the common screen-printed Al rear side and Ag pads for soldering are used:

- Group 1: "**FoilMet®**"- PERC cells with 10 µm thick Al foil as rear electrode
- Group 2: "**PVD Al**"- PERC cells with 2 µm or 4 µm thick PVD Al rear electrode
- Ref.: "**SP Al**"- PERC cells with ∼14 µm screen-printed Al rear side and Ag pads

For the mechanical and electrical contact formation of the 10 µm thick Al foil to the rear side of the FoilMet® cells (group 1, green in Figure 5.10), the FoilMet® LMB laser process with a cross dash pattern is applied. This process was published by John *et al.* in 2020 [46] and is described in detail in Section 2.1.3. After the FoilMet® laser process, the cells are characterized by *I-V* measurements and EL imaging.

To test the developed wet-chemical process on an alternative Al rear side metallization, solar cells with PVD Al rear side are manufactured (group 2, orange in Figure 5.10). After the LCO process, Al is evaporated by electron-beam PVD under high vacuum.

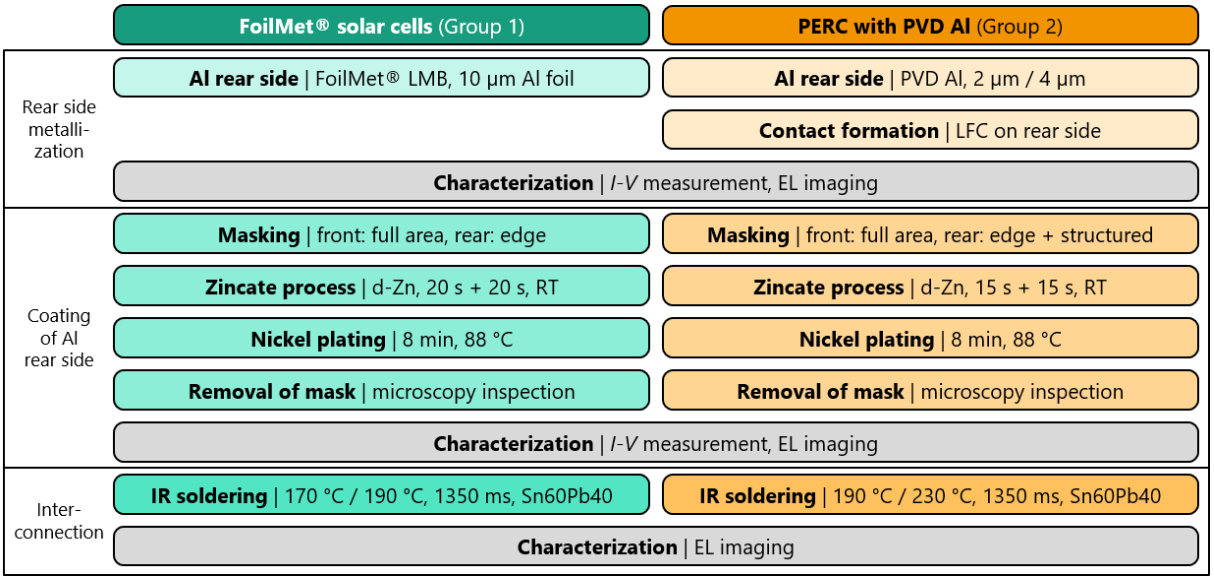

Figure 5.10.: Experimental process flow for wet-chemical coating the Al rear side of PERC solar cells. Green: process route for FoilMet® cells with Al foil rear side. Orange: process route for PERC solar cells with PVD Al rear side.

Two different layer thicknesses of PVD Al are tested: 2 µm and 4 µm. After the Al deposition, **l**aser **f**ired **c**ontacts (LFC) are applied on the cell rear side[1] to form the Al-Si contact [42, 210]. Finally, the cells with PVD Al are characterized by *I-V* measurements and EL imaging as well. The third group serves as reference group and consists of classical state-of-the-art PERC cells. They feature a **s**creen-**p**rinted (SP) Al rear side with local Ag pads to provide solderability. The wet-chemical coating process for the rear side of Si solar cells is described in detail in the following.

5.4.2. Wet-Chemical Coating Process for PERC

In general, the coating process used for the solar cell rear side is the same as developed for the 200 µm thick Al foils, introduced in Section 3.1.2 and applied in Sections 5.1 to 5.3. During processing of the solar cells, the bath time for Zn treatment is adopted to yield an optimized coating result.

FoilMet® Solar Cells

For the FoilMet® cells with 10 µm thick Al foil, it is supposed that a similar Zn bath time is required as for the thick Al foil; the alloy as well as the rolling process and the surface morphology of the foils are identical. The only difference is the thickness of the Al foil. The 10 µm thick foil is attached to the FoilMet® cell; the used laser process locally changes the surface quality of the Al. The experimental process flow for coating

[1] Experimental parameters for LFCs on 2 µm thick PVD Al: pulse energy: 400 kJ, pitch: 350 µm. Parameters for 4 µm thick PVD Al: pulse energy: 450 kJ, pitch: 380 µm.

the rear side of FoilMet® solar cells is as well given in Figure 5.10. To protect the cell front side and avoid shunting at the cell edges, the solar cells are placed into a mask of polypropylene (s. Figure 5.11 a)). The cells are then processed with a double zincate (d-Zn) process for 20 s each (*cf.* Equations 3.1 and 3.2), including a cleaning step with nitric acid (*cf.* Equation 3.3). Ni is subsequently deposited by electroless plating for 8 min in the electrolyte (s. Figure 5.11 b)). After rinsing, the mask is removed and the homogeneity of the Ni layer is checked by optical microscopy.

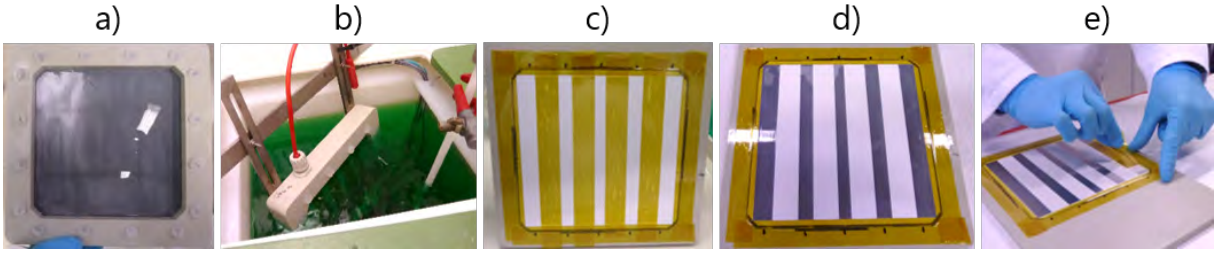

Figure 5.11.: Photographs during different steps of wet-chemical processing PERC solar cells a) & b) with FoilMet® rear side and c) - e) with PVD Al rear side. © Fraunhofer ISE

Since the rear side is full area coated[2] (approx. 150 mm × 150 mm), a bath control is conducted every two wafers. The following parameters are measured: density of the Zn bath (g/ml), NaOH content of Zn bath (g/l), Ni content within the Ni electrolyte (g/l), Ni hypophosphite content (g/l), pH value of Ni electrolyte and the wafer mass before and after coating (mg). Due to the manual laboratory setup, most of the wafers cracked during processing. Five FoilMet® solar cells coated with d-Zn+Ni are processed successfully. For those wafers, a change in mass of $+(421 \pm 26)$ mg is measured. As the measurements are conducted promptly after Ni deposition, it is assumed that remains of DI water are left over between Al foil and Si wafer and therefore significantly contribute during weighing.

PERC with PVD Al Rear Side

Group 2, cells with a PVD Al rear side, is coated in a similar way. To cover the front side and the edges, the cells are placed sunny-side down on a polypropylene plate and fixed with Kapton® tape at the edges. Furthermore, four stripes of Kapton® are used to mask the rear side in a 5BB-design: five stripes of about 1 cm width are kept free to allow for coating, whereas the rest is covered to reduce the consumption of the chemicals. Figure 5.11 c) shows the rear side of a cell with PVD Al, fixed onto the polypropylene plate and masked with tape. In d), the cell after Zn treatment is shown and in e) the lift-off of the Kapton® tape after Ni plating can be seen. The process time for Zn treatment on PVD Al is reduced to 15 s + 15 s d-Zn.

Again, the characteristics of the Zn bath are checked every two wafers to keep the process conditions constant. For the second group, a mean weight of $+(123 \pm 29)$ mg (on 4 µm PVD Al) and $+(146 \pm 31)$ mg (on 2 µm PVD Al) per wafer is measured after the

[2]Due to the mechanical instability of the very thin Al foil, it is not possible to use tape to locally mask the rear side.

coating process. The handling of this cell group is easier than for the FoilMet® cells since the rear side is more robust regarding masking. Processing of this group ends up in five coated wafers with 2 µm PVD Al and seven coated wafers with 4 µm PVD Al.

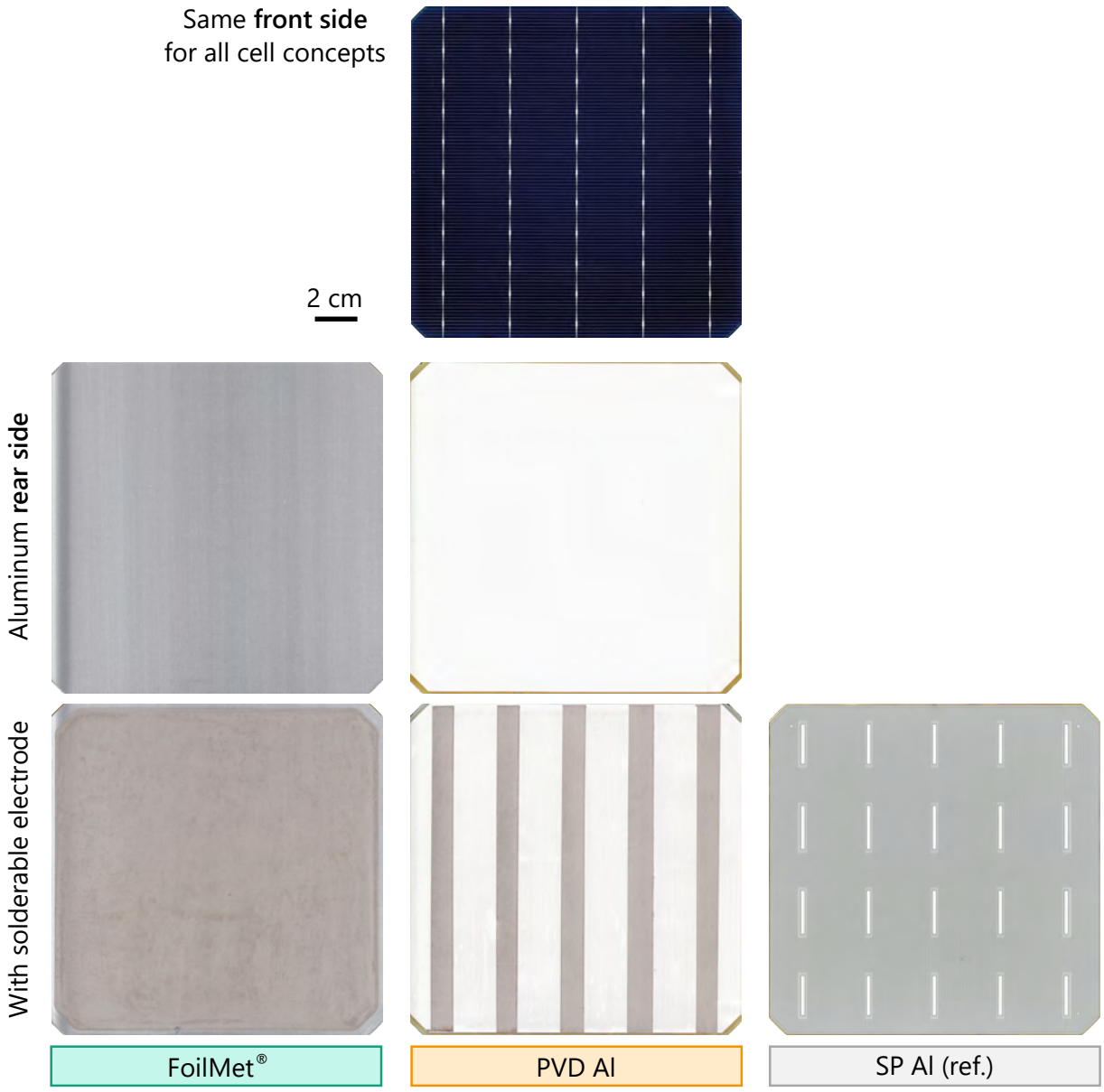

Figure 5.12.: Top view photographs of the different Si solar cells. All cells are psq monofacial *p*-type PERC cells with 156.75 mm edge length. The front side metallization is the same for all cell concepts, consisting of a 5BB H-pattern layout, screen printed and fired. The Al rear side electrode is either an Al foil (FoilMet® concept), PVD Al or screen-printed (SP) Al. To contact the rear side by soldering, the cells are coated wet-chemically (FoilMet® & PVD Al) or feature Ag pads (state-of-the-art PERC solar cells as reference).

In Figure 5.12, photographs of the processed solar cells are shown. The front side (same for all three cell concepts), pictured on the top, features a 5BB H-pattern layout of screen-printed and fired Ag paste as electrode. The layout of the busbars is tapered with a pad width of $w_{\mathrm{Pad}} = 0.8\,\mathrm{mm}$. The rear sides of the cells are given below. First, the Al electrode is shown: 10 µm thick Al foil for the FoilMet® concept, 2 µm or 4 µm PVD Al and approx. 14 µm screen-printed Al for the reference group.[3] Below, the Al surfaces after adding a solderable area are shown: the FoilMet® cell after full-area wet-chemical coating with d-Zn + Ni, the PVD Al with five coated stripes treated with d-Zn + Ni and finally the Ag pads on the SP Al rear side.

Electrical Characterization after Coating

It has not been investigated yet if the used wet-chemical coating process might damage the solar cell. For the original FoilMet® approach, this issue is not relevant since the coating process is performed prior to the laser attachment of the Al foil to the Si solar cell. However, within this work, the changed fabrication sequence can lead to cell damage, which should be excluded for further data analysis. To evaluate a successful implementation of the coated Al foil onto solar cell rear sides, the electric parameters on cell level are investigated. The results are presented in detail in the Appendix A.8.2.

The *I-V* evaluation shows that the coating of the cell rear side does not influence the cell performance for both types of solar cells. One would assume that a Ni-coated Al foil (or PVD Al) would be easier to contact with the pins during *I-V* measurement in contrast to uncoated Al with native oxide. For the present samples, this effect could not be found and may be dominated by other issues regarding solar cell performance, discussed in Section A.8.2.

Additionally, EL images of the coated solar cells are exemplarily shown for each cell type in the appendix in Figure A.9. No indication for cell damage of inhomogeneous coating is found.

For the interconnection, Cu ribbons are soldered to the electrodes of all three solar cell groups on an fully-automated stringer. The procedure as well as the results after interconnection are discussed in the following section.

5.4.3. Industrial Solar Cell Interconnection

For the solar cell interconnection, an industrial stringer "TT1800" of the company *teamtechnik GmbH* is used. The general working principle of the involved process steps in described in Section 2.2.4 in detail. According to the presented soldering profile in Figure 2.14, all solar cells are interconnected with a cycle time of 1950 ms per cell to realize an industrially feasible process. For the analysis of the solderable Al on cell level, each solar cell is contacted on the front and rear side with five ribbons each, yielding "1-cell-strings" as demonstration device. For this, stretched Cu ribbons of 0.90 mm width and 0.22 mm height, coated with Sn60Pb40 of about 15 µm thickness are soldered to the screen-printed Ag front busbars and the coated Al rear side. To remove the oxides, a no-clean flux from

[3] Not shown in Figure 5.12 since the Ag pads are always printed before the Al paste.

kester is sprayed onto the corresponding metallization on front and rear, immediately before heating. Table 5.2 gives an overview on the process set-parameters (times and temperatures) for soldering FoilMet® solar cells and the PERC cells with PVD Al rear side. Additionally, the reference group with screen-printed PERC cells is processed within the same run.

Table 5.2.: Soldering parameters of the industrial stringer TT1800 for the interconnection of FoilMet® solar cells, PERC with PVD Al rear side and PERC with screen-printed (SP) Al rear side.

Cell type	**Cycle time**	**Soldering parameters**			**Hotplate temperature**	
	t_{cycle} (ms)	T_{s}^{1} (°C)	T_{s}^{2} (°C)	t_{s} (ms)	$T_{\mathrm{HP}}^{\mathrm{min}}$ (°C)	$T_{\mathrm{HP}}^{\mathrm{max}}$ (°C)
FoilMet®	1950	170	190	1350	75	175
PVD Al	1950	190	230	1350	75	175
SP Al	1950	190	230	1350	75	175

The soldering time $t_{\mathrm{s}} = 1350\,\mathrm{ms}$ is equal for all groups. The listed parameters are set-parameters. Within the stringer, the temperature control during IR soldering is realized by a pyrometer measurement on the solar cell rear side. In case of a lower or higher cell temperature than $T_{\mathrm{s}}^{\mathrm{i}}$, the stringer automatically adjusts the power of the IR lamps. Since the cell rear sides feature different emissivities, the actual soldering temperature will be slightly different for the same settings. In a preliminary test with FoilMet® solar cells, the emissivity of the Al foil has been determined,[4] so that the conventional settings, used for common PERC solar cells, could be changed. Due to a much lower emissivity of the Al foil ($\varepsilon_{\mathrm{Al\ foil}} < 0.1$) compared to SP or PVD Al ($\varepsilon_{\mathrm{SP\ Al}} = 0.36 \pm 0.02$, $\varepsilon_{\mathrm{PVD\ Al}} = 0.19 \pm 0.01$), the set-temperatures were lowered to $T_{\mathrm{s}}^{1} = 170\,°\mathrm{C}$ and $T_{\mathrm{s}}^{2} = 190\,°\mathrm{C}$ instead of $T_{\mathrm{s}}^{1} = 190\,°\mathrm{C}$ and $T_{\mathrm{s}}^{1} = 230\,°\mathrm{C}$ for the other two groups (*cf.* Table 5.2).

Mechanical Properties

After soldering, a successful mechanical interconnection can be tested by a 90° peel force measurement, according to the procedure on Al foil. For solar cells, the interconnection on both cell sides has to be evaluated separately, wherefore a much higher amount of samples is required. Compared to a 200 µm thick Al foil, the ∼180 µm thick crystalline Si wafer is a more fragile substrate and in most cases does not withstand the high peel forces observed for Ni-coated Al foils (*cf.* Section 5.2). Therefore, most of the cells have to be fixed on a substrate to perform a reliable measurement.

To define the baseline for the mechanical strength of solder joints of state-of-the-art Si solar cells, the peel force is measured on front and rear side of the reference screen-printed group. For solder joints with Sn60Pb40 on screen-printed and fired Ag busbars, the force is determined to be $(1.31 \pm 0.39)\,\mathrm{N/mm}$, normalized to the contact width $w = 0.8\,\mathrm{mm}$ for the pads of the front busbars. For the rear side, $(0.95 \pm 0.55)\,\mathrm{N/mm}$ for the joints

[4] The emissivity ε is temperature dependent and is evaluated between RT and 225 °C every 25 K. The stated value implies mean and standard deviation over this temperature range.

on the screen-printed and fired Ag pads are reached. Here, the measurement values are normalized to the ribbon width of 0.9 mm as the contact width is mostly defined by this width. The data can be found in the appendix in Figure A.10.

Figure 5.13 shows the results of the peel force measurement on the coated FoilMet® rear side (green) and coated PVD Al (orange). Due to ablation of the Al foil from the Si wafer at the laser contacts at (0.32 ± 0.04) N/mm, no reliable statement of the actual strength of the solder joints can be made. The force-path-diagram in green on the right shows two examples for ribbon 3 (middle of solar cell) and ribbon 4 peeled off.

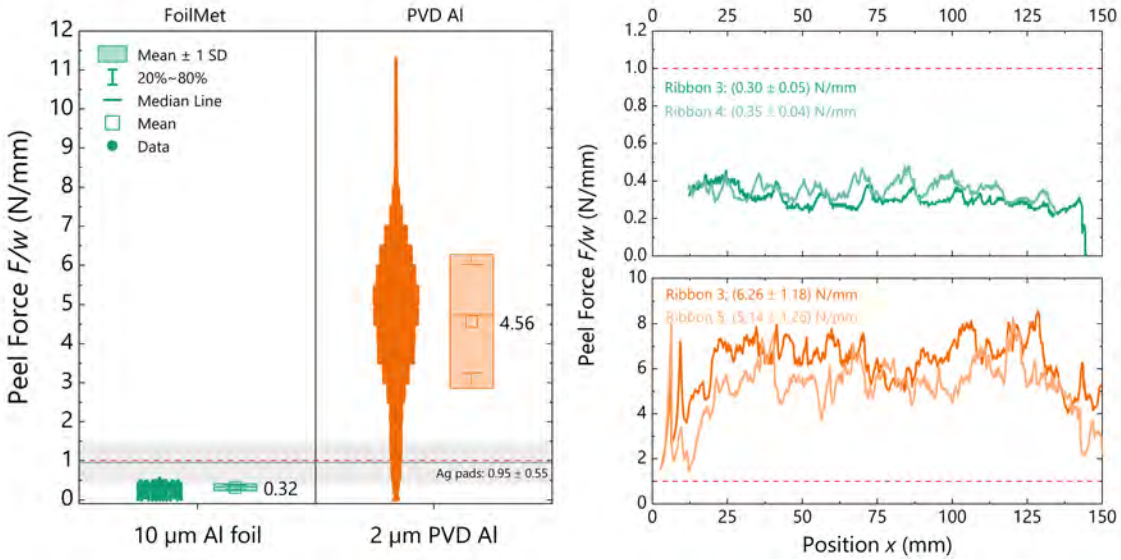

Figure 5.13.: Peel force of soldered ribbons (Sn60Pb40) onto different solar cells, wet-chemically coated with d-Zn + Ni. The force is normalized to the ribbon width of 0.9 mm. The box plots show all measurement values recorded over five peel force measurements for 150 mm evaluation length. The peel force achieved on the PERC reference with Ag pads on the rear side is marked in gray.

The peel forces achieved on Ni-coated PVD Al are much higher at (4.56 ± 1.30) N/mm, also illustrated by the two examples for ribbon 3 and 5 on the right side. Since no significant deviation between the ribbons soldered to the middle of the solar cell (*i.e.* ribbon 3) and the ribbons in the outer parts (*i.e.* ribbon 1 and 5) is found, a homogeneous solder joint formation on the whole solar cells is supposed.

After the peel force measurement, the fracture pattern of the PVD Al rear side is analyzed by SEM and EDX in top view mode. One representative example is given in Figure 5.14.

The SEM image already reveals a mixed fracture, very similar to the results found on 200 µm thick pure Al foil after peeling off the ribbons (*cf.* Figure 5.6 and 5.7). By using EDX, a clear statement on the elemental distribution can be made. Beside the cohesive failure within the solder and the adhesive failure at the interface solder/Ni, another adhesive failure is observed. The interface PVD Al/Si wafer seems to be weaker

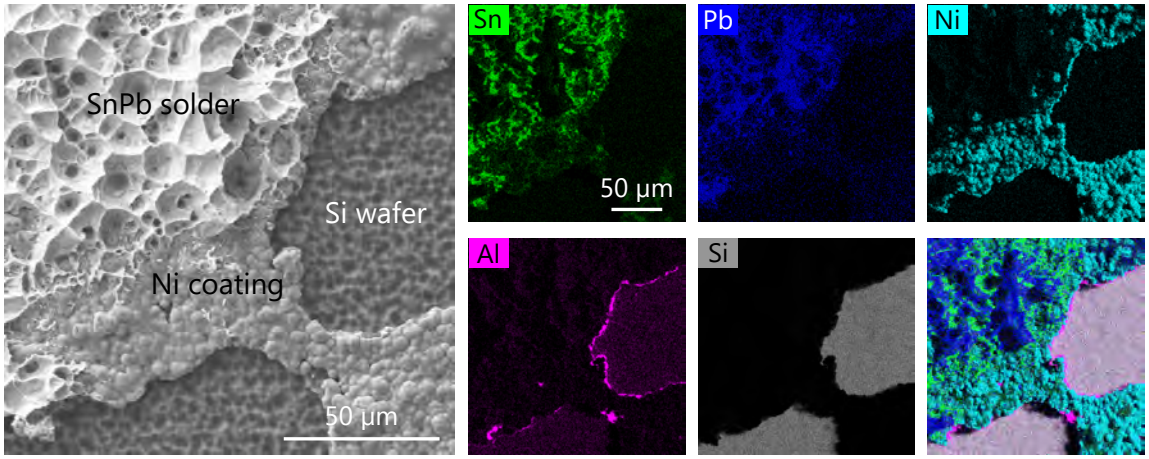

Figure 5.14.: Fracture after the peel force measurement on Ni-coated PVD Al rear side of a Si solar cell. SEM (20 kV) and EDX is used to identify the failure mode and correlate the elements. A mixed fracture, very similar to the results found on pure Al foil, is found.

than the bonding between PVD Al and Ni coating, since the latter one is only found sporadic. This again confirms the successful coating process of the PVD Al rear side of the solar cells and strong solder joints.

The presented results prove a successful industrial interconnection process with wet-chemically modified Al surfaces. The mechanical strength of the solder joints is high enough for string handling and module integration. The experimental procedure for the integration in a PV module is summed up in the following, afterwards focusing on reliability tests and the corresponding module characterization.

5.4.4. Module Integration and Climate Chamber Tests

The ribbons, soldered onto the solar cells, are cross connected and the cells are then laminated into 1-cell-modules, as shown in Figure 5.15. On the module's front side, 3 mm thick float glass is used and a conventional EVA as encapsulant for the interconnected solar cells. One group of modules is built with a conventional white PET **b**ack**s**heet (BS) for the module rear side. This standard module setup (glass/EVA/white BS) is used for thermal cycling (TC) tests to assess the performance of solder joints on the cells for the classical IEC test with 200 thermal cycles [79]. Another set of modules is built with transparent BS and tested in DH at 85 °C and 85 % relative humidity. This second test is performed to evaluate the stability of the coatings on the rear side. To gain a better insight and observe possible corrosion, transparent instead of the conventional white BS is used for the DH modules. The general module setup is sketched in Figure 5.15 a) in a cross section view. The modules are laminated according to the process described in Section 2.1.4. In Figure 5.15 b), the photograph shows one of the 1-cell-modules from the cell rear side (PVD Al with local Ni coating) before DH climate chamber test.

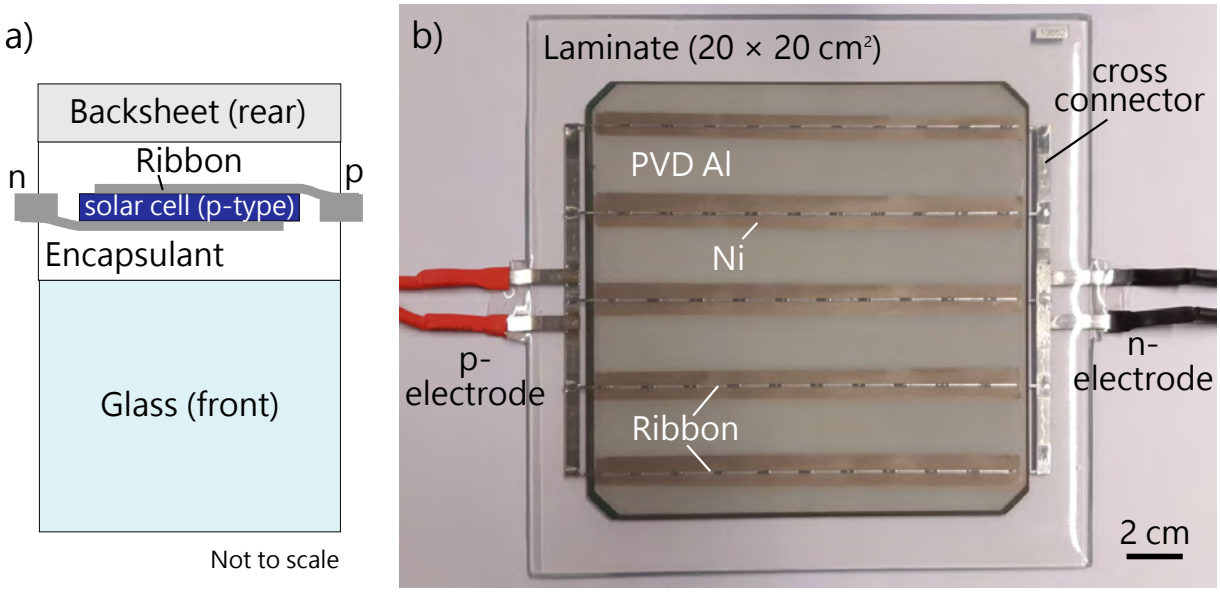

Figure 5.15.: a) Sketch of cross section of 1-cell-modules for climate chamber tests, depicting the involved material order. b) Photograph of a 1-cell-module with transparent backsheet and PVD Al rear side, locally coated with d-Zn + Ni to provide solderability for the five ribbons on the rear side.

The initial characterization of all modules is done by *I-V* and EL measurements. To determine the relative change of the electric parameters, the *I-V* values after climate chamber testing are normalized to the initial values for each module, *i.e.* a negative change indicates a loss whereas a positive change states a gain (*cf.* also Section 3.4.1). To assess the change in electrical performance, V_{oc}, I_{sc}, pFF, FF and P_{mpp} are analyzed.

Thermal Cycling

Figure 5.16 shows the relative change of these five values after TC 50, TC 200 and TC 400, normalized to the initial values before aging. Each of the three graphs includes one solar cell concept. The red dotted line at $-5\,\%$ indicates the critical limit stated in the standard IEC 61215 for a maximum degradation after TC 200 or DH 1000 for certification of solar modules [79].

Unfortunately, three of five **FoilMet®** solar cells cracked during soldering, so that only two modules could be built for this group. One of them is exposed to TC (green dots), whereas the other one serves as reference module without climate chamber testing (gray squares). After TC 200, the module shows a relative change of $(-0.75 \pm 2.31)\,\%$ in P_{mpp}, dominated by a change in fill factor of $\Delta FF = (-1.44 \pm 0.24)\,\%$. Since the pFF stays constant, resistive losses occurred during aging.

Within the five modules with **PVD Al** rear side, the highest spread is measured in the *I-V* data (orange dots, second graph). While three modules show less than $\Delta P_{mpp} = -2.5\,\%$ after TC 200, one module drops to $\Delta P_{mpp} = -4.2\,\%$ and another one to $\Delta P_{mpp} = -10.4\,\%$.

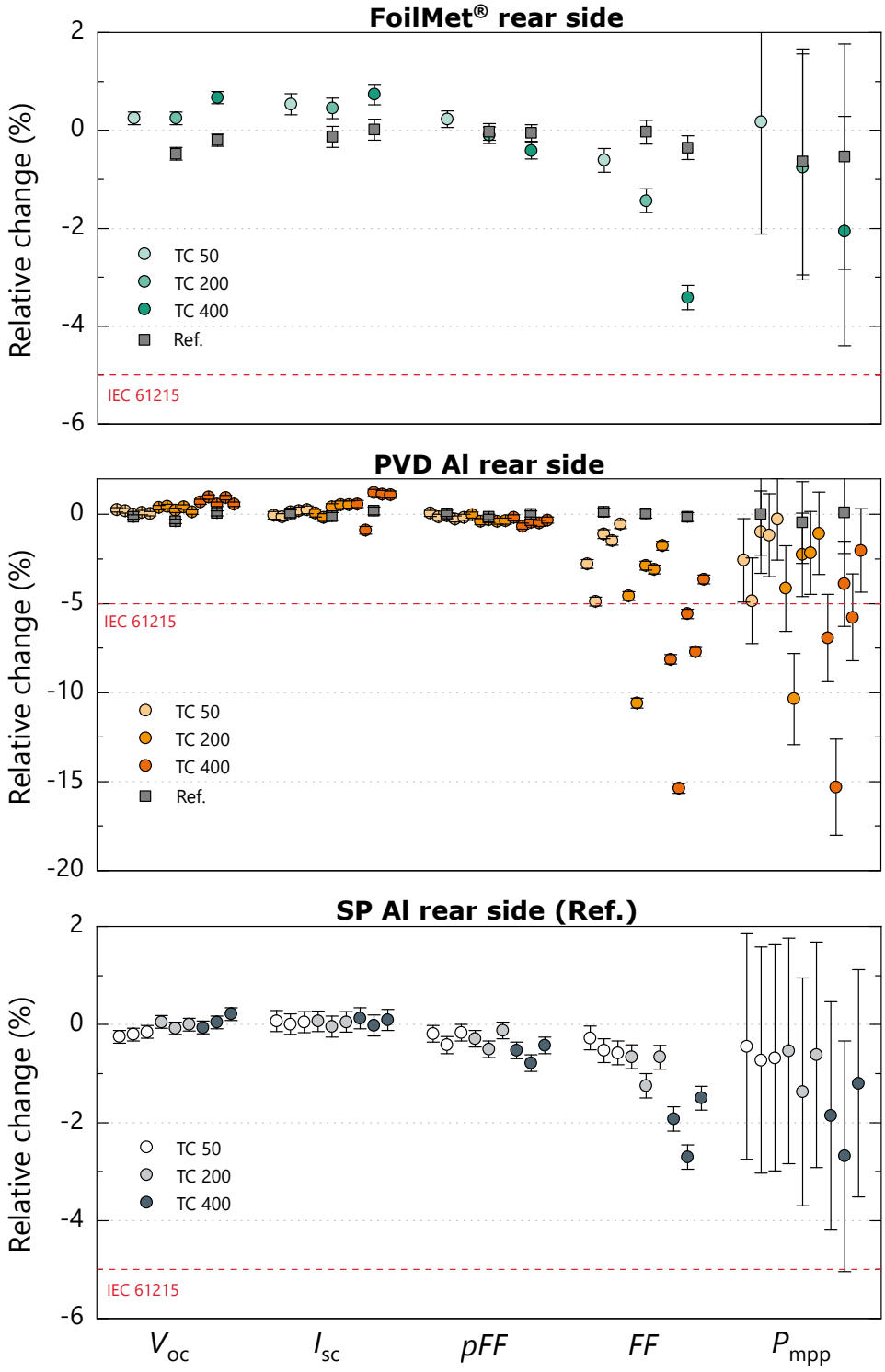

Figure 5.16.: Relative change of the *I-V* parameters of 1-cell-modules after TC testing. Each data point represents one module whereas the errors indicate the measurement uncertainty. For the first two groups, one module serves as measurement reference each (squares, not aged).

This means that four out of five modules pass the test according to the IEC criteria. Again, the loss of power is dominated by a reduction of the fill factor, caused by an increase in series resistance (*i.e.* no change in *pFF*).

The reference cell concept with the **SP Al** rear side also shows a slight degradation in *FF* and P_{mpp}, given in Figure 5.16 in the bottom graph. Here, three modules are tested in TC, all showing similar changes of the *I-V* parameters. The results fit quite well to the experiences of other in-house work with 1-cell-PERC-modules after TC testing.

As expected, the *I-V* data of all three groups show the metallization and/or the interconnected parts to be the critical components during TC testing. A degradation of those will lead to a higher series resistance and a loss in fill factor, which influences the module power. Additionally, the encapsulant and the backsheet affect the mechanical stability of the module and therefore the results after TC [211–213]. For all modules tested within this work, no variation of the module materials is performed, whereas this aspect is not further considered. More in-depth analysis of the possible failure modes is given later in this chapter in Section 5.5.

Damp Heat

Another insightful test is the damp heat test, conducted at 85 °C and 85 % relative humidity. These test conditions can reveal further degradation mechanisms which can occur in the field, *e.g.* corrosion, delamination or discoloration [187]. Coating of Al could lead to corrosion problems due to the difference in electrochemical potential of the involved metals. For the samples of this study, this test is applied to test the rear side coatings for their chemical stability [79]. Four modules are tested in DH.

Figure 5.17 shows the relative change after DH 1000 for two modules with solar cells with **PVD Al** rear side (+ one reference module) and two modules with solar cells with **SP Al** rear side (+ one reference module). Comparing the *FF* losses, the modules with PVD Al show a higher reduction in *FF* of $\Delta FF_{\mathrm{PVD}} \approx -1.7\,\%$ than the modules with SP Al ($\Delta FF_{\mathrm{SP}} \approx -0.6\,\%$). Since both reference modules do not show any loss in *FF*, this effect is caused by an increase in series resistance due to changes in metallization or interconnection and the involved interfaces. On the one hand, the DH test may lead to corrosion, increasing the series resistance. On the other hand, the modules pass through half a thermal cycle, namely from RT to 85 °C and back to RT, which could influence the interconnection.

However, for the cells with **SP Al**, a loss in power is caused by a loss in open circuit voltage V_{oc} and short circuit current I_{sc}, which both show relative changes for both modules between 1 % and 2 %. Since both cell types (PVD Al and SP Al) originate from the same cell batch and feature the same front side, one could assume that the losses in V_{oc} and I_{sc} are most likely caused by the cell rear side for the SP Al modules. The optical inspection of the cell rear side via the transparent backsheet does neither reveal discolorations (which would be an indicator for *e.g.* corrosion) nor cracks in the cells or interconnectors. Nevertheless, the absolute values of the electrical cell parameters with PVD Al are significantly lower than for the cells with SP Al or Al foil ($\sim 600\,\mathrm{mV}, \sim 635\,\mathrm{mV}$). Therefore, light and/or temperature induced degradation (LID, LeTID) of the solar cells may be more

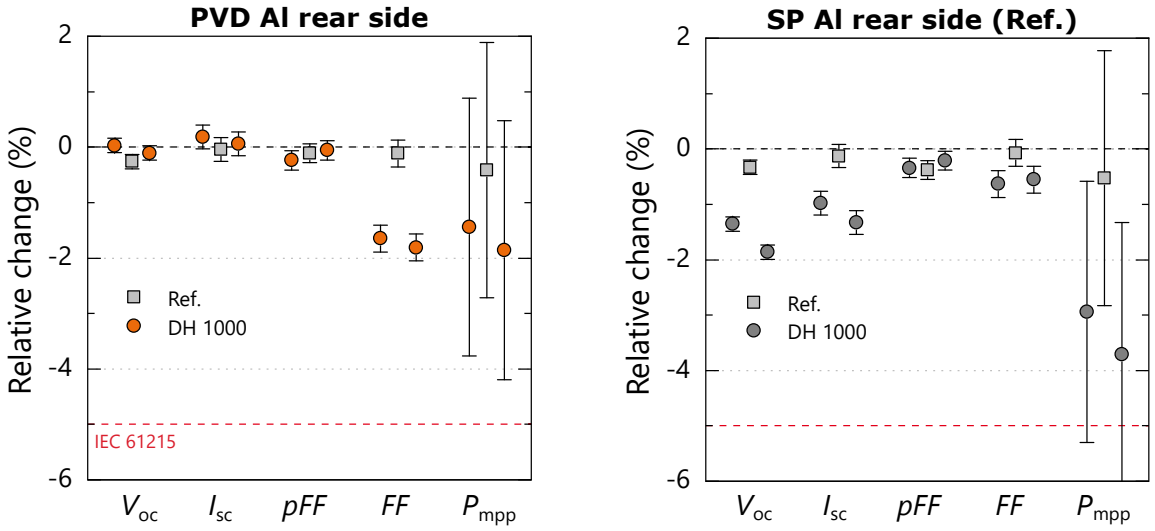

Figure 5.17.: Relative change of the *I-V* parameters of 1-cell-modules after DH testing. Each data point represents one module whereas the errors indicate the measurement uncertainty. For each group, one module serves as measurement reference (squares, not aged).

pronounced for the modules with SP Al, leading to a reduction in V_{oc} and I_{sc}. This effect is already visible on cell level and addressed in Section A.8.2.The *I-V* parameter changes for all four modules are uncritical and the P_{mpp} does not exceed the critical degradation level of $-5\,\%$ at all.

Conclusion

The global electrical *I-V* parameters of cells and modules are used to quantify the influence of the coating process on cell level as well as after TC and DH on module level. The peel force measurements of soldered ribbons and climate chamber tests (TC 400) both proof a successful industrial interconnection of wet-chemically coated PERC cells with alternative Al rear sides. The stability of the solder joint (and therefore the coating) is shown in DH 1000.

5.5. Failure Analysis on String and Module Level

The *I-V* parameters of a Si solar cell or PV module provide a global assessment of the electrical performance. Especially the fill factor and the cell and module power are calculated quantities and influenced by different parameters. To further analyze the origin of the observed losses, the following section presents spatially resolved luminescence measurements at different stages of the samples. Additionally, it is essential to evaluate the quality of the solder joints, according to the developed procedure on Al foils. This helps to understand possible interconnection failures. Contact angle measurements allow to benchmark the wettability of the coating on solar cells, influencing the solder joint forma-

tion. Furthermore, the conducted SEM analysis gives insight into the joint microstructure and the involved interfaces to gain a deeper understanding of the material behavior.

5.5.1. Wettability on Ni-Coated PVD Al

The coating process has not been tested in detail on PVD Al before, but the quality of the resulting Ni layer is essential to yield a good soldering result. Therefore, contact angle measurements with liquid solder are performed on the rear side of a PERC solar cell with 2 µm thick PVD Al and locally plated Ni after d-Zn treatment. The results are given in Figure 5.18.

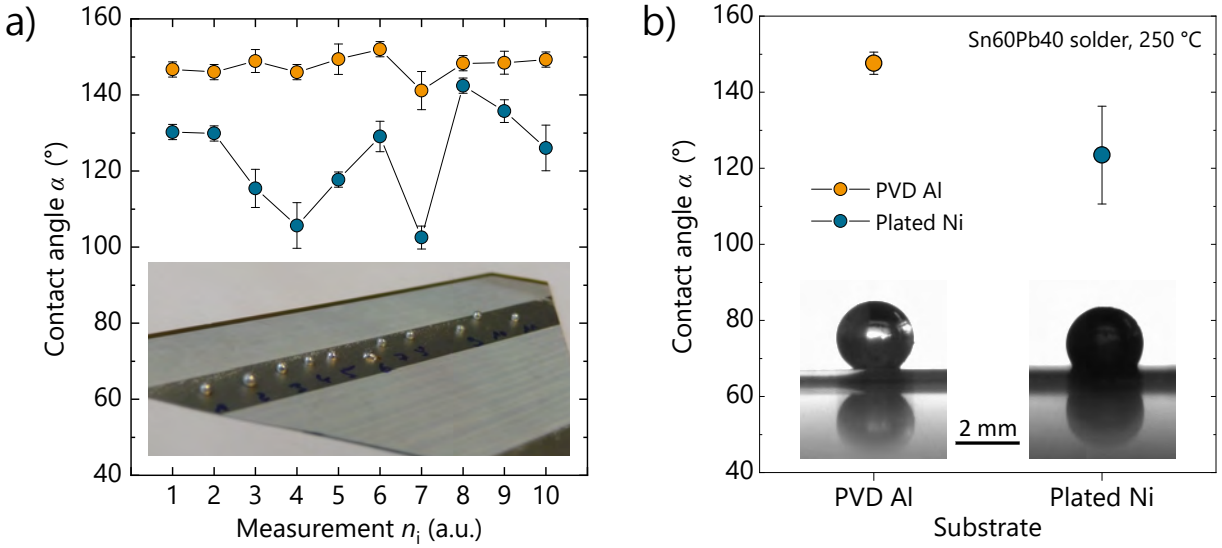

Figure 5.18.: Contact angle measurement on the rear side of a PERC cell with 2 µm PVD Al, locally coated with Ni (8 min plating) after d-Zn (15 s + 15 s) treatment. a) 10 measurements each with Sn60Pb40 at 250 °C. Each data point shows the mean of left and right contact angle with corresponding deviation. b) Mean values and standard deviation of the measurements shown in a). The Ni coating causes a reduction of $\Delta\alpha = 27.5°$ to improve wetting.

Ten measurements on the Al surface (orange) and ten measurements on plated Ni (blue) are performed, each showing the mean value of left and right contact angle. The contact angle on PVD Al yields $\alpha_{\mathrm{Al}} = (145.7 \pm 7.1)°$, which is in the same range as the value obtained for a pure Al foil ($(141.7 \pm 4.3)°$, *cf.* Figure 5.3). After Ni coating, wetting with liquid solder could be improved and a reduction of the contact angle to $\alpha_{\mathrm{Ni}} = (120.0 \pm 22.6)°$ is measured. This value strongly deviates from the Ni-coated Al foil ($(27.7 \pm 2.9)°$). The large standard deviation for the measurements on PVD Al with Ni is noticeable. This indicates an inhomogeneous coating, resulting from the manual handling during Zn treatment. Additionally, the PVD Al is rougher than the Al foil before the treatment, which influences the quality of the coating and the contact angle measurement.

5.5.2. Electrical Inspection of Soldered Cells

In Figure 5.19, three EL images, one of every group after soldering, are presented. The images are not scaled equally for a better visualization of the cell-specific effects. Soldering of the **FoilMet®** solar cell was successful; the whole cell shows a more or less homogeneous EL signal. No cracks or inactive areas are found. The two small horizontal lines with a lower signal in the middle of the cell are finger defects on the front electrode. They may arise from paste interruptions during screen printing [214]. A closer look to the EL image reveals light spotted regions, especially in the outer cell range. This effect is caused by the Al foil rear side and most probably results from inhomogeneous contact formation, also visible before soldering (*cf.* Figure A.9). Due to the elevated temperature during soldering, the air, enclosed between Al foil and Si wafer expands, which may lead to local peeling of the LMB contacts.

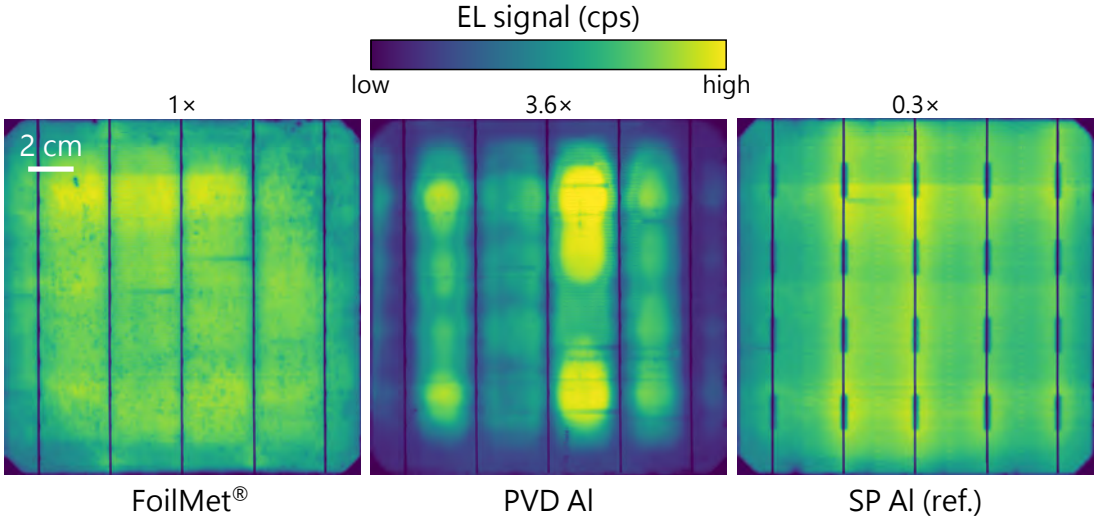

Figure 5.19.: EL images of three strings, one of each cell type. The colorbar shows the EL signal on a linear scale. The images are not scaled equally. The scaling factor of the EL signal is given above the images.

For the solar cells with **PVD Al** rear side (middle EL image), the regions between the busbars yield a significantly higher EL signal than the cell edges. Compared to the EL images on cell level (*cf.* Figure A.9), it is supposed that these regions benefit from the heat during soldering. The shape of the brighter regions correlates to areas where the IR light is reflected onto the cell,[5] *i.e.* the hottest regions during soldering. Unfortunately, no *I-V* data is available of the interconnected state of the solar cells which could give information on the global open circuit voltage V_{oc} and short circuit current I_{sc}.

To exclude a degradation of these solar cells for the darker parts of the EL image, one solar cell with PVD Al is used to measure the EL as well as the PL signal on cell level and after IR soldering (string level). The results are presented in Figure 5.20. The used solar cell has a 4 µm thick PVD Al rear side metallization, coated locally with d-Zn +

[5]Not only direct IR light contributes to the soldering process but also reflected IR light, especially at the ribbons and the downholding unit on top of the solar cells.

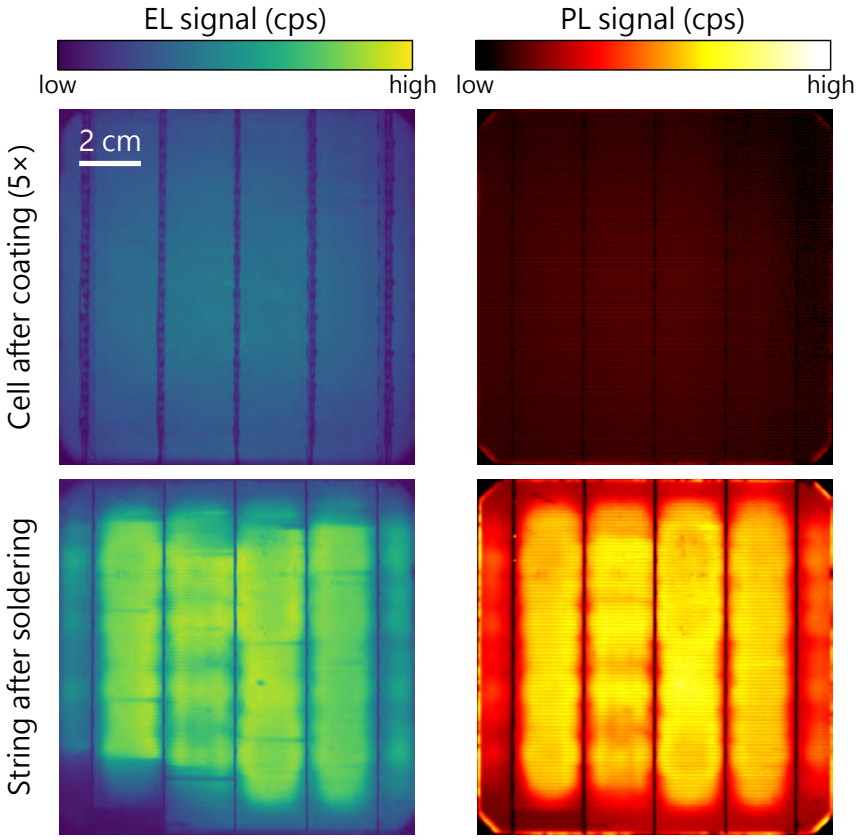

Figure 5.20.: EL and PL images of a cell with 4 µm thick PVD Al rear side metallization locally coated with d-Zn + Ni on cell and string level. The colorbars show the EL and PL signal on a linear scale. The images of the cells (top row) are scaled 5× brighter than the images on string level (bottom row).

Ni. The top images are taken within the same measurement setup. For the measurement on string level, two different setups had to be used. Although the signal of the top images is enhanced by a factor of 5, they still feature a lower signal than the images after soldering. Here, the EL as well as the PL signal are higher and not as homogeneous as before, indicating an influence of the IR heat on the solar cell. In the bottom left corner of the string, the solder joints on the two outer busbars are not intact. A poor contact of the ribbons leads to less current flow and therefore to a lower EL signal of the solar cell. In contrast, the PL signal in this corner is high, revealing a working device. Since both measurements exhibit more (band-to-band) radiative recombination than the images on cell level, one could conclude that the solar cells with PVD Al benefit from the IR radiation during soldering. Since the production process for the rear side (LCO, PVD Al, LFC) was not optimized within this thesis, most likely the Al-Si contact formation on the rear side is improved by additional heat during soldering. The actual cell temperature during soldering is not measured but is estimated to be between 220 °C and 260 °C for a maximum solder duration of 2 s. Since the melting points of Al and Si and its eutectic are in a much higher temperature range above 500 °C [100], the contact formation is promoted by bulk diffusion at the contacts [215, 216].

To prove the quality of the solder joints after stringing, metallographic cross sections are prepared for microstructural analysis by optical microscopy, SEM and EDX. The results on string level are presented in the following.

5.5.3. Microstructural Analysis after Soldering

Figure 5.21 shows optical microscopy (top row) and SEM images (bottom row) of cross sections of all three groups after the interconnection process on the industrial stringer. On the front side of the solar cells, the Cu core of the ribbon is joint to the Ag busbar. For different cross sections, the width of the front busbar may vary due to the tapered design. Misalignment of the ribbon may lead to a horizontal mismatch and therefore to non-optimal spreading of the solder during soldering. Considering the cell-to-module (CTM) gains and losses, this misalignment causes additional shading in the PV module and contributes to a reduction of the k_7-factor within the CTM calculation [217]. In the top middle image, the bottom ribbon shows a prominent accumulation of solder below the ribbon. This is due to small holes in the conveyor belt of the stringer which allows the solder to collect when liquid.

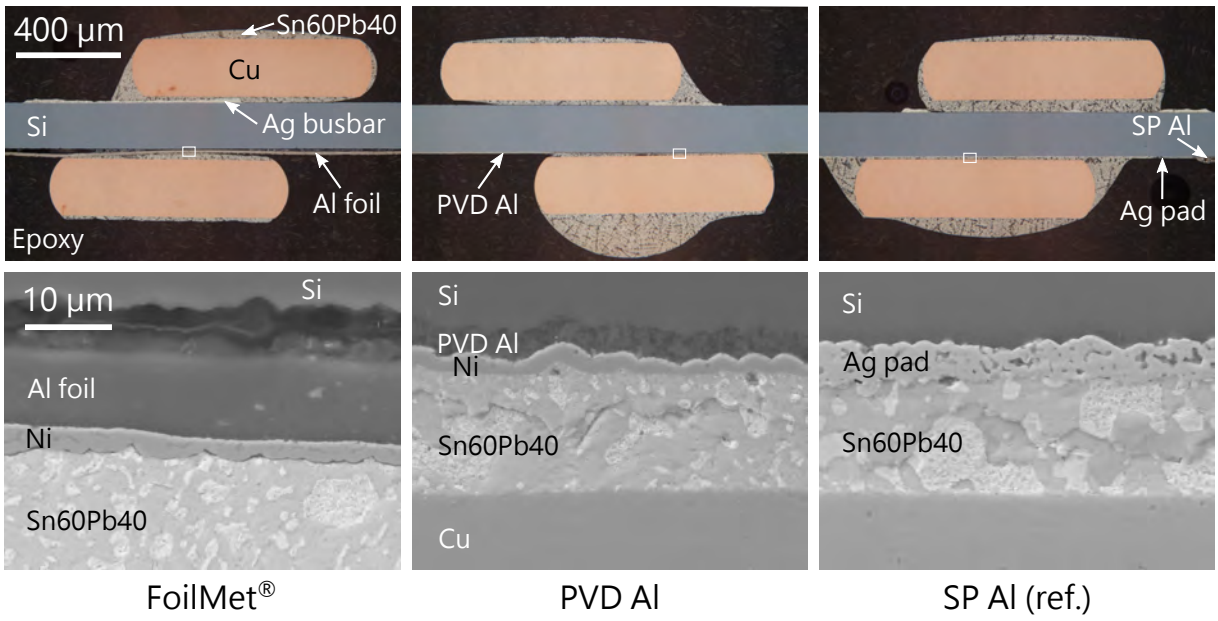

Figure 5.21.: Optical microscopy (top row) and SEM images (bottom row, 20 kV) of cross sections after soldering the three cell types.

In the cross section of the **FoilMet®** solar cell, the gap between Si wafer and Al foil is visible. The width of this gap varies. In the SEM enlargement, the Ni layer shows the same morphology as found for the coated Al foil in Figure 5.8. The Sn60Pb40 solder is in direct contact with the Ni, whereas the interface does not seem to have the same quality as for the Al foils. Different cross sections of this sample type are investigated. In some cases, the solder does not wet the Ni surface. The most common solder joint is given in Figure 5.21 bottom left. Other parts of the joints, less frequent, show a similar joint as

shown in Figure 5.8 with SnPbAg. The thickness of the Ni layer varies between 1.5 µm and 2.8 µm for the evaluated samples. Such inhomogeneties of the Ni quality and thickness may be due to the manual coating process, not fully optimized regarding handling of the solar cells. The joint microstructure demonstrates a successful solder joint formation for the FoilMet® solar cells.

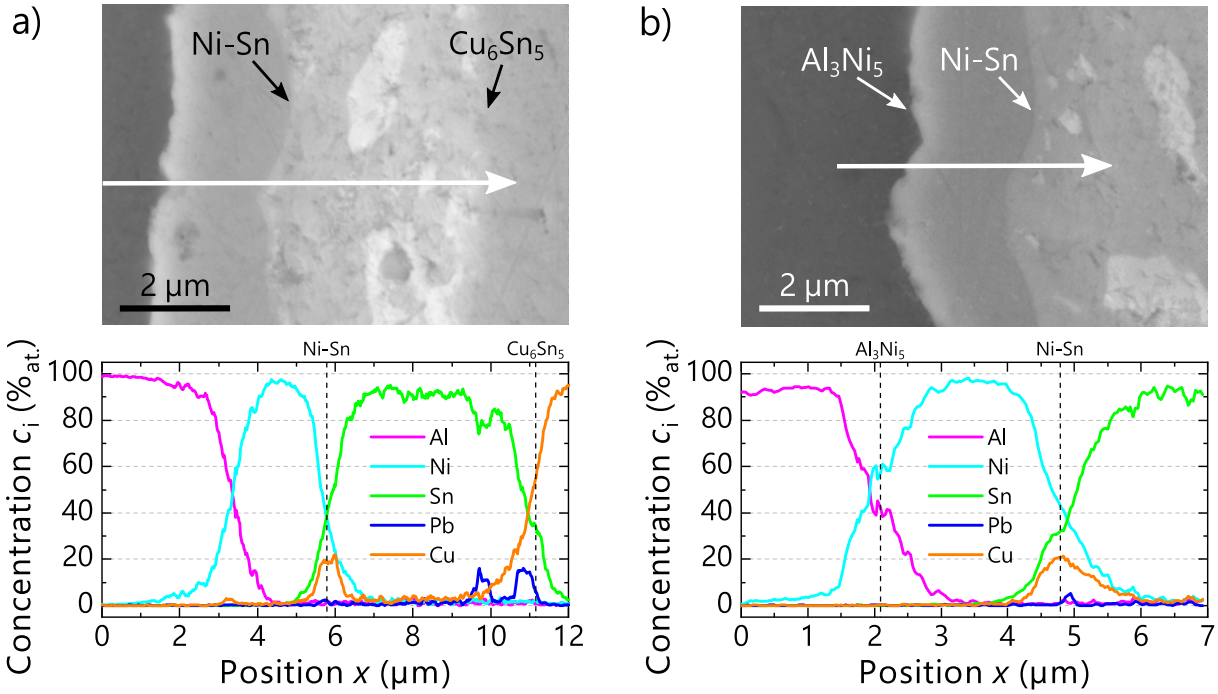

Figure 5.22.: SEM cross section images (20 kV) and corresponding line scans of solder joints on the rear side of solar cells. a) FoilMet® solar cell with Al foil (magenta), plated Ni (cyan) and Sn60Pb40 (Sn: green, Pb: blue) solder-coated Cu (orange) ribbon. b) Solder joint on PERC cell with PVD Al rear side (magenta) and plated Ni.

A close-up of a solder joint on a FoilMet® solar cell rear side is given in Figure 5.22 a), taken at 20 kV. The image is tilted in a way that the line scan below follows the arrow from left to right. Neither voids nor cracks are visible within the solder joint and the involved interfaces. The quantification by EDXS reveals two main findings. First, an accumulation of Cu is found on top of the Ni layer. At this position, Ni and Sn may form an intermetallic phase, stable at RT, most likely a thin Ni_3Sn_2 layer. However, Cu is not dominating at this position, whereas a ternary phase of $(Cu,Ni)_xSn_y$ could be excluded. The thin Cu layer is formed on top of the Ni layer due to the asymmetry of the solder joint (*cf.* Section 5.3) [199, 207]. Secondly, the line scan indicates the presence of Cu below the Ni layer at the interface to the Al. At this point, the amount of Cu is not critical for the solder joint or the semiconductor. In general, Cu diffusion towards the Si wafer could be disadvantageous due to the formation of defects within the bandgap causing unwanted recombination [21]. The findings correlate well with the results obtained for solder joints on Al foil and the growth of the Cu layer when exposed to heat (*cf.* Figure 5.9).

In the middle of Figure 5.21, a solder joint on a solar cell with **PVD Al** rear side is shown. One part of the joint on the cell rear side is enlarged in the SEM image. The measurement of the PVD Al layer thickness on top of the Si wafer at several positions yields $d_{\mathrm{PVDAl}} = (3.3 \pm 0.2)\,\mu\mathrm{m}$ and $d_{\mathrm{Ni}} = (1.8 \pm 0.1)\,\mu\mathrm{m}$ for the plated Ni. The solder joint shows a similar structure to the joints on Al foil. Cu accumulation is measured on top of the Ni layer as well, quantified by the line scan in Figure 5.22 b). Again, a diffusion zone of Ni and Sn at this interface is found. In contrast to the Al foil, the PVD Al seems to be more disposed for phase formation with Ni, resulting in a Al_3Ni_5 binary phase at the interface. In general, phase formation indicates a diffusion zone which is required for a firmly bonded joint. If the IMC layer gets dominant within the solder joint, cracks and embrittlement may occur [92, 106, 218]. For the joints on PVD Al, a minor amount of Cu is found below the Ni layer, but only at few parts of the joints.

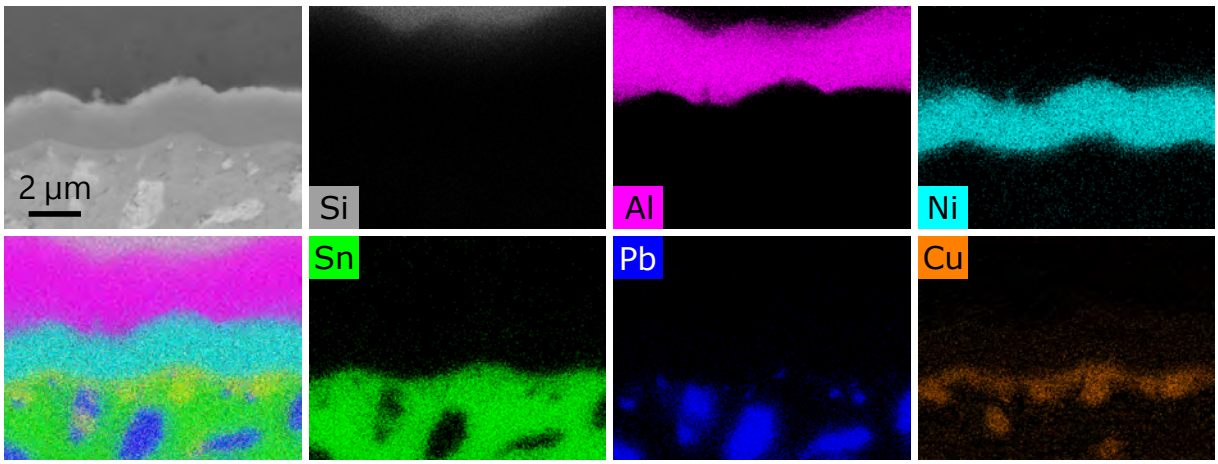

Figure 5.23.: SEM image and corresponding EDX mapping of a solder joint (Sn60Pb40) on Ni-coated PVD Al on a Si solar cell rear side. The cross section is prepared after IR soldering on an industrial stringer.

To analyze the element distribution within a larger area of the solder joint, an EDX mapping is performed. Figure 5.23 shows the complete SEM image of Figure 5.22 b) and the corresponding element maps. The Cu map (orange) nicely shows the Cu accumulation at the Ni interface. Within this region, no additional Ni is found. Indeed, the signal of Sn (green) correlates. Both supports the assumption of a binary phase of Sn-Ni and no ternary Sn-Ni-Cu phase. Within the selected section of the solder joint, no Cu at the Al-Ni interface is found.

In good agreement to the findings of the microstructural analysis on thick Al foil (*cf.* Section 5.3), no Zn is found within the cross sections, indicating a complete removal during wet-chemical processing (*cf.* Section 3.1.2).

5.5.4. Electroluminescence Imaging after Thermal Cycling

To investigate the *FF* losses in more detail, EL measurements have been performed initially and after 50, 200 and 400 thermal cycles, shown in Figure 5.24. The **FoilMet®** module is given on the left. After TC 50, two striking defects with a lower EL signal can be noticed: Perpendicular to the busbars, repeated lines of low signal are found. This is a typical defect, correlated to the detachment of fingers on the cell front side. This prevents the current from entering the silicon during the EL measurement, so that the signal is reduced. Therefore, during normal cell operation, the generated current cannot be collected in this area, which reduces the *FF*. The second defect is found in parallel to the busbars, more pronounced at the outer regions. Such a defect can be caused by detachment of the Al foil from the silicon on the rear side. Due to the CTE mismatch between Cu ribbon, Sn60Pb40 solder, Al and Si, thermomechanical stress is induced within the TC test. At the outer parts of the ribbons, the stress is more pronounced (*cf.* Figure 2.15). Additionally, the laser of the FoilMet® process may be slightly out of focus in the outer cell edges, so that the LMB contacts may not have the same quality as in the inner part of the cell. Both defects become stronger after TC 200 and TC 400. Nevertheless, with $\Delta P_{\mathrm{mpp}} = (-0.75 \pm 2.31)\,\% < -5\,\%$ after TC 200, the FoilMet® module passes the IEC test on a very good level. It should be mentioned, that an unwanted optical camera-based artefact is also visible within the presented luminescence images, especially in the top right image of the cell with SP Al in Figure 5.24. The EL signal is radially reduced in intensity towards the edges of the image, interfering with the physical luminescence. This effect is called vignetting and reported in literature for solar cells and modules [183, 184].

To exclude a degradation on cell level at the busbar regions, PL images of the module are taken after TC 200, as seen in Figure 5.25. The FoilMet® module, given on the left, does show a very homogeneous PL signal without any defects of the solar cell. One could assume a slight reduction of the PL signal in the busbar region of the outer cell parts. Nevertheless, a reduction of the PL signal due to optical effects by *e.g.* flux residues is also possible and cannot be distinguished at this stage.

To understand the strong fluctuation in *FF* after TC of the modules with **PVD Al** rear side (*cf.* Figure 5.16), the EL images of those five modules are compared (not shown here). It is conspicuous that one module shows a significant higher amount of finger defects on the front side than the others. This module shows the highest losses in *FF* and P_{mpp}. Most probably, the front side grid was attacked by the Zn treatment due to the suboptimal manual masking used here. For these five modules, the *FF* is further reduced due to another effect, described in the following: The EL image of one of the modules with $\Delta P_{\mathrm{mpp}} = -2.3\,\%$ is given in Figure 5.24 in the middle. Note that the EL signal of the images corresponding to the modules with PVD Al are enhanced by a factor of 2. All five modules show a significant reduction of the EL signal between cell edge and first busbar after TC, already present in the initial state.

To explain this effect, a closer look to the relevant interconnected part is necessary. Figure 5.26 a) shows the cross section introduced before (s. Figure 5.21), highlighting the relevant quantities: width of the Cu core of the ribbon $w_{\mathrm{Cu}} = 0.9\,\mathrm{mm}$, width of the

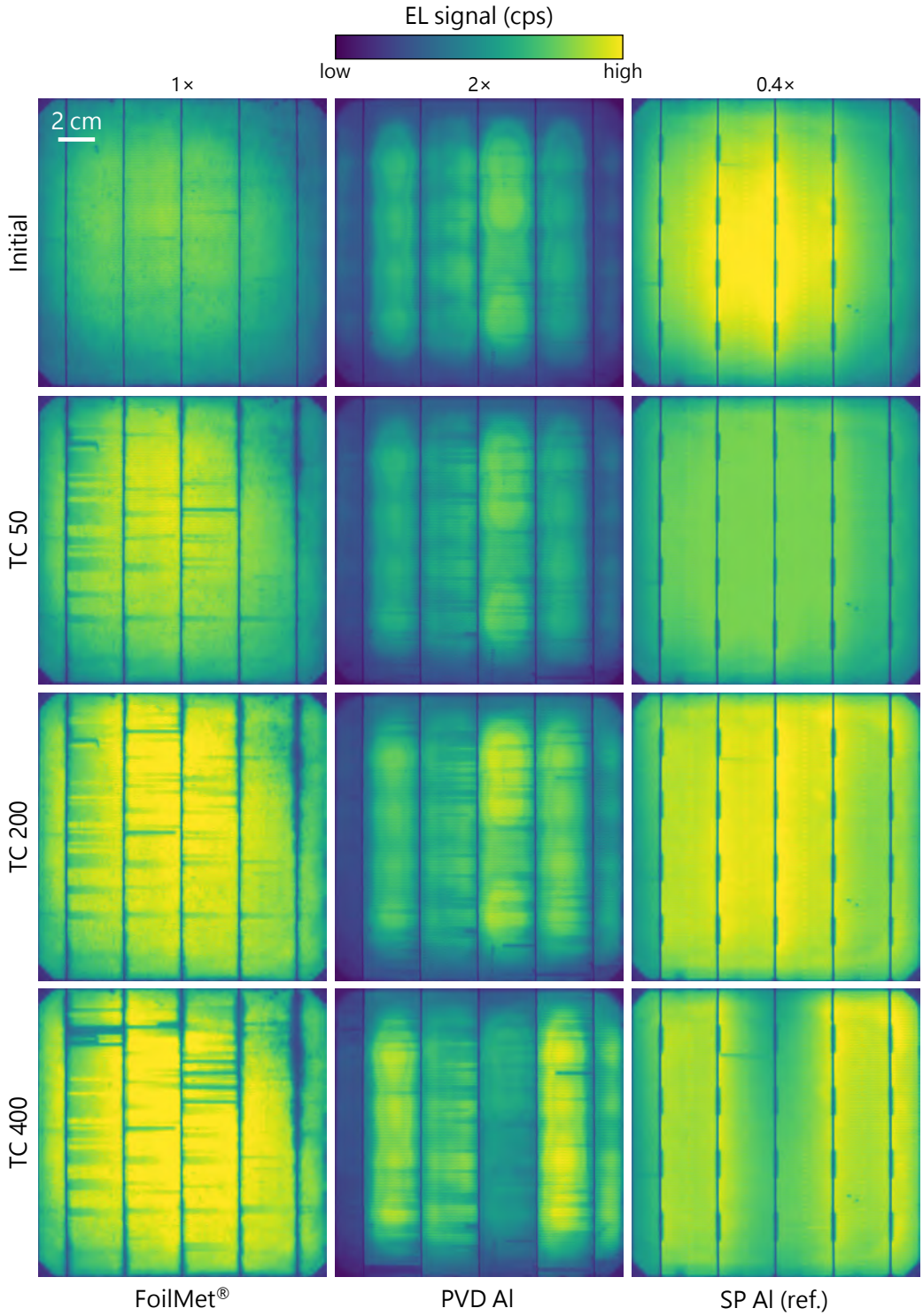

Figure 5.24.: EL images of 1-cell-modules: initially, after TC 50, TC 200 and TC 400. One module for each cell type is shown. The images are not scaled equally; the scaling factor for the EL signal is given above the images. The EL signal is given on a linear scale.

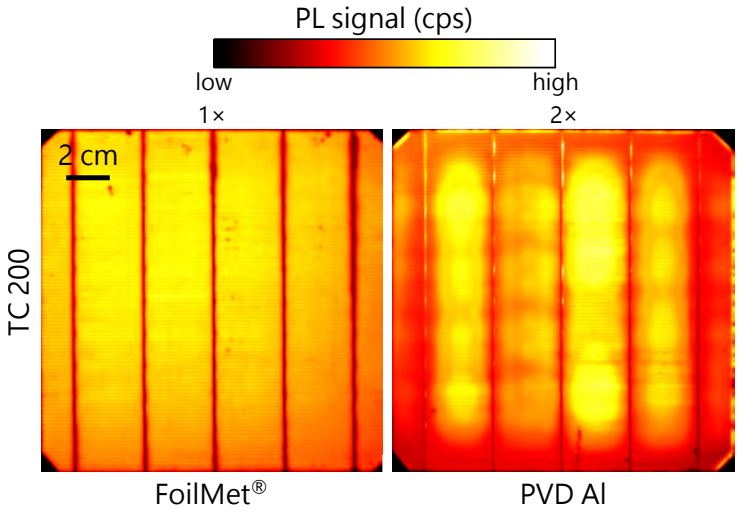

Figure 5.25.: PL images of 1-cell-modules after TC 200. The images are not scaled equally, the scaling factor is given above the images. The PL signal is given on a linear scale.

spreading of the solder w_{SnPb} depending on the position x_{i}, width of the tapered busbar w_{BB}, as well depending on x_{i}. A clear misalignment of the upper ribbon to the busbar is visible, caused by not ideal alignment of the ribbon onto the busbar during the industrial soldering process.

This effect is sketched in Figure 5.26 b) in top view. On the right side of the Cu core, the solder can spread over the busbar during soldering, whereas a large part of the fingers is also contacted below the ribbon. During thermal cycling, the Cu core expands/contracts more than the Si during heating/cooling (*cf.* CTE values in Table 2.3). Since the solder is not liquid and can not buffer the mechanical stress, this contraction leads to a ten-

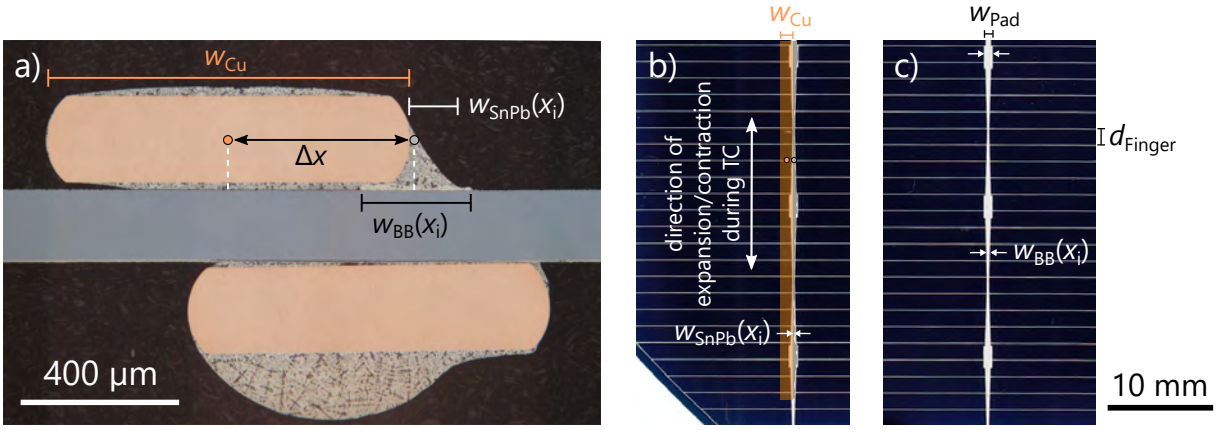

Figure 5.26.: Misalignment Δx of the outer ribbon after soldering the cells with PVD Al rear side. a) Optical microscopy image of the interconnected outer busbar in cross section view. b) and c) show photographs (top view) of the solar cell front side. The misalignment of the ribbon is sketched in b).

sile force to the fingers below the ribbon between +85 °C and −40 °C. The fingers only measure a width of about 35 µm and can not withstand the tensile forces in the direction of the busbar. Thermal cycling causes cutting of the fingers from the busbar, whereas the current of the region on the left side of the busbar can not be collected, leading to a reduced EL signal and a loss in *FF*. In the presented example in Figure 5.26 a), the misalignment of the top ribbon measures about $\Delta x = \frac{1}{2} \cdot w_{\mathrm{Cu}} = 450\,\mu\mathrm{m}$. This highlights the high accuracy required for the alignment of ribbon and busbar (at least $< 450\,\mu\mathrm{m}$) to not damage the solar cell metallization.

For completeness, also the PL image of a module with PVD Al after TC 200 is shown in Figure 5.25 on the right. Here it can be seen that the observed pattern from EL is repeated, again underlining the changes within the semiconductor.

For the reference group with **SP Al**, the EL images in Figure 5.24 on the right show a homogeneous EL signal as well and no dominant failure modes.

5.5.5. Electroluminescence Imaging after Damp Heat Testing

Figure 5.27 shows the corresponding EL images of the modules in the initial state and after DH 1000. Only a small impact of the DH test on the EL signal for the modules with PVD Al is found.

An overall reduction of the EL signal of the modules with SP Al correlates well with the losses in V_{oc} and I_{sc}. Additionally, the higher amount of Cu within the solder joint region does not seem to have a measurable impact on module level.

The results of the DH test underline that the coating process does neither have a negative influence on the overall electrical performance of the PV module, nor on the interconnection. Future experiments could address FoilMet® modules with wet-chemical rear side coating in a DH test. However, based on the presented results, it is very likely that neither critical failures would occur.

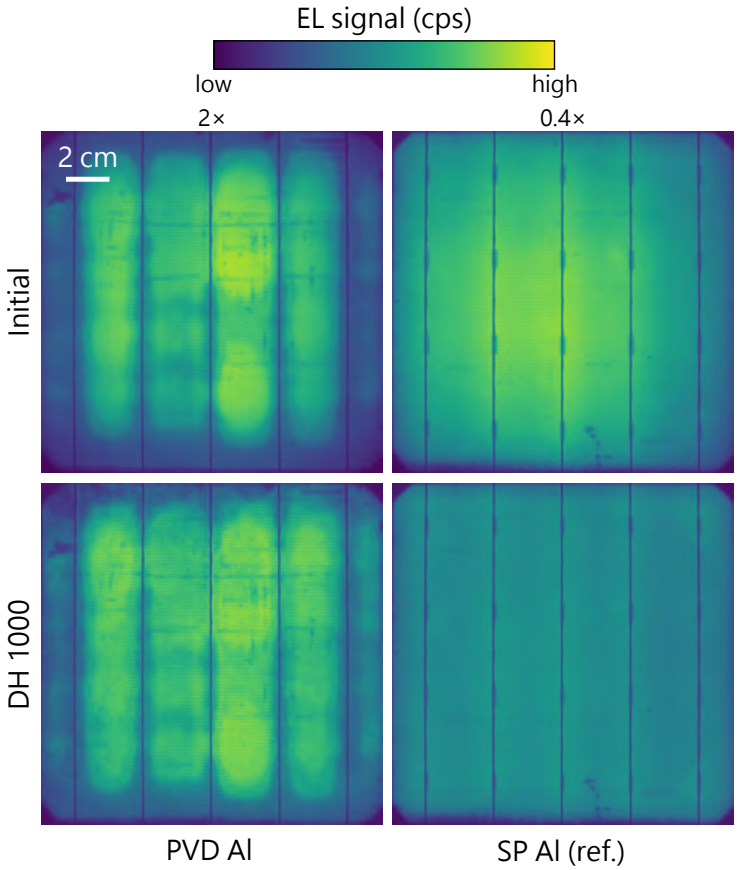

Figure 5.27.: EL images of 1-cell-modules, initial and after DH 1000. Solar cells with PVD Al rear side (left) and SP Al rear side (right) are tested under DH condition. The images are not scaled equally; the scaling factor is given above the images. The EL signal is given on a linear scale.

5.6. Chapter Summary

Within this chapter, direct contacting of Al substrates by soldering in ambient air is realized by wet-chemical coating. The focus is set on solder joints on 200 µm thick Al foils, treated with a **double zincate process** for 30 s + (15-30) s and subsequent **Ni plating** for 8 min. The Ni surface provides a solderable coating which can be contacted with Sn-based solders for process times < 5 s. Detailed analysis on the initial performance of the solder joints is performed, including mechanical strength after soldering and after isothermal aging. Since, the Ni surface provides good **wettability** (contact angle $\alpha < 60°$ for liquid Sn60Pb40 at 250 °C), the **mechanical stability** of the joints, tested by a 90° peel force measurement, is very good ($F/w \approx 5.6$ N/mm). Both properties show a stable performance when exposed to higher temperatures for longer times (250 °C, 100 min and 85 °C, 1000 h).

In extension of known literature, the presented results give a detailed analysis of the **solder joints on microstructural level** and their **long-term stability**. Metallographic cross sections of the solder joints and the fracture pattern after the peel force measurement are analyzed. SEM and EDX investigations show small diffusion zones at the interfaces Al/Ni and Sn/Ni and no notable brittle intermetallic phase formation. For all joints, as well as for the aged samples, a **mixed fracture** pattern with different fracture modes is observed after the peel force measurement. Therefore, the quality of all interfaces (Al/Ni, Ni/Sn, Sn/Cu) is similar and highly reliable, resulting in excellent and uniform peel forces > 4 N/mm. This shows the high potential of this material combination and the suitability of the simple and short soldering process to yield strong and stable solder joints on Al foils.

In addition to the process development, the coating process is also demonstrated on **Si solar cells with different Al rear side electrodes**. A successful transfer to 10 µm laser-bonded Al foil (FoilMet® solar cells) and 2 µm - 4 µm thick PVD Al is shown. The coating as well as the interconnection are **stable within TC 200 and DH 1000 on module level**, resulting in power degradation < 5 %. The analysis of the different interconnected solar cells shows very similar findings to the joint analysis on thick Al foil. Therefore, the preliminary investigation on thick Al foils is a justified cost-effective alternative as initial assessment.

6. Sputtered Functional Stacks on Aluminum Surfaces

Within this chapter, coating of Al surfaces by magnetron sputtering is investigated as a method to provide very thin solderable layers of different thickness and functionality. The development of the sputter stacks has been done in cooperation with experts at Fraunhofer ISE regarding inline coating technologies for solar applications. To implement the sputter coating process of Al foils on an industrial roll-to-roll unit, parts of the experiments have been conducted with an external partner (ROWO Coating). The contribution of this work is a detailed analysis of the solder joints to understand the interfacial reactions and optimize the sputter stack for the desired application. Within the collaboration at Fraunhofer ISE, one patent has been submitted, addressing the novelty of the developed layers and their functionality [219]. In addition, parts of the results of this work have been published by the author in 2017 [188] and 2018 [189].

*In the first **Section 6.1**, the sputter-coated surface on 200 µm thick Al foils is characterized by SEM top view images. The wettability with liquid solder is analyzed by optical contact angle measurements and quantitatively compared to results of a wetting balance test. Secondly, the mechanical strength of the solder joints is evaluated by 90° peel force measurements for a variety of different material and thickness combinations of the sputter stack. The results are shown in **Section 6.2**. The fracture pattern is briefly analyzed by SEM and in addition a detailed microstructural analysis at higher magnifications is presented in **Section 6.3** by TEM and EDX. In **Section 6.4**, the contact resistance is measured, including isothermal aging and damp heat test of small glass laminates. The results of the process transformation of this coating technique to Si solar cells is presented in **Section 6.5**, focusing on the influence on the solar cell performance and the results of the industrial interconnection process. Finally, a failure analysis is performed on string and module level within **Section 6.6**. For this, I-V and EL measurements are used to characterize the resulting loss in power of the modules after TC and DH climate chamber test. This analysis is complemented by SEM cross sections to assess the microstructure of the solder joints within the PV module.*

The analysis of this chapter should provide insight into the quality of solder joints on sputter-coated Al foils. The **scope of this chapter** is to use the detailed analysis of the solder joints, provided by different characterization methods, to identify an optimal material and thickness combination of the sputter stack. The transfer of the process to Si solar cell rear sides is tested and the practical feasibility for an industrial application in the photovoltaic industry is evaluated.

Challenges for Sputter-Coating of Al and Choice of Material

The possibility to deposit several thin layers of a wide range of different materials with a high reproducibility and homogeneity is one of the major advantages of sputtering. To make this approach economically viable for the application on Si solar cells, the total stack thickness has to be reduced as much as possible, while maintaining a good adhesion of the solder joints and a low contact resistance at the involved interfaces. Therefore, the focus is set on very thin total stack thicknesses below 100 nm. One challenge here is to deposit a thin homogeneous layer over the whole sample. To provide *e.g.* a certain Ag to Cu ratio, small amounts of Cu are deposited on top of Ag, as *e.g.* Ag/Cu 10/2 nm. However, sub 5 nm layers do not form a "closed layer" film and are only given as nominal values here.

As introduced in Section 3.1.3, multilayer stacks of several metals are sputtered onto the Al substrate. Since the bond strength to Al is of major importance, an adhesion layer of either Cr or NiCr is deposited first. In case of thin coatings, Al diffusion towards the surface could lead to the formation of Al_2O_3 and a loss in adhesion. Therefore, a diffusion barrier is sputtered, either of NiCr or pure Ni. To provide solderability, the top layer should be wettable with liquid SnPb-based solder alloys. For this, pure metals as Ag, Cu or Ni can be used, as well as certain alloys of AgCu or AgNi. Depending on the choice of material of the top layer, an additional layer is required to prevent oxidation, since oxygen diffusion is very likely for thin sputter stacks.

To gain a broad understanding of the influence of these layers on the solder joints on Al, a large variation of materials and thicknesses is investigated within this work. The possibility to deposit these layers in-house at Fraunhofer ISE allows for process flexibility and a fast evaluation of several material combinations.

Notation for Sputter Stacks

The developed functional sputter stacks are multilayer stacks of either two, three or four layers of different compositions. They are sputtered one after another without breaking the vacuum in the sputter chamber. Within this work, the notation for the layer sequence is given as **A/B/C** with **a/b/c nm** thickness, whereas layer A is sputtered directly on top of the Al substrate, followed by layer B and C. The corresponding layer thicknesses are given in the same order, as well separated by a slash each. The experimental uncertainty for the thickness of each layer is stated as 10 % of its nominal thickness.

To not overload the graphs with data of different sputter stacks, but still providing as much information on the stacks as possible, the following short notation is introduced:

$$x\mathrm{L} - d \tag{6.1}$$

whereas x states the total number of layers and d the total thickness of the stack. For the stack Cr/NiCr/Ag with 10/23/30 nm, the short notation would give 3L-63. The notation does neither consider the involved materials nor their order sputtered onto the Al substrate. In case this information is of relevance, details are given within the text and the corresponding figures.

6.1. Surface Properties

The deposition of very thin metal layers by sputtering offers a solderable coating on Al, mostly preserving the surface morphology of the substrate below. In case of Al foils, the rolled surface dominates the resulting morphology of the sputtered layers. A very thick sputtered layer of *e.g.* pure Ni would result in a comparable surface as the plated Ni layer, which would result in similar contact angles of liquid solder. The thinner the sputter stack, the more essential is the homogeneity of the layer. To guarantee a successful solder joint formation, a homogeneously closed sputter stack on top of the Al with a good wettability is required. Within this section, the surface after coating is characterized by SEM in top view mode and by wetting tests with liquid solder. The results will be presented in the following section.

6.1.1. Initial Characterization of Sputter-Coated Al Foil

Figure 6.1 shows top view SEM images of the surface of an Al foil after sputtering NiCr/AgCu with 10/30 nm. The morphology looks identical to the uncoated foil (*cf.* Figure 5.1), not influenced by the 40 nm thin sputter stack. Due to the high acceleration voltage of 20 kV, some Fe grains within the Al foil are also visible.

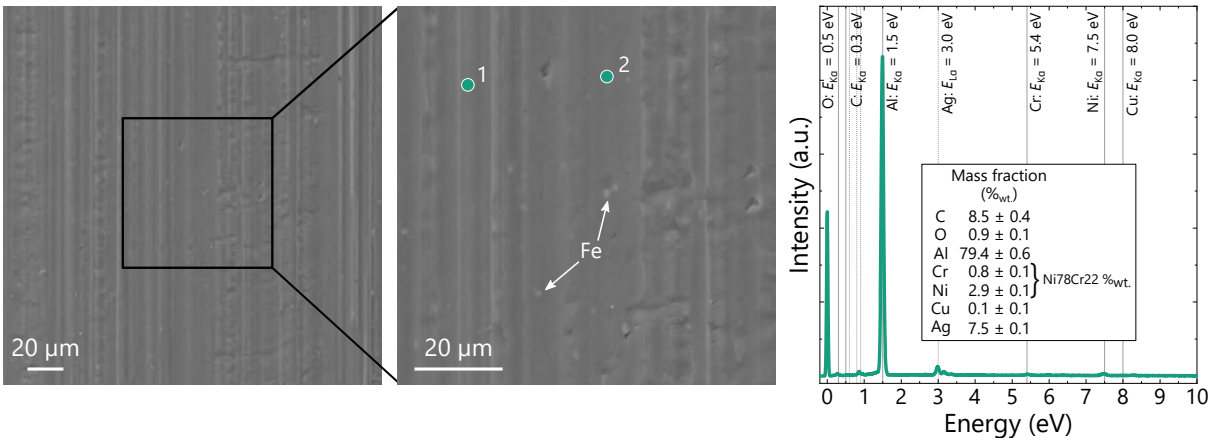

Figure 6.1.: Surface of sputter-coated (NiCr/AgCu 10/30 nm) Al foil before soldering. Top view SEM images (20 kV) and EDX spectrum measured at position 1 and 2. The energies of the elemental spectral lines K_α (solid) and L_α (dotted) are marked. The textbox summarizes the elemental distribution of the point scans 1 & 2.

The graph on the right shows the EDX spectrum of two point scans, after subtracting the signal of the background. Solid and dotted vertical lines mark the energies of the X-ray emission peaks K_α and L_α of the elements, respectively. The results of the quantification are listed in the textbox, yielding a composition of 78 $\%_{wt.}$ Ni and 22 $\%_{wt.}$ Cr, in good agreement to the nominal values. Beside the large Al signal, a significant amount of Ag of the sputter stack is measured, whereas 2 $\%_{wt.}$ Cu of the top layer is not detectable.

The solderability of the foils after sputtering is characterized by wetting tests, presented in the following Section 6.1.2. Sputter stacks of different metals and thicknesses are compared to identify good wettability with liquid Sn60Pb40 for the soldering process of Al rear sides of Si solar cells.

6.1.2. Optical Contact Angles on Sputter-Coated Al Foil

As conducted for wet-chemically coated Al foils (*cf.* Section 5.1.2), **o**ptical **c**ontact **a**ngle (OCA) measurements serve to quantify the degree of wetting during heating in equilibrium state. The following section presents the results of OCA measurements, also focusing on the comparison between the used solder alloys Sn60Pb40 and Sn62Pb36Ag2. The main evaluation should answer the question which influence the materials of the different layers and their thickness have on surface wettability.

Section 6.1.3 introduces another method to quantify the wettability of a metal surface: the wetting balance. The wetting force is measured time-dependent to characterize the wettability of a selection of four sputter stacks on Al foils. This method is not highly popular in PV and is tested as alternative characterization method to the OCA measurement.

OCA measurements are conducted for a number of sputter stacks with varied thicknesses and material combinations. For a detailed overview on all contact angle measurements performed within this work, the reader is referred to Figure A.11 in the Appendix 6.1.2. The evaluation, presented in the following, show extractions to visualize trends found for different sputter coatings.

Impact of Total Stack Thickness

On the left in Figure 6.2, the optical contact angle α is given for Al foils coated with different sputter stacks. The color code for the stacks is fixed within this chapter and in agreement with the data given in the appendix. On the x-axis, the thickness of the solderable layer is shown, *i.e.* Ag, Ag/Cu or AgCu. The total thickness of the stack is represented by the shape of the symbols. With increasing thickness of the solderable layer, the contact angle decreases. The reference system 3L-63 of Cr/NiCr/Ag with 10/23/30 nm thickness (black) already provides very good wetting with a contact angle of $(30 \pm 8)°$. To identify the lower limit of α, a simple stack of NiCr/Ag with a total thickness of 1250 nm is characterized (light blue reversed triangle), yielding $(30 \pm 5)°$. Some of the stacks, also the reference 3L-63, achieve this lowest value for α. A minimal thickness of the solderable layers of about 20 nm seems to be sufficient for good wetting ($\alpha \leq 30°$); no significant improvement is achieved for thicker layers.

The thickness of the bottom layers, consisting of Cr/NiCr or only NiCr, plays a minor role for wettability. A decrease in thickness of the NiCr layer does not influence wetting until the critical total thickness of the stack is reached (*cf.* Figure A.11).

Ag and Cu have a dissolution rate in liquid Sn60Pb40 of $1.8\,\mu m\,s^{-1}$ and $0.13\,\mu m\,s^{-1}$ at 250 °C, respectively [7]. Therefore it is assumed that the top layer provides the initial wetting but quickly dissolves in the liquid solder. This leads to a direct contact between

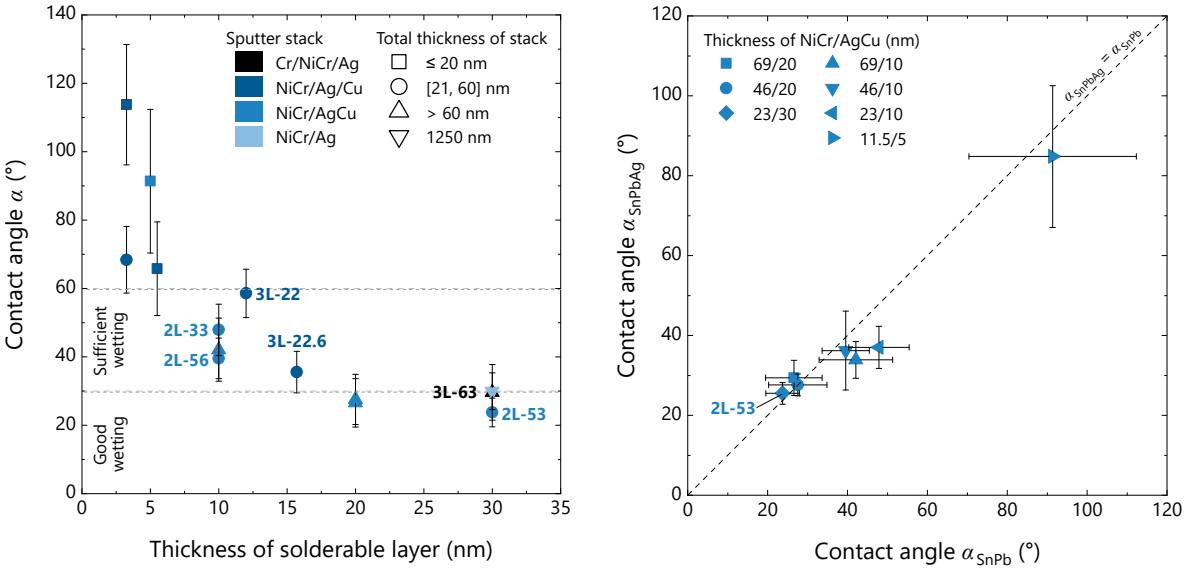

Figure 6.2.: Optical contact angle α of different sputter stacks on Al foil. The tests are conducted with Sn60Pb40 at 250 °C at ambient air. The error bars state the standard deviation of 10 measurements each. Left: Contact angle in dependence of thickness of solderable top layers (Ag, Ag/Cu, AgCu). Right: Comparison of contact angle of Sn60Pb40 and Sn62Pb36Ag2 at 250 °C on NiCr/AgCu of different layer thickness.

solder and NiCr. The dissolution rates of Ni and Cr are much lower in Sn60Pb40 (Ni: $< 10^{-5}\,\mu m\,s^{-1}$ and Cr even less) [7], whereas only solid diffusion may lead to further material exchange within the measurement time of 5 s to 30 s. In addition, Ag is used to prevent oxygen diffusion towards the stack. Therefore, a thicker solderable layer may lead to less oxidation of the NiCr or even the Cr or Al interface.

In consideration of these measurements, a total thickness of a sputter stack of about 25 nm to 60 nm would be advantageous for coating Al foils (dots in the graph), since thicker stacks do not further improve wetting. This would result in a top layer of about 20 nm thickness of Ag, Ag/Cu or AgCu and bottom layers of Cr/NiCr or NiCr with a maximum thickness of 40 nm. For thicker stacks, no significant improvement of the solderability is expected. For the implementation in the PV value chain, the process time should be kept short and the material consumption as low as possible. Since the development of the stacks is not in the focus of this thesis, no systematic variation of the layer thickness is given. Some of the most promising material combinations are identified, aiming a very thin layer while maintaining good wettability. They are marked with their short names within the graph and summarized at the end of this section.

Influence of Ag in SnPb Solder Alloys

On the right side in Figure 6.2, the measurement data of the group NiCr/AgCu (royal blue) is plotted for two different solder alloys. It is known that a small amount of Ag in the solder improves wetting due to a reduction of the surface tension [16]. This effect is visible in the data for thinner AgCu layers (triangles). Additionally, the solubility of Ag of the sputter stack in Ag-containing solder is lower than within the Ag-free alloy SnPb, which also improves wetting due to reduced Ag leaching [7]. For the stacks with 69/20 nm, 46/20 nm and 23/30 nm, the OCA measurements with Sn60Pb40 and Sn62Pb36Ag2 yield the same contact angles of about 30°. In case of a thinner AgCu layer (triangles), most likely the Ag content within the solder improves wetting. These two solder alloys are used for the formation of solder joints within this work. Whereas Sn62Pb36Ag2 is used with manual soldering to prepare samples for peel force and contact resistance measurements on Al foils, the alloy Sn60Pb40 is used in the industrial stringer for the interconnection of solar cells. The comparison of these two alloys given in Figure 6.2 shows very similar results regarding wetting so that no significant influence on further results within this thesis is expected.

6.1.3. Wetting by Determination of Wetting Force

There exist several other options to evaluate the wettability of a metal surface. In microelectronics, the wetting balance has shown to be a powerful tool to find an optimal process window for soldering small components. This method provides a dynamic measurement of the wetting force depending on time at elevated temperature, as introduced in Section 3.3.1. This allows to make a reliable statement on the wetting time t_w, *i.e.* the minimum time required to get the component wetted by the liquid solder, the degree of wetting and the ability of possible dewetting over time.

The wetting balance enables a fast characterization of different components, which allows a wide variation of solder alloy, flux and bath temperature. For solar cell metallization, this method has been tested [220] but has shown to be challenging due to an extensive procedure and highly fluctuating measurement results.

Based on the promising results discussed in the last section, this method has been tested for four of the coated Al foils, to investigate the applicability of the wetting balance for such samples. In this study, the use of samples made from Al foils realizes an advantage over earlier studies in the context of PV, where solar cell cutouts had to be used, which induced significant uncertainties [220].

Wetting Balance Tests with Coated Al Foils

Figure 6.3 on the left shows 12 measurements of one sample type carried out on a wetting balance according to the Wilhelmy plate method [171]. The samples are cut out of a 200 µm thick Al foil, coated with Cr/NiCr/Ag on both sides with 10/23/30 nm thickness (stack 3L-65). The resulting force F is recorded over time t for 10 s in total (*c.f.* Section 3.3.1). Since the measured force F stabilized after some seconds and does not show any further changes, only the first 4 s are plotted.

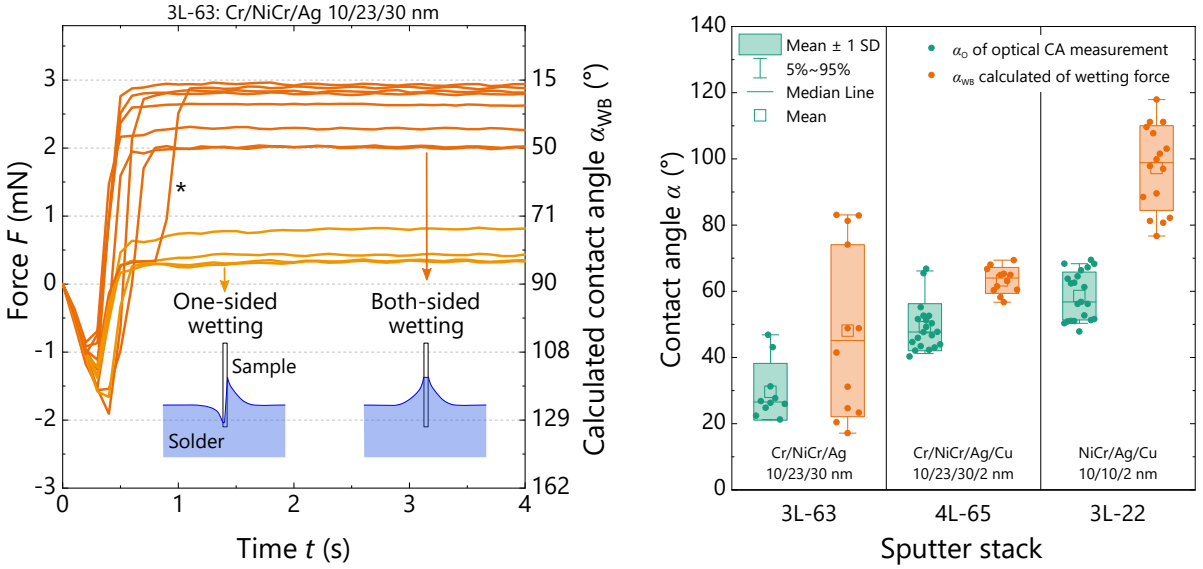

Figure 6.3.: Left: Wetting curves of sputter-coated Al foil showing 12 measurements of one sample type (Al foil with 3L-63). Right: Contact angle of optical contact angle (CA) measurement α_{O} (green) and calculated contact angle α_{WB} of wetting force (orange) for three different sputter stacks.

When the measurement starts and the sample touches the solder bath, the surface tension of the bath leads to a decrease of the force until wetting sets in. The mean wetting time t_{w} of this sample type is very fast with $(0.4 \pm 0.1)\,\mathrm{s}$. After $\sim 0.6\,\mathrm{s}$, mainly two regimes of the resulting force are found. The first set increases to a maximum force F_{max} of 2 mN to 3 mN (darker orange), whereas the other set stays between 0 mN and 1 mN (light orange). Visual inspection of the samples after the test supports the assumption of one-sided wetting for a third of the samples (light orange, 4 out of 12) and successful both-sided wetting for the others. During one of the measurements ($\star$), the sample is first wetted on one side changing to both-sided wetting at about 1 s.

Using Equation 3.10, the contact angle α_{WB} can be derived from the maximum force F_{max} after wetting. The corresponding values for α_{WB} are given on the right y-axis. In case of a successful wetting of the whole sample, a contact angle between 15° to 50° (mean: $(32 \pm 12)°$) is found for this sputter-coated Al foil. These values are in good agreement to the contact angle of $(30 \pm 8)°$ obtained by the optical measurement for stack 3L-63 (*cf.* Figure 6.2 left).

Comparison of Wetting Methods

Using the wetting balance, in total four sputter stacks are characterized for further exploration of the method. The detailed measurement results can be found in the Appendix A.9.2. Figure 6.3 presents the calculated contact angle α_{WB} of three of these measurements in orange in the graph on the right. For comparison, the data of the

optical contact angle measurement for the same three sputter stacks is given in green[1]. Table 6.1 summarizes the mean values and statistical errors (neglecting possible systematic measurement differences as presented for stack 3L-63). Compared to literature, these values are in the expected range, as also listed in Table 6.1, despite some deviations of the measurement details.

Table 6.1.: Measurement results of wetting tests for three sputter-coated Al foils. Wetting time t_w and maximum force F_{max} are measured with a wetting balance. The resulting contact angle α_{WB} is calculated of F_{max} by using Equation 3.10. For comparison, the measured optical contact angles α_O are listed, as well as literature values for pure Cu and Ni surfaces, measured with Sn63Pb37 at 255 °C.

			Contact angle		
Surface	**Time**	**Max. force**	**Wetting balance**	**Optical**	**Ref.**
	t_w (s)	F_{max} (mN)	α_{WB} (°)	α_O (°)	
Cu		2.7		18	[221, 222]
Ni		0.9		60	[221, 222]
3L-63	0.4 ± 0.1	1.9 ± 1.0	48 ± 25	30 ± 8	this work
4L-65	0.4 ± 0.1	1.4 ± 0.2	63 ± 4	49 ± 7	this work
3L-22	0.6-10.0	-0.4 ± 0.7	97 ± 12	59 ± 7	this work

The data of the wetting balance test for stack 4L-65 shows very small deviations across all samples, yielding $\alpha_{WB} = (63 \pm 4)°$. This result is slightly higher than the values of the optical measurement $\alpha_O = (49 \pm 7)°$. A similar trend is found for samples with the thin stack 3L-22 with $\alpha_{WB} = (97 \pm 12)° > \alpha_O = (59 \pm 7)°$. For this sample, the wetting force is much more fluctuating, resulting in higher deviations within α_{WB}. In literature, it has also been reported that the Wilhelmy plate methods yields higher contact angles than the static optical measurement [223].

For a reliable evaluation of the two methods, some systematic differences have to be considered: In general, the course of the force curves strongly depends on the involved materials. For example, the solid content of the flux influences the wetting force [220]. For the OCA measurements, a no-clean non-rosin flux with a solid content of $\sim 2\,\%$ is used, whereas the samples for the wetting balance are fluxed with another flux with a solid content of $\sim 6\,\%$. This should influence the measurement results but is not further investigated in this study. The OCA measurements are carried out with Sn60Pb40 at a temperature of 250 °C, whereas for the tests with the wetting balance Sn63Pb37 at 230 °C is chosen. The alloy as well as the bath temperature influences the maximum force [222, 224, 225].

Another difference is the heating of solder and sample. During the OCA measurement, the solder becomes liquid by contacting the heated sample. Since the sample is heated to 250 °C before the solder is in contact, the surface may change (*e.g.* oxidize). In the wetting balance, the sample is indirectly heated by contacting the solder bath. Normally,

[1] In this context, the index "O" for *optical* is added to α_O to distinguish between the two methods.

the bath is much larger than the sample so that influences of the sample on the bath can be neglected. However, dissolution of metals in the bath are very likely, especially for Cu and Ag.

Characterization of wettability using the wetting balance is error-prone, as has been discussed in literature [173,224]. This conclusion has also been reported by Moyer *et al.* in 2009 and Wendt *et al.* in 2011 for Si solar cells [220, 226]. For a PERC cell architecture, the electrodes (front busbars, rear pads) are local screen-printed structures, consisting of a sintered Ag metallization paste (*cf.* Section 2.1.3). To not harm the solar cell, a wetting test has to be performed locally. Beside the OCA measurement, another setup of the wetting balance could be used. In this, a piece of solar cell with metallization is attached to a liquid solder ball. The advantage of a dynamic characterization with a wetting balance over the static OCA test is the access to time-dependent data, allowing to simulate the soldering process. However, this method shows a wide spreading of the data[2] and could not be easily implemented as a fast characterization tool for the wettability of the solar cell electrodes.

Relevant Stacks for Soldering

Regarding wettability of sputter-coated Al foils, the sputter stacks listed in Table 6.2 should be considered for further evaluations.

Table 6.2.: Collection of the most promising sputter stacks evaluated by wetting tests with liquid Sn60Pb40 at 250 °C.

Stack	Layer	Thickness d_i (nm)	Opt. contact angle α (°)	Remark
4L-65	Cr/NiCr/Ag/Cu	10/23/30/2	49 ± 7	Ref. with Cu
3L-63	Cr/NiCr/Ag	10/23/30	30 ± 8	Ref. w/o Cu
3L-22.6	NiCr/Ag/Cu	6.9/15/0.7	36 ± 6	
3L-22	NiCr/Ag/Cu	10/10/2	59 ± 7	"Thin stack"
2L-53	NiCr/AgCu	23/30	24 ± 4	2-layer stack

For short soldering times as used in PV, the thickness of the sputter stack can be reduced to below 50 nm. However, a solderable top layer of a minimum thickness of 15 nm to 20 nm should be sputtered on top. Considering these findings, Al foils can be made solderable by thin sputter stacks. The strength of this solder connection is investigated in the following section.

[2]The lower the wettability of the surface, the greater are the deviations within one measurement (*cf.* stack 3L-22 and 3L-42 in Figure A.12 c) and d)).

6.2. Mechanical Properties

The samples for the investigation of the peel strength are prepared by manual soldering. Onto the 200 µm thick sputter-coated Al foils, at least five Cu ribbons with Sn62Pb36Ag2 coating are soldered in parallel over a length of $\sim$ 150 mm each (*cf.* Section 3.3.2). The evaluation of the 90° peel force shows that the manual sample preparation strongly influences the results of the measurement. For the majority of the measurements, a standard deviation of $\sim 2\,\mathrm{N/mm}$ is found over the peeling length of 150 mm.

A summary of all results of the peel strength of solder joints on sputter-coated Al foils is given in the appendix in Figure A.13. Each data point represents the characterization of one foil, coated with a certain stack (color code). The graph illustrates the strong inherent variation of the data due to manual sample preparation and the large systematic measurement errors. The following sections focus on trends found and will show extractions of these data. The color code for the sputter stacks, introduced in the previous section, will be used continuously.

6.2.1. Dependence of Adhesion on Layer Thickness

The FoilMet® approach must be an economically viable alternative to the current PERC cell technology. This means that the coating of the Al foil must be kept at a competitive cost. Sputtering, as a deposition process, has not only an expensive vacuum chamber but also a comparatively low rate of deposition. By keeping the sputtered films as thin as possible, less material and higher throughput velocities can be achieved which drives the costs down only then making the sputtered solderable layer system a financially viable option.

Previous work at Fraunhofer ISE on vacuum insulation glazing has shown that a stack with a total thickness of 300 nm, consisting of Cr/NiCr/Ag with 100/100/100 nm layer thickness provides good solderability regarding wetting and mechanical strength of the joints [227]. The solder joints were formed by oven soldering for 20 min to 30 min using an Sn-based solder alloy. Within this work, this sputtered solderable and functional stack is used as a starting point and tested on Al foils, targeting to reduce the total thickness d of the stack as much as possible.

In Figure 6.4 on the left, the measured peel force is shown for different thicknesses of each layer of the stack Cr/NiCr/Ag. For increasing layer thickness of NiCr (x-axis), the strength of the joints increases. Two trends for stacks with fixed Cr and Ag layers are depicted by the dark blue ($10/d_{\mathrm{NiCr}}/10$ nm) and green ($50/d_{\mathrm{NiCr}}/50$ nm) lines. The thickness of Cr and Ag play a minor role for the adhesion (*cf.* peel force at a fixed NiCr thickness). The thicker the total thickness d of the stack and the NiCr layer d_{NiCr}, the less influence of each layer thickness on adhesion is measured.

The graph on the right in Figure 6.4 shows the stack NiCr/AgCu. Two changes of the materials are made: First, the Cr layer is omitted due to its low impact on the performance if the NiCr layer is thick enough ($d_{\mathrm{NiCr}} \geq 23\,\mathrm{nm}$). Second, a small amount of Cu is added to the top layer: Ag98Cu2. Investigations in other internal work have shown that this prevents agglomeration of the top Ag layer upon heating (*cf.* Figure A.14 in the appendix). Within this thesis, it has been found that the exact amount of Cu does not

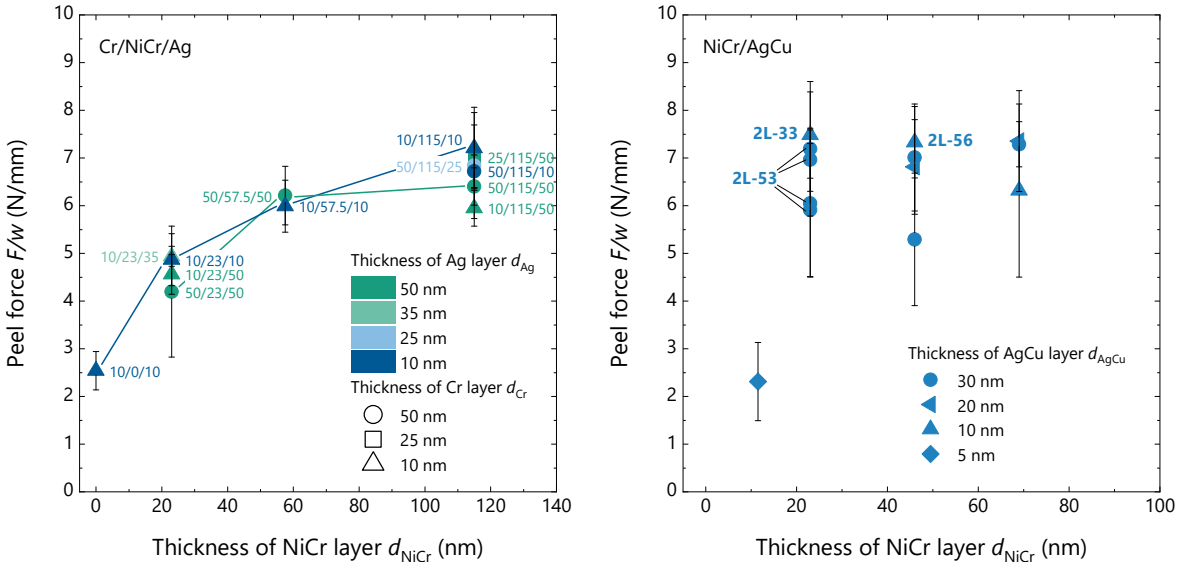

Figure 6.4.: Peel force measurement of sputter-coated Al foils. Each data point includes mean and standard deviation of at least five tests. Left: Three-layer stack Cr/NiCr/Ag. Right: Two-layer stack NiCr/AgCu.

influence the peel strength after soldering (*cf.* Figure A.14 bottom right). To preserve the excellent wettability of the Ag layer as long as possible, only 2 $\%_{wt.}$ Cu are added.

Within the measurement uncertainties, no change in adhesion has been found for all combinations of the NiCr/AgCu system, neither at 23 nm to 69 nm layer thickness of NiCr, nor for the 10 nm to 30 nm thick AgCu layers. The diamond symbol represents the stack NiCr/AgCu with 11.5/5 nm, yielding (2.3 ± 0.8) N/mm. Probably, the thickness of the solderable AgCu layer, as well as the total thickness are too thin to yield force values comparable to the other stacks. In accordance to the results found for wettability, the solderable top layer has to be 15 nm to 20 nm thick to provide high peel forces between 5 N/mm and 8 N/mm. In general, the peel forces found for sputter-coated Al foils are on a very high level and most likely, a peel force of about 2 N/mm would also be sufficient to form a reliable solder joint. These findings are in agreement to literature [145]. Only a few of the investigated sputter stacks show peel forces lower than 2 N/mm (*cf.* Figure A.13 and A.14).

6.2.2. Fracture Mechanism of Solder Joints

The fracture pattern of the soldered and peeled samples nearly looks the same for all samples under investigation. In accordance to the high peel forces, a mixed fracture pattern is found by the analysis of SEM top view images. An example of the two-layer system NiCr/AgCu with 10/30 nm is presented in Figure 6.5.

All images are taken in top view mode and show details of the sample surface after the 90° peel force measurement. In a), the whole width of the fracture after peeling the

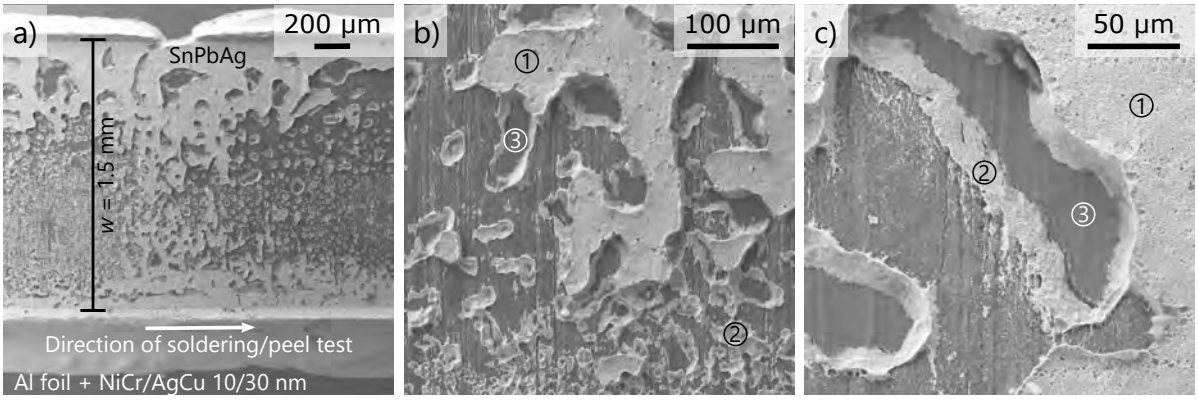

Figure 6.5.: SEM images (top view, 20 kV) of the fracture pattern after the peel force measurement. A solder joint on a 200 µm thick Al foil, sputter-coated with NiCr/AgCu with 10/30 nm is characterized. The analysis of the fracture reveals a mixed fracture pattern.

ribbon (width $w = 1.5\,\mathrm{mm}$) is shown. The brighter parts correspond to remnants of the SnPbAg solder, the darker parts show the sputter-coated Al foil. To understand the failure mode in detail, it would be interesting to identify the weakest interface. However, due to the thin sputter coating, it is not possible to make a reliable statement on the interface Al/coating/solder. In the enlargements in b) and c), at least three main failure modes can be identified: an adhesive failure on top of the solder at the interface to the Cu core of the ribbon (①), a cohesive failure within the solder (identified by solder remnants, ②) and finally an adhesive failure at the solder/NiCr interface or at the NiCr/Al interface (③). For the latter, the interface of failure can not be identified, although EDXS is conducted. At some positions, no remnants of solder are found on the Al foil, which could also be a hint to insufficient wetting or flux remnants, leading to organic inclusions.

6.2.3. Solder Joint Adhesion after Isothermal Aging

The long-term stability of the solder joints at elevated temperatures is tested by isothermal aging of the joints at 85 °C at ambient air. For this investigation, five different sputter stacks are chosen. The results are presented in Figure 6.6.

The reference system Cr/NiCr/Ag with 10/23/30 nm (black triangles) stays stable at about 5 N/mm over the whole aging time of 1500 h. The same sputter stack but with additional 2 $\%_{\mathrm{wt.}}$ Cu within the AgCu top layer (light green triangles) starts at the same force level. Within the first 500 h, the force decreases to 3.5 N/mm and stabilizes. This effect may be due to the additional Cu, promoting phase formation at the interface which probably leads to oxidation from the edges and a loss in adhesion.

Comparing the other four-layer stacks (squares), two main findings can be made. All stay on a similar force level, whereas the stack with Cu/Ag (gray square) yields the highest values. No significant difference between a Cu top layer of 4.5 nm or 1.5 nm thickness could be measured (green squares). In addition, it is not possible to compare

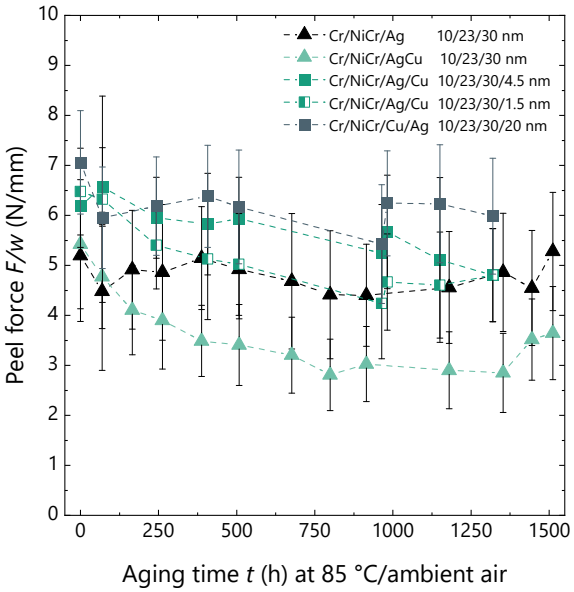

Figure 6.6.: Peel force measurement of sputter-coated Al foils after isothermal aging at 85 °C at ambient air. The 200 µm thick Al foils are coated by sputtering with different stacks (legend). The solder joints are formed by manual soldering of Sn62Pb36Ag2-coated Cu ribbons with no-clean flux. Each data point represents mean and standard deviation of ten peel force measurements.

this very thin Cu thickness with the amount of Cu provided by the AgCu alloy. Therefore, no clear statement could be made.

One sample of the group Cr/NiCr/Ag/Cu 10/23/30/4.5 nm (green squares) was aged at 85 °C for 1800 h in total (not shown here) and additionally stored for about a year (9300 h) at RT and ambient air. The peel force measurement of ten ribbons yields (5.3 ± 0.9) N/mm, confirming very reliable solder joints.

The peel force of the solder joints on all four sputter stacks at least stay above 3 N/mm within 1500 h of aging. This indicates no critical interface which would cause failure within the joint. The differences in the sputter stacks mainly result from the top layer (since the Cr/NiCr layers are kept constant) and from manual sample preparation. Due to the low thickness of the stacks, the failure could not be analyzed on microstructural level in detail.

Selected Stacks for Strong Solder Joints

Regarding peel strength of solder joints on sputter-coated Al foils, a variety of stacks could be used for the desired application on solar cell rear sides. The following table summarizes the most promising combinations, regarding layer thickness (as thin as possible while maintaining adhesion) and high peel forces.

Table 6.3.: Collection of the most promising sputter stacks evaluated by 90° peel force measurements after soldering with Sn62Pb36Ag2.

Stack	**Layer**	**Thickness** d_i (nm)	**Peel force** F/w (N/mm)	**Remark**
4L-65	Cr/NiCr/Ag/Cu	10/23/30/2	5.0 ± 0.6	Reference with Cu
4L-64.5	Cr/NiCr/Ag/Cu	10/23/30/1.5	6.6 ± 0.1	
4L-43.5	Cr/NiCr/Ag/Cu	10/23/10/0.5	4.3 ± 0.7	
3L-63	Cr/NiCr/Ag	10/23/30	6.9 ± 0.7	Reference w/o Cu
3L-22.6	NiCr/Ag/Cu	6.9/15/0.7	4.8 ± 0.1	
3L-22	NiCr/Ag/Cu	10/10/2	3.3 ± 0.5	"Thin stack"
2L-53	NiCr/AgCu	23/30	6.5 ± 1.3	

Isothermal aging of several stacks has shown to be uncritical for the mechanical strength of the solder joints, as well as storage tests of the soldered samples for a couple of month at ambient air and RT. Some stacks show a slight loss in adhesion, most likely due to oxidation but all stabilize at a very high force level of $\geq 3\,\mathrm{N/mm}$.

6.3. Microstructure of Cross Sections

To gain a deeper understanding of the reasons behind the measured results (s. Section 6.1 and 6.2) of the solder joints on the most interesting sputter stacks, the relevant interfaces are analyzed by means of cross sections. By using optical, scanning electron and transmission electron microscopy, the following scientific questions should be answered:

- How does the sputter stack look like after soldering? Which layers are still visible and which layers dissolve within the solder?
- Which layer of the stack promotes the strong adhesion after soldering?
- Which (intermetallic) phases are formed at the interfaces?
- Does Al or oxygen diffusion occur?
- How does the interface Al/Cr look like?

Figure 6.7 a) shows the involved materials for a solder joint on a sputter-coated Al foil in a cross section view. The solder (here alloy Sn62Pb36Ag2) of the Cu ribbon contacts the sputter layer 4L-67.5, consisting of Cr/NiCr/Ag/Cu with a thickness of 10/23/30/4.5 nm for the presented microscopy image in Figure 6.7 b). The region of interest is marked with a white rectangle. The solder joint along the interface appears homogeneous and void-free. On the right hand side of the image, the good wetting (small contact angle, *cf.* Figure A.11) can be clearly observed. The 4-layer stack used here has a total nominal thickness of about 68 nm, which makes it hard to identify or even quantify different layers. Electron microscopy allows for a detailed analysis at a higher magnification.

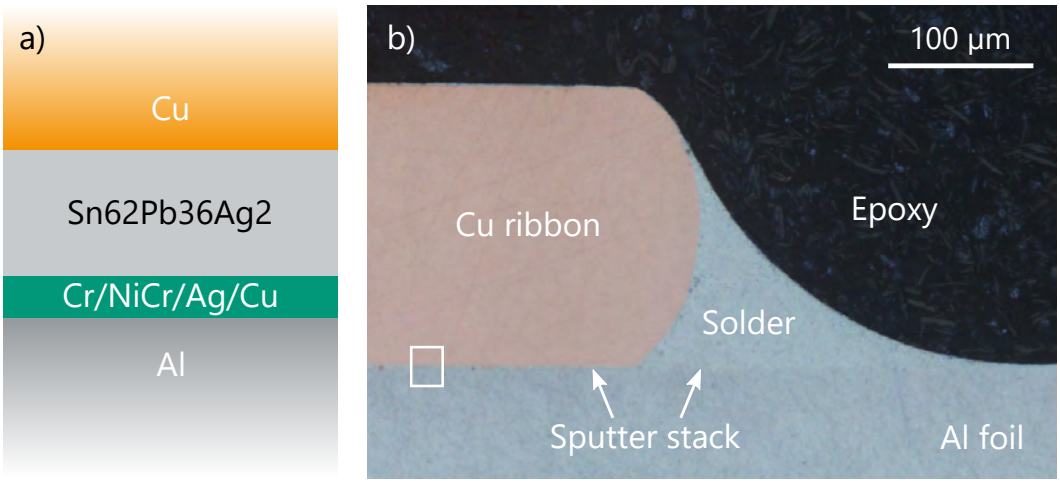

Figure 6.7.: Solder joint on sputter-coated Al foil in a cross section view. a) Sketch of the involved materials (not so scale). b) Optical microscopy image of an embedded solder joint (Sn62Pb36Ag2) on a 200 µm thick Al foil, coated with Cr/NiCr/Ag/Cu of 10/23/30/4.5 nm thickness.

6.3.1. Initial Assessment of Solder Joints by SEM

To avoid damaging of the delicate interface by mechanical polishing, a cross section of the solder joint is prepared by ion beam polishing. Figure 6.8 shows the corresponding SEM cross sections with increasing magnification from left (a) to right (c), using 5 kV acceleration voltage and the InLens detector to obtain a high material contrast. The Pb-rich phases of the solder seem to be contracted within the Sn matrix. This effect has been observed already for temperature-sensitive materials during the ion polishing process [228]. Heat, which is generated by the ion beam irradiation during ion milling, causes thermal deformation and could be avoided by *e.g.* active sample cooling. This effect does not influence the interface of interest, marked with the white rectangle.

Figure 6.8 c) shows the Sn/Al interface with the solderable sputter stack (nominal thickness 68 nm) on top of the foil. Directly on top of this layer, a prominent phase formation can be found. The observed features do not form a uniform layer and show local thickness variations between 100 nm and 200 nm. The magnification as well as the resolution of the used SEM setup restrict a reliable quantification of the present phases. Additionally, the involved materials (*i.e.* Sn, Pb) feature large atomic numbers, whereas high acceleration voltages > 15 kV are required for element mappings. This in turns may lead to a drift during the EDX measurement occurring for long measurement times.

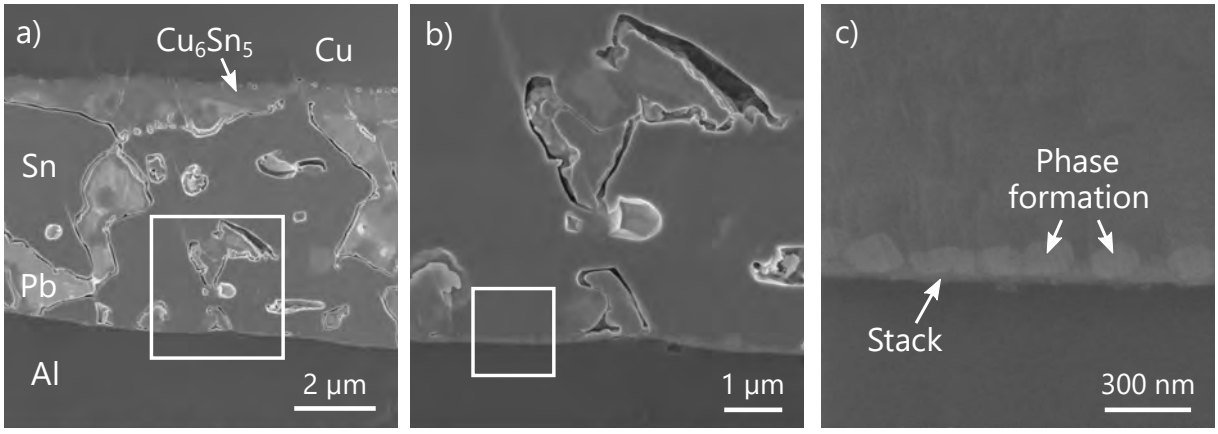

Figure 6.8.: SEM cross section images after ion-polishing (5 kV, InLens detector). Sn62Pb36Ag2-coated Cu ribbon, soldered on top of sputter-coated Al foil. The sputter stack (4L-67.5: Cr/NiCr/Ag/Cu 10/23/30/4.5 nm) can be estimated in c).

6.3.2. Characterization of Interfaces by TEM

To get insights into the interfacial reactions, a TEM analysis is performed for solder joints on two different sputter stacks:

- Sputter stack **4L-114**: Cr/NiCr/Ag/Cu with 10/50/50/4 nm layer thickness
- Sputter stack **3L-22**: NiCr/Ag/Cu with 10/10/2 nm layer thickness

The first one, 4L-114 with a nominal thickness of 114 nm, serves as "thick reference stack" to study the interfacial reactions in detail. The second stack (nominal thickness 22 nm) is one of the most promising thin sputter stacks, evaluated by OCA and peel force measurements (see Sections 6.1, 6.2). In Figure 6.9 a), four TEM bright field images are amalgamated to exhibit a total length of 4.4 µm allowing to show the interfaces of the sputter stack 4L-114.

The light gray region in the lower part of the images shows the Al foil substrate, which appears bright in TEM BF mode. With $m_{\mathrm{Al}} = 27\,\mathrm{u}$, Al is the lightest element involved in this sample (beside oxygen), so that most of the electrons of the incident beam are directly transmitted (*i.e.* unscattered) into the detector. In the upper half of the images, several regions of various brightness and structure can be found. A harsh edge of those regions indicate a change in crystal orientation or rather the end of the crystal. This leads to the assumption of several different phases present in the region above the sputter stack, correlating to the SEM image shown in Figure 6.8 c). This "band" of phases is much thicker than the remaining (visible) part of the sputter stack.

The interfaces solder/stack/Al are enlarged in Figure 6.9 b) and c). The actual thickness d is measured at five positions within each image, yielding $d = (67.5 \pm 3.3)\,\mathrm{nm}$, which is 41 % thinner than the nominal value of $d = 114\,\mathrm{nm}$. The measurements are done vertically, disregarding a possible rotation of the sample. As already explained earlier, it is reasonable that most of the top layers (Ag, Cu) diffuse into the solder and the visible

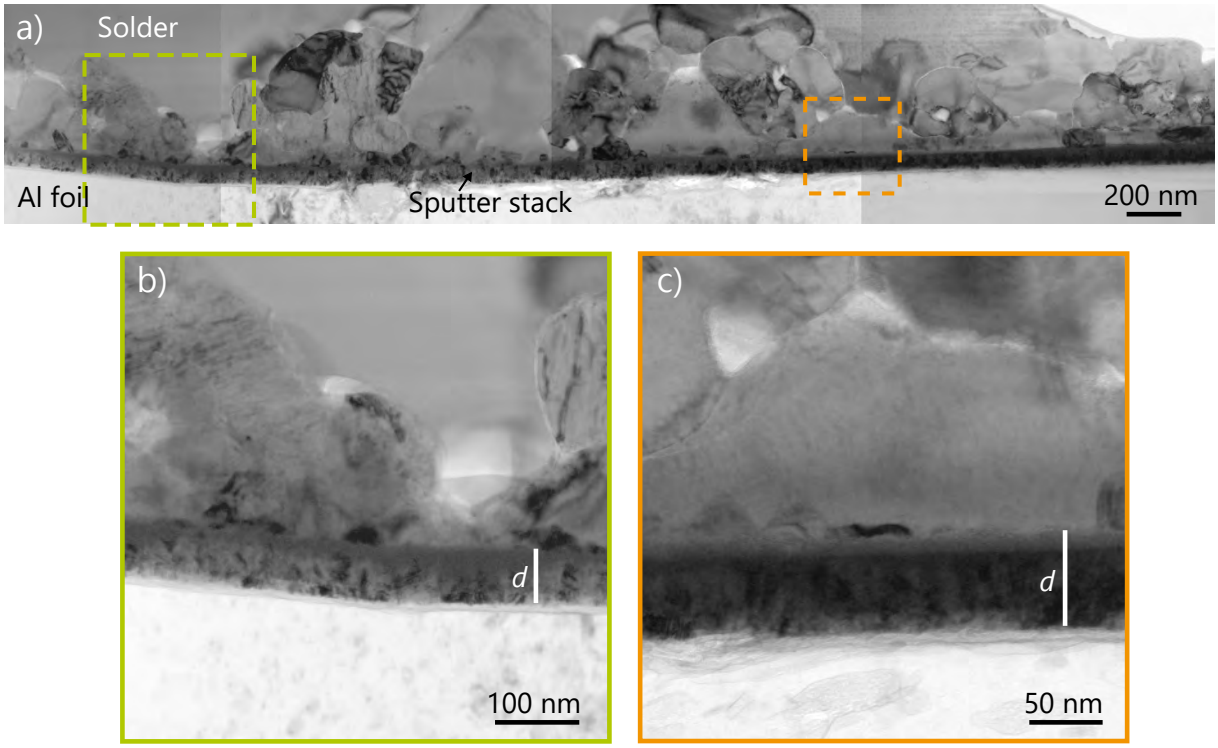

Figure 6.9.: a) TEM bright field images (four consecutive images) along the interface with the solder joint on the sputtered layer: Cr/NiCr/Ag/Cu with a nominal thickness of 10/50/50/4 nm. b) and c) show close-ups for two different positions.

edge of the stack is the NiCr layer ($d_{\mathrm{Cr}} + d_{\mathrm{NiCr}} = (60 \pm 6)\,\mathrm{nm}$). Nevertheless, Ag has a similar atomic mass to Sn ($m_{\mathrm{Ag}} = 108\,\mathrm{u}$, $m_{\mathrm{Sn}} = 119\,\mathrm{u}$), whereas both layers are difficult to distinguish within the TEM BF image. The element distribution at the interface will be analyzed by EDX(S) in Section 6.3.3.

During magnetron sputtering, columnar growth of the film may take place, depending on the deposition pressure and temperature. Figure 6.9 b) and c) show the poly-crystalline structure of the sputter stack since the contrast in TEM BF mode indicates different crystal orientations. It is also striking that the total stack seems to consist of two different regions (top and bottom part). This could rather indicate a difference in material or orientation.

The solder joint on top of the thin sputter stack 3L-22 (NiCr/Ag/Cu with 10/10/2 nm), is shown in the TEM BF images in Figure 6.10 a) for a total length of approximately 4.2 µm along the interface. The general appearance of the image is similar to the thick stack in Figure 6.9, consisting of Al foil, sputter stack and phases built at the interface. Figure 6.10 b) and c) show two positions of the interface at higher magnification. The presence of the thin stack could be assumed but is difficult to quantify here. Conspicuous is the additional difference in contrast within the Al foil, along the direction of the interface, clearly visible in Figure 6.10 b). Since the difference in contrast is small compared to Al, it is assumed that an additional structure with a similar crystal orientation and atomic

mass is present, *e.g.* an amorphous Al_2O_3 layer. It is also possible that those grains forming this additional layer are tilted, which generates a contrast difference in the BF image.

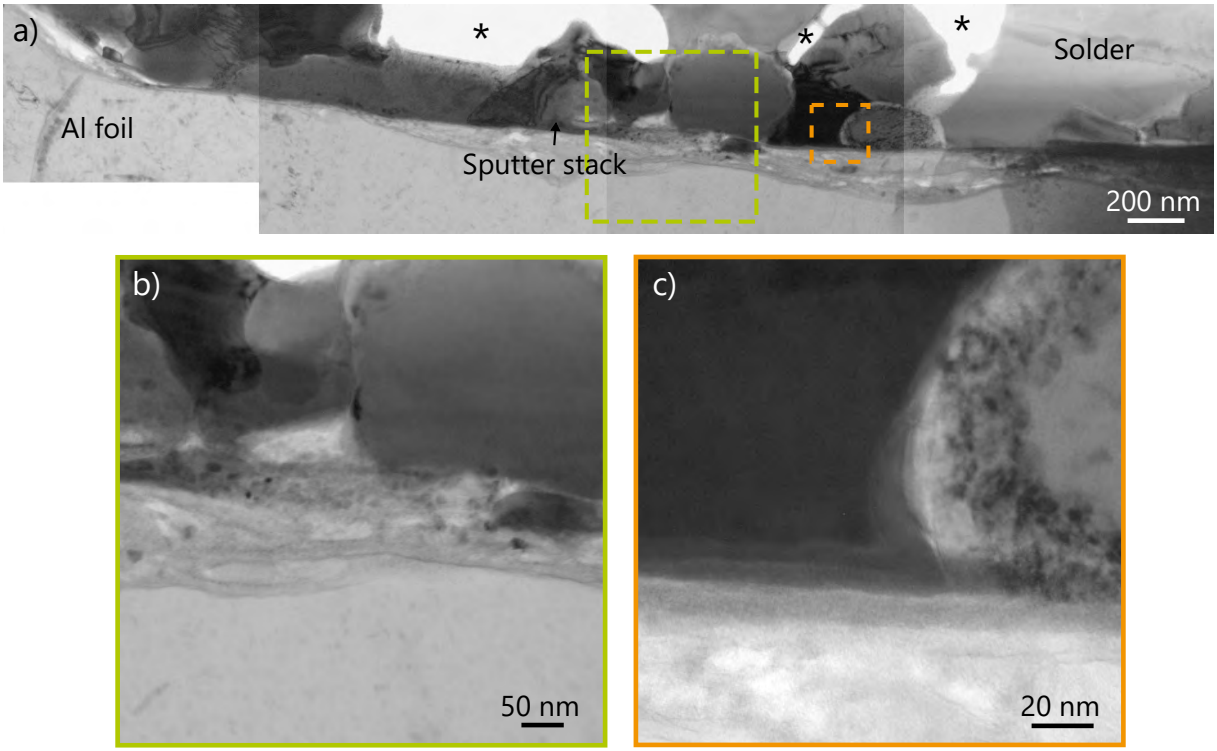

Figure 6.10.: a) TEM bright field images (four consecutive images) along the interface with the solder joint on the sputtered layer: NiCr/Ag/Cu with 10/10/2 nm. At the positions marked with a star ($\star$), the lamella features holes caused by FIB milling. b) and c) show close-ups for two different positions.

6.3.3. Analysis of Different Layer Functionality by EDXS

In TEM mode, EDX is much more accurate than in combination with a conventional SEM, because the lamella is very thin (mostly $d < 50\,\text{nm}$) and therefore the excitation volume is much smaller. This requires a longer measurement time due to less signal, but provides results with a much higher resolution than for conventional EDX.

Figure 6.11 presents an image taken in STEM HAADF mode of the TEM sample with the thick sputter stack 4L-114. The interfaces along the stack are shown. In the DF mode, elements with high atomic number are more diffracted than lighter elements, therefore appear brighter. The element distribution at the interfaces is quantified by EDX. The investigated area is marked with a rectangle. Additionally, several positions are marked with letters A-H, quantified by EDXS as well. The results of the EDX analysis are presented in the following.

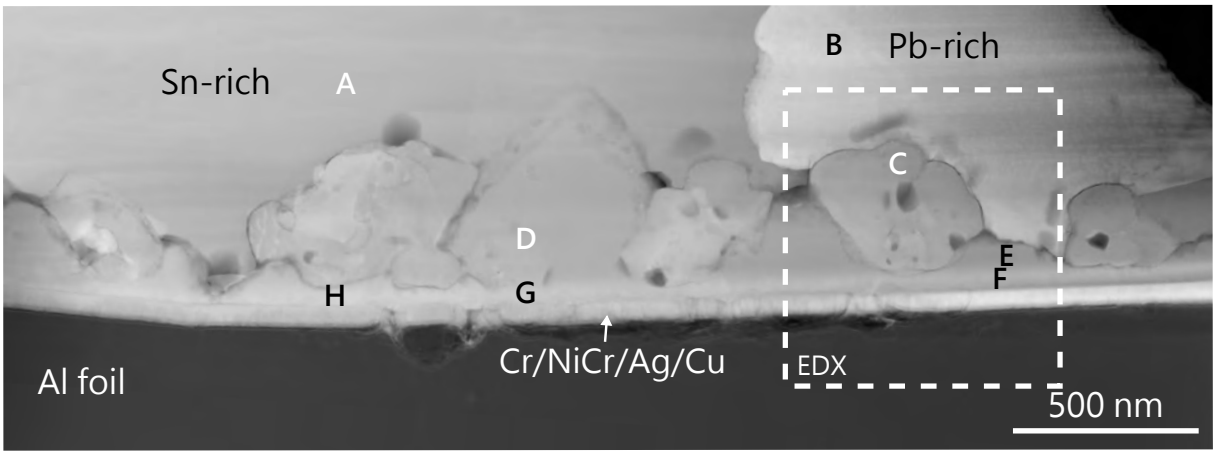

Figure 6.11.: STEM HAADF image of the interface of the solder joint on the sputtered layer 4L-114: Cr/NiCr/Ag/Cu with a nominal thickness of 10/50/50/4 nm. Several positions are marked with letters A-H. Their exact composition is listed in Table 6.4.

Element Quantification of Interfacial Phases

Figure 6.12 shows two line scans perpendicular to the surface normal of a solder joint on the thick stack 4L-114. The image on the left, taken with STEM HAADF mode, displays the region marked in Figure 6.11, mirrored vertically. Within the Pb-rich region in the top left of the image, horizontal features are visible, which are due to the preparation of the lamella by FIB. This effect is called curtaining [176] and does not remarkably influence the information provided by the TEM images. Both line scans are conducted for an evaluation width of about 150 nm. Line scan 1 clearly shows the two bottom layers of the 4-layer stack: Cr (yellow) at a peak position of $x \approx 87\,\mathrm{nm}$ and NiCr (cyan & yellow) at a peak position of $x \approx 104\,\mathrm{nm}$, whereas the NiCr peak is broader, as expected.

The **NiCr layer** consists of $80\,\%_{\mathrm{wt.}}$ Ni and $20\,\%_{\mathrm{wt.}}$ Cr. The conversion into atomic percent using Equation A.9 yields Ni = $78.0\,\%_{\mathrm{at.}}$ and Cr = $22.0\,\%_{\mathrm{at.}}$. This corresponds to a Ni:Cr ratio of 3.5:1.0. The calculation of the Ni:Cr ratio out of the measured concentration c_{i} is 3.0:1.0 for line scan 1 and 2.9:1.0 for line scan 2. This implies a marginal diffusion of Ni into the solder, whereas Cr stays constant. Other quantification of the NiCr layer of the sputter stack along the whole sample yield similar values, partially perfectly matching the ratio of 3.5:1.0, indicating no atomic change within the layer.

Both line scans reveal thin **oxygen layers** (light khaki) present at the interfaces below and above the sputter stack. Before sputtering, plasma etching is used to clean the surface and partially remove the native Al_2O_3. Without breaking the vacuum, the layers are deposited. Nevertheless, a thin oxygen layer remains apparently. The quantification of line scan 2 at $x \approx 118\,\mathrm{nm}$ yields $(24.3 \pm 0.5)\,\%_{\mathrm{at.}}$ Al and $(33.7 \pm 1.0)\,\%_{\mathrm{at.}}$ O. This ratio of 1.0:1.4 suggests the present layer to be native Al_2O_3 (ratio 1.0:1.5), existent before sputtering the first layer (Cr) of the stack. The thickness is supposedly $< 5\,\mathrm{nm}$, also indicating a native oxide layer.

The second accumulation of oxygen arises on top of the NiCr layer at $x \approx 129\,\mathrm{nm}$ (line

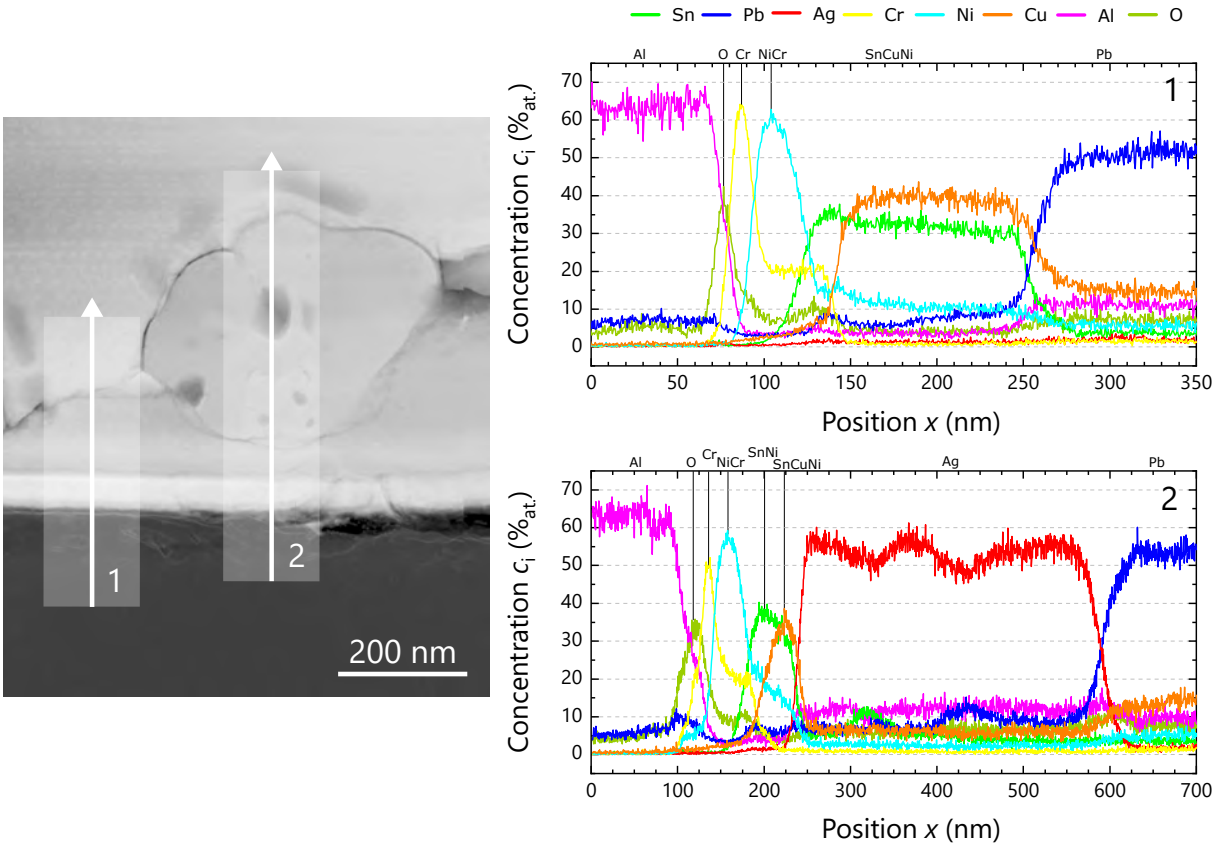

Figure 6.12.: TEM DF image with two EDX line scans across the interface of stack 4L-114 showing the composition and the involved materials. Evaluation width of each line scan: 150 nm.

scan 1) and $x \approx 178$ nm (line scan 2). One possibility may be the formation of a thin layer of oxygen after sputtering and before soldering (although the samples were stored in nitrogen). During this time period, the top layers Ag/Cu with 50/4 nm thickness may oxidize. Most likely, Cu does not form a homogeneously closed layer. Ag is permeable for oxygen, whereas the oxide layer forms on top of the NiCr layer. Further diffusion of O into the NiCr layer or a binding to Cr is also likely. In both line scans, a ratio of 1.0:0.5 for Cr:O is found, which leads to the assumption that metallic Cr does no longer exist, but oxidic Cr within these several nm.

Spacial Distribution of Elements at the Interface

An EDX mapping of the same region of the sample is presented in Figure 6.13 with the same color code for the elements. A lamellar-like oxide layer below the sputter stack is clearly visible, as well as a marginal O accumulation on top of the NiCr layer. This thin layer correlates well with an interruption within the Ni map (cyan) on top of the stack.

The mapping as well as the line scans do also reveal information on the region above the sputter stack. First, a **SnNi dominating phase** in the form of an homogeneous layer for about 20 nm thickness is present, consisting of $\sim 35\,\%_{at.}$ Sn and $\sim 15\,\%_{at.}$ Ni.

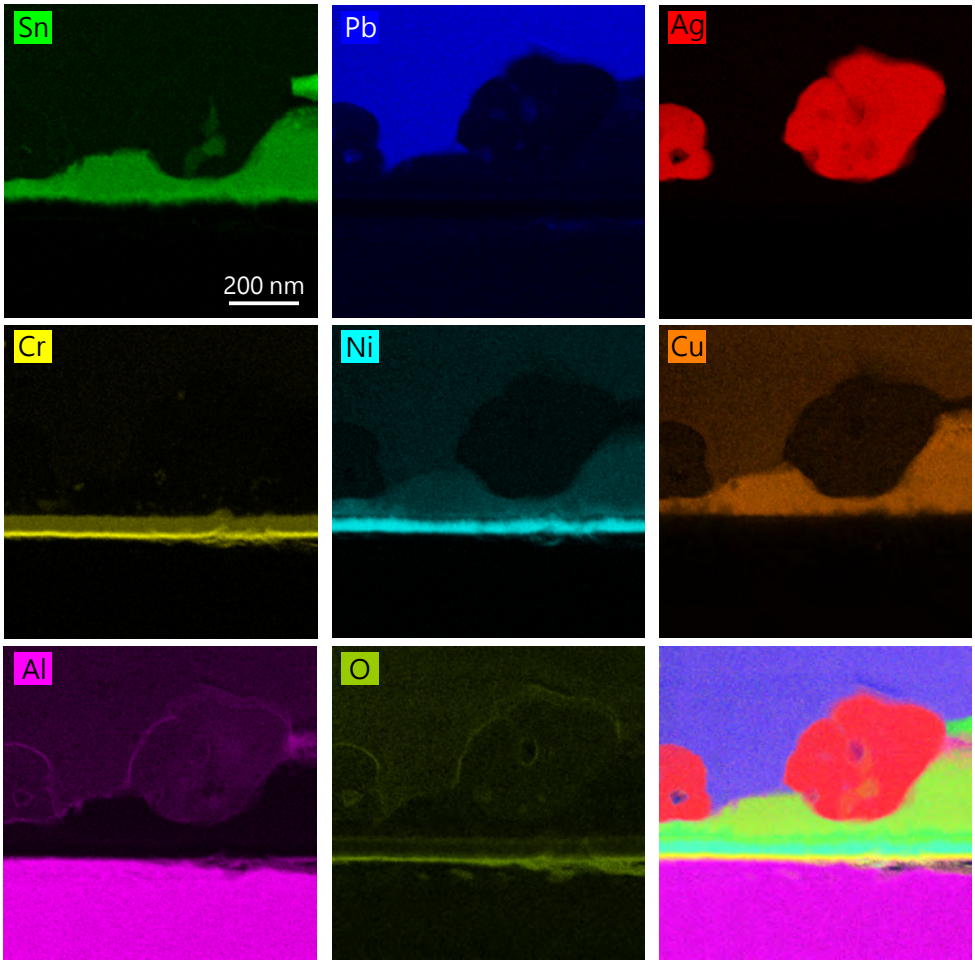

Figure 6.13.: EDX mapping of a solder joint on Cr/NiCr/Ag/Cu sputter-coated Al foil, with a nominal thickness of 10/50/50/4 nm of the 4-layer sputter stack 4L-114. The presented section can be found in Figure 6.11 and Figure 6.12.

In Figure 6.11, this band is marked with **F** and the corresponding quantification is listed in Table 6.4. At a Sn/Ni interface, three phases can form: Ni_3Sn, Ni_3Sn_2 and/or Ni_3Sn_4, which are all stable at RT (for more information, see Figure 2.9 (phase diagram of NiSn)). The dominating phase is Ni_3Sn_4 in a Sn-rich environment [229]. Nevertheless, the quantification of the Sn-rich band along the interface let suppose none of those stoichiometries to be present. Additional analysis at point **G** yield similar concentrations for Sn and Ni. The soldering time (*e.g.* the time above the liquidus temperature of the SnPbAg solder) was very short ($< 5\,s$), whereas the formation of defined (intermetallic) phases in the liquid state is unlikely [229]. It is supposed that most of the phases built by solid state diffusion after soldering at RT. Another possibility is phase formation during cooling. However, for a fast cooling rate ($40\,K\,s^{-1}$ to $100\,K\,s^{-1}$) as used here, a layer thickness of Ni_3Sn_4 far below $1\,\mu m$ is expected [229]. Only at point **H**, where the phase is more prominent, a ratio of Ni:Sn with 1.0:1.2 matches the stoichiometry of the Ni_3Sn_4 IMC (1.0:1.3).

Table 6.4.: Element quantification at eight different positions of the solder joint on the thick sputter stack 4L-114, marked within Figure 6.11. Data is extracted from corresponding line profiles. The measurement accuracy is limited to ±5 % relative.

	Concentration c_i(%$_{at.}$)						
	Sn	**Cu**	**Ni**	**Ag**	**Pb**	**Al**	Phase
A	37	28	-	-	-	-	Sn-rich
B	-	32	-	-	42	-	Pb-rich
C	< 4	-	-	55	< 9	12	Ag-rich
D	36	37	11	-	-	-	SnCuNi
E	32	40	11	-	-	-	SnCuNi
F	35	-	15	-	-	-	SnNi
G	42	-	17	-	-	-	SnNi
H	22	-	18	-	-	-	SnNi

Point **D** and **E** mark the **SnCu-rich region** of the solder joint. A concentration of $\sim 32-36\,\%_{at.}$ Sn, $\sim 37-40\,\%_{at.}$ Cu and $\sim 11\,\%_{at.}$ Ni is found (*cf.* Table 6.4). It is assumed that the IMC crystal structure is the hexagonal η-Cu_6Sn_5 structure [230]. It is known that Ni-free Cu_6Sn_5 transforms from hexagonal η-structure to monoclinic η'-structure on cooling below 186 °C [231,232]. Nogita *et al.* report that $\sim 9\,\%_{at.}$ Ni in the IMC can stabilize the hexagonal structure and therefore it becomes stable at RT [232]. Several analysis of point **D**, **E** and other positions (not shown here) within the SnCu-rich region lead to the assumption of a $Cu_6Ni_1Sn_5$ stoichiometry. The Ni content of about $11\,\%_{at.}$ Ni indicates a hexagonal η-$(Cu, Ni)_6Sn_5$ structure, even at RT. Additional analysis with SAED in STEM mode is performed but could not be evaluated for the present structure. It is supposed that both, the hexagonal (η-$(Cu, Ni)_6Sn_5$) and monoclinic ($(Ni, Cu)_3Sn_4$) crystal structure contribute to the signal, whereas a superposition of differently orientated nanocrystals is measured [233–235].

Obviously, the high amount of Cu in the interfacial region does not only originate from the $\sim$ 4 nm thick top layer of the sputter stack. It is well known that Cu is soluble in molten tin-lead solders [7, 16] and several Cu-Sn IMCs are formed, predominantly at the Cu/solder interface (*cf.* Figure 6.8 a)) [231, 236]. For a temperature of 250 °C, the dissolution rate of Cu in eutectic tin-lead solder is about 0.2 µm/s [16]. For the present sample, soldered for a minimum of 2 s at 250 °C, this would mean 0.4 µm for Cu, 4.0 µm for Ag and <0.1 nm for Ni in Sn [7].[3] The basic contribution of Cu originates from the core of the ribbon supporting the IMC formation in the interfacial region. Additionally, it has to be mentioned that the enhancement of the Cu amount within the **Pb-rich region** ($32\,\%_{at.}$) is a measurement artefact. Due to the large atomic number of Pb ($Z = 82$), some electrons are back-scattered and hit neighboring components within the vacuum chamber as *e.g.* the pole shoe which contains Cu. Those excited X-rays contribute to the

[3]For Ni, the dissolution in eutectic tin-lead solder is rather low. For temperatures above 400 °C, it becomes noteworthy: 10 nm/s at 400 °C and 60 nm/s at 500 °C [7].

signal within the Pb-rich phase. This effect is also observed within the **Sn-rich region** (28 $\%_{\text{at.}}$), but less pronounced due to the smaller atomic number of $Z = 50$ for Sn (*cf.* backscatter coefficient [237]). A concentration gradient of Cu within the solder joint due to dissolution of Cu of the ribbon during the soldering process is very likely but could not be quantified at this point.

As mentioned recently, Ag has the highest dissolution rate (4.0 µm/s) in tin-lead solder compared to the other involved materials. The EDX data supports the assumption that the 50 nm thick Ag layer is completely dissolved within the solder. The mapping in Figure 6.13 as well as line scan 2 in Figure 6.12 show Ag agglomeration along the interface. Preferably, these Ag-rich phases are located between the Sn-rich matrix of the solder and the SnCuNi-rich phases in the interfacial region. An EDX mapping along the whole length of the TEM sample illustrates the distribution of the Ag-rich phases and can be found in the Appendix (*cf.* Figure A.15 and A.16). Quantification of the **Ag-rich regions**, *e.g.* at point **C**, yields $> 50\,\%_{\text{at.}}$ Ag, in combination with Al, Pb and Sn. Since the amount of Sn is negligibly small ($< 4\,\%_{\text{at.}}$ Sn), the presence of the Ag_3Sn IMC is excluded. It is more likely that a solid solution of Ag, Al and Pb is existent here. Within the microstructural analysis of the solder joints on roll-cladded Al in Section 4.3.2, a similar accumulation of Ag close to Al interface has been found (*cf.* Figure 4.8).

6.3.4. Investigation of Ultra-Thin Sputter Stack

The same analysis is conducted with the TEM sample with the thin sputter stack 3L-22: NiCr/Ag/Cu with 10/10/2 nm nominal thickness. In Figure 6.14, the section for EDX mapping and line scans is marked with a white dashed line, as well as several positions A-G for quantification. Due to less material within the sputter stack, it is more challenging to understand the interfacial reactions and quantify the present phases for this sample, whereas the EDX mapping is the most inspiring method.

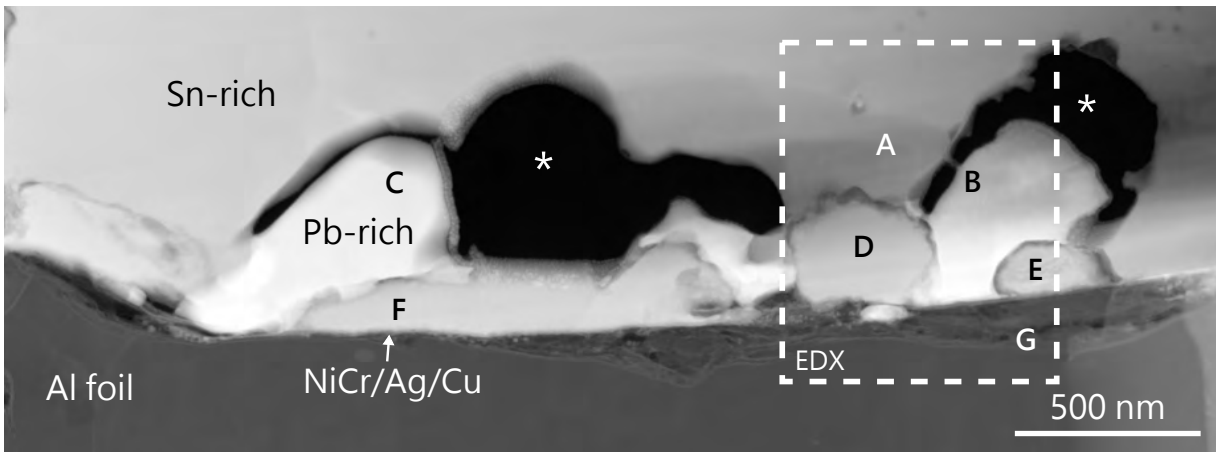

Figure 6.14.: STEM HAADF image of the interface of the solder joint on the sputtered layer 3L-22: NiCr/Ag/Cu with a nominal thickness of 10/10/2 nm. Several positions are marked with letters A-H. Their exact composition is listed in Table 6.5. At the positions marked with a star ($\star$), the lamella features holes caused by FIB milling.

Spacial Distribution of Elements at the Interface

Figure 6.15 shows the mappings for the involved elements.[4] The presence of **oxygen** within the top 100 nm of the Al foil is conspicuous. Compared to the quality of the solder joint on the thick stack, more oxygen seems to be present. Since both samples are prepared identically, one could assume that not only the native Al_2O_3 layer contributes to this layer, but also oxidation of the Al surface by oxygen diffusion through the thin stack, within the time period between sputtering and soldering ($\sim$ 30 d). The corresponding line scans 1 and 2 in Figure 6.16 support this assumption since the ratio of Al:O does not match 1.0:1.5 (as for Al_2O_3). The results of a quantitative evaluation at point **G** are listed in Table 6.5.

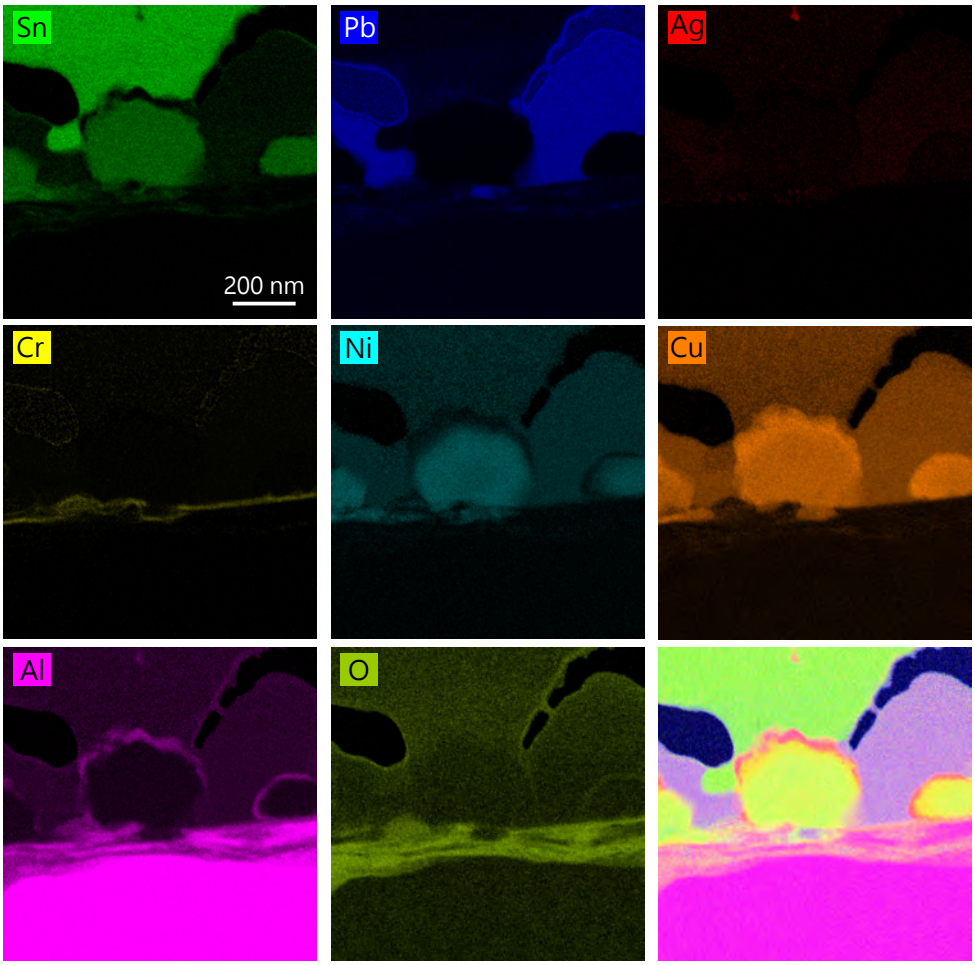

Figure 6.15.: EDX mapping of a solder joint on NiCr/Ag/Cu sputter-coated Al foil, with a nominal thickness of 10/10/2 nm of the 3-layer sputter stack. The presented section can be found in Figure 6.14 and Figure 6.16.

In contrast to the first TEM sample with stack 4L-114, the **NiCr layer** is no longer present as-deposited. Within the EDX map of Cr (yellow) in Figure 6.15, a thin Cr layer

[4] In the appendix, Figure A.17 shows an EDX mapping over the whole length of the sample along the interface.

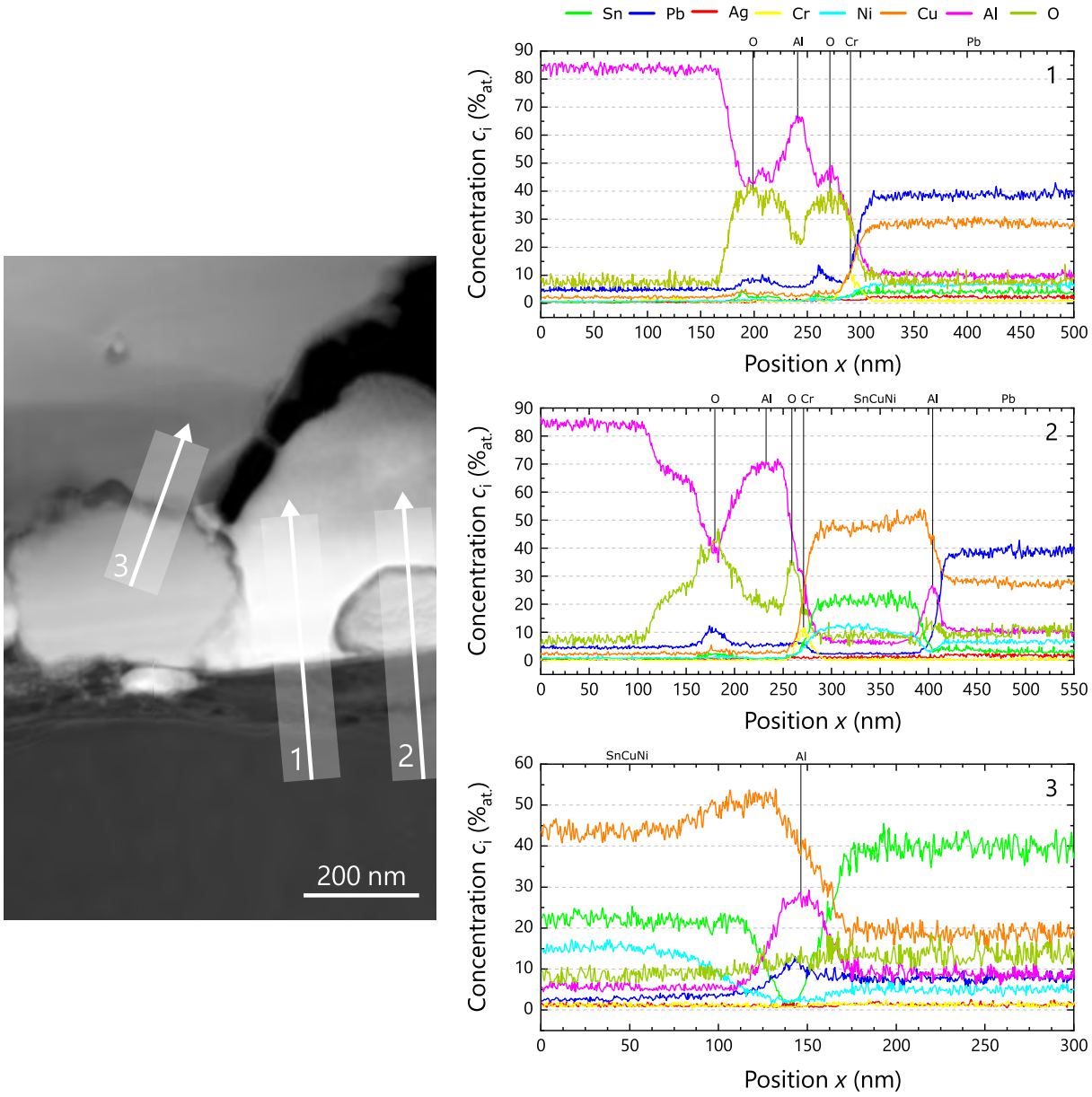

Figure 6.16.: TEM DF image with three EDX line scans showing the composition and the involved materials of a solder joint on sputter-coated Al. Evaluation width of each line scan: 100 nm.

is visible, featuring local distortions. For this sample, no additional Cr layer was deposited below the NiCr layer: the Cr atoms were sputtered in combination with Ni by using a NiCr target, distributed atomically with 80 $\%_{wt.}$ Ni and 20 $\%_{wt.}$ Cr. Nevertheless, a thin Cr layer seems to remain, while Ni dissolves in the solder. Most probably, this process already happens during soldering.

Within the selected area for this TEM sample, no **Ag-rich phases** can be found. Most likely, the 10 nm thick Ag layer of the sputter stack completely dissolves in the solder (*cf.* high dissolution rate of Ag within SnPb solder for 250 °C). Additionally 2 $\%_{wt.}$ Ag within

the used solder alloy do not lead to Ag agglomeration within the analyzed region.

Since there is less Ni to contribute to intermetallic phase formation, no **SnNi-rich phase** is detected for the solder joint at the interface to the thin sputter stack. In accordance with the previous findings, several phases consisting of **SnCuNi** are present. The quantified positions are marked with **D**, **E** and **F** within Figure 6.14. The quantitative results for the thin sputter stack are listed in Table 6.5. With $\sim$16 $\%_{\text{at.}}$, the concentration of Ni is slightly higher than for the first sample with the thick stack (11 $\%_{\text{at.}}$ Ni). Due to the absence of the SnNi-rich phase, more Ni contributes to a ternary phase formation. Also Cu has a higher amount of $\sim 44 - 47\,\%_{\text{at.}}$ Cu then found for the other sample, and dominates in this ternary phase. Within the analysis, it was not possible to refer the found stoichiometry to a specific IMC.

Table 6.5.: Element quantification at seven different positions of the solder joint on the thin sputter stack 3L-22, marked within Figure 6.14. Data is extracted from corresponding line profiles. The measurement accuracy is limited to $\pm 5\,\%$ relative.

	Concentration $c_{\text{i}}(\%_{\text{at.}})$						
	Sn	**Cu**	**Ni**	**Pb**	**Al**	**O**	Phase
A	40	19	-	-	-	< 15	Sn-rich
B	-	29	-	39	-	-	Pb-rich
C	-	27	-	45	-	-	Pb-rich
D	22	44	15	-	-	-	SnCuNi
E	21	47	12	-	-	-	SnCuNi
F	23	44	17	-	-	-	SnCuNi
G	-	-	-	< 10	41	44	AlO_x

Element Quantification of Interfacial Phases

In Figure 6.15, the overlapping image in the bottom right reveals a kind of "shell" around the SnCuNi-rich regions (reddish haze). The element mapping shows an accumulation of Cu (orange) and Al (magenta), also visible in the TEM DF image and line scans 2 and 3 in Figure 6.16. The binary phase diagram of Al and Cu (*cf.* Appendix A.4) shows several stable phases at RT. A phase formation with Cu dominance is likely. For the present study, it is important to mention that Al of the substrate seem to diffuse towards the sputter stack into the solder. The amount of Al is rather small. Nevertheless, the chosen NiCr layer of 10 nm thickness is not able to suppress Al diffusion completely. This has to be considered for the application, since Al diffusion could lead to oxidation and therefore to mechanical and electrical failure of the solder joint. The analysis on material level has shown that such thin sputter stacks can still provide strong ($F/w = (3.3 \pm 0.5)\,\text{N/mm}$, *cf.* Figure A.14) and highly conductive ($\rho_{\text{c}} \approx (1 \pm 1)\,\mu\Omega\,\text{cm}^2$, *cf.* Figure 6.17) joints after soldering.

Within the **Pb-rich** phase, again a significant amount of Cu is measured: $\sim 28\,\%_{\text{at.}}$ Cu at point **B** and **C**. This measurement is in agreement with the quantification of the Pb-rich

phase of the TEM sample with the thicker stack 4L-114 and attributed to the secondary signal of back-scattered electrons of the Cu pole shoe. The concentration within the **Sn-rich** phase (point **A**) is in accordance to the previous sample as well. Only a higher amount of oxygen is detected here.

Conclusion

The microstructural investigations performed on two samples with different sputter stacks provide a deeper understanding of the role of the involved materials and their interfacial reaction within the solder joint. A thin 3-layer stack 3L-22 (NiCr/Ag/Cu 10/10/2 nm) and a thicker 4-layer stack 4L-144 (Cr/NiCr/Ag/Cu 10/50/50/4 nm) perform similar at the interface to the Sn62Pb36Ag2 solder joint. For thicker bottom layers (here Cr/NiCr with 10/50 nm), Al diffusion could effectively be reduced and oxidation of the Al surface prevented. If they are too thin (here NiCr 10 nm), two oxide layers are found: at the interface Al/stack (oxidation of Al) and on top of the NiCr layer. For both investigated stacks, different (intermetallic) phases are found in the interfacial region. While most of the Cr layer remains unaffected and still provides a firm bonding to the Al, the Ni of the NiCr layer contributes to a SnNi phase and/or a ternary CuNiSn phase. The stoichiometry for these phases depends on the local distribution of the involved metals within the joint. This is also the case for Ag agglomeration which is partly observed near the interfaces.

Both sputter stacks provide very strong solder joints (F/w =4 N/mm to 6 N/mm, *cf.* Figure A.14). It is assumed that the persistence of the Cr layer significantly contributes to the mechanical strength of the joints, also the present NiCr layer (without pure Cr below). The formation of several phases within a region of about 500 nm on top of the interface Al/stack implies diffusion processes of the metal layers of the stack and the Sn of the solder alloy, indicating a proper solder joint. The presence of Ni (pure Ni or NiCr) supports diffusion and phase formation at the interface. For coating of Al surfaces, NiCr with a composition of Ni80Cr20, is an optimal layer to provide adhesion to the substrate and prevent or even reduce Al and oxygen diffusion. In combination with a solderable top layer of Ag or Ag98Cu2, the coated Al can be contacted by Sn-based solder alloys within short soldering times < 5 s.

6.4. Electrical Properties

For the implementation of solder joints on coated Al in Si solar cells, the contact resistance has to be low and stable within the PV module for a long time period during operation. To evaluate the electrical resistance on material level, samples for contact resistance measurements are fabricated out of sputter-coated Al foils.

6.4.1. Dependence of Solder Joint Resistance on Layer Thickness

In a first experiment, several sputter stacks are tested, to value the impact of the metals and their thickness. The contact resistance of solder joints, fabricated with Cu ribbons

coated with Sn62Pb36Ag2 solder, is measured as described in Section 3.3. The values are normalized to the contact area to obtain the specific contact resistance R_c. Figure 6.17 presents the results for different stacks in the graph on the left.

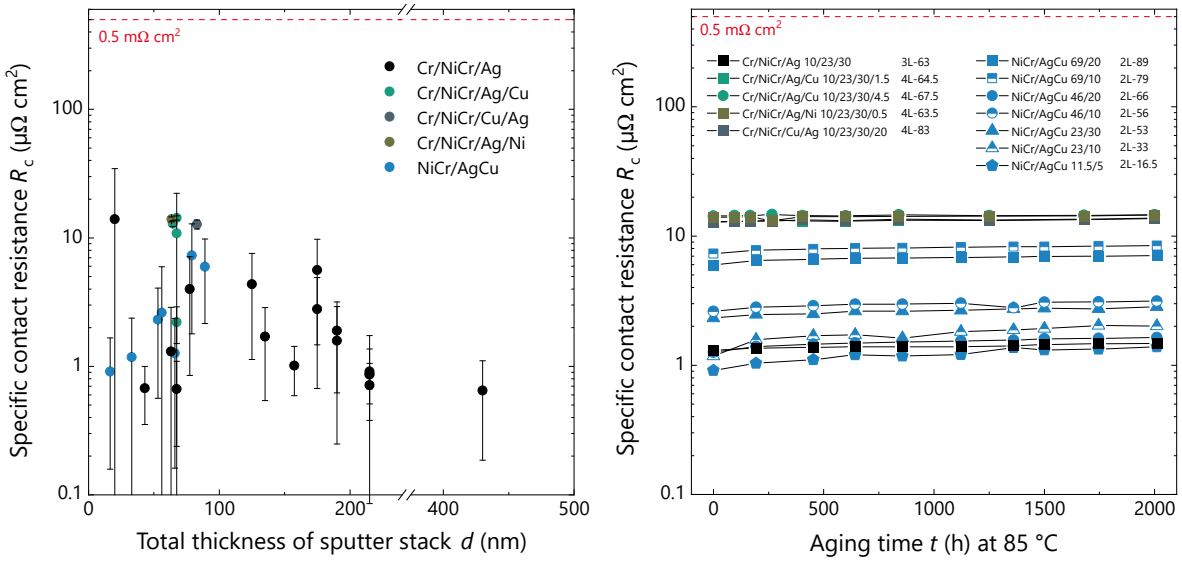

Figure 6.17.: Specific contact resistance R_c of solder joints on sputter-coated Al foils, presented for different sputter stacks. Left: Dependence of R_c on the total thickness of sputter stacks d. Right: Specific contact resistance after isothermal aging of the solder joints at 85 °C in ambient air. Note the logarithmic scale of the y-axis in both graphs.

The specific contact resistance R_c is plotted against the total thickness d of the sputter stacks. For most of the samples, a specific contact resistance between $R_c = 1\,\mu\Omega\,\mathrm{cm}^2$ to $10\,\mu\Omega\,\mathrm{cm}^2$ is found. The lower R_c of the solder joints on a Si solar cell, the lower the cell-to-module (CTM) loss due to soldering. According to Zemen *et al.*, values smaller than $500\,\mu\Omega\,\mathrm{cm}^2$ have a negligible influence on the CTM loss and do not affect the fill factor of the solar cell [180].

Each data point in Figure 6.17 states mean and standard deviation over 8 to 14 solder joints. The large measurement errors are due to the small values of R_c near the resolution limit of the measurement device. In the given measurement range for R_c, the statistic errors mostly are in the same order of magnitude.

Within their measurement errors, the solder joints on all sputter stacks show a similar electrical performance. All involved materials are metals, wherefore good metal contacts with low values for R_c are found. One of the factors most influencing R_c most likely is the manual fabrication of the solder joints. Especially residues of flux influence the solder joint resistance [16], due to organic residues with a higher resistance or even insulating properties. However, a good quality of the solder joints, *i.e.* a homogeneous metal contact without voids over the whole contact area, is of minor importance here. The contact area measures at least $A = 0.5\,\mathrm{cm} \times 0.15\,\mathrm{cm}$, neglecting deviations in A. As shortly discussed in the Experimental (Section 3.3), the transfer-length method (TLM) is not reasonable for these soldered contacts since they are not metal-semiconductor contacts. Accordingly,

the evaluation of the transfer length L_T of these samples mostly yields values $L_T \ll 1\,\text{mm}$, illustrating the "oversizing" of the solder joints in these measurements with a current of 100 mA.

In literature, values for R_c of soldered ribbons on Ag pads on solar cell rear sides of about $R_c \approx 100\,\mu\Omega\,\text{cm}^2$ have been reported [238]. Especially the contacts on the cell rear side (conventionally solder joints on Ag pads) have a larger impact on module power in case of solder failure modes than the front contacts [239]. For Si solar cells, different contact resistances contribute to the overall resistance losses in the PV module [240]. Under this consideration, the soldered contacts play a minor role [180]. However, it has been shown that good wettability and homogeneously soldered contacts over the cell are essential to avoid a loss in power after thermal cycling. The results, presented in this chapter for solder joints on sputter-coated Al, are promising for a good performance on the solar cell rear side. One has to keep in mind that the joints, measured within this study, are fabricated on 200 µm thick Al foils. On the rear side of a FoilMet® solar cell, the Al foil is thinner (10 µm) and the LFC or LMB metal-semiconductor contacts between the Al foil and the Si wafer will most likely dominate the overall contact resistance of the rear contact.

6.4.2. Solder Joint Resistance after Isothermal Aging

The right graph in Figure 6.17 shows the specific contact resistance of solder joints on twelve different sputter coatings on Al foils. The statistical errors displayed in the graph on the left are neglected here to not overload the graph. Considering these errors, no difference between the different stacks are found. Isothermal aging at 85 °C does not lead to a change in R_c. If diffusion processes take place, *e.g.* Al diffusion, oxygen diffusion or Ni or Sn diffusion (*cf.* Section 6.3), no influence on the electrical properties of the solder joints is measurable.

To accelerate the solder joint aging, the aging temperature of the samples presented in Figure 6.17 on the right is increased to 125 °C. The samples are aged for additional 2000 h and R_c is measured after distinct time steps according to [185]. The results are shown in Figure 6.18.

The electrical resistance of four of these two-layer stacks (squares, dots) slightly increases within 500 h of aging at 125 °C and then saturate. Note the non-logarithmic scale of R_c. The thinnest stacks (2L-53, 2L-33, 2L-11.5) show an increase of R_c, which does not saturate within the overall aging time. Since the involved materials are the same for all seven stacks, the thickness of the bottom layer (NiCr) seems to be the dominant factor. The top layers Ag and Cu quickly dissolve within the liquid solder during soldering, which leads to a direct contact of solder and NiCr. The thinner the NiCr layer, the more susceptible is the solder joint resistance to elevated temperatures. Most likely, oxidation of one of the interfaces (after a possible diffusion of Al) leads to an increase of R_c. However, this increase is not critical for the PV module due to the already long measurement time, the selected temperature of 125 °C and the still low values for R_c.

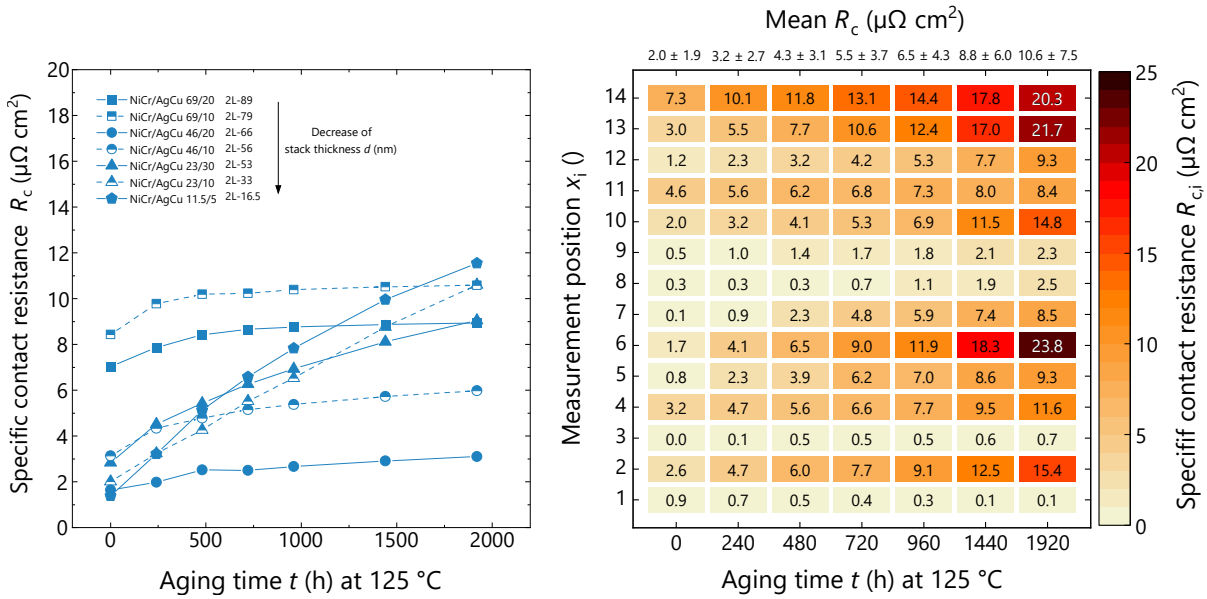

Figure 6.18.: Left: Specific contact resistance R_c of the solder joints of Figure 6.17 left, aged for additional 2000 h at 125 °C in ambient air. Right: Specific contact resistance per solder joint $R_{c,i}$ of the samples with stack 2L-33 (blue triangle half filled of graph on the left).

The graph on the right shows the measurement data of stack 2L-33 (blue triangles half filled in left graph). In total, 14 solder joints x_i (y-axis) are characterized upon aging (x-axis). The color code gives the specific contact resistance $R_{c,i}$, measured for each joint. It becomes apparent that an increase in the mean R_c given in the graph on the left is caused by degradation of single solder joints ($x_i = 2, 6, 10, 13, 14$; order on y-axis is arbitrary). Although the resistance of all joints slightly increases, five of them boost the mean specific contact resistance from $R_c = (2.0 \pm 1.9)\,\mu\Omega\,\mathrm{cm}^2$ to $R_c = (10.6 \pm 7.5)\,\mu\Omega\,\mathrm{cm}^2$ within ~ 2000 h of aging at 125 °C. It has to be considered that the measurement time is already chosen very long (uncritical range for PV module) and resistances are all in the uncritical range $\ll 500\,\mu\Omega\,\mathrm{cm}^2$, featuring large measurement errors in the same order of magnitude.

6.4.3. Solder Joint Resistance after Damp Heat Test

The change of the electrical parameters of the solder joints within a PV module can also be analyzed under damp heat conditions. In addition to isothermal aging, the influence of moisture is addressed here. To continue the evaluation on material level, 8 samples are prepared for contact resistance measurements. They are laminated into the classical module setup, consisting of 4 mm thick front glass (10 cm × 10 cm), two layers of EVA and a white backsheet. A photo is given in Figure 6.19 on the left. 10 µm thick Al foils, coated with Cr/NiCr/Ag/Cu with a nominal thickness of 10/23/30/4.5 nm (4L-67.5), are used for this investigation. The coated side of the foil, contacted by Sn62Pb36Ag2-coated Cu ribbons, is placed into the laminate facing the backsheet, as it would also be in the original

module setup with a FoilMet® solar cell. Figure 6.19 right shows the results of the specific contact resistance upon aging in damp heat conditions (85 °C, 85 % rel. humidity).

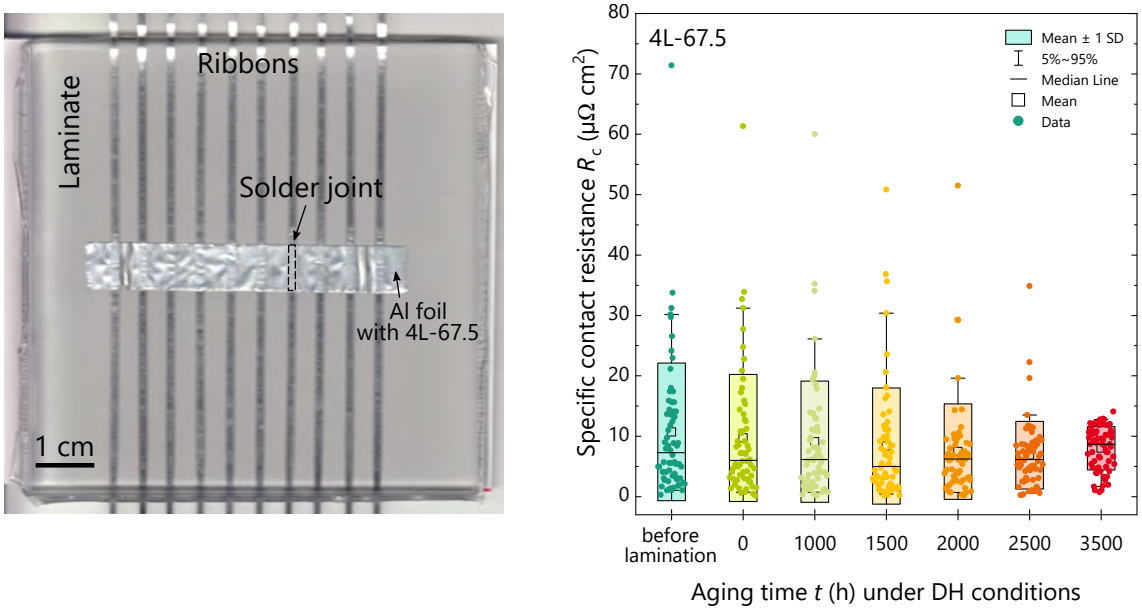

Figure 6.19.: Left: Photo of the front side of a laminate for contact resistance measurement after DH aging. Right: Specific contact resistance R_c of laminates with solder joints on sputter-coated (4L-67.5) Al foils. The samples are aged under DH conditions.

The specific contact resistance R_c of all 64 solder joints stays constant at a mean value of about 7 µΩ cm² to 10 µΩ cm², neither influenced by the lamination process, nor by DH aging. The outliers at higher resistances are not the same for each step on the x-axis. The range and standard deviation of the data diminish with time in damp heat climate chamber, which could be caused by the measurement procedure and sample contacting.

Conclusion

The specific contact resistance R_c is characterized for solder joints on several two-, three- and four-layer sputter stacks (2L-d, 3L-d, 4L-d). All joints have small resistances in the range of 1 µΩ cm² to 10 µΩ cm², showing no systematic differences between the involved metals or their thicknesses. In general, a thicker sputter stack prevents oxidation of the Al surface upon aging, which increases the thermal stability of the joints.

The results on material level, presented in Sections 6.1 to 6.4 show a good quality of all solder joints on different sputter stacks on Al foils. These are ideal conditions for the implementation into a Si solar cell, *i.e.* the rear side of a FoilMet® solar cell. The next section will present results on cell and module level, testing two of the sputter stacks: 4L-65 (thicker 4-layer stack, reference), 3L-22 (thin stack).

6.5. Implementation in Si Solar Cells and Modules

By analogy with the solar cell and module production, presented in Section 5.4 for wet-chemically coated Al, this section will focus on the same groups of solar cells, yet consisting of sputter-coated Al rear sides. The procedure for cell manufacturing is exactly the same as presented before, resulting in three different groups: **FoilMet®**, **PVD Al** (2 µm and 4 µm thickness) and **SP Al** as state-of-the-art reference. The experimental process flow is sketched in Figure 6.20, whereas the color code for FoilMet® (green) and PVD Al (orange) remained the same as introduced in the previous chapter. The only difference in processing is the rear side coating of the solar cells, which is described in detail in the following.

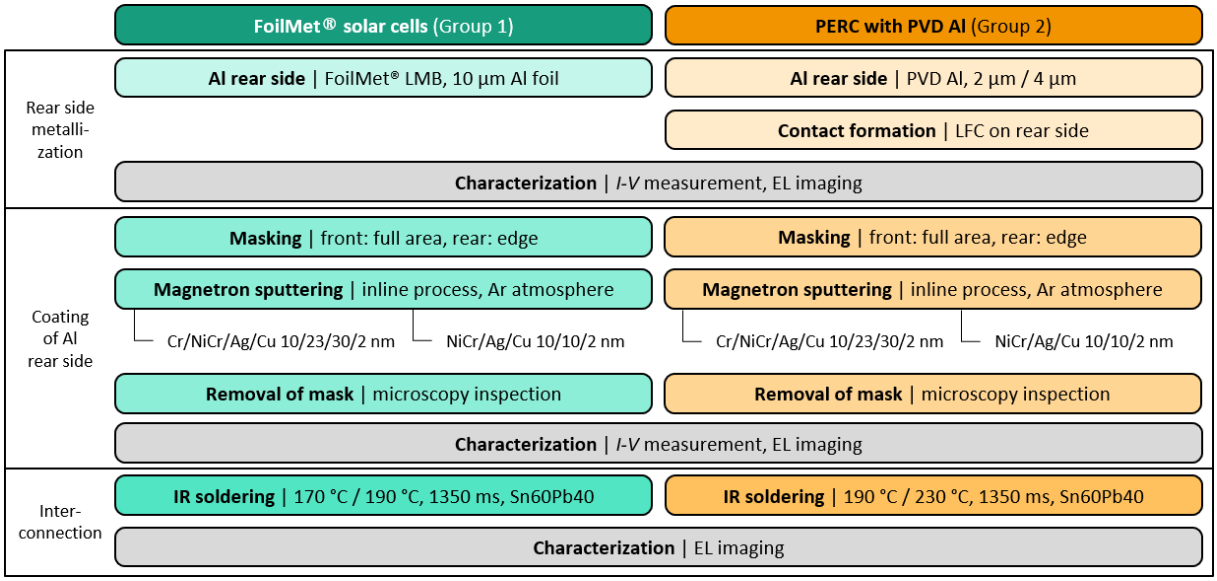

Figure 6.20.: Experimental process flow for sputter coating the Al rear side of PERC solar cells. Green: process route for FoilMet® cells with Al foil rear side. Orange: process route for PERC with PVD Al rear side.

6.5.1. Sputter Coating Process for PERC

The sputter coating process, introduced in Section 3.1.3, is conducted on an inline tool with a large sputter area. The solar cells are placed onto the tray with their rear sides facing up (s. photos in Figure 6.21). The edges of each cell are masked with a rectangular mask of steel and fixed on the coach with Kapton® tape. Then, the same sputter process as introduced for the Al foils in Section 3.1 is carried out to coat the rear side of the solar cells with a multilayer stack. The reference sputter stack and the thin stack, characterized by TEM, are chosen for the implementation in solar cells:

- Sputter stack **4L-65**: Cr/NiCr/Ag/Cu with 10/23/30/2 nm layer thickness
- Sputter stack **3L-22**: NiCr/Ag/Cu with 10/10/2 nm layer thickness

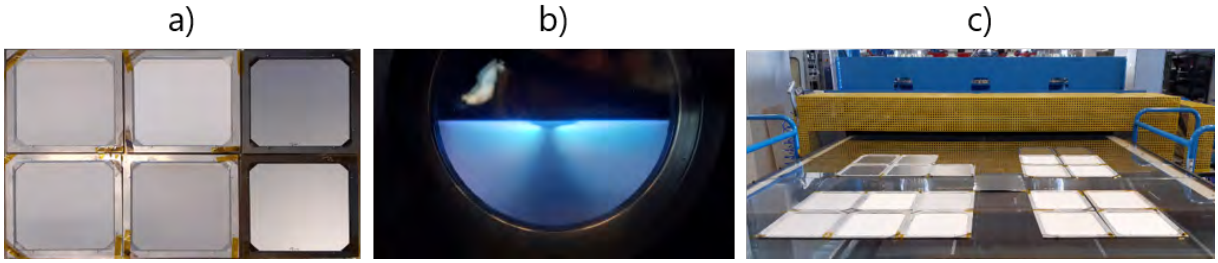

Figure 6.21.: Photographs before and during sputter coating of PERC solar cells on an inline magnetron sputter tool at Fraunhofer ISE. © Fraunhofer ISE

Half of the cells of each group is coated with one of these two stacks, so that there is no difference in coating of the rear side of the FoilMet® cells and the cells with PVD Al. Both are full area coated since additional masking (beside the edges) would neither be beneficial nor disadvantageous for the processing or the cell results. Figure 6.22 shows an overview of the cell rear sides of each group in the final state. For a detailed insight into the front side and the Al rear before coating, it is referred to Figure 5.12.

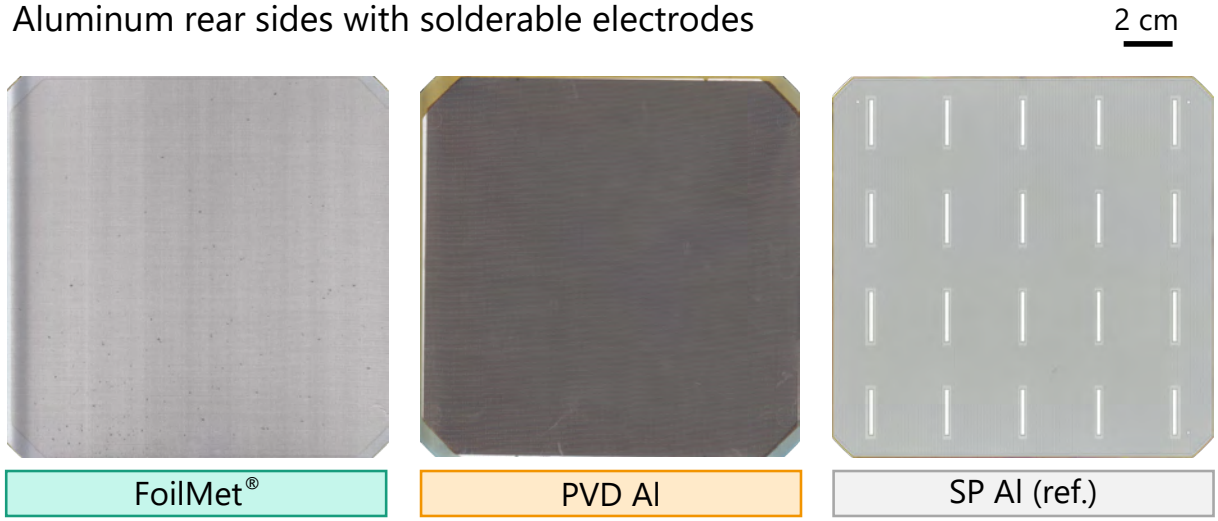

Figure 6.22.: Top view photographs of the Si solar cells processed within this work. All cells are psq monofacial *p*-type PERC cells with 156.75 mm edge length. The front side metallization is the same for all cell concepts, consisting of a 5BB H-pattern layout, screen printed and fired. The Al rear side electrode is either an Al foil (FoilMet® concept), PVD Al or screen-printed (SP) Al. To contact the Al rear side by soldering, the cells with FoilMet® and PVD Al rear side are sputter-coated. The state-of-the-art PERC as reference features Ag pads.

Within this thesis, no variation of the sputter stack for the application on PVD Al has been performed. Since the surface morphology of PVD Al differs from Al foil, most likely this will influence the quality of the stack, even for thin layers.

Additionally, it has not been investigated yet if the used industrial sputter coating process might damage the solar cells. For the original FoilMet® approach, this issue is

not relevant since the coating process is performed prior to the laser attachment of the Al foil to the Si solar cell. However, within this work, the changed fabrication sequence can lead to cell damage, which should be excluded for further data analysis. To evaluate a successful implementation of the sputter-coated Al foil onto solar cell rear sides, the electric parameters on cell level are investigated. The results are presented in detail in the Appendix A.9.5.

For sputter-coated solar cells, no damage of the cells after coating is found. The used inline sputter process can be implemented in manufacturing of solderable Al rear sides (Al foil, PVD Al) of Si solar cells to provide an alternative to Ag pads. This enables to use the conventional interconnection process on an industrial stringer, addressed in the following section.

6.5.2. Industrial Solar Cell Interconnection

The interconnection of the three cell groups, including the state-of-the-art PERC with Ag pads, is performed on the industrial stringer "TT1800" with exactly the same parameters as given in Section 5.4.3 in Table 5.2. The appearance of the PVD Al cell rear side after sputtering (*cf.* Figure 6.22 middle) is significantly darker than before coating (only PVD Al). This leads to an increase of the emissivity of the rear side from $\varepsilon_{\mathrm{PVDAl}} = 0.19 \pm 0.01$ to $\varepsilon_{\mathrm{PVDAlSputter}} = 0.42 \pm 0.02$. Since this value was not available at the moment of cell interconnection at the stringer, it is supposed that this cell group is soldered with a lower temperature than expected.[5]

After soldering on the industrial stringer, the quality of the solder joints is examined by visual inspection. On PVD Al with the thinner stack 3L-22, the ribbons do not stick at all, whereas this group could not be used for module integration. Wetting of the cell rear sides with liquid solder proves a successful solder joint formation which allows for string handling with all cells of the other groups. Before module integration, the mechanical stability of the joints is characterized by 90° peel force measurements, presented in the following.

Mechanical Properties

Figure 6.23 shows the normalized peel force F/w, measured on the sputter-coated solar cell rear side of FoilMet® solar cells (green) and cells with PVD Al (orange), both coated with 4L-65. The box plots show all measurement values recorded over five peel force measurements each, for 150 mm evaluation length in 15 µm steps. The gray regime marks the reference peel force measured on conventional Ag pads: $(0.95 \pm 0.55)\,\mathrm{N/mm}$. The corresponding data can be found in the appendix in Figure A.10. As can be seen in the detailed figure on the right, the peel force of the FoilMet® rear side yields a constant

[5] The expected cell temperature can be extracted from the soldering profile given in Figure 2.14 in the Fundamentals 2.2.4. For a monofacial PERC solar cell, the emissivity of the rear side is $\varepsilon_{\mathrm{SPAl}} = 0.36 \pm 0.02$. The presented profile (red curve) corresponds to this set value, leading to a peak temperature of $T_{\mathrm{peak}} \approx (195 \pm 2)\,°\mathrm{C}$. The increase in emissivity to $\varepsilon_{\mathrm{PVDAlSputter}} = 0.42 \pm 0.02$ for sputter-coated PVD Al most likely leads to a temperature decrease of $\Delta T \approx -10\,\mathrm{K}$. This would lead to insufficient melting of the Sn60Pb40 alloy ($T_{\mathrm{sol}} = 183\,°\mathrm{C}$, $T_{\mathrm{liq}} = 190\,°\mathrm{C}$) and to incomplete solder joint formation.

force level at (0.41 ± 0.05) N/mm due to ablation of the Al foil from the Si wafer. These force values do not characterize the solder joint and underestimate the actual force of the contact since the force F is normalized to the ribbon width $w = 0.9$ mm. The actual contact area of this fracture is defined by the LMB contacts and is much smaller than 0.9 mm × 150 mm. The results are in good agreement to peel forces on wet-chemically coated FoilMet® rear sides (*cf.* Figure 5.13).

For the group with PVD Al, solar cells with 2 µm and 4 µm thick PVD Al and sputter stack 4L-65 are tested. The peel force does not depend on the thickness of the PVD Al, whereas the graphs only show an example for 2 µm thick PVD Al rear side (orange). These values show a wide spreading and yield a mean force of (0.26 ± 0.33) N/mm. The graph on the right in Figure 6.23 shows a force-path-diagram of ribbon 1 and ribbon 3 of one solar cell with PVD Al rear side. Ribbon 1, as well as ribbon 5 (not shown) yield significantly lower peel forces than ribbon 3, soldered onto the middle of the solar cell. This supports the assumption of a too low soldering temperature, leading to inhomogeneous heating. The outer part of the cell is colder, whereas the solder does not (fully) melt for a sufficient period of time, leading to an incomplete solder joint due to insufficient wetting.

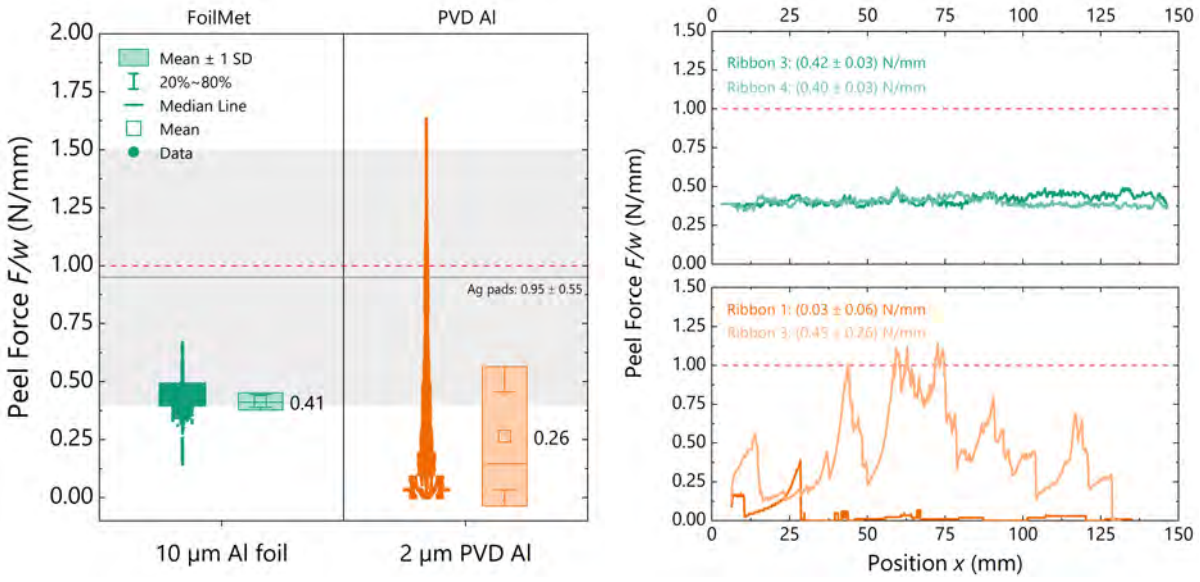

Figure 6.23.: Peel force of soldered ribbons (Sn60Pb40) onto different solar cells, sputter-coated with stack 4L-65. The force is normalized to the ribbon width of 0.9 mm. The box plots show all measurement values recorded over five peel force measurements for 150 mm evaluation length each. The peel force achieved on the same cell type with Ag pads on the rear side is marked in gray with corresponding standard deviation.

Figure 6.24 shows SEM top view images of the sputter-coated PVD Al rear side after peeling off the ribbons. On the left, PVD Al with the thin stack 3L-22 is presented. Only small remnants of solder can be found and no indications for solder joint formation are observed. On the right, a fracture after the peel force measurement on PVD Al with the thick stack 4L-65 is presented. Most of the fracture area is covered with remnants of

Sn60Pb40. The failure is cohesive within the solder or adhesive between substrate and solder. Due to the reduced signal of the sputter stack in the top view mode (*i.e.* the stack is too thin to contribute to the EDX signal), no distinct statement can be made on the interface of failure at Al/stack, stack/solder or even within the sputter stack.

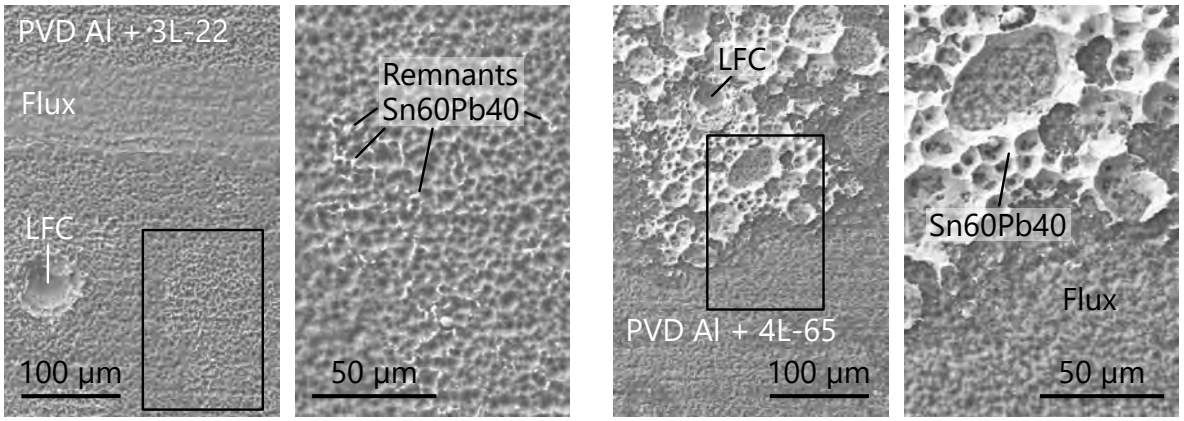

Figure 6.24.: SEM top view images (20 kv) of the fracture after the peel force measurement on the solar cell rear side with sputter-coated PVD Al. Left: PVD Al with stack 3L-22. No solder joint formation is observed, leading only to small remnants of Sn60Pb40. Right: PVD Al with stack 4L-65, showing a mixed fracture: cohesive within the solder and adhesive at the interface to the substrate.

Both solar cell types yield lower mean peel forces than the reference system with Ag pads. However, it is supposed to allow for string handling and module integration. As discussed earlier (s. Section 5.4.3), mostly the mechanical connection of the Al foil to the Si wafer or the thin Al foil itself are the limiting parts on the solar cell rear side of the FoilMet® concept. The measured peel force is also much lower than the values received on material level on 200 µm thick Al foils. On the one hand, this is due to the direct transfer to the industrial soldering process on the stringer. Within this thesis, this process could not be optimized due to absence of appropriate solar cells. On the other hand, the thin Al foil limits the measurement of the strength of the solder joints itself. In general, it is supposed that comparable force values to those found on thick Al foils can be reached after the industrial interconnection process of both solar cell concepts.

6.5.3. Module Integration and Climate Chamber Tests

For module integration of the soldered strings, the manufacturing procedure described in Section 5.4.4 is conducted. Again, one set of 1-cell-modules is built with the conventional module materials (glass/EVA/white BS) for TC tests, whereas a transparent backsheet is used for the second set of modules for DH tests. Two of those modules for DH, one of every cell type, are shown in Figure 6.25 from the cell rear side.

To evaluate the electrical performance of the modules, *I-V* and EL measurements are conducted before climate chamber testing. Afterwards, the modules are exposed

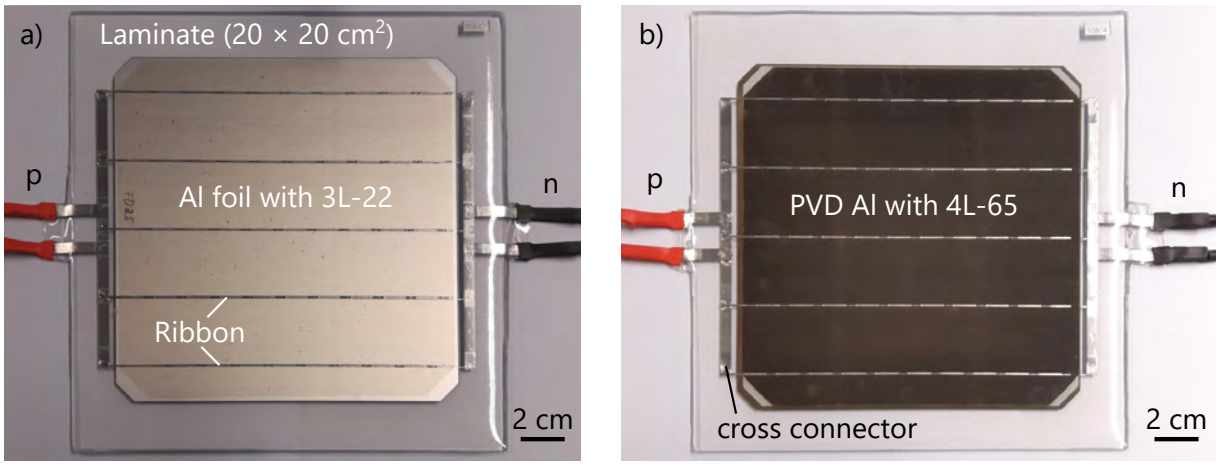

Figure 6.25.: Photographs of 1-cell-modules with transparent backsheet for DH testing. a) FoilMet® module with sputter-coated rear side (stack 3L-22). b) Module with PVD Al rear side with sputter stack 4L-65.

to TC 400 (steps at TC 50 and TC 200) and DH 1000, respectively. The following two sections present the results after TC and DH, whereas the *I-V* parameters are normalized to the initial values to state the electrical changes caused by aging.

Thermal Cycling

The normalized *I-V* results after TC 50, TC 200 and TC 400 are given in Figure 6.26 for the FoilMet® modules (top), the modules with PVD Al (middle) and the state-of-the-art PERC with SP Al rear side (bottom). For the first two groups, dots represent the thicker sputter stack 4L-65, triangles the thin stack 3L-22. The red dotted line at −5 % indicates the critical limit stated in the standard IEC 61215 for a maximum power degradation after TC 200 or DH 1000 as certification for solar modules [79].

All four **FoilMet®** modules show a similar behavior, without any difference between the coating. The power degradation of about −2.7 % after TC 400 is driven by a change of the fill factor of −3.1 % without a significant degradation in *pFF*. The effect already starts after 50 cycles for all four modules. In addition, one module shows a slightly stronger degradation of the *pFF* after TC 50 and TC 200, a second one after TC 400.

Three modules with **PVD Al** rear side are tested in TC, all coated with 4L-65 on the rear. V_{oc} as well as *pFF* stay constant, whereas a *FF* degradation sets in already after 50 cycles. This leads to a power degradation so that half of the modules pass the IEC criterion of less than −5 % power degradation after TC 200. After 400 cycles, one module shows a significant reduction in I_{sc}. The reason for this remains unclear at this point, but is not related to interconnection as checked by EL imaging.

For the modules with the state-of-the-art cell with **SP Al**, a typical power degradation of about −2 % is measured after TC 400, also caused by a degradation of the fill factor.

More in-depth analysis of possible failure modes is given later in this chapter in Section 6.6.

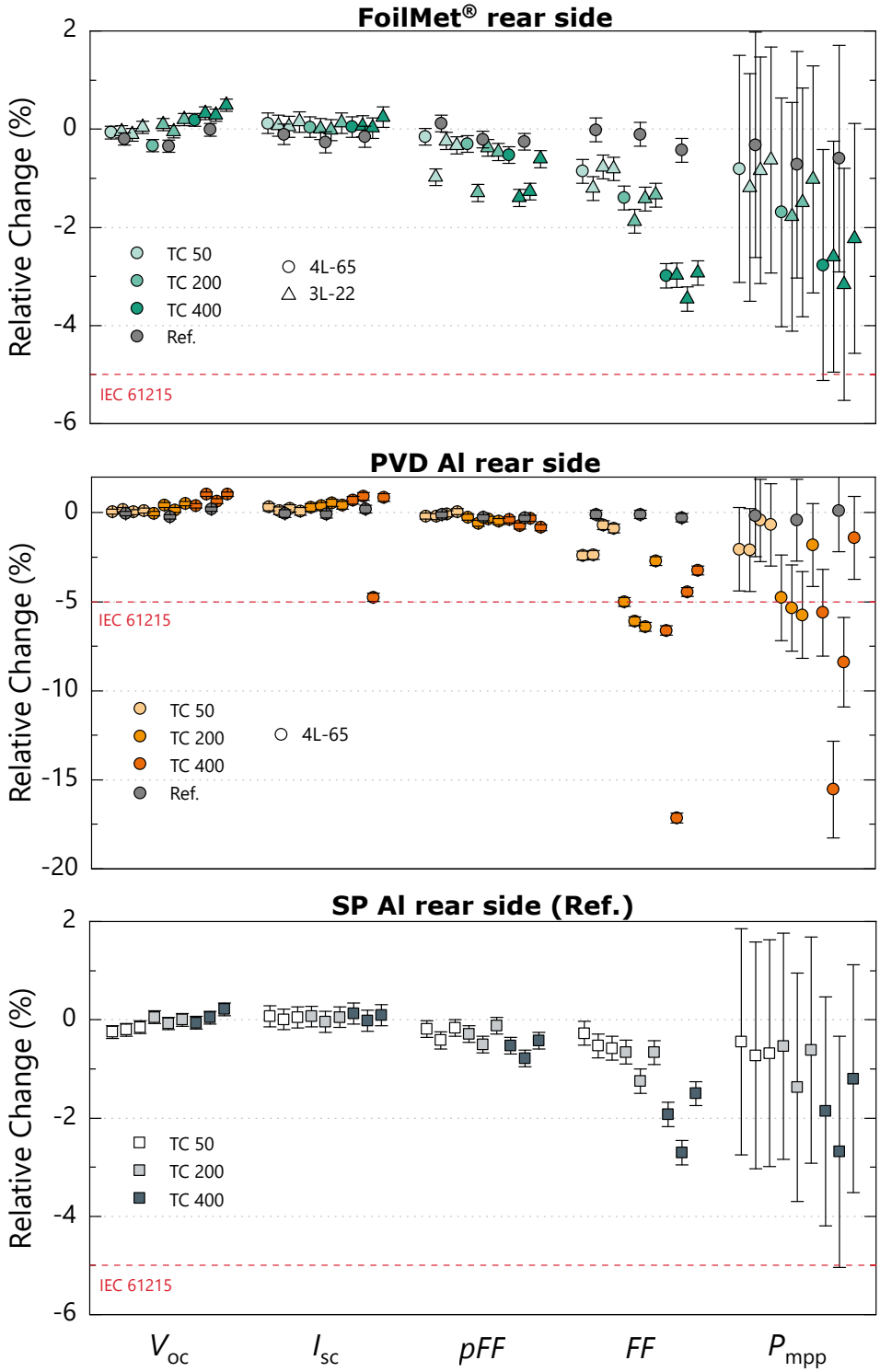

Figure 6.26.: Relative change of the *I-V* parameters of 1-cell-modules after TC testing. Each data point represents one module whereas the errors indicate the measurement uncertainty. Two sputter stacks are tested: Cr/NiCr/Ag/Cu (4L-65, dots) and NiCr/Ag/Cu (3L-22, triangles). The first two groups contain a measurement reference module of the same cell type each (gray squares), which is not aged.

Damp Heat

In total, six 1-cell-modules are tested for heat (85 °C) and moisture (85 % rel. humidity) for 1000 hours in a damp heat test according to IEC 61215 [79]. This test is performed to evaluate a possible power degradation of the modules induced by any chemical reactions, as corrosion, oxidation or phase formation of the involved materials. Compared to the SP Al reference modules, the FoilMet® as well as the modules with PVD Al contain additional metals as Ni and Cr on the cell rear side. On the one hand, the elevated temperature may lead to diffusion of metals into the semiconductor, which could induce recombination losses and a reduction in V_{oc} [21]. On the other hand, corrosion or oxidation of the coated surface could affect the solder joint and lead to an increase in R_s and a reduction of FF.

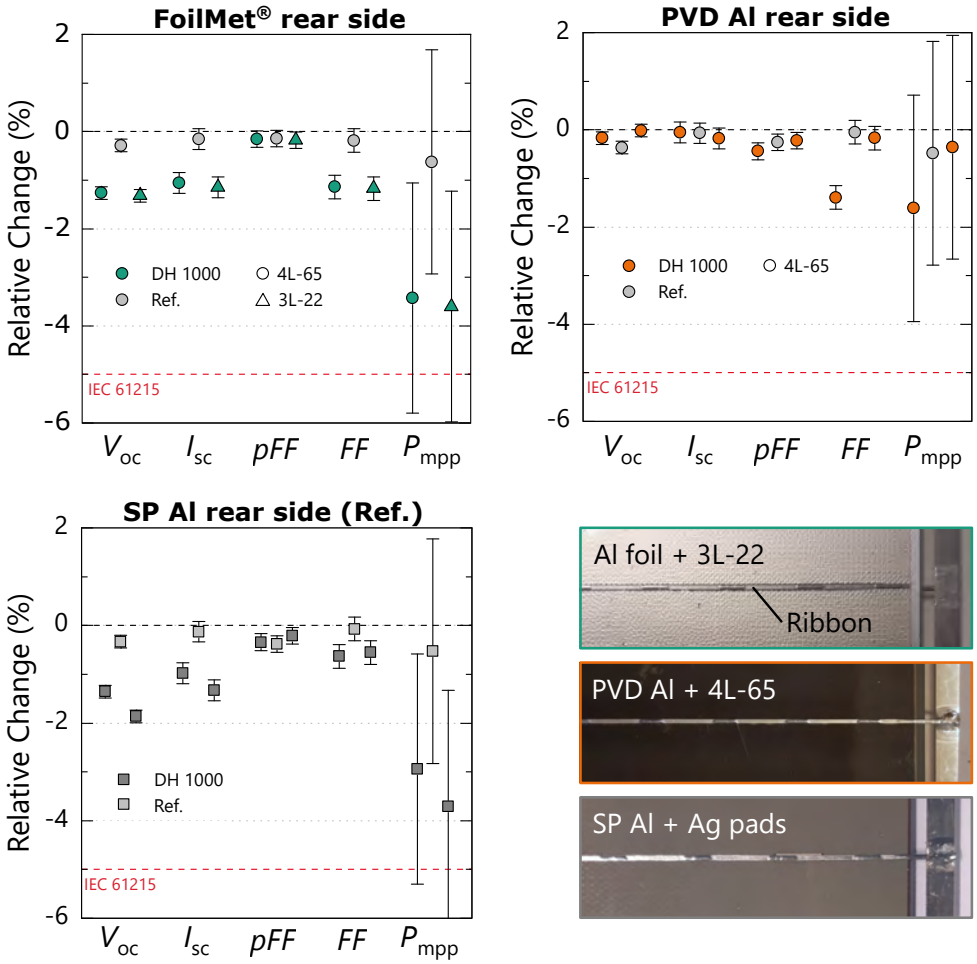

Figure 6.27.: Relative change of the *I-V* parameters of 1-cell-modules after DH testing. Each data point represents one module whereas the errors indicate the measurement uncertainty. Two sputter stacks are tested: Cr/NiCr/Ag/Cu (4L-65, circles) and NiCr/Ag/Cu (3L-22, triangles). The gray dots represent the reference modules which are not aged. The photos in the bottom right show a part of each module rear side after DH 1000.

Figure 6.27 shows the results of the *I-V* measurement of six 1-cell-modules after DH 1000. In addition, three photos of parts of the module rear side are shown in the bottom right exemplarily. Compared to the optical appearance of the modules before aging, no discoloration, corrosion or delamination is found.

The **FoilMet®** modules show a decrease in V_{oc}, I_{sc} and FF of around $-1\,\%$ relative to the electrical parameters before aging. These influence the module power, leading to a reduction of $\Delta P_{mpp,FoilMet} \approx -3.5\,\%$. Both FoilMet® modules perform similar; no influence of the sputter stack (circles, triangles) is measured. The module used as measurement reference (grey square), stays constant, whereas the DH test is supposed to induce these electrical changes.

The two PERC modules with the **SP Al** reference (graph bottom left) show exactly the same trend after DH 1000, whereas the degradation measured for the modules with PVD Al is negligible small. All modules are fabricated of PERC precursors of the same production run, only the cell rear side differs. This degradation effect is mostly likely attributed to LID and/or LeTID, as introduced earlier in this thesis (*cf.* Section 5.4.2) [241,242]. Most likely, the regeneration process, conducted before each *I-V* measurement, was not sufficient to regenerate and stabilize the PERC solar cells. The FoilMet® modules perform on the same level as the reference modules with SP Al. The only difference is $\Delta FF_{FoilMet} \approx -1.1\,\%$ and $\Delta FF_{SPAl} \approx -0.6\,\%$. The slightly stronger decrease of FF for the FoilMet® modules could be caused by an increase of the series resistance (pFF stays constant) due to a degradation of the solder joints on the cell rear side. This effect has also been found for the modules tested in TC (*cf.* Figure 6.26). Within the DH 1000 test, the modules pass half of one cycle of the TC test, namely from RT to 85 °C and back to RT. This already induces stress into the solder joints and the LMB contacts at the FoilMet® rear side.

The lowest impact of the DH conditions is found for the two modules with the **PVD Al** rear side, coated with stack 4L-65. Whereas one module does not show any changes of the electrical parameters, the other one shows a degradation in fill factor of $\Delta FF_{PVDAl} = (-1.40 \pm 0.24)\,\%$. The difference between these two modules could be attributed to different temperatures within the solder joint during soldering, leading to incomplete contact formation for one of the modules and is further analyzed by EL within the following section.

The results, obtained for the different modules at elevated temperatures and moisture are in good agreement to the findings on sputter-coated Al foils. No decrease in peel force (s. Figure 6.6) or increase in series resistance (s. Figure 6.18 and 6.19) after isothermal aging (or DH) is found.

Conclusion

The successful transfer of the sputter coating process to the rear side of solar cells is shown by *I-V* measurements on cell level. The interconnection process by IR soldering is realized on an industrial stringer for Si solar cells with a FoilMet® concept and PVD Al rear side. 90° peel force measurements of the ribbons on the rear side are used to evaluate the soldering result. A failure of the Al foil contacts to the Si (LMB contacts) is found, resulting in $(0.41 \pm 0.05)\,\mathrm{N/mm}$ peel force and a mixed fracture on the PVD Al rear side

with $(0.26 \pm 0.33)\,\mathrm{N/mm}$. This large deviation on the PVD Al rear side arises from a non-optimized soldering process (soldering temperature too low) and leads to a fill factor degradation of 1-cell-modules after TC. Beside this effect on the cells with PVD Al rear side, all modules pass the IEC criterion of $\Delta P_{\mathrm{mpp}} \leq -5\,\%$ after TC 200 and DH 1000 and perform similar than the SP Al reference.

6.6. Failure Analysis on String and Module Level

The *I-V* parameters of the 1-cell-modules, presented in Figure 6.26 and 6.27, indicate several parallel effects of the solar cells, the interconnection and the module materials which contribute to the overall change of the electrical parameters. To separate these effects and evaluate the influence of the solar cell rear side, local analysis are performed by EL imaging and SEM analysis of the solder joints on microstructural level. The results are presented in the following.

6.6.1. Electrical Inspection of Soldered Cells

Figure 6.28 shows three EL images of solar cells after soldering. The images are not scaled equally to provide a better visualization of the cell-specific effects. The scaling factor is given above the images. Some horizontal artifacts perpendicular to the busbars arise from stitching several EL images to obtain one image for one solar cell. The interconnection process for all three cell groups was successful. The EL signal of the **FoilMet®** solar cell is homogeneous over most of the cell area, yielding less counts along the fifth busbar on the right side. Since this reduction in counts is equal from top to bottom of the fifth busbar, it is likely that one of the ribbons on front or rear side does not sufficiently connect the electrode of the cell. Another reason could be an inhomogeneous current flow from the outer cross connector into the solar cell.[6] The FoilMet® solar cell, presented in Figure 6.28 on the left, is coated with the 4-layer stack 4L-65 on the rear side. As already shown by the *I-V* measurement, sputter coating with the tested different stacks does not influence the solar cell performance. An additional EL image of a FoilMet® solar cell with stack 3L-22 on the rear is given in the appendix in Figure A.20. For all FoilMet® solar cells, not cracks or other defects related to interconnection are found. This shows a successful process transfer of the interconnection of coated Al foils to a Si solar cell rear side on industrial level.

For the group with **PVD Al**, EL imaging could only be done for the soldered cells coated with 4L-65 since the interconnection was impossible for the thinner stack 3L-22. The result of one solar cell with PVD Al after soldering is given in the middle of Figure 6.28. Compared to the EL image of the FoilMet® solar cell, the EL signal has to be enhanced by a factor of 20 to gain information on the interconnection process. This is basically due to the significantly lower V_{oc} of this cell group, compared to the others

[6] While solar cells are contacted by pins from top and bottom during *I-V* and EL measurements, soldered cells/strings have to be contacted from the sides by the overlaying ribbons or cross connectors.

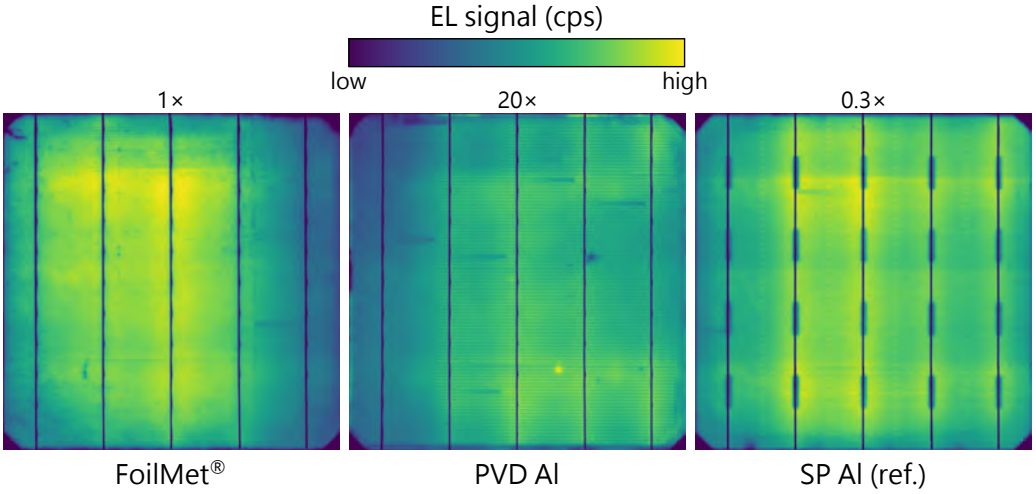

Figure 6.28.: EL images of three interconnected solar cells, one of each cell type. Both, the FoilMet® and the PVD Al solar cell are sputter-coated with stack 4L-65 on the rear side to provide solderability of the Al surface. The colorbar shows the EL signal on a linear scale. The images are not scaled equally. The scaling factor is given above the images.

(*cf.* Figure A.18). The measured EL signal shows a reduction on the first busbar, similar to the effect found for the FoilMet® solar cell on the left and and the SP Al reference on the right. A misalignment of one of the outer ribbons is very likely, as this reduction in signal is also found for other cells of this group.

Comparing the EL image of the solar cells with PVD Al with the same solar cells but coated wet-chemically (*cf.* Figure 5.19 middle), two distinctive features are found. First, the cell with d-Zn+Ni on the rear side featuers a higher EL signal than the cell coated with sputter stack 4L-65. Second, the sputter-coated cell does show a much more homogeneous EL signal, with the absence of brighter regions between the busbars. Both observations support the assumption of a too low soldering temperature for the solar cells with PVD Al and sputter coating. As described in Section 5.5, the PVD Al rear side of the solar cell benefits from the heat during soldering for contact formation between Al and Si. This leads to a higher open circuit voltage of $V_{\mathrm{oc}}(\mathrm{d-Zn+Ni}) = 617\,\mathrm{mV}$ compared to $V_{\mathrm{oc}}(\mathrm{Sputter}) = 607\,\mathrm{mV}$ (measured on module level). For all modules of this group, also no interconnection-specific defects could be found.

The interconnection process on the industrial stringer with a throughput of 1.95 s has been shown for two alternative PERC-based solar cell concepts, featuring a solderable Al rear electrode and omitting the Ag pads on the rear. The IR soldering process is realized with industrially established equipment and materials in Si photovoltaics. The evaluation of the solar cells after soldering using EL imaging shows a successful solder joint formation. In the following, the microstructure of the joints on the rear side is analyzed in detail to value the quality of the solder joints and assess the interfacial reactions.

6.6.2. Microstructural Analysis after Soldering

After soldering on the industrial stringer, small pieces along the busbars are cut out of the solar cells, embedded into epoxy and polished. These metallographic cross sections are analyzed by optical microscopy and SEM to evaluate the solder joints. Figure 6.29 shows an overview of solder joints on front and rear side of each solar cell group in the top row.

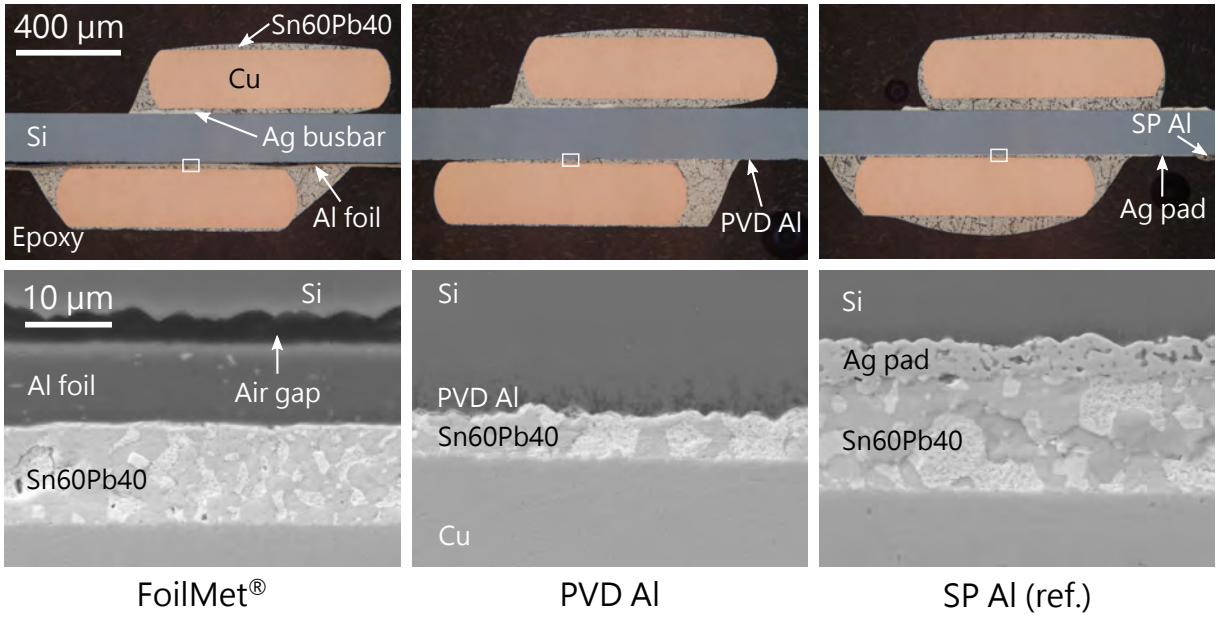

Figure 6.29.: Cross sections of solar cells after soldering on an industrial stringer. Top: Optical microscopy images. Bottom: SEM images of relevant interfaces of the solder joint on the solar cell rear side, coated with stack 4L-65 for the FoilMet® and the PVD Al cell.

The optical microscopy images nicely show the misalignment of ∼200 µm to 300 µm of the top ribbons for each solar cell group, causing the failure on the front side during TC.

The bottom row shows enlargements of the solder joints on the solar cell rear sides. On the left, the **FoilMet®** concept is presented. The air gap between Si wafer and Al foil measures about ∼ 5 µm and exists over most of the length of the inspected cross sections. The Sn60Pb40 layer is in direct contact with the Al foil. Only a thin bright line indicates the presence of the sputtered layer (here 4L-65) on top of the Al foil. The solder joint does not show any cracks or voids at the interfaces and wetting of the coated solar cell rear side is good, yielding a similar contact angle than the screen-printed reference. In the microscopy image in the top, it can be seen that the Al foil is lifted up upon cooling after soldering. This leads to an enlargement of the air gap between Al and Si. It is most pronounced at the end of the ribbon (left/right) where the liquid Sn60Pb40 solidifies and contracts during cooling. This enlargement of the air gap may lead to local damage of the LMB contacts (*i.e.* ablation from Si wafer) and therefore to less contacts and a reduced current flow.

The middle part of Figure 6.29 shows a solder joints on a solar cell with **PVD Al** rear side, coated with sputter stack 4L-65. Wetting of the rear side seems to be restricted, indicated by limited spreading of the solder (resulting in a larger contact angle). However, the SEM image shows a firm bonding between the PVD Al and the Sn60Pb40 layer, without cracks or voids. The surface morphology of the PVD Al layer is mainly given by the etched rear side of the Si wafer. Therefore, the sputter stack has to cover a larger surface area, compared to the planar Al foil.

On the right, the **SP Al** reference is shown, as already introduced in Section 5.5.4. in Figure 5.21. On the rear side, the solder contacts the screen-printed Ag pad, which normally has a thickness between 2 µm to 5 µm.

6.6.3. Electroluminescence Imaging after Thermal Cycling

The EL images of one module of each group are given in Figure 6.30 initially and after 50, 200 and 400 temperature cycles. Due to the different values for V_{oc} between the three groups, the images are not scaled equally. The scaling factor is given above the images.

Already after TC 50, the **FoilMet®** modules show ablation of the rear LMB contacts (Al/Si), pronounced most in the top right corner along the busbar. These blurry areas with a lower EL signal occur at the edges of the busbars, where the stress between Cu ribbon and solar cell is enhanced during temperature changes (*cf.* Figure 2.15). For some solar cells with a lower adhesion between Al and Si, this effect is already observed by visual inspection after soldering. An example is given in Figure A.21 in the appendix. As shown before, the Sn60Pb40 solder also contributes to the ablation of the Al foil in the regions beside the Cu core of the ribbon (s. Figure 6.29). The ablation of the Al foils has already been reported for wet-chemically coated FoilMet® solar modules in Section 5.5.4, indicating a failure independent of the coating process. Most likely, this ablation dominates the reduction in fill factor, which is increasing from $\Delta FF_{\mathrm{TC50}} = -0.9\,\%$ to $\Delta FF_{\mathrm{TC400}} = -3.1\,\%$ with increasing number of TC cycles. In addition, the lift-off of the Al foil below the solder of the ribbon during cooling after soldering may induce initial defects and support the failure along the busbars during TC. For the module after TC 400, a horizontal line scan is added to visualize the broadening of the dip in the EL signal around the busbars caused by foil ablation. The presented EL images for this group show a FoilMet® solar cell, coated with the thin stack 3L-22. In accordance with the *I-V* data (*cf.* Figure 6.26), no difference for modules with FoilMet® solar cells coated with the thin and thick stack are found. Additional EL images can be found in the Appendix A.9.8. Compared to the reference group with SP Al, the FoilMet® modules perform on a similar level. All four modules pass the IEC test with a maximum power degradation of $\Delta P_{\mathrm{mpp}} \leq -5\,\%$ after TC 200. Even the extension of the test to TC 400 leads to a mean power degradation of approximately $-2.7\,\%$ for the four modules.

The middle column of Figure 6.30 shows a module with one of the cells with **PVD Al** rear side coated with the sputter stack 4L-65. From the top image (initial) to the bottom image (TC 400), the cell area on the left side between edge and first busbar shows

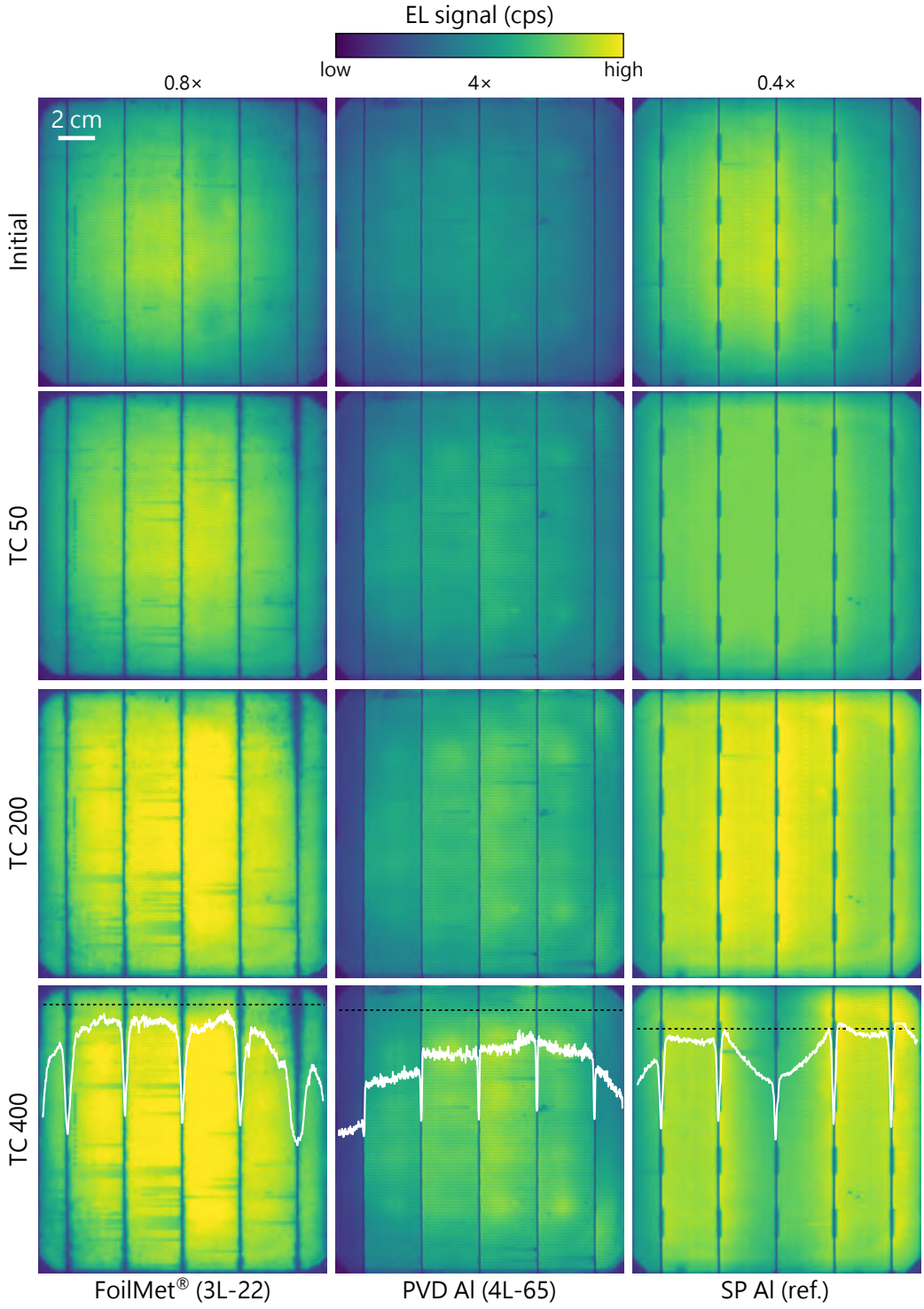

Figure 6.30.: EL images of 1-cell-modules: initially, after TC 50 and after TC 200. One module for each cell type is shown. The images are not scaled equally; the scaling factor is given above the images. The EL signal is given on a linear scale. For TC 400, horizontal line scans at the positions of the dashed black lines are added (not scaled equally). Additional data for TC 400 is given in the appendix in Figure A.21.

a decreasing EL signal upon aging. As explained earlier in Section 5.5.4 in Figure 5.26, a misalignment of ribbon and busbar leads to finger interruptions during TC and to a disconnected part of the solar cell. This finding correlates well to the EL image on string level (*cf.* Figure 6.28 middle), revealing less current flow in this cell region. Since this effect occurs for both coating approaches, it is very likely that it can be attributed to the fingers on the solar cell front side. The effect is also visible in the overlaying line scan. Beside this, the EL signal is more or less homogeneous over the cell area for the solar cells with PVD Al. One could assume some brighter parts with more EL signal to become apparent in the regions between the busbars, which would explain the little increase of the V_{oc} upon aging.[7]

This group (four modules) shows a wide spreading in FF between $\Delta FF = (-3.2 \pm 0.3)\,\%$ and $\Delta FF = (-17.2 \pm 0.3)\,\%$ (*cf.* *I-V* data in Figure 6.26 middle). The EL image presented here corresponds to the first module with $\Delta FF = (-6.6 \pm 0.3)\,\%$. Since all four modules and the measurement reference perform different in TC, a detailed comparison of all EL images and the *I-V* curves seems reasonable. The results are summarized in the Appendix A.9.9, since this analysis does not focus on the interconnection.

To summarize the findings, two modules of the group with PVD Al pass the IEC test and even one module shows $\Delta P_{\mathrm{mpp}} = (-1.4 \pm 2.3)\,\%$ after TC 400. This shows the potential and general proof-of-principle of the approach. By optimizing the soldering process (*i.e.* increasing the soldering temperature), the ribbons on the solar cell rear side would stick better and the degradation in FF (and therefore P_{mpp}) can be reduced.

6.6.4. Electroluminescence Imaging after Damp Heat Testing

After 1000 hours of exposure to damp and heat (DH 1000), the modules are characterized by *I-V* measurements and EL imaging. As presented at the end of the last Section 6.5.3, for the two FoilMet® modules as well as for the reference group, a degradation in V_{oc} and I_{sc} between $-1\,\%$ to $-2\,\%$ is found, which is not measurable for the modules with PVD Al (due to their already lower V_{oc} level). This degradation is confirmed by a reduction of the EL signal from the initial measurement to the measurement after DH 1000. The corresponding EL images of one of the aged modules each is shown in Figure 6.31.

A homogeneous degradation over the whole cell area is measured after DH 1000. This decrease of the electrical cell parameters is in an uncritical range for all tested modules (2 per group) and all of them pass the IEC criterion of $\leq -5\,\%$ relative loss in power.

The *I-V* data also reveal a decrease in fill factor of $\Delta FF_{\mathrm{FoilMet}} = -1.6\,\%$, $\Delta FF_{\mathrm{PVDAl}} = -1.7\,\%$ and $\Delta FF_{\mathrm{SPAl}} = -0.6\,\%$, while the pFF remains unaffected. Since no specific defects, *i.e.* cell cracks, finger interruptions, inactive areas or Al foil ablation, are found, this reduction is most likely related to oxidation or corrosion of parts of the cell or coating, leading to an increase in series resistance. Visual inspection of the transparent modules rear side does not show any apparent discoloration (*cf.* photos in Figure 6.27).

[7] The increase in V_{oc} is marginal of $\sim \Delta V_{\mathrm{oc}} = 0.8\,\%$ and it should be noted that the EL images are already enhanced by a factor of 4.

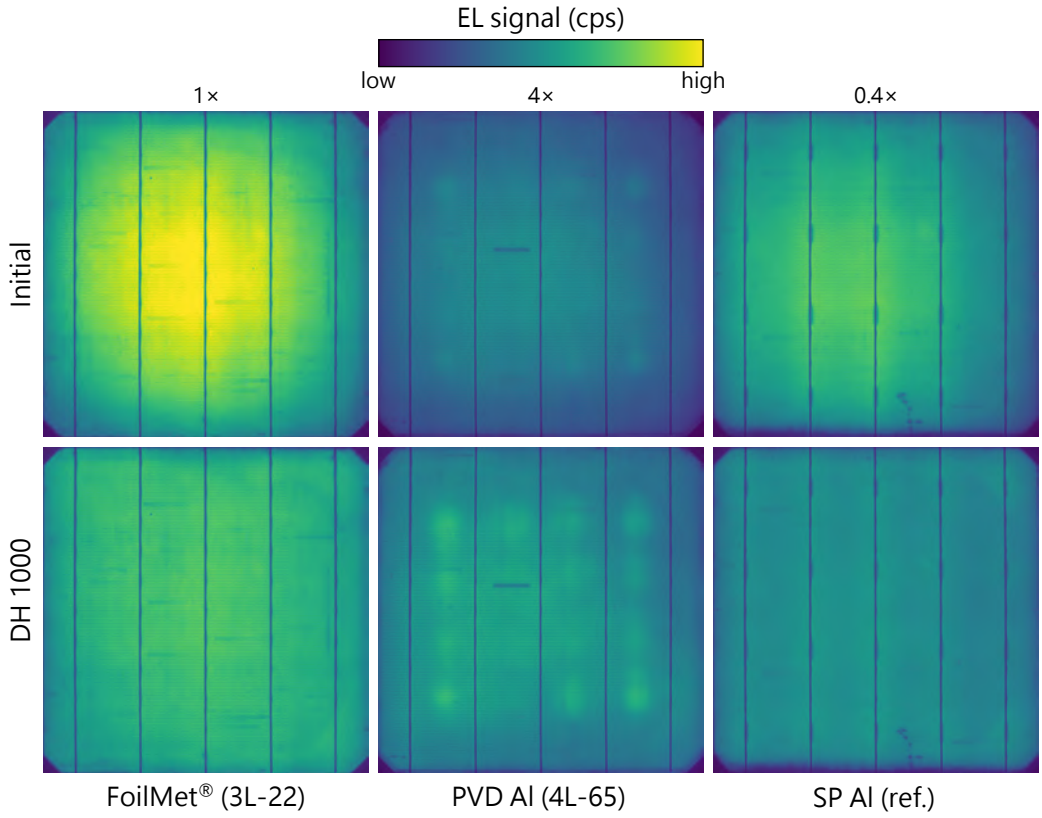

Figure 6.31.: EL images of 1-cell-modules, initial and after DH 1000. Solar cells with FoilMet® rear side (left), PVD Al rear side (middle) and SP Al rear side (right) were tested under DH condition. The images are not scaled equally; the scaling factor is given above the images. The EL signal is given on a linear scale.

Conclusion

The microstructure of the solder joints on the solar cell rear sides is very similar to those found on the pure Al foils. A good wetting of the sputter-coated Al surfaces (foil, PVD Al) by Sn60Pb40 solder leads to homogeneous and mostly void-free solder joints. Some outer ribbons show a misalignment to the busbar, leading to an inhomogeneous current flow through the solar cell, which is proven by EL imaging. For the group with PVD Al, this leads to inactive cell area between cell edge and first busbar. 1-cell-modules with solar cells with PVD Al show strong deviations in the EL images, due to inhomogeneous and not-optimized soldering. For the modules with FoilMet® solar cells, ablation of the Al foil on the rear side in the outer regions of the busbars are found, leading to the measured decrease in fill factor. For all modules tested under damp heat conditions, no specific features related to interconnection failure or corrosion of the involved materials is found.

6.7. Chapter Summary

This chapter focuses on the evaluation of solder joints on sputter-coated Al surfaces. The coating of Al by magnetron sputtering allows for the deposition of very thin metal layers of different functionality. Within the first sections of this chapter, a variety of material combinations is tested regarding their suitability for the desired implementation on the Al rear side of Si solar cells. This enables direct contacting of the Al electrodes by industrially established soldering techniques of the photovoltaic industry.

To provide initial **wettability** of the coated Al surface, the solderable top layer of the sputter stack (Ag, Ag/Cu, AgCu) is essential and a critical minimal thickness of 15 nm to 20 nm is found by optical contact angle measurements with liquid Sn60Pb40. The total thickness of the sputter stack should be around 25 nm to 60 nm, while a bottom layer (Cr/NiCr, NiCr) thicker than 40 nm does not further improve wetting.

Due to very good wettability with contact angles between 25° to 40°, solder joint formation is successful on a variety of different metal stacks. While reducing the total stack thickness below 100 nm, high peel forces of about 5 N/mm to 8 N/mm could be maintained. Upon isothermal aging at 85 °C, all tested joints are stable with at least $\geq$ 3 N/mm. The bottom layers (Cr, NiCr) have the largest influence on **mechanical strength**. A minimum thickness of $\sim$ 20 nm in combination with a solderable top layer of 10 nm to 20 nm leads to strong and stable solder joints under the tested conditions.

The **microstructure** of solder joints on Al foils, coated with very thin multifunctional sputtered layers and the interfacial reactions are investigated in detail by electron microscopy. Using TEM, it could be shown that a Cr layer of 10 nm below 50 nm of NiCr and an Ag/Cu top layer remains after soldering and both (Cr and NiCr) build a diffusion barrier against oxygen from the top and Al from the bottom. Both effects are observed for a thinner stack with only 10 nm of NiCr below a thin solderable Ag/Cu layer. A thicker sputter stack acts as diffusion barrier and prevents oxidation of the Al surface. Ag as well as Cu of the top layer(s) directly dissolve in the liquid SnPb solder during soldering. On top of the remaining NiCr layer of the sputter stack, a thin SnNi phase of 20 nm is formed, if the Ni content in the sputter stack is high enough ($\sim$ 50 nm of NiCr). The most prominant phase found at the interface of the solder joint is a SnCuNi phase. Cu most likely originates from the Cu core of the ribbon and diffuses towards the interface after dissolution. Ag agglomerates near the interface and does not form any measurable intermetallic compounds.

The **contact resistance** of these metallic contacts is characterized for different sputter stacks on Al foils. All contacts provide a low specific contact resistance in the range of 1 µΩ cm^2 to 10 µΩ cm^2. Neither isothermal aging nor damp heat exposure of the samples within small laminates does influence the resistance. The bottom layer (NiCr) does have a major impact. If it is too thin, oxidation of the Al surface is likely, leading to an increase in resistance. The evaluation of several "identical" solder joints shows that an increase in resistance upon aging can mostly be attributed to single joints.

The transfer of the approach from material level into a **Si solar cell** is tested for two different sputter stacks. Neither an influence of the sputter process on the solar cell performance, nor of the different metals and thicknesses of the stacks are found. Both stacks

are able to provide solderability of the Al foil rear side of FoilMet® solar cells on industrial tools using high throughput cycle times of $\sim 2\,\mathrm{s}$, which allows for interconnection and module integration. The tested **1-cell-modules** pass the IEC criterion of $\leq -5\,\%$ loss in power after TC 200 and DH 1000 and yield similar results as the state-of-the-art PERC structure with screen-printed Al paste and solderable Ag pads on the rear side. As proof-of-principle, solar cells with PVD Al rear side are coated with both sputter stacks. The three-layer stack with a thickness of $d = 22\,\mathrm{nm}$ is too thin to provide a homogeneous coating of the PVD Al layer. For a four-layer stack with $d = 65\,\mathrm{nm}$, a successful module integration is shown.

7. Comparative Analysis of Investigated Coatings

This chapter collects the key findings from the three experimental result chapters and discusses them in the broader context. In ***Section 7.1.1****, the general experimental approach is critically reviewed and important learnings for future work are given. Afterwards, derived properties of solder joints on different coatings are recapitulated in* ***Section 7.1.2****. These serve as a guideline for the developed evaluation of solder joints on coated Al.* ***Section 7.2*** *reviews the implementation of solderable coatings on different levels in PV module production. At last, projections for other applications outside of PV are made in* ***Section 7.3****.*

7.1. Solderable Coatings on Al

7.1.1. General Approach

For the evaluation of solder joints on coated Al, different characterization methods have been used within this work. Due to the wide variety of different methods and the correlation between results, an overall understanding of the solder joint formation and their physical properties is derived. While applications might require very thin Al foils (down to 10 µm), robust 200 µm thick Al foil is chosen for the fundamental investigations on material level. This allows for a holistic characterization, simplifies sample preparation and handling and allows to draw general conclusions for this material system. The special focus on such material science aspects of the involved materials is also beneficial to optimize the coating process on Al, to yield optimally soldered components. The analysis of the solder joints of solar cells and modules confirms the fundamental findings obtained on pure Al foils.

One challenge is the necessity to perform manual contact soldering. While *e.g.* automated IR soldering would have been preferred, this could not be used due to the low emissivity of the Al foil in the NIR spectral range. The peel force measurements revealed large systematic errors, supposedly due to manual soldering. However, since most of the material combinations yield overall high peel forces, this is of minor importance. While general and qualitative deductions could be made within this work, this should be considered for future investigations.

Additionally, the overall significance of the 90° peel force measurement for solder joints on Si solar cells as defined in DIN EN 50461 can be questioned. String handling during module manufacturing and temperature cycles during operation of the PV module are the major mechanical influence on the joints after soldering. Yet, the correlation of strong

solder joints (characterized by a 90° peel force measurement) with failure of PV modules (*FF* loss) is not given implicitly [63].

The results of the optical contact angle measurements correlate well with the received peel forces: the general trend of small contact angles yielding high peel forces is found for most of the investigated material combinations in this work (*cf.* Figure A.23, illustrating the correlation for peel force and contact angle). OCA measurements should be used as a meaningful pretest before conducting other extensive characterization of new materials.

The initial peel force after soldering does not necessarily correlate to the long-term stability of solder joints upon (isothermal) aging: Solder joints on the composite Al/Ni yield lower peel forces ($\sim 3\,\mathrm{N/mm}$) than for Al/SnCu ($\sim 6\,\mathrm{N/mm}$) and even Al/SnPbAg ($\sim 4\,\mathrm{N/mm}$). Nevertheless, the joints on Al/Ni are the most reliable ones and do not show any loss in adhesion upon isothermal aging at 85 °C.

Microstructural investigations using electron microscopy have been used in this work, as a very powerful tool to analyze the interfacial reactions of the solder joints. Naturally, cross sections represent a specific location within the joint. Nevertheless, such investigations contribute significantly to the fundamental understanding. While the amount of samples is limited due to high preparation effort, multiple cross sections of each sample have been diligently studied, to improve the reliability of the analysis. The presented examples in previous chapters have been chosen to best illustrate these overall findings.

Finally, results on contact resistance are a helpful indicator for the electric properties of the solder joints. However, the measurement on material level cannot fully capture all the resistive losses due to interconnection on module level. To fully assess the influence of coating and solder joints in future work, contact resistance measurements should be carried out on solar cell sample structures or on module level.

7.1.2. Solder Joints on Coated Al

An overall impression of the results obtained for solder joints for the three different coating approaches of Al for the most promising material combinations is listed in Table 7.1. In addition to these (mostly) quantitative results, the microstructural analysis and the transfer to Si solar cells and modules is summarized in Figure 7.1.

The evaluation of the material combinations in this work has shown that the interface between Al and coating is the most important one for successful soldering on Al. Small interfacial bonding after roll cladding, a not optimized Zn treatment or a too thin (sputtered) adhesion layer lead to insufficient contact formation to the Al substrate and joint failure after soldering.

All materials selected as “top layer” of the coatings, ensure good solderability with SnPb-based alloys due to good wetting properties: Sn62Pb36Ag3, Sn99Cu and Ni as claddings, as well as plated Ni and sputtered Ag or Ag98Cu2 top layers show small contact angles of 25° to 50°. These are ideal conditions for successful solder joint formation and

high peel forces. The results for the most promising material combination of each approach are summarized in Table 7.1. In combination with a good quality of the aforementioned Al/coating interface, mixed fracture patterns and no dominant failure mechanism are found after the peel force measurement.

Table 7.1.: Obtained results for Sn62Pb36Ag2 solder joints on 200 µm thick coated Al foils and loss in power of 1-cell-modules with FoilMet® solar cells. For each coating approach, the best material combination is shown. The listed values for the sputter stack state ranges since many similar stacks provide good results.

	Roll cladding Sn99Cu1	**Wet-chemical** d-Zn + Ni	**Sputtering** NiCr/Ag/Cu
Thickness of coating d	$\sim 45\,\mu m$	$\sim 2\,\mu m$	$\sim 50\,nm$
Contact angle α (°)	good wetting -	very good wetting $(32.6 \pm 4.3)°$	very good wetting 24° to 50°
Peel force F/w (N/mm) IA (1000 h, 85 °C)	sufficient $(6.1 \pm 1.7)\,N/mm$ $(5.2 \pm 1.0)\,N/mm$	sufficient $(5.6 \pm 1.2)\,N/mm$ $(4.4 \pm 1.7)\,N/mm$	sufficient $(4 - 7)$ N/mm $> 4\,N/mm$
Spec. contact resistance R_c ($\mu\Omega\,cm^2$) IA (1000 h, 85 °C)	very low $(0.9 \pm 0.1)\,\mu\Omega\,cm^2$ stable	- - -	very low $< 10\,\mu\Omega\,cm^2$ stable
Transfer to 10 µm Al foil	challenging	successful	successful
Loss of power ΔP_{mpp} after TC 200 (%)	- -	little $< -2\,\%$	little $< -2\,\%$

The transition from 200 µm thick Al foil to thinner coated foils < 50 µm has shown to be challenging. First investigations have been performed within the context of this work. While coating by sputtering has shown to be easily scalable to thinner substrates, the processes for roll cladding and wet-chemical coating have to be adapted. Manufacturing a solderable composite of roll-cladded Al foil with a thickness of < 50 µm is very ambitious and further developments are necessary, due to the major importance of the Al/cladding interface [195,243–245]. A wet-chemical coating can be realized on automated inline tools, but handling of thin Al foil remains challenging.

The evaluation of solder joints on thin sputter-coated Al foil, as presented in this work, was used to transfer the sputter coating process to the industrial partner *ROWO Coating*. They implemented a roll-to-roll process on an industrial sputter coater for very thin Al foil, demonstrating the industrial feasibility of this approach.

The usable thickness of coatings on Al foils strongly depends on the choice of material and coating technique. While sputtered layers of even $\sim 20\,nm$ have shown to provide

a reasonable solderable coating on Al for the intended application, roll-cladded coatings would always remain thicker due to the manufacturing process.

The electrical properties of the metal contacts have shown to be uncritical, even for non-optimized coatings and solder joints. Diffusion and phase formation at the interfaces is advantageous, promoting contact formation and mechanical strength of the solder joints.

The strongest and most reliable solder joints (mechanically and electrically) have been found on 200 µm thick Al foils with coatings consisting of Ni. The composite Al/Ni, the plated Ni layer on Al and the very thin Ni80Cr20 layer of the sputter stack all significantly promote good solder joint formation, whereat a homogeneous bonding to the Al substrate is realized. Beyond the scope of this thesis, peel force measurements on other sputter-coated substrates (Cu foil, glass) have shown to yield similar strong solder joints (*cf.* Figure A.23 right). This illustrates the general applicability of thin Ni-containing sputter stacks to allow for soldering of "challenging" joining partners.

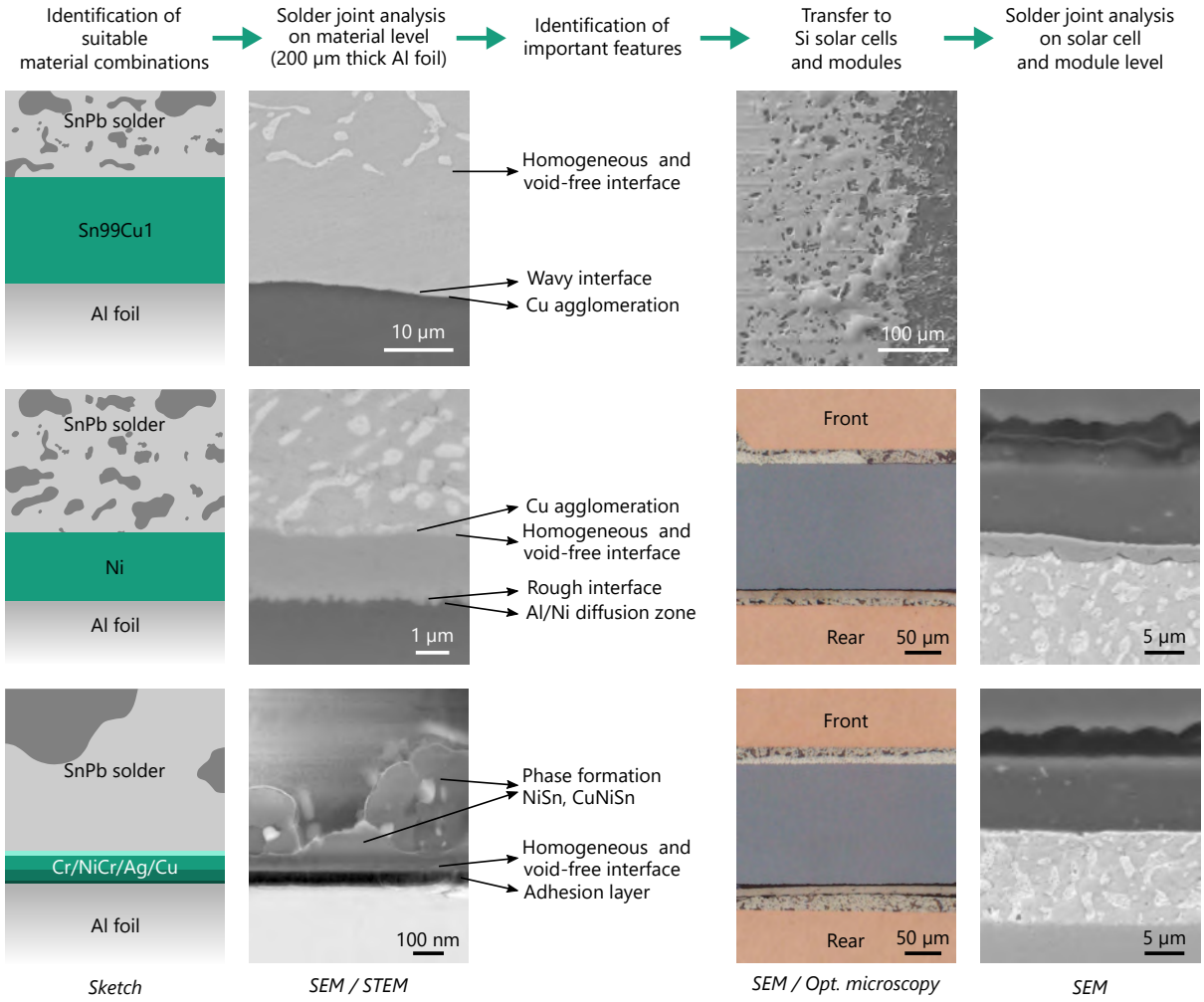

Figure 7.1.: Illustration of the assessment of different coatings, relevant features and the transfer to silicon solar cells.

The compilation of microstructural results in Figure 7.1 first shows three examples for suitable material combinations (sketches in first column). The suitability has been derived across multiple samples and experiments.

The microstructure of the solder joints is analyzed in detail and general findings are indicated in Figure 7.1. Several features are present across the different coating approaches, underlining their relevance for the formation of reliable solder joints. The transfer to solar cells and modules is illustrated by cross sections of the solar cell, or, in the case of roll cladding, by the dominating failure (melting of cladding) prohibiting the transfer. The solder joint on the silicon substrate shows some differences, but the main attributes persist, illustrating the successful transfer of two approaches.

The overall quality of the solder joints evaluated within this work (regarding the investigated properties), is on a very high level compared to common solder joints on Si solar cell (*cf.* Table 7.1). The main reason are the different joining partners. Screen-printed Ag does not withstand such high peel forces as seen for the Al coatings ($\sim 6\,\mathrm{N/mm}$) and the microstructure at the interface does only show Ag_3Sn phase formation.

At the current development stage of solder joints on thin Al foils (as for the FoilMet® solar cell), other aspects of solar cell and module manufacturing will be dominating the performance, as discussed later.

7.1.3. Assessment of New Coating Approaches

Several conclusions should be drawn from this work, as a general guideline for future investigations. In this work, robust Al foil was chosen as the substrate instead of more fragile silicon solar cells. Such general evaluation on material level is very meaningful and should be used as a strong and easy tool for characterization of new approaches. The combination of different characterization techniques is useful for a profound understanding of the solder joint formation and material interactions. This can be directly used to optimize the coating process, based on the revealed correlations. For the special challenge of providing a solderable layer on top of Al, this interface is of major importance for the success of the approach. For new coating processes, this should therefore be in focus.

Even before the in-depth characterization of the solder joints, the initial assessment of the coating was shown to already reveal fundamental properties and issues (homogeneity, wettability). Therefore, quick and meaningful characterization methods (such as OCA) are very beneficial.

Lastly, also the details of the interconnection process are important for the applicability of a coating approach. Solder alloy, flux, temperature range and soldering time influence the required thickness of the coating layer and the choice of materials. Low-temperature soldering on the other hand would most probably allow to use the roll-cladded Al/SnPbAg composite in combination with SnBi solder alloys and reduced soldering temperatures.

7.2. Implementation in Silicon Solar Cells and Modules

7.2.1. Solder Joints in FoilMet® Modules

From the three coating methods evaluated in this thesis, sputter coating and wet-chemical processes are already used in silicon solar cell manufacturing. Sputter coating is established for *e.g.* the deposition of transparent conductive oxides on SHJ solar cells and wet-chemical metal deposition is used in alternative metallization techniques such as plating.

Roll cladding on the other hand is not yet used in silicon solar cell manufacturing. However, the approach of the intended FoilMet® process route involves a decoupling of the foil coating process from the rest of solar cell and module production: Thin Al foils with a solderable coating are attached as the rear side electrode by a suitable laser process.[1] As discussed above, all coating techniques offer the possibility of prior coating thin Al foil in principle. For sputter coating, this has already been realized on industrial scale in cooperation with *ROWO Coating* (s. Section 7.1.2).[2] Their Al foils were processed together with Al foils coated on the horizontal sputter coater at Fraunhofer ISE (*cf.* Section 3.1.3). Both are attached to FoilMet® rear sides by adopted laser processes. Then, both groups are interconnected by IR soldering on the industrial stringer and a successful series interconnection of ten FoilMet® solar cells could be shown (s. photo on the left in Figure 7.2).

In general, the FoilMet® solar cell concept offers several advantages over the common PERC structure, as discussed in literature [40]. One of the most challenging process steps is certainly the laser process for the cell rear side (LFC [41], LMB [46,247] or others [47]). By adapting the laser process to the reflectivity and heat properties of the Al foil, a precise electrical contact to the Si wafer is established while reducing the induced damage of the solar cell.

However, considering module integration, these contacts also have to ensure the mechanical attachment of the foil to the Si, withstand string handling during module manufacturing and further stresses during the operation of the module. For solar cell performance, the air gap between Al foil and Si wafer improves the optics of the cell [40]. It could not be verified within this work if this holds through after lamination of the module and could be further investigated.

In combination with the stiff and strong solder joints on coated Al, critical failure modes have been identified in this work: during TC, Al foil ablation is observed, most prominent at the end of the soldered ribbons, due to extraction and contraction of the components under TC. However, the FoilMet® modules tested in this work, all pass the IEC test and show $< -2\,\%$ loss in power after 200 cycles (s. also Table 7.1), on the same level as the state-of-the-art PERC reference with Ag pads (s. Figure 7.2 right).

[1] In the previous chapters, the coating is applied to the foil after the attachment, to omit the laser process adaptation in this work.

[2] A current cost estimation for the industrial implementation of very thin sputter-coated rear sides of FoilMet® solar cells and modules has been presented in [246].

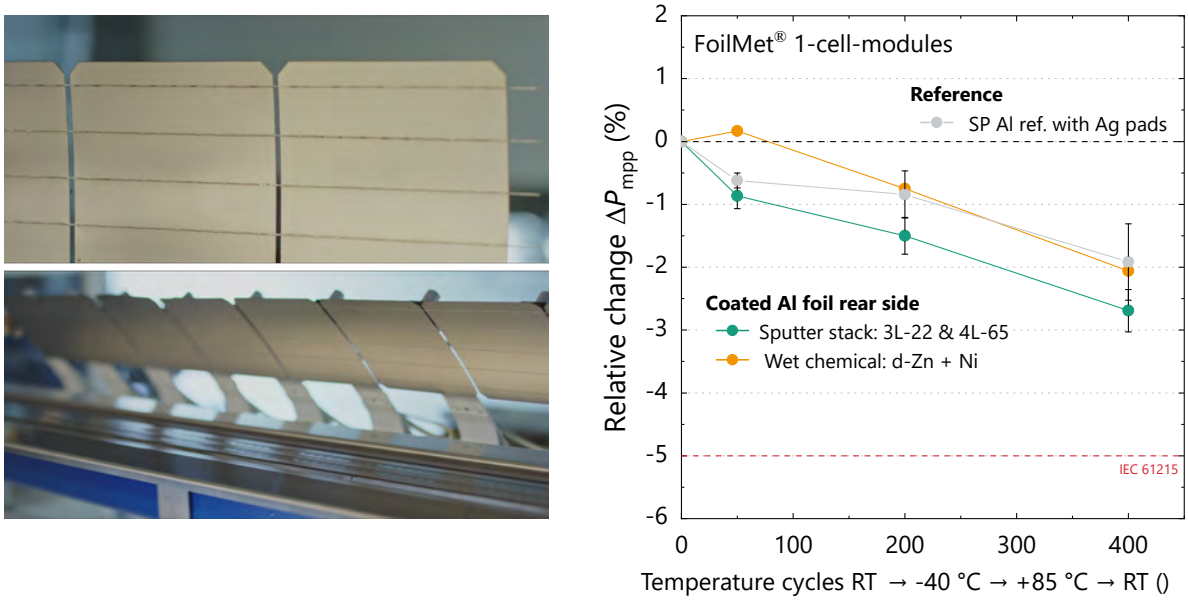

Figure 7.2.: Left: Photos of a string with 10 interconnected FoilMet® solar cells, processed on an industrial stringer at Fraunhofer ISE by IR soldering. © 2020 IEEE [247]. Right: Results of 1-cell-modules with FoilMet® solar cells after TC climate chamber testing. Four modules with sputter-coated Al foil (3× 3L-22, 1× 4L-65) and one module with wet-chemically coated Al foil rear side are tested. All modules show $< -2\,\%$ loss in power after 200 cycles of TC on the same level as the SP Al reference with Ag pads.

Transfer to Other Solar Cell Concepts

The FoilMet® solar cell architecture (*cf.* Section 2.1.3) is limited to monofacial cell concepts due to full coverage of the rear side with Al foil. There are other ideas in progress for using the Al foil only in the cell gaps between two bifacial [248] or shingled solar cells [249].

Since most of the Si solar cells feature Al electrodes, direct contacting of Al will remain of high interest for the photovoltaic industry. This work has shown that wet-chemical and sputter coating can also be used to successfully coat PVD Al electrodes.[3] Both coatings can be realized either as full-area coating or only for local structures by using masks.

[3]Beside the PVD Al process presented in this work (s. Section 5.4.1), thermal evaporation has also been tested with sputter coating by the author, giving similar results. Additionally, other researcher reported on solderable PVD Al for Si solar cells recently [250]. Furthermore, the wet-chemical treatment has been tested on state-of-the-art PERC rear sides with SP Al to replace the Ag pads. The results are published by the author in [188] and presented in the appendix in Figure A.7.

7.2.2. Industrialization of Interconnection Process

The in-depth analysis of the solder joints on coated Al of Si solar cells shows the successful implementation of the soldering process on the industrial stringer (s. Chapter 5, Chapter 6). It has therefore been shown that established equipment of PV industry and common materials (SnPb alloys, no-clean flux) can be used. Additionally, the process is conducted with a high throughput on an inline tool, to allow for the interconnection of about 1800 solar cells per hour (cycle time of 2000 ms per solar cell).

To obtain the best soldering results for any solar cell concept, the temperature profile has to be reviewed. FoilMet® solar cells with coated Al foil and PERC cells with coated PVD Al rear side have shown to be solderable within the common temperature range, used for state-of-the-art PERC solar cells and SnPb solder alloys.

Alternative Interconnection Processes

In PV module manufacturing, SnPb solder alloys are still dominant [11]. Currently, PV is excluded from the RoHS regulations. If this would change within the next years, SnPb will be most probably replaced by appropriate lead-free alloys as *e.g.* SnBi [57, 97].

On the one hand, Bi might reduce the wettability compared to Pb, as seen for Cu surfaces [7]. This could then lead to lower peel forces. On the other hand, wetting and mechanical strength of the joints evaluated in this work are both on a very good level. Therefore, the author suggests that the investigated approaches remain valid, upon changing of the alloy to SnBi base or other low-temperature solders (*cf.* Section 2.2.2).

Furthermore, SnBi-based alloys could be even advantageous to reduce the thermo-mechanical stress to the Al foil on the FoilMet® rear side, since some Bi alloys are known to shrink at a lower rate upon cooling than other solders and expand when solidify [82, 251, 252] or even show almost no change of volume for the combination of Bi with Sn [253].

The usage of round Cu wires instead of Cu ribbons could also be an interesting approach. They are already used for MBB interconnection or SWCT®, mostly in combination with low-temperature alloys [52, 54, 254, 255]. Wave-shaped wires offer the possibility for stress reduction after soldering [51, 120] and could be used to avoid Al foil ablation on the FoilMet® rear side.

Instead of soldering, interconnection with electrically conductive adhesives (ECAs) also provides a low-temperature joining technique. Here, stresses are reduced due to the deformation of the ECA joint during TC [61, 65, 66, 256]. Beyond the scope of this thesis, peel force and specific contact resistance is measured on different sputter-coated Al foils after contacting with ECA. While coating does not influence the peel force (adhesive failure between ECA and ribbon), the contact resistance is significantly reduced. After isothermal aging, R_c increases and exceeds the critical value of $0.5\,\mathrm{m\Omega\,cm^2}$ after a certain time at elevated temperature. The results can be found in the appendix in Figure A.24.

7.2.3. Implementations of Solderable Al Foils

In the context of Si PV, (coated) Al foil is currently not widely-used but could be considered for future developments on cell and module level. Especially roll-cladded Al components offer a huge potential for PV applications. While the module frame mostly consists of extruded Al, Al foil is used in multilayer Al backsheets as diffusion barrier [76].

The advantage of solderable Al can be exploited in the replacement of Cu by Al ribbons. The investigated 200 µm thick composites of Al/SnPbAg, Al/SnCu and Al/Ni can be used to replace solder-coated Cu ribbons. Ribbons could also be manufactured from sputter coated Al foil. Al has a similar electrical conductivity compared to Cu (*cf.* Figure 1.1), so that the dimensions of the ribbons only have to be modified slightly. The replacement of Cu ribbons by Al ribbons would save costs and prevent Cu oxidation and diffusion. After the rolling process of Al foils, the foil is annealed and features a low yield strength of $< 50\,\mathrm{MPa}$ [196, 257]. This has shown to be advantageous as mechanical property of a ribbon to reduce thermomechanical stress after interconnection of Si solar cells [121, 122]. However, to implement such ribbons in the current process, coatings have to be present on both sides of the ribbon and an additional solder paste has to be applied.

Within this thesis, Al ribbons of the composite SnPbAg/Al/SnPbAg (two-sided) have been manufactured and used to interconnect a common PERC solar cell by IR soldering. No additional solder paste was required since the melting point of the coating (here Sn62Pb36Ag2) is low enough to melt during soldering. A successful interconnection as a proof-of-concept could be confirmed by EL imaging.

7.3. Potential Applications in Other Fields

In the 20th century, the usage of Al in industry has increased drastically. The reason for this are the unique advantages of this metal, which lead to manifold fields of application addressed in several textbooks [17, 128, 169, 196, 258, 259]. A short insight is given in the appendix in Section A.2. Prominent applications of Al are: mechanical engineering, packaging industry, aerospace, automotive, electrical industry, battery technology, construction and building technology. Depending on the application and its functionality, the Al component is used as *e.g.* extruded product, tube, rolled product, casthouse product or powder.

For most of these applications, the Al components are welded or brazed to other metals or glued to polymers if no electrical connection is required. To realize an electrical Al connection, high joining temperatures $> 500\,^{\circ}\mathrm{C}$ are used and strong and reliable solder joints on Al can be obtained. The reduction of the process temperature mostly leads to insufficient bonding, especially when joined at ambient air. Therefore, currently soldering of Al is not (or only rarely) used in industry. The widespread conclusion that Al is not solderable has largely lead to avoidance of the metal Al for solder connections. However, there exist some interesting applications for solderable Al (foils), which are shortly addressed in the following.

The potential for the usage of solderable Al (foils) in other sectors than PV depends on the requirement for the Al component. In general, soldered Al joints do have a reduced stability and resistivity against corrosion compared to brazed or welded Al joints. The presented results of this work show the overall potential of the coating approaches and the stability of the solder joints under the tested conditions, derived for PV. Several discussions with industry experts in the field of rolled Al products have obtained interesting possible applications in other fields, listed below. Some findings of this work might be utilized, while additional adjustments may be required:

- Chiller and heat exchanger in *e.g.* automotive industry [128, 195, 243–245, 260]
- Thin Al foils in battery technology as cathode foil [195, 243, 244, 261]
- Cladded Al foils as corrosion barrier or refinement [128, 245]
- Wire bonding of Al foils in power electronics [243, 244, 260]
- Thin Al foil used for packaging industry, *e.g.* sealing by induction soldering [245]
- Replacement of Cu wires by Al wires [245]
- Exchange of solder alloy, as *e.g.* SnAgCu for microelectronics[4] [7]
- To avoid aggressive fluxes developed for contacting Al [128]
- In combination with other soldering techniques as oven soldering, ultrasonic soldering or soldering in vacuum [7]
- General replacement of metals as Ag, Ni or Cu by Al due to its several advantages

[4] Additional amounts of Ag or Cu within the solder (*e.g.* in SnAgCu solder alloys) could lead to a reduced leaching of the top layer (Ag, Ag/Cu, AgCu) of the developed sputter stacks and to additional phase formation at the interface supporting long-term stability.

8. Conclusion and Outlook

In this work, a detailed evaluation of solder joints on different coatings on Al surfaces is performed. The obtained understanding of the material interactions is used to identify strengths and weaknesses of the different approaches. The established knowledge is transferred to Si solar cells for direct contacting of the Al rear side by an industrial soldering process. The most important findings of the three main goals of this work (*cf.* Section 1.3) are summarized in the following.

Investigation of Coatings on Al Regarding Solderability

Nearly all coatings show very good wetting with liquid Sn60Pb40 at 250 °C and ambient air, resulting in small contact angles of 25° to 50°. Here, the appropriate choice of the top layer (Sn99Cu1, Ni, Ag, Ag98Cu2) is essential, to achieve good solderability, as demonstrated.

In the case of very thin solderable layers, the coating technique and the bonding mechanism to the Al surface becomes dominating after soldering. For mechanical bonding by roll cladding, melting of the coating occurs for thin coatings ($< 50\,\mu m$), if the soldering temperature reaches the melting point of the cladding. In addition, micro cracks in the cladded layer cause oxidation of the Al surface below. Both aspects lead to degradation of mechanical and electrical properties. In case of very thin sputter coated layers, a total layer thickness of about 50 nm is sufficient to achieve a mechanically and electrically stable solder joint. For $< 30\,nm$ sputtered layer stacks, oxidation of the Al surface is observed, as well as Al diffusion into the solder joint.

These findings correlate with the material choice of the coating. For all approaches, Ni has shown to be a promising metal for coating Al. It provides solderability with interconnection materials used in PV and enables highly conductive, strong and reliable joints. As already reported in literature [229], the combination of Ni with Cr (*e.g.* Ni80Cr20) improves the functionality of the coating by enhancing the adhesion to Al while preventing Al diffusion.

Analysis of Solder Joints on Coated Al and Their Long-Term Stability

An in-depth evaluation of SnPb-based solder joints on various coatings on Al surfaces is done regarding mechanical, electrical and microstructural properties. The tested material combinations show (90°) peel forces on a very good level $> 3\,N/mm$. Also the specific contact resistance proves highly conductive joints with $< 20\,\mu\Omega\,cm^2$. No significant difference for the mechanical and electrical parameters is observed for coatings with good initial solderability. Both parameters are stable upon isothermal aging at 85 °C (or even 125 °C). Therefore, no critical failure is found for such solder joints on coated Al.

These findings are strongly supported by the results of microstructural analysis. Interfacial reactions are analyzed by cross section samples. For most of the investigated microstructures, no specific formation of IMCs is found. On the one hand, the soldering time of $< 5\,\mathrm{s}$ is very short and no additional heat exposure to promote phase formation is conducted. On the other hand, the diffusivity of the involved metals is very low. For all coatings containing Ni, a marginal diffusion zone of NiSn is found at the interface coating/solder. Within the resolution of the used EDX device in combination with metallographic cross sections, a correct quantification of thin IMCs $< 1\,\mu\mathrm{m}$ is not possible.

For sputter-coated Al foil with Cr/NiCr/Ag/Cu of 10/50/50/4 nm thickness, the interfacial region is analyzed by TEM in combination with EDX, yielding much higher resolutions for quantification. A $\sim$20 nm thin NiSn phase (at some positions the Ni_3Sn_4 IMC is present) is formed, directly below a ternary phase of $Cu_6Ni_1Sn_5$.

A remarkable finding is Cu diffusion through the SnPb solder in case of Ni presence within the joint. Due to the asymmetry of the joints (Cu ribbon/SnPb solder/Ni coating), most likely a Cu concentration gradient along the joint occurs, leading to Cu agglomeration at the Ni interface upon time. No distinct phase formation is measured.

Cu agglomeration is also measured for the Cu/SnPb/Sn99Cu1/Al joints of the roll-cladded samples. By adding $1\,\%_{\mathrm{wt.}}$ Cu into the Sn cladding layer, adhesion to the Al foil is increased.

In general, the observations of the solder joints show that diffusion zones and phase formation support mechanical strength of the joints, while the electric properties remain unaffected for the investigated parameter range.

Process Transfer to Industrial Infrared Soldering

In addition to the fundamental assessment, the process transfer for soldering of coated Al surfaces on established interconnection equipment of PV is evaluated. For wet-chemically and sputter-coated Al surfaces, this has successfully been demonstrated for IR soldering on an industrial stringer. The typical temperature range, used for SnPb-based solder alloys, could be used in combination with no-clean flux. For each of the tested coatings (2 µm plated Ni after Zn treatment, 65 nm thick 4-layer sputter stack of Cr/NiCr/Ag/Cu), several Si solar cells with Al foil rear side (FoilMet®) or PVD Al rear side are processed. A reliable interconnection process with a high throughput of $< 2\,\mathrm{s}$ per solar cell could be realized for both cell types.

The stability of the solder joints, as well as the coatings is shown with 1-cell-modules in TC and DH climate chambers. All FoilMet® modules yield $< -2\,\%$ loss in power after TC 200, on the same level as the state-of-the-art PERC reference modules (with Ag pads). This proves the industrial potential of reliable solder joints on coated Al in a PV module and the possibility for coating Al of other solar cell concepts.

Outlook

In this work, it is shown that a high variety of material combinations is of great benefit to find an optimal coating for Al. In cooperation with a manufacturer of roll-cladded composites, a similar optimization of the coating could be aimed by careful **matching of**

the cladding process, the used material combination and the desired Al foil thickness of $< 50\,\mu m$. The combination of roll cladding with electroless plating should be considered as well. After thinning of the Al foil, plating of Sn or Ni can be performed to allow for solderability of the thin Al foil [195]. For the wet-chemical coating approach, the **Ni plating time could be further reduced** (currently: 8 min of plating leads to $\sim 2\,\mu m$ of plated Ni), since the sputtered Ni layer has shown to work successfully with a thickness far below 500 nm.

The analysis on material level shows that the usage of a **simple and cost-efficient sample structure** (here coated 200 µm thick Al foil) can generate a fundamental understanding of the material interactions. Additionally, **optical contact angle measurements** are demonstrated as a strong method to evaluate the solderability of a metal surface, in good agreement with the obtained peel force after soldering. This approach could be used to estimate the **potential of solderable coatings** for Si solar cells in future work.

The results on module level show **strong, highly conductive and reliable solder joints**, while the adhesion of the thin Al foil (in combination with these joints) is the critical interface for a stable module performance. The mechanical stability of the laser contacts between Al foil and Si wafer should be optimized by using TC climate chamber tests as criterion for the overall stability of this approach. Current work of John *et al.* already prove significant improvement of the mechanical contacts without further damage of the semiconductor [46]. In addition, smaller ribbons or wave-shaped wires could be tested for **stress-reduced interconnection** of FoilMet® solar cells. To consider a possible future annulment of the RoHS exclusion for PV, and to develop a "green" module, soldering with **lead-free alloys** (*e.g.* SnBi) should be evaluated and compared to the obtained results of this work.

The developed processes for direct contacting Al surfaces on Si solar cells by soldering offers the possibility for the application on **other monofacial solar cell concepts**. In this work, a successful transfer to PERC solar cells with PVD Al has already been shown for wet-chemical and sputter-coated Al.[1]

For a successful transfer to mass production and to show the overall potential of the developed approaches, full-size modules[2] with sputter-coated Al foil should be manufactured and tested according the requirements given in the IEC standard [79]. At the final point of this thesis, the most industrially feasible production of a **full-size FoilMet® module** would include the industrial roll-to-roll sputter coating of the Al foil with a $< 50\,nm$ thick 2-layer system of NiCr/AgCu. This solderable Al foil can then be used within the FoilMet® solar cell fabrication route (*cf.* [43, 188]) to be attached to the rear side of the Si wafer by a laser process. The results of this thesis demonstrate that the established solder interconnection process and module lamination of PV can then be applied to process high-efficient PERC modules with Al foil rear side and less Ag consumption.

[1] In addition, solar cells with thermally evaporated Al have been tested with sputter coating, yielding similar results to the presented solar cells with PVD Al (not shown in this work).

[2] Instead of a 60-cell-module with full-size solar cells, the interconnection of 72 half cells should be considered since this will also reduce the stress to the Al foil after interconnection.

A. Appendix

A.1. Photovoltaic Energy in the Global Context

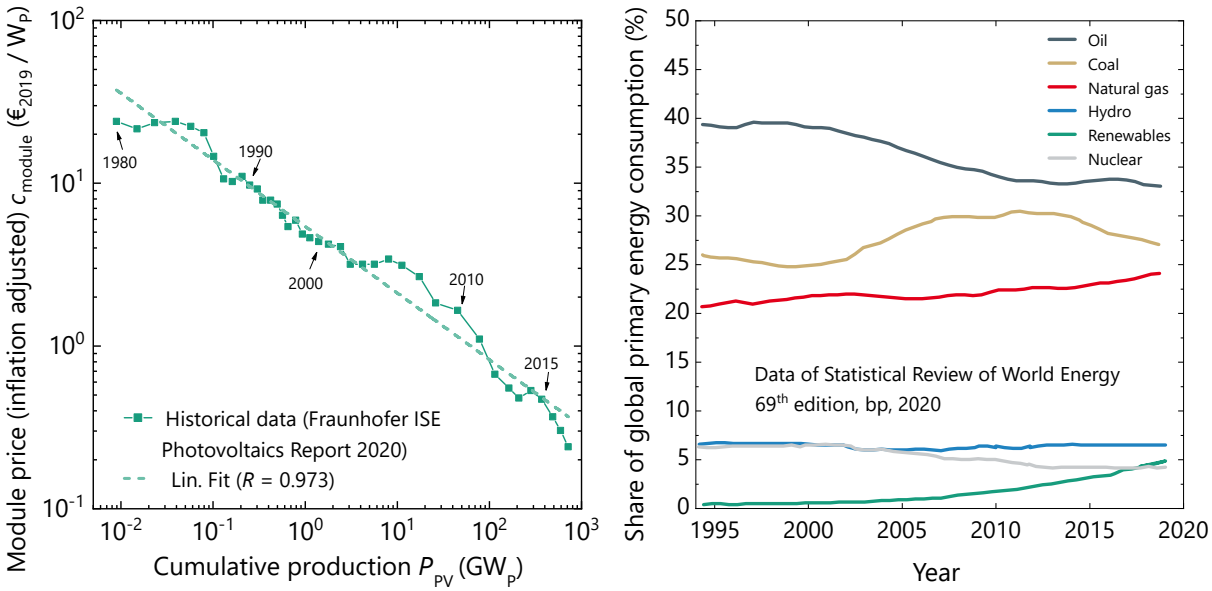

Figure A.1.: Left: Learning rate for PV. Data taken from the Fraunhofer ISE Photovoltaics Report 2020 [4]. The fitted linear trend implies a price reduction of 24 % for every doubling of cumulative production. Right: Share of global primary energy consumption for different technologies. Data taken from Statistical Review of World Energy 2020 [10]. In 2019, the share of renewables rose to 5.0 % for primary energy consumption and to 10.4 % for total electricity generation.

A.2. The Century of Aluminum

At the end of the 19th century, Al became popular and an economic competitor. In 1886, Hall and Héroult developed the first cost-effective method to extract Al from aluminum oxide. One year later, Bayer's method for extraction of Al from bauxite became popular and is, until today, the most common technique used for Al extraction [17]. The value chain of Al is sketched in Figure A.2 from the raw material to the final product, including recycling.

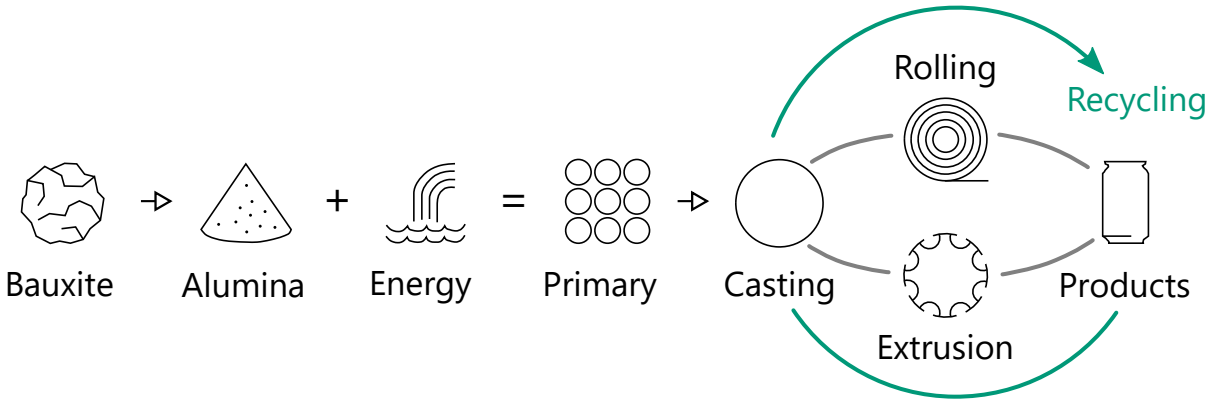

Figure A.2.: Sketch of aluminum value chain. Redrawn after [262].

In the 20th century, the usage of Al in industry has increased drastically. The reason for this are the unique advantages of this metal, which are summarized in the following [6, 17, 128, 169, 196]:

- High electric conductivity ($\sigma_{Al} = 37.7 \times 10^6\,A\,V^{-1}\,m^{-1}$)
- Good thermal conductivity ($\lambda_{Al} = 235\,W\,m^{-1}\,K^{-1}$)
- High reflectance ($> 85\,\%$ for 200 nm to 900 nm)
- High strength-to-weight ratio
- Resistant to corrosion, long-lifetime
- Low oxygen permeability
- Passivating properties
- Light-weight ($\rho_{Al} = 2.7\,g\,cm^{-3}$)
- Cost-efficient (<1 € per kg)
- Most frequent metal in earth crust, good availability
- High recyclability (for secondary Al 95 % less energy is required)

The textbooks "Aluminium-Taschenbuch 1-3" are highly recommended, providing an in-depth insight into the world of aluminum [128, 169, 196].

A.3. Resistive Losses per Solder Joint

In a state-of-the-art PERC solar cell architecture with five busbars, the current of the solar cell is split up to five solder joints. For the cell operating in mpp mode, this results in

$$I = \frac{1}{5} \cdot I_{\mathrm{mpp}} \tag{A.1}$$

$$\approx \frac{1}{5} \cdot 9\,\mathrm{A} = 1.8\,\mathrm{A}. \tag{A.2}$$

for each joint. The solder joint itself measures a width of approximately 0.8 mm (busbar width) and a length of $l \approx 0.15\,\mathrm{m}$. Neglecting the solder layer, the cross section A of the ribbon is

$$A = 0.90\,\mathrm{mm} \times 0.22\,\mathrm{mm} \tag{A.3}$$

$$= 0.20\,\mathrm{mm}^2 = 0.2 \times 10^{-6}\,\mathrm{m}^2. \tag{A.4}$$

With the conductivity of Cu $\sigma_{\mathrm{Cu}} = 58.1\,\mathrm{AV^{-1}m^{-1}} = \frac{1}{\varrho_{\mathrm{Cu}}}$, the loss in power due to the interconnection can be estimated by

$$P = I^2 \cdot R \tag{A.5}$$

$$= I^2 \cdot \varrho_{\mathrm{Cu}} \cdot \frac{l}{A} \tag{A.6}$$

$$= (1.8\,\mathrm{A})^2 \cdot \frac{1}{58.1\,\mathrm{AV^{-1}m^{-1}}} \cdot \frac{0.15\,\mathrm{m}}{0.2 \times 10^{-6}\,\mathrm{m}^2} \tag{A.7}$$

$$\approx 40.5\,\mathrm{mW}. \tag{A.8}$$

This results in a loss in power of less than 1 % for each ribbon of a 5BB interconnection. For a holistic calculation considering all effects of the interconnection, it is refereed to literature, addressing also *e.g.* optical losses due to shading [123, 238, 263, 264].

A.4. Layout for FEM Simulation

In the industrial soldering process, the Cu ribbons are joined to the front busbars and rear pads of the solar cell. Due to the different CTE values of Si, Ag metallization and Cu (*cf.* Table 2.3), thermomechanical stress is induced during cooling. To visualize the stress distribution, a **f**inite **e**lement **m**odel (FEM) is used and a simulation conducted by Andreas Beinert using COMSOL Multiphysics [118]. The results are presented in Section 2.2.4.

Figure A.3 shows the geometry of the simulated solar cell on front and rear side. In addition, the layout after interconnection with ten Cu ribbons (five on the front and five on the rear) is given.

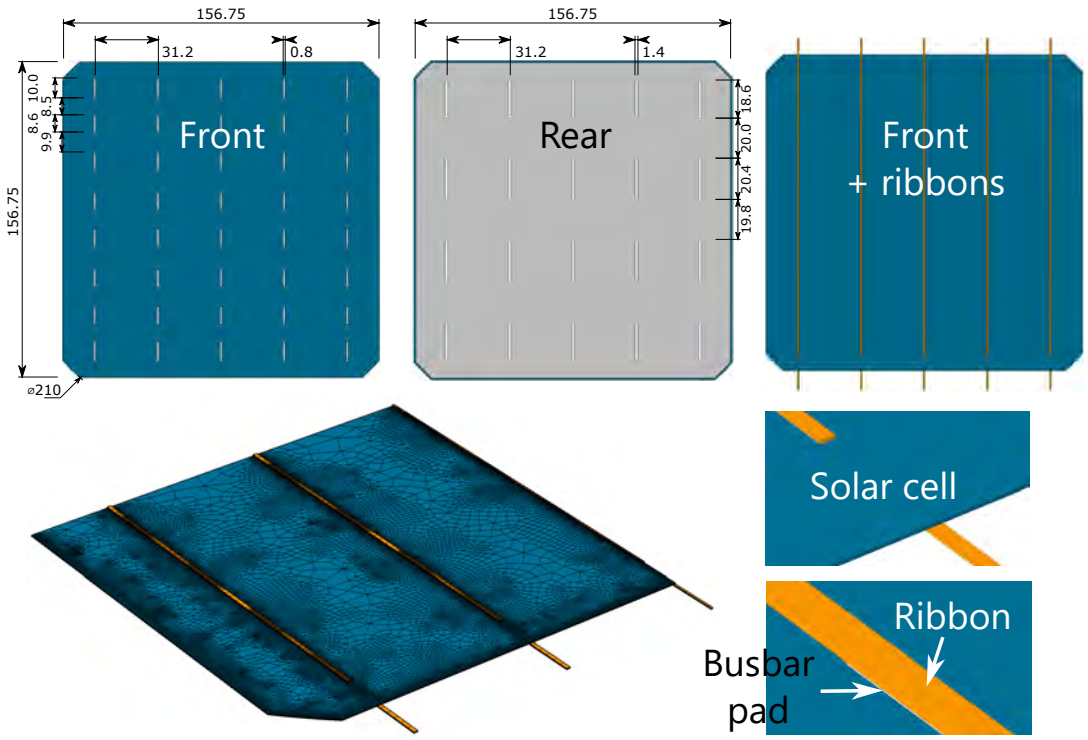

Figure A.3.: Layouts for FEM simulation of thermomechanical stress after soldering a monofacial solar cell. Front side: 5BB design with 8 pads per busbar. Rear side: full area Al electrode with 4 Ag pads per busbar. Ribbons: Cu core of 0.800 mm × 0.215 mm without solder layer. All numbers given in mm.

The simulation is done for one interconnected solar cell of Cz-Si with 156.75 mm edge length, pseudosquare (210 mm diameter) and a thickness of 180 µm. The solder layer on the ribbon is neglected, whereas the height of the ribbon is extended from 200 µm to 215 µm. The input parameters for the simulation (geometries, CTE, Young's modulus E, Poisson's ratio ν) are listed in Table A.1.

Table A.1.: Input parameters for FEM simulation on thermomechanical stress upon cooling a solar cell after the soldering process.

	Solar cell	**Front pads**	**Rear pads**	**Rear side**	**Ribbon**
Material	Si	Ag paste	Ag paste	Al paste	Cu
Length (mm)	156.75	var.	var.	156.00	156.75
Width (mm)	156.75	0.80	1.40	156.00	0.80
Height (µm)	180	30	15	15	215
CTE ($10^6\,\mathrm{K}^{-1}$)	2.3 - 4.7	10	10	16	17
E (GPa)	Stiffness	7	7	6	70
ν (-)	matrix	0.37	0.37	0.34	0.35
Ref.	[107–109]	[110, 111]	[110, 111]	[112]	[113]

A.5. Phase Diagrams

Typically, the concentration c of an alloy is given as the weight fraction of the element Y on the total weight of the alloy ($\%_{\mathrm{wt.}}$). In physics, the concentration is normally given in atomic percent ($\%_{\mathrm{at.}}$). The conversion of a binary alloy XY (in $\%_{\mathrm{wt.}}$) into xy (in $\%_{\mathrm{at.}}$) is

$$\mathrm{x}(\%_{\mathrm{at.}}) = \frac{\mathrm{X}(\%_{\mathrm{wt.}})/m_{\mathrm{X}}}{\mathrm{X}(\%_{\mathrm{wt.}})/m_{\mathrm{X}} + \mathrm{Y}(\%_{\mathrm{wt.}})/m_{\mathrm{Y}}} \cdot 100 \tag{A.9}$$

m_{X} and m_{Y} are the atomic weights (in u). For the solder alloy Sn60Pb40 (given in $\%_{\mathrm{wt.}}$), the composition in atomic percent is $72\,\%_{\mathrm{at.}}$ Sn and $28\,\%_{\mathrm{at.}}$ Pb.
W

The most important binary phase diagrams for this thesis are given in Figure A.4. A collection of binary and ternary phase diagrams, as well as a fundamental introduction into the theory of phase diagrams can be found in the ASM handbook on alloy phase diagrams [100].

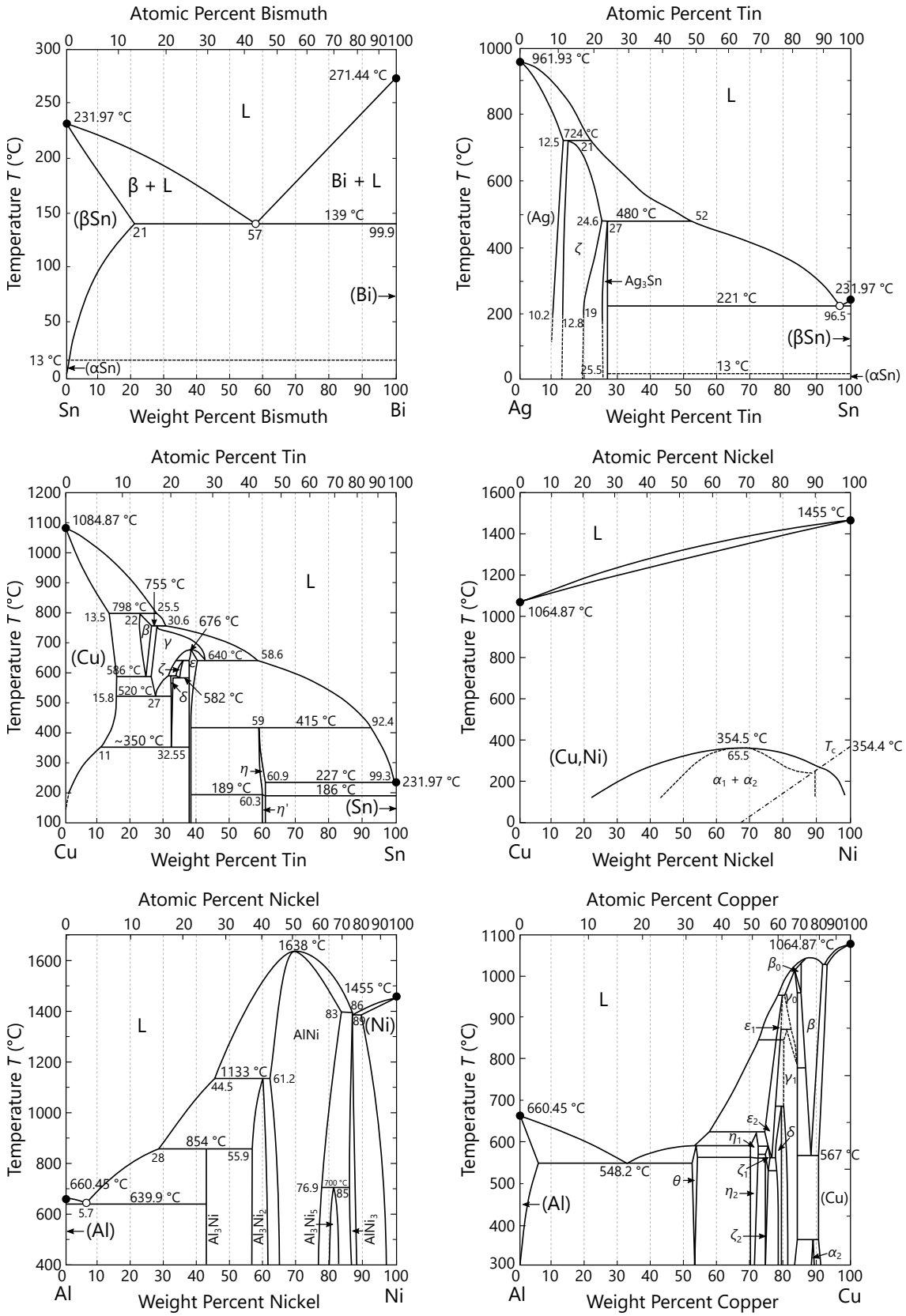

Figure A.4.: Phase diagrams of different binary alloys. Redrawn after [100].

A.6. Preparation of Samples by Metallography

For cross section analysis, the sample of interest is cut to defined dimensions and the cross section has to be polished [265]. Depending on the involved materials and the size of the sample, either focused-ion beam (FIB) or mechanical polishing can be performed. The latter one is mostly used in this work, since the solder joints on Al foils, on solar cells or within the solar module make up a too large area to be polished by an ion beam.

A cutting machine "Isomet High Speed Pro" of *Buehler* is used to cut the sample into the desired dimensions ($\sim 2\,\text{cm} \times 2\,\text{cm}$). Figure A.5 shows the different process steps.

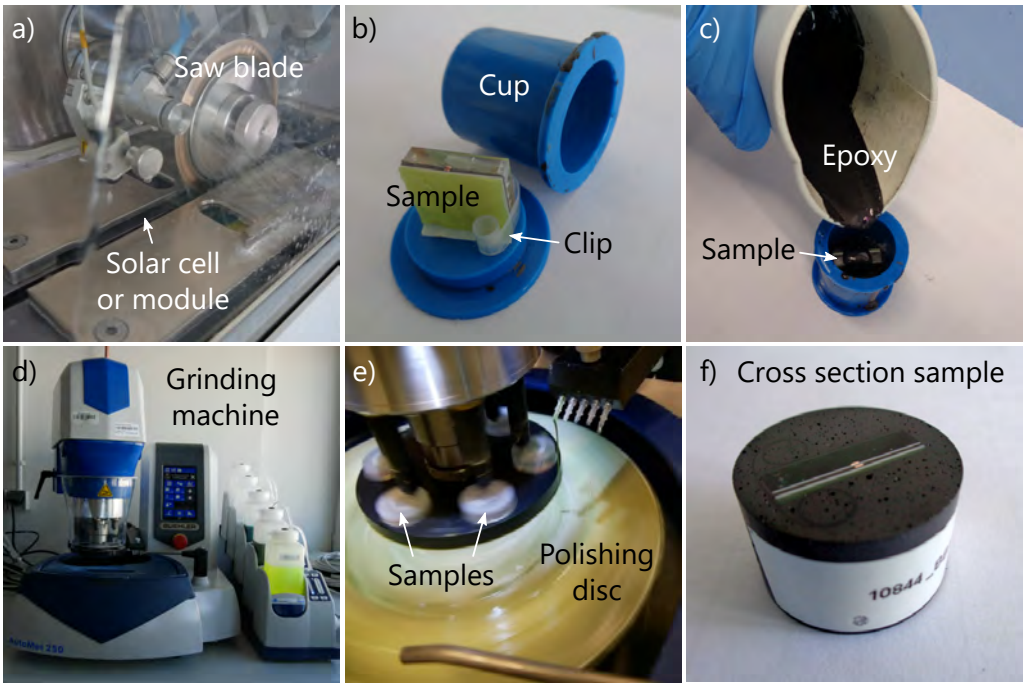

Figure A.5.: Preparation of cross sections by metallography. a) Cutting of sample with a cutting machine. b)-c) Embedding of sample into graphite-containing epoxy. d)-e) Mechanical polishing of the sample. f) Final cross section sample (diameter: 25 mm). © Fraunhofer ISE

After cutting, the sample is mounted to the ground of a cup using a small clip. For embedding, an epoxy is filled into the cup, fully covering the sample. For the samples investigated within this thesis, graphite-containing epoxy is used to allow for SEM analysis of the cross section samples. After hardening of the epoxy, the sample can be removed from the cup and put into the grinding machine. A machine "AutoMet™ 250 Pro" of *Buehler* is used, allowing for simultaneous polishing of six samples. Different polishing discs are utilized to mechanically remove material from the top of the cross section by pushing the sample towards the rotating discs. By adjusting the polishing recipe, disc and/or suspension (grain size), the rate of material removal can be reduced, going to finer polishing after each step. The quality of the cross section is checked by optical microscopy. Figure A.5 f) shows the final cross section sample, here of a FoilMet® solar module with solder joints.

A.7. Additional Data of Solder Joints on Roll-Cladded Al Foils

For the roll-cladded system Al/SnPbAg, the contact resistance is measured after exposure to damp and heat. The results are presented in Section 4.4.2. Figure A.6 illustrates the trend of the specific contact resistance for increasing aging time.

Assuming $R_c \propto t^{1/3}$, the critical value of $R_c = 500\,\mu\Omega\text{cm}^2$ [180] would be reached at around $t \approx 19\,700\,\text{h}$ ($\approx 2.2\,\text{a}$).

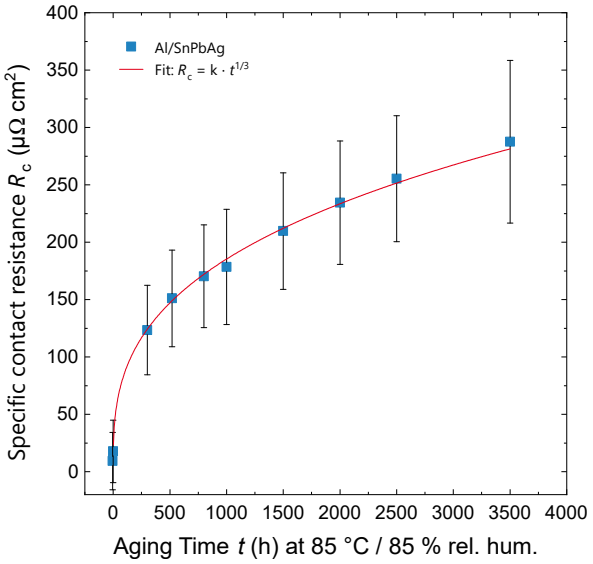

Figure A.6.: Specific contact resistance R_c of solder joints on composite Al/SnPbAg, laminated into glass/EVA/backsheet. The resistance is measured after damp heat testing. Fit quality: $R^2 = 0.995$ with $k = 18.5\,\Omega\text{cm}^2\text{h}^{-1/3}$.

A.8. Additional Data of Solder Joints on Wet-Chemically Coated Al Surfaces

A.8.1. Solder Joints on Screen-Printed Al

The process sequence used for wet-chemical treatment of FoilMet® solar cells and PERC with PVD Al rear side is tested on state-of-the-art PERC solar cells with screen-printed (SP) Al as well. Figure A.7 shows SEM cross sections after each process step.

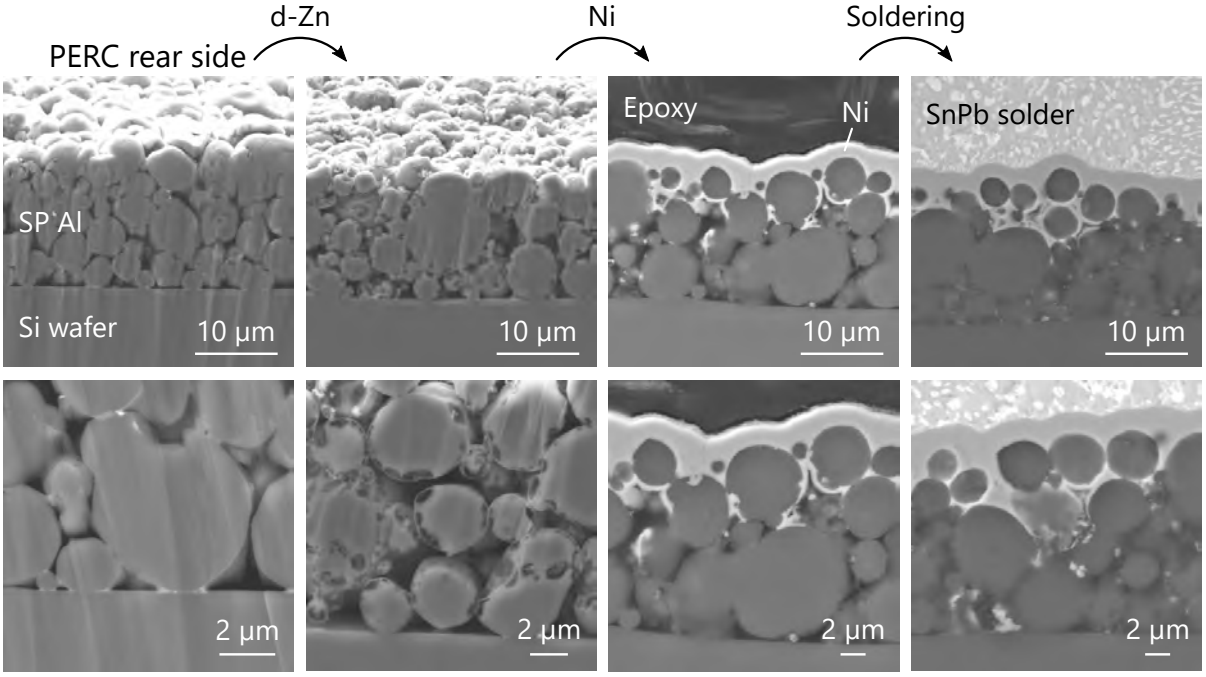

Figure A.7.: SEM images (10 kV, 20 kV with solder) of wet chemical treatment of PERC Al rear side. To provide solderability, the screen-printed (SP) Al on the rear side is treated with a double zincate (d-Zn) process, followed by electroless Ni plating.

The zincate process attacks the surface of the spherical Al particles, whereas parts of the spheres withstand the Zn solution. Most probably, the Al_2O_3 layer is locally thinner or the chemical reaction partly stronger (*i.e.* longer), resulting in the structures found in the images in the second row in Figure A.7. Ni plating leads to a 2 µm to 5 µm thick Ni layer, with a similar appearance as found on Al foil and PVD Al (*cf.* Sections 5.3 and 5.5.3). The Ni layer is closed and void-free, providing good solderability.

After soldering, a 90° peel force measurement reveals an adhesive failure between Al and Si wafer and low peel forces $< 0.2\,\mathrm{N/mm}$. Since these Al pastes are not optimized for a strong adhesion to the wafer, this interface is currently the limiting part of the interconnection. Further discussion can be found in the author's publication [203].

A.8.2. *I-V* Data of Solar Cells before and after Wet Chemical Coating

Figure A.8 shows the *I-V* data of the five FoilMet® cells (green) and the 12 cells with PVD Al (orange), all coated with d-Zn+Ni on the rear side. In light green/orange, the initial *I-V* data is given, in darker green/orange, the corresponding data after coating (*cf.* Section 3.4.1 for evaluation of *I-V* data). Additionally, uncoated cells are measured as reference for each group. Their mean value and corresponding standard deviation is given by the grey squares, serving as measurement control.

The efficiency level of the PERC cells with **PVD Al** is about 3 % lower than for the FoilMet® cells. This is basically due to the not optimized process route for evaporation of Al by PVD and subsequent local alloying by LFCs. The optimization of this process chain was not focus of this thesis. Additionally, this process combination is limited to a maximum voltage level, depending on the quality of the Si wafer [266], which was not considered here. No measurable difference between 2 µm and 4 µm thick PVD Al could be found. Therefore, the results presented in the next sections are not split anymore. The difference in thickness is kept in mind for the result discussion of the climate chamber tests on module level.

Overall, the **FoilMet®** cells show a slight reduction in open circuit voltage V_{oc} and short circuit current I_{sc} after coating, resulting in a loss in power of $\Delta P_{mpp} = -0.13\,\mathrm{W}$. For the five FoilMet® reference cells, theses losses also occur, which refers to a general cell effect, not correlated to the wet-chemical coating process. PERC-based solar cells with a *p*-doped Si wafer have been shown to feature degradation effects after processing, induced by light (**l**ight **i**nduced **d**egradation: LID) and elevated temperature (**l**ight and **e**levated **t**emperature **i**nduced **d**egradation: LeTID) [241, 242]. To separate these unwanted cell effects in the experiments, it is recommended to undergo a degradation and regeneration process before the *I-V* measurement [267]. This can be realized by light soaking, where the cells are illuminated with a light source for at least 48 h [268]. This procedure is not done for the presented solar cells. Due to limited process capacity, the *I-V* measurements before and after coating were taken up to six month apart.

Furthermore, a reduction in fill factor *FF* due to an increase in series resistance R_s is measured for the FoilMet® solar cells. All reference cells show the same absolute change, whereas one can suppose this effect occurring from the pin contacting during *I-V* measurement. Two solar cells feature a significantly lower *FF* of around 77.6 % and a higher series resistance. These two cells are processed slightly different from the other three FoilMet® cells. Within the Zn bath, these cells are held vertically, whereas the others stayed horizontally within the bath. The latter may lead to a slightly longer process time and therefore to a more homogeneous Ni layer. The results in Section 5.4.3 will show, that with these two cells, the automated interconnection process failed because most of the ribbons do not stick well to the Ni-coated Al foil.

EL images of the coated solar cells are exemplarily shown for each cell type in Figure A.9, presented in the following.

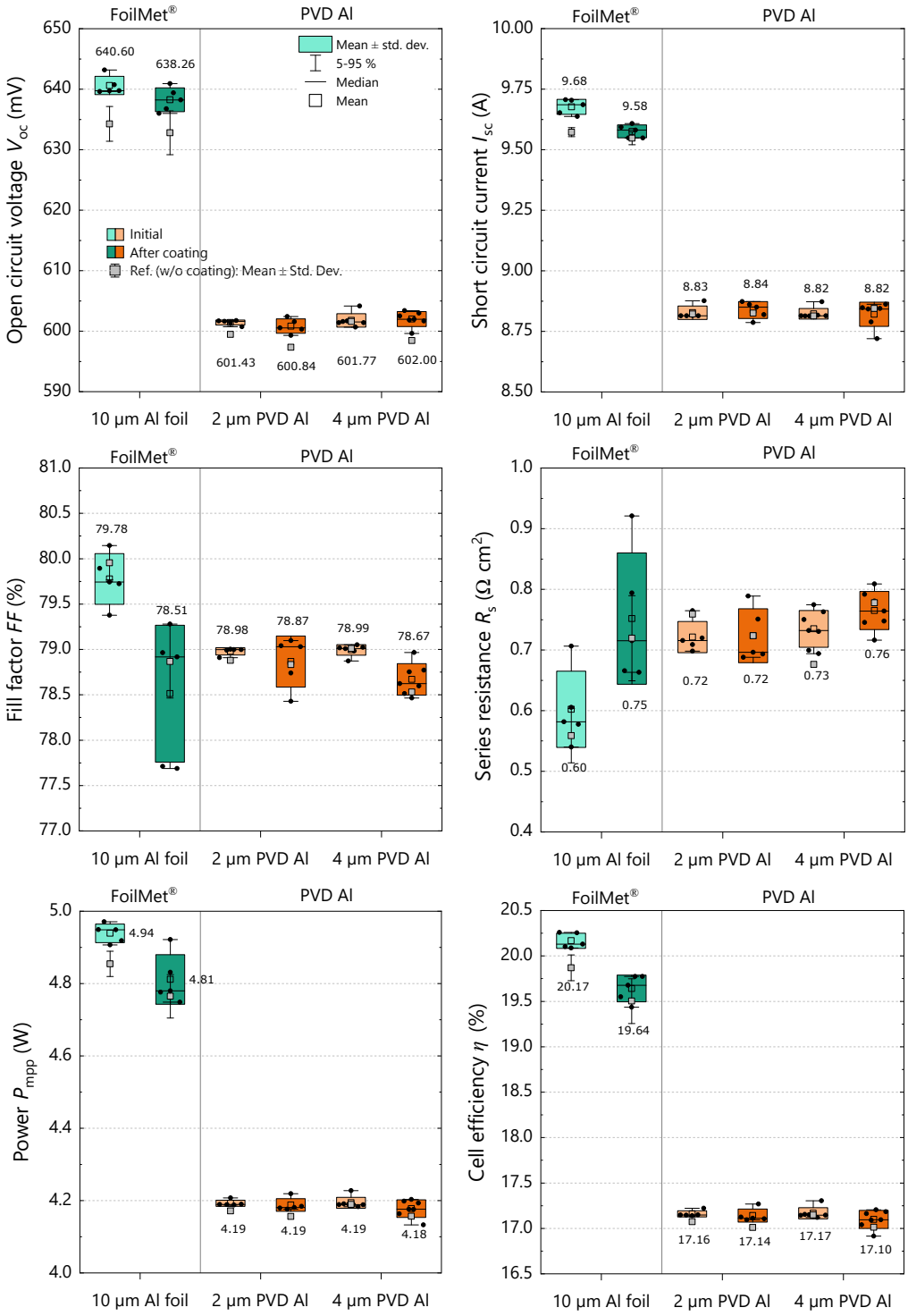

Figure A.8.: *I-V* data of solar cells (FoilMet® and PVD Al rear side), before and after wet-chemical coating (d-Zn + Ni) of the rear side electrode.

A.8.3. EL Images of Solar Cells after Wet-Chemical Coating

To characterize the electrical performance of the solar cells, *I-V* measurements are performed. This initial characterization is done for every solar cell within this thesis, before module integration. The data is provided in the corresponding section for solar cells with wet-chemical coating on the rear side (*cf.* Section 5.4.2). In addition, state-of-the-art PERC solar cells with screen-printed Al and Ag pads on the rear side are characterized.

To obtain local information on the cell performance and identify cell cracks, finger defects or other recombination losses, electroluminescence (EL) imaging is conducted of each solar cell. The results are given in the following, presenting an EL image of one solar cell of each processed group.

It should be mentioned that the signal for the cells with PVD Al is much lower than for the FoilMet® cell and the SP Al reference due to a much lower V_{oc}. Therefore, the signal for this EL image is multiplied by a factor of 3.6, while keeping the measurement conditions constant. In contrast, the SP reference has a higher V_{oc} than the FoilMet® cells (not shown in the *I-V* data), whereas the EL signal is scaled down by a factor of 0.3. These scaling factors are given above the images and should be kept in mind during comparison.

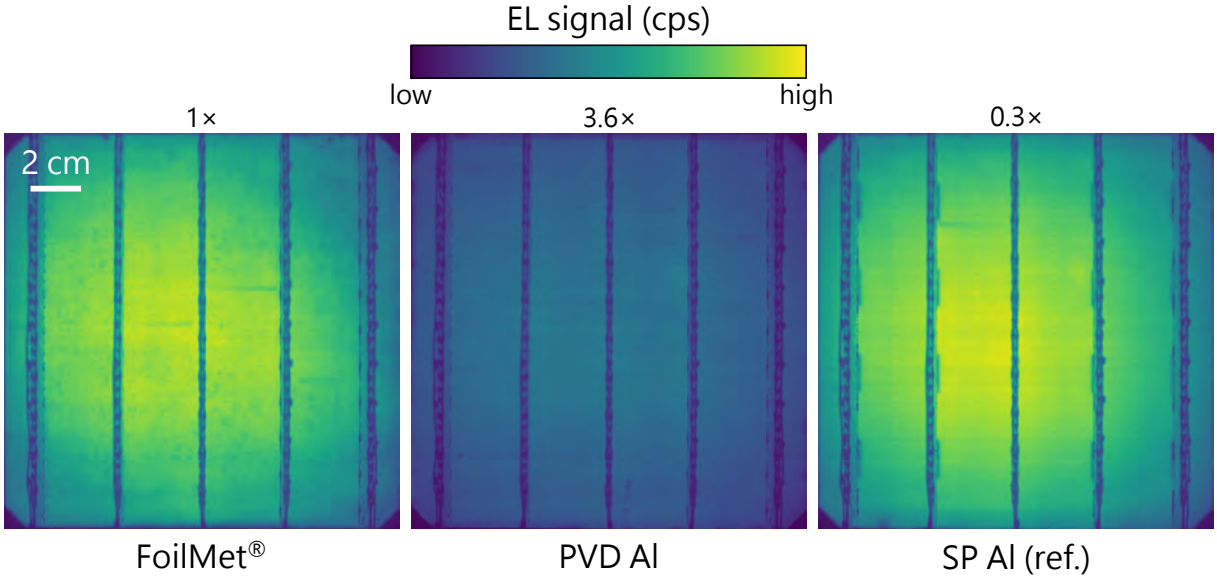

Figure A.9.: EL images of three solar cells after wet chemical coating with d-Zn + Ni, one of each cell type. In accordance with the *I-V* results, no striking issues could be found; all images feature a homogeneous EL signal.

A.8.4. Peel Force after Soldering on PERC Solar Cells

As reference to FoilMet® solar cells and PERC with PVD Al rear side, the state-of-the-art PERC solar cell with Al paste and Ag rear pads is processed. After the interconnection on the industrial stringer, the peel strength of solder joints on front and rear side is evaluated by a 90° peel force measurement. Figure A.10 shows the results of the peak evaluation (metallization with pad design) yielding $(1.31 \pm 0.39)\,\mathrm{N/mm}$ (normalized to the pads width $w = 0.8\,\mathrm{mm}$) and $(0.95 \pm 0.55)\,\mathrm{N/mm}$ (normalized to the contact width $w = 0.9\,\mathrm{mm}$) for front and rear side, respectively. The latter one is stated as reference level in the corresponding graphs for peel force measurements on coated solar cell Al rear sides (*cf.* Figure 5.13 and Figure 6.23).

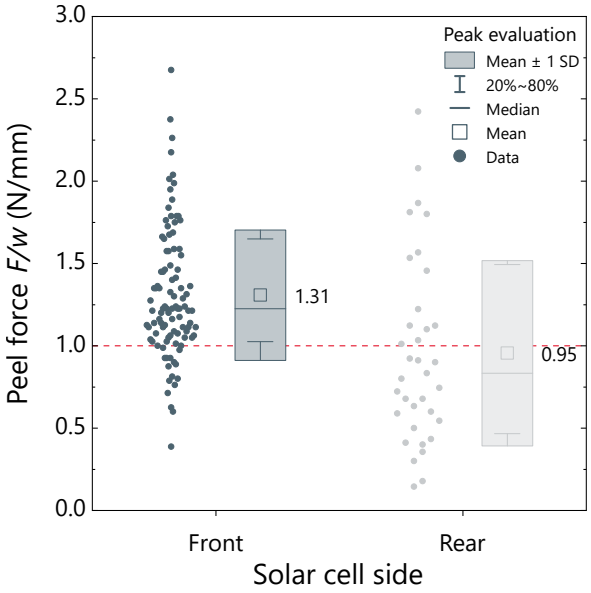

Figure A.10.: Peel force of front and rear side of PERC reference solar cell after soldering. The obtained values serve as reference to the other two cell groups, since they are processed from the same solar cell batch.

A.9. Additional Data of Solder Joints on Sputter-Coated Al Substrates

In Chapter 6, a huge amount of different sputter stacks (variation of layer material and thickness) is tested on Al foils. To focus on the main aspects, only extractions of the data are given. In the following sections, the complete data obtained for each investigation is shown. The color code for the different stacks is kept constant.

A.9.1. Measurement Data of Optical Contact Angle

For five different stacks, the optical contact angle α is measured with liquid Sn60Pb40 on a hotplate. The results of this wetting test is given in Figure A.11 for different materials and thicknesses.

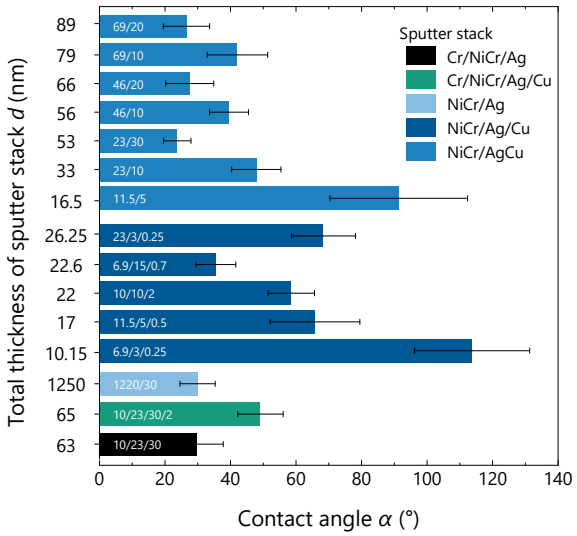

Figure A.11.: Optical contact angle α of different two-, three- and four-layer sputter stacks on Al foil. The tests are conducted with Sn60Pb40 at 250 °C at ambient air. The error bars state the standard deviation of 10 measurements each. Within one group (color code), the data is arranged according to the total thickness d of each stack.

A.9.2. Measurement Data of Wetting Balance

In addition to optical contact angle measurements, four samples of sputter-coated Al foils are characterized with a wetting balance. The results and a comparison to the optical contact angle is given in Section 6.1.2. Figure A.12 shows the measurement data, obtained by recording the force F over the measurement time t during the test.

On the y-axis on the right side, the calculated contact angle α_{WB}, using Equation 3.10, is given. The exact procedure is described in the Experimental 3.3.1.

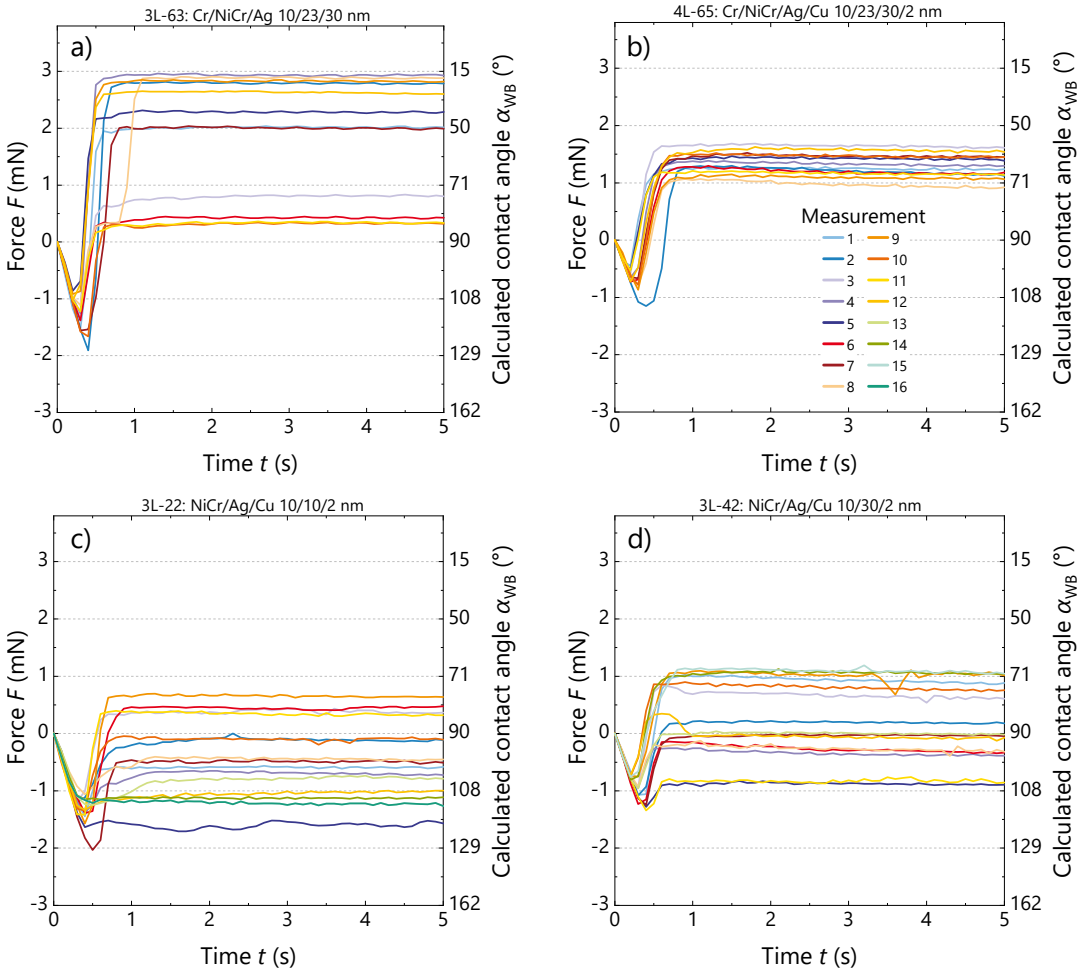

Figure A.12.: Measurement data of wetting test performed with a wetting balance. A solder bath with Sn63Pb37 at a temperature of 230 °C is used. Directly before the test, the samples are fluxed. For each sample, at least 12 measurements are conducted. Four different sputter stacks are deposited onto 200 µm thick Al foils on both sides. The detailed measurement procedure is described in the Experimental 3.3.1.

A.9.3. Adhesion of Solder Joints

Figure A.13 contains the data of all combinations, tested to evaluate solder joints on sputter-coated Al foil. The normalized peel force is plotted against the total thickness of the sputter stacks. The color code gives the different stacks, whereas the symbols state the number of layers and the material of the top layer.

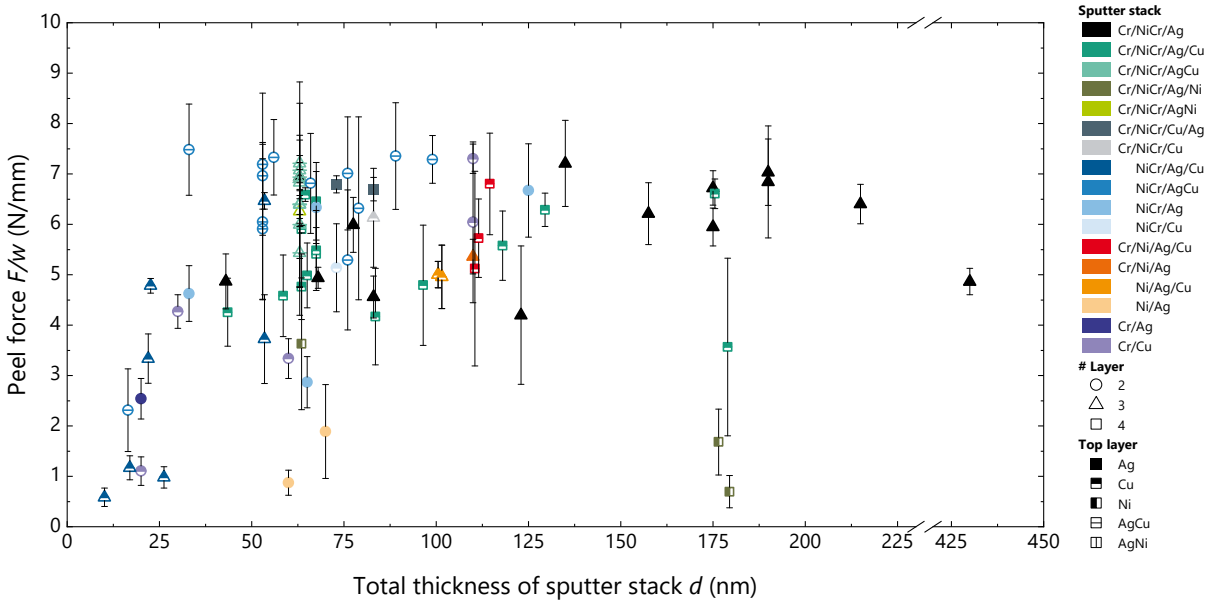

Figure A.13.: Data of peel force measurement (according to DIN EN 50461 [174]) of solder joints on 200 µm thick Al foils with different sputter coatings (color code). The solder joints are created by manual soldering with a soldering iron at 280 °C with Sn62Pb36Ag2. To provide solderability of the Al foils, they are coated with either a two-, three- or four-layer stack (shape of symbols). Each data point includes at least four measurements over a length of 150 mm.

The achieved peel strength depends on the chosen material of the stack, as well as on the layer thickness. A systematic evaluation is given in Section 6.2. A more detailed visualization of the (same) data is given in Figure A.14 on the left. On the right hand side, the influence of Cu within the top layer is shown by SEM top view images and the measured peel force for the variation of the Cu content within the top layer of stack Cr/NiCr/AgCu 10/23/30 nm.

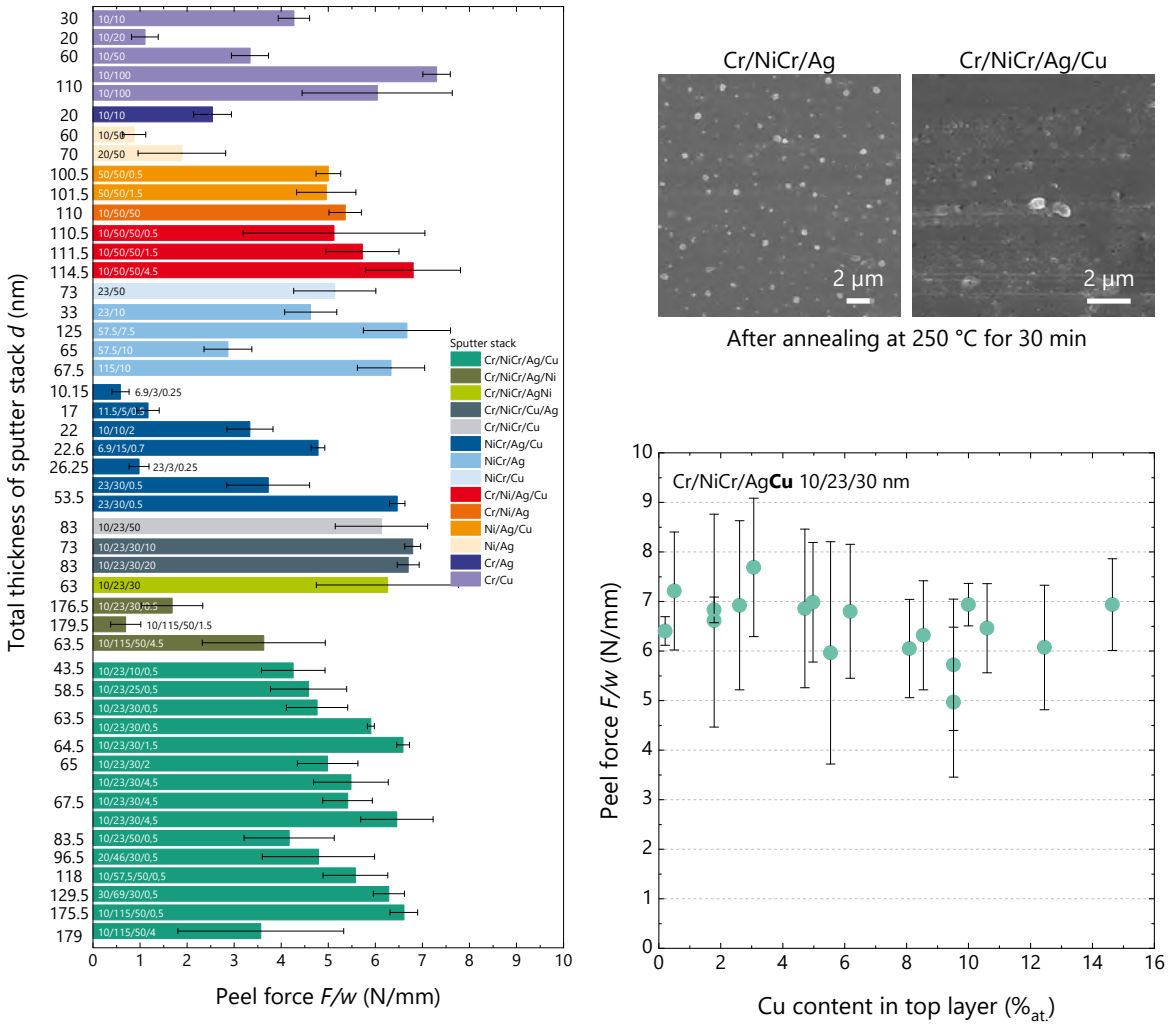

Figure A.14.: Additional data of peel force measurement, arranged by the sputtered solderable coating (color code). Left: Overview on different stacks, which are not shown in detail in Section 6.2. Right: SEM top view images of coated Al foil, without and with additional Cu layer on top. After annealing for 30 min at 250 °C, the Ag layer agglomerates, which can be reduced by additional Cu (© Fraunhofer ISE). The graph shows the variation of the Cu content in the top layer AgCu to investigate the influence on the mechanical strength of the solder joints.

A.9.4. Additional Measurements of TEM Samples

For microstructural analysis of solder joints on sputter-coated Al, two material systems are selected and a TEM analysis is performed. The results are presented in Section 6.3.2 to 6.3.4.

Figure A.15 shows an HAADF TEM image and the corresponding EDX map of a solder joint on a coated Al foil. The Al is coated with the stack 4L-144 (Cr/NiCr/Ag/Cu 10/50/50/4 nm). The images show the complete lamella, analyzed in detail in Section 6.3.

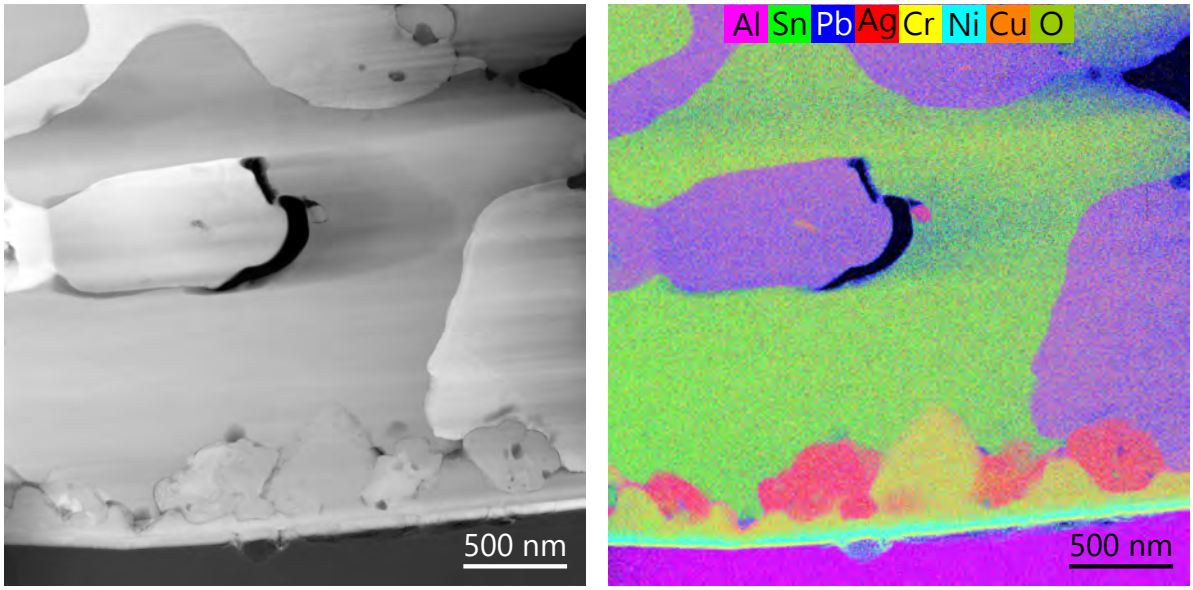

Figure A.15.: HAADF TEM image and corresponding EDX mapping of solder joint (Sn62Pb36Ag4) on sputter-coated (4L-114: Cr/NiCr/Ag/Cu 10/50/50/4 nm) Al foil. Details are given in Figure A.16

Figure A.16 shows the different maps for the elements in the interfacial region. The presence of a closed Cr and NiCr layer over the whole sample length is clearly visible, as well as several phases formed above the stack.

Additionally, a second TEM lamella is investigated with the thinner stack 3L-22 (NiCr/Ag/Cu 10/10/2 nm). The mapping of the interfacial region over the whole sample is presented in Figure A.17.

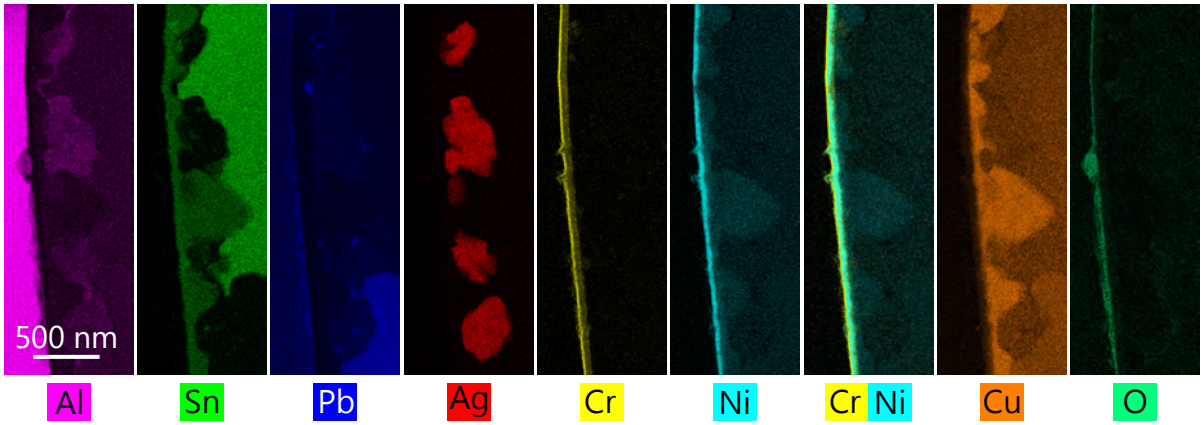

Figure A.16.: EDX mapping of interface of solder joint (Sn62Pb36Ag4) on 200 µm thick sputter-coated (4L-114: Cr/NiCr/Ag/Cu 10/50/50/4 nm) Al foil. An overview is given in Figure A.15.

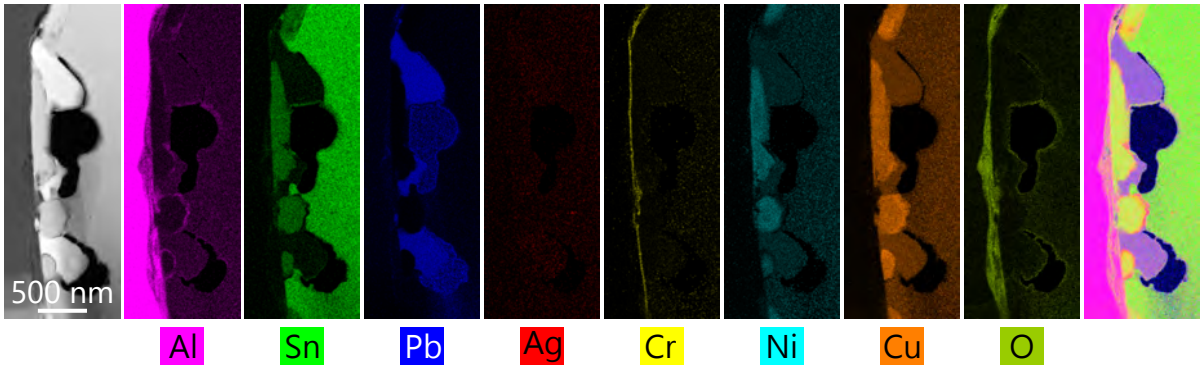

Figure A.17.: EDX mapping of interface of solder joint (Sn62Pb36Ag4) on 200 µm thick sputter-coated (3L-22: NiCr/Ag/Cu 10/10/2 nm) Al foil.

A.9.5. *I-V* Data of Solar Cells before and after Sputter Coating

Before and after the sputter coating process of the rear side of solar cells, all cells are characterized by *I-V* measurements, as described in detail in the Experimental in Section 3.4.1. The *I-V* parameters are plotted in Figure A.18 for 11 FoilMet® solar cells (green) and 7+7 solar cells with PVD Al rear side (orange). The light colors represent the data before, the darker colors after sputtering. Additionally, uncoated cells are measured for each group as measurement control. Their results are represented by the gray squares, indicating mean and standard deviation. Overall, the data looks very similar to the *I-V* parameters before and after wet-chemical coating, presented in Section 5.4.2 in Figure A.8. All conclusions apply for the present data as well and will shortly be summarized in the following.

The difference in photo conversion efficiency of about 3 % between FoilMet® and PVD Al is caused by the not optimized process chain for evaporation of **PVD Al** and the application of LFCs. The solar cells with PVD Al rear side feature about 35 mV lower open circuit voltage V_{oc} as well as 0.8 A less current I_{sc} in the short circuit condition. The optimization of the cell fabrication is not in the focus of this thesis. Beside this, no measurable difference before and after coating could be found for those cells. Also no impact of the Al layer thickness of 2 µm and 4 µm could be found.

In addition, no influence of the sputter process on electrical cell parameters is found for the **FoilMet®** solar cells. The small changes in V_{oc}, I_{sc}, fill factor *FF* and series resistance R_s are also present for the five reference cells (grey squares) and are caused by unwanted LID and LeTID effects of the cells (*cf.* Section 5.4.2).

To fully exclude any sputter damage of the cells, EL images for each group are exemplarily given in the appendix in Figure A.19, showing no striking issues.

As introduced before, two different sputter stacks are tested for this approach: the 4-layer stack **4L-65** with 65 nm total thickness and the 3-layer stack **3L-22** with 22 nm total thickness. Since the sputter coating process for them is very similar,[1] no influence on cell performance is measured. Therefore the *I-V* data in Figure A.18 is not split.

[1] The main differences are the missing Cr layer and the shorter sputter time for the stack 3L-22.

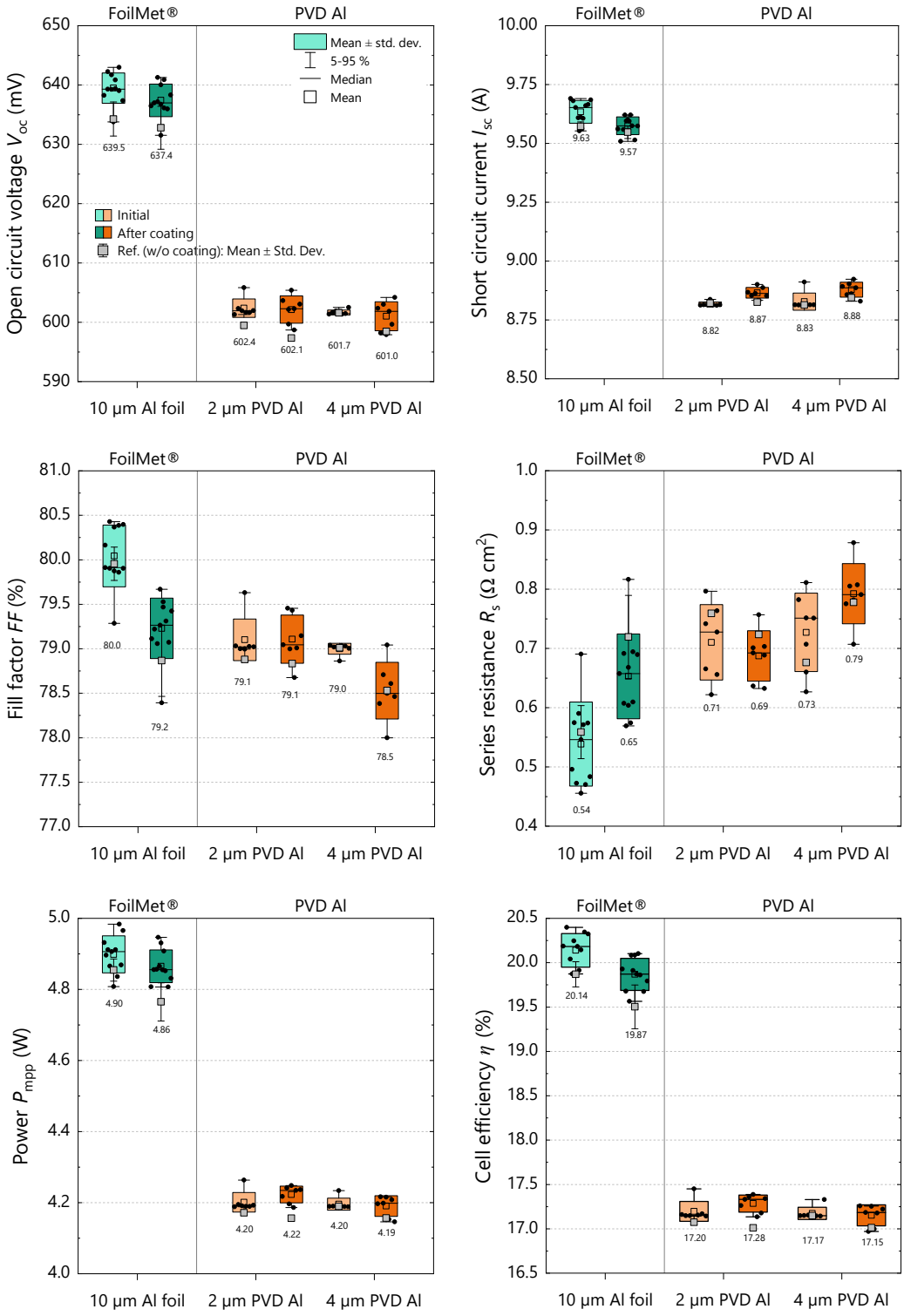

Figure A.18.: *I-V* data of solar cells (FoilMet® (green), PVD Al (orange) rear side), before and after sputter coating of the rear side electrode.

A.9.6. EL Images of Solar Cells with Sputter-Coated Rear Side

To characterize the electrical performance of the solar cells, *I-V* measurements are performed. This initial characterization is done for every solar cell within this thesis, before module integration. The data is provided in the corresponding section for solar cells with sputter coating (*cf.* Section 6.5.1) on the rear side. In addition, state-of-the-art PERC solar cells with screen-printed Al and Ag pads on the rear side are characterized.

To obtain local information on the cell performance and identify cell cracks, finger defects or other recombination losses, electroluminescence (EL) imaging is conducted of each solar cell. The results are given in the following, presenting an EL image of one solar cell of each processed group.

It should be mentioned that the signal for the cells with PVD Al is much lower than for the FoilMet® cell and the SP Al reference due to a much lower V_{oc}. Therefore, the signal for this EL image is multiplied by a factor of 3.6, while keeping the measurement conditions constant. In contrast, the SP reference has a higher V_{oc} than the FoilMet® cells (not shown in the *I-V* data), whereas the EL signal is scaled down by a factor of 0.3. These scaling factors are given above the images and should be kept in mind during comparison.

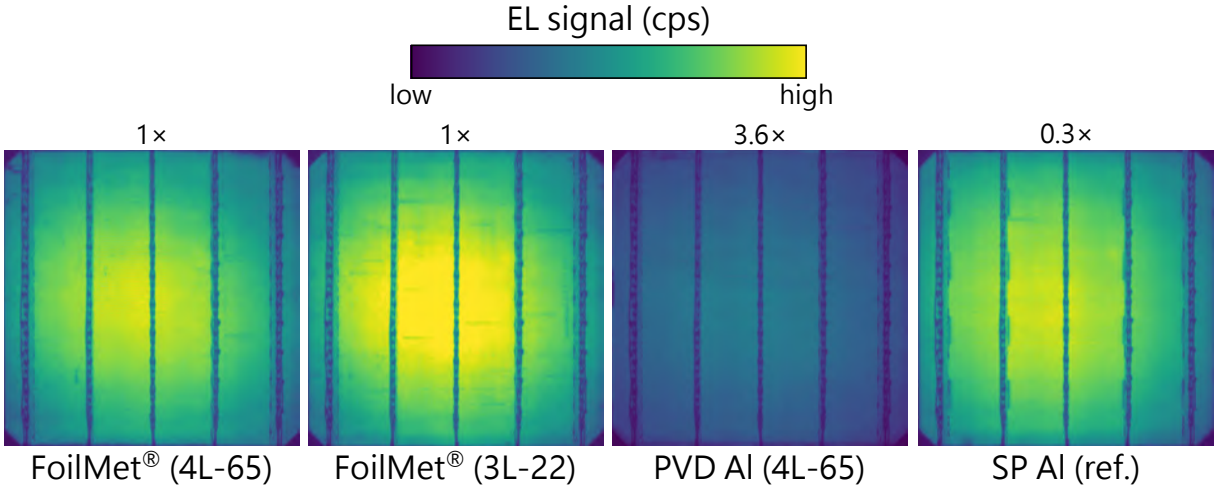

Figure A.19.: EL images of four solar cells after sputter coating with stack 4L-65 and 3L-22. In accordance with the *I-V* results, no striking issues could be found; all images feature a homogeneous EL signal.

A.9.7. EL Images of Solar Cells after Soldering

The following figure provides additional EL images of two FoilMet® solar cells, coated with a 4-layer stack Cr/NiCr/Ag/Cu (4L-65) and a 3-layer stack NiCr/Ag/Cu (3L-22), compared to a SP Al reference. All cells are interconnected with Sn60Pb40 ribbons on an industrial stringer. El imaging is performed after soldering.

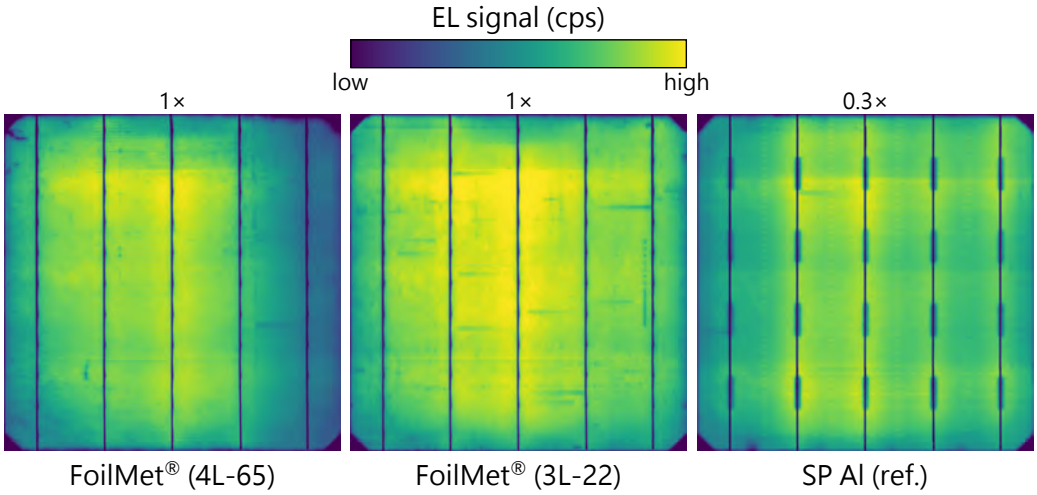

Figure A.20.: EL images after soldering FoilMet® solar cells, coated with sputter stack 4L-65 and 3L-22. The image on the right shows the PERC reference with screen-printed Al rear side and Ag pads. The colorbar shows the EL signal on a linear scale. The scaling factor of the EL signal is given above each image.

A.9.8. Additional EL Images of FoilMet® Modules

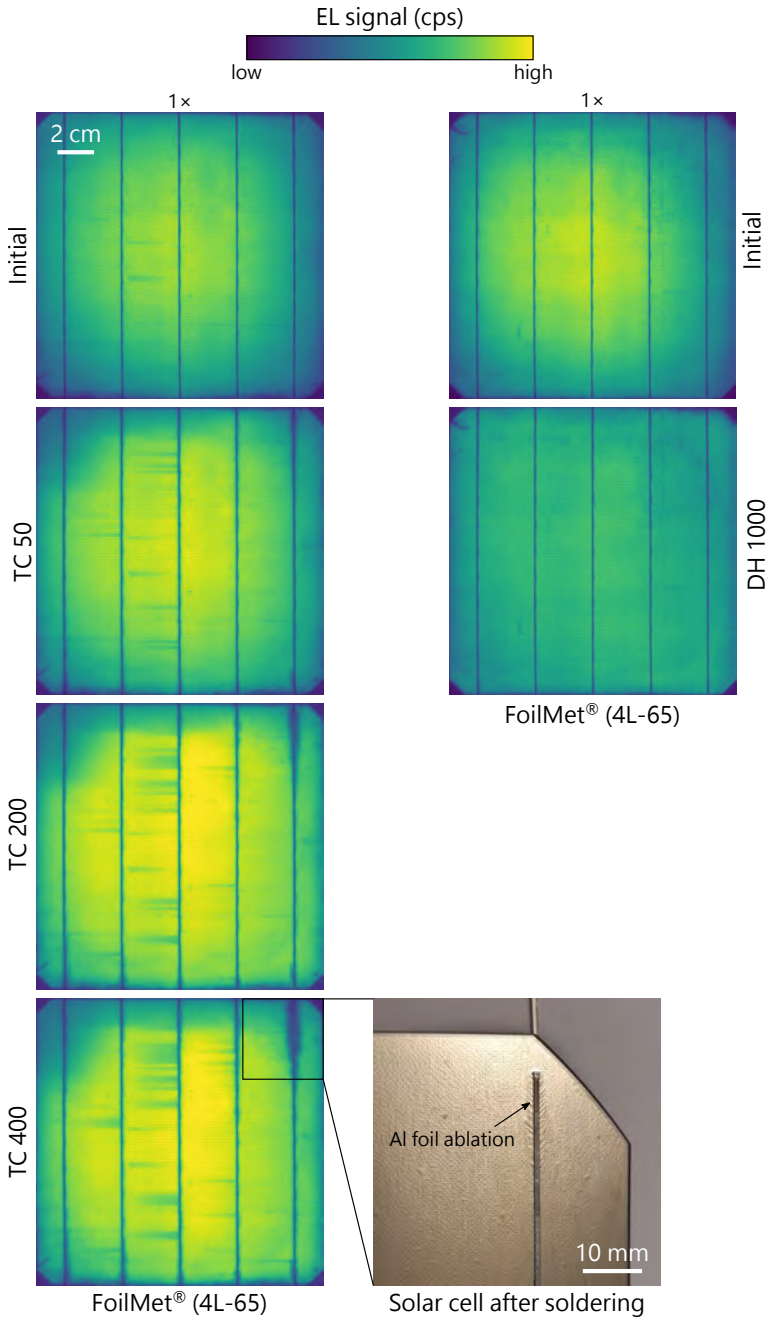

Figure A.21.: EL images of two FoilMet® 1-cell-modules: initially and after TC (left) or DH (right) testing. Both modules are sputter-coated with stack 4L-65 on the rear side. The images are scaled equally. The EL signal is given on a linear scale. In addition, a photograph of a FoilMet® solar cell after soldering is shown to visualize the observed Al foil ablation at the end of the ribbons. The selected photo intentionally shows one of the worse solar cells featuring a lower adhesion between Al and Si than the used solar cells in this work.

A.9.9. Modules with PVD Al rear side after TC testing

The large variation of the *I-V* parameters and the different appearance of the solar cells with PVD Al rear side within the EL images is analyzed in detail. Figure A.22 shows the EL images after TC 400 on the left and the corresponding *I-V* curves on the right. Four modules "1-4" are aged, whereas one module is used as measurement reference. The absolute *I-V* parameters of each module after aging are listed as well.

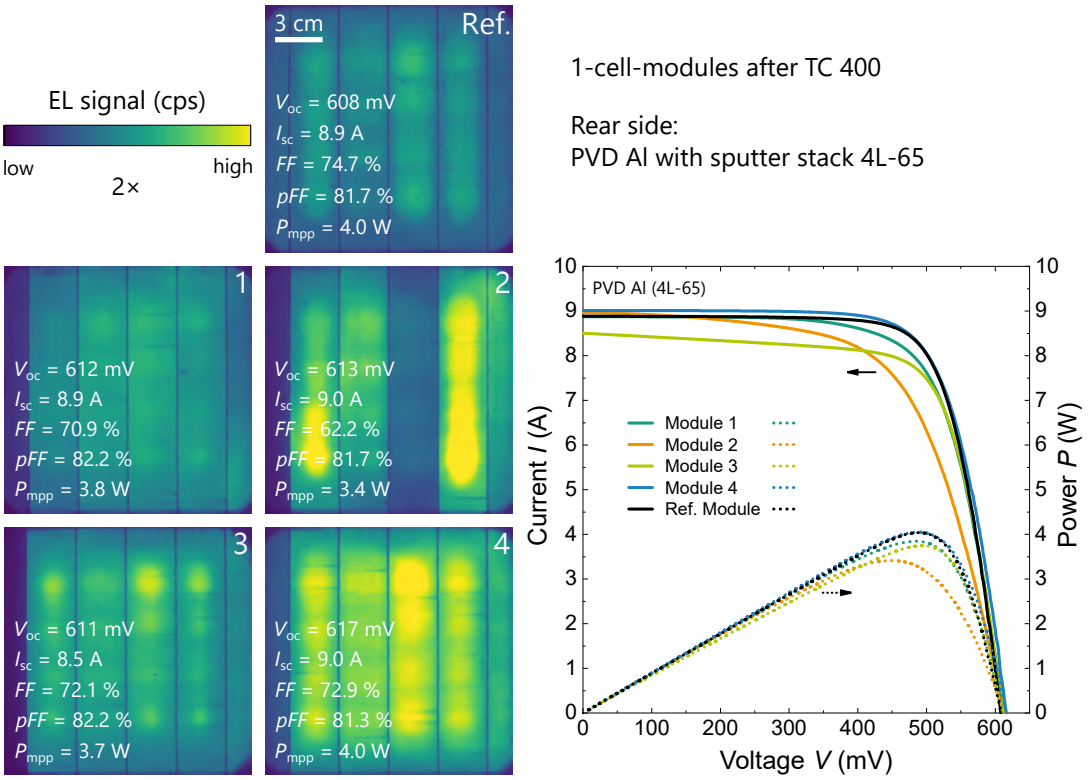

Figure A.22.: EL images (left) and *I-V* graph (right) of four modules after TC 400 and one reference. The solar cells consist of a PERC architecture with PVD Al rear side, coated with the sputter stack 4L-65.

Compared to the reference module (black curve), the fourth module (blue curve) performs very similar. While the *FF* is about 2 % abs. lower for module 4, its V_{oc} is higher. Compared to the initial *I-V* parameters of both modules (which are identical within the measurement uncertainties), the V_{oc} of module 4 increased by (6.3 ± 0.6) mV. Since 85 °C within the climate chamber is too low to improve the Al-Si rear contact further, it is supposed that the PERC structure regenerates due to B-O LID [269]. This cell-specific effect can be observed for all modules, *i.e.* increase in V_{oc} (*cf.* *I-V* data in Figure 6.26) and increase in counts of EL signal (*cf.* EL images in Figure 6.30).

A.10. Further Results

To extend the knowledge generated in this work, additional experiments are carried out for suitable coating approaches. The graphs in the following show results which should be considered for future work.

Figure A.23 left gives an overview on all data generated for different coatings of Al for the strength of the solder joints (y-axis: peel force) and the wettability (x-axis: contact angle). Despite large systematic errors due to manual soldering, the overall trend of an increasing peel force for decreasing contact angle (good wettability) becomes apparent.

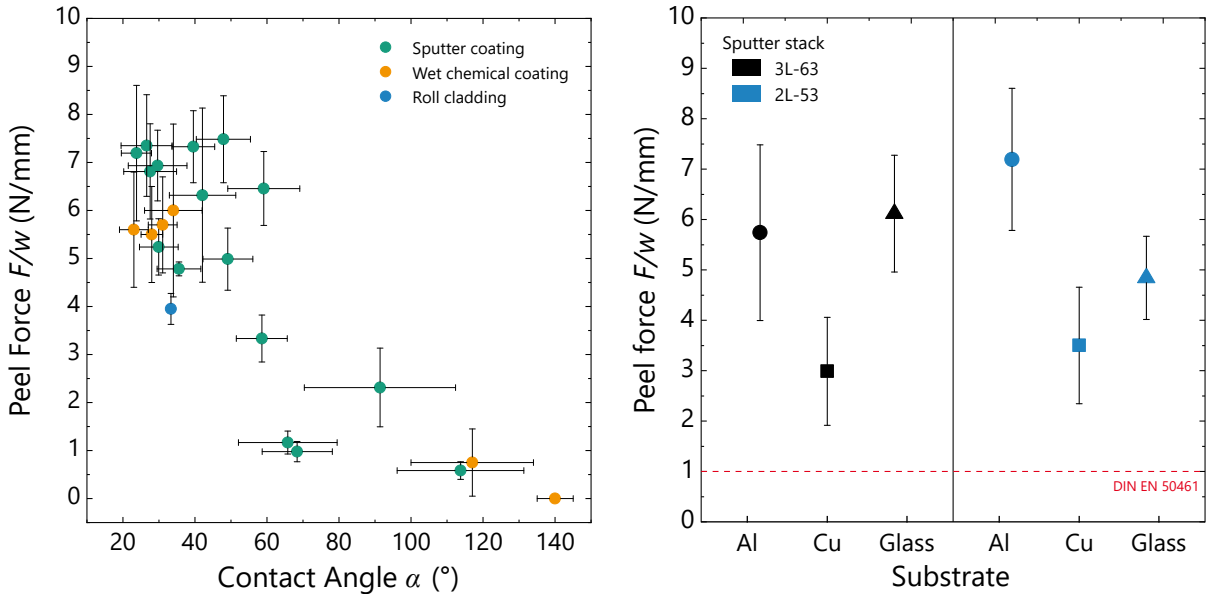

Figure A.23.: Left: Correlation between optical contact angle and peel force of results obtained in this word. Right: Peel force of solder joints on different sputter-coated substrates: Cr/NiCr/Ag 10/23/30 nm (3L-63), NiCr/AgCu 23/10 nm (2L-53).

The graph on the right shows the peel force of sputter-coated Al foils, Cu foils and glass substrates. Two different sputter stacks (color code) are tested on different substrates. This shows the suitability of the developed sputter stacks to provide a solderable coating on several surfaces.[2]

[2]The obtained peel force for the Cu foil is lower than expected due to a poor Cu surface quality (oxidized, dirt).

In addition to soldering, joining with electrically conductive adhesives (ECAs) is used as alternative interconnection technology in the photovoltaic industry. For sputter-coated Al foils, this approach is tested for two different sputter stacks. The results are shown in Figure A.24.

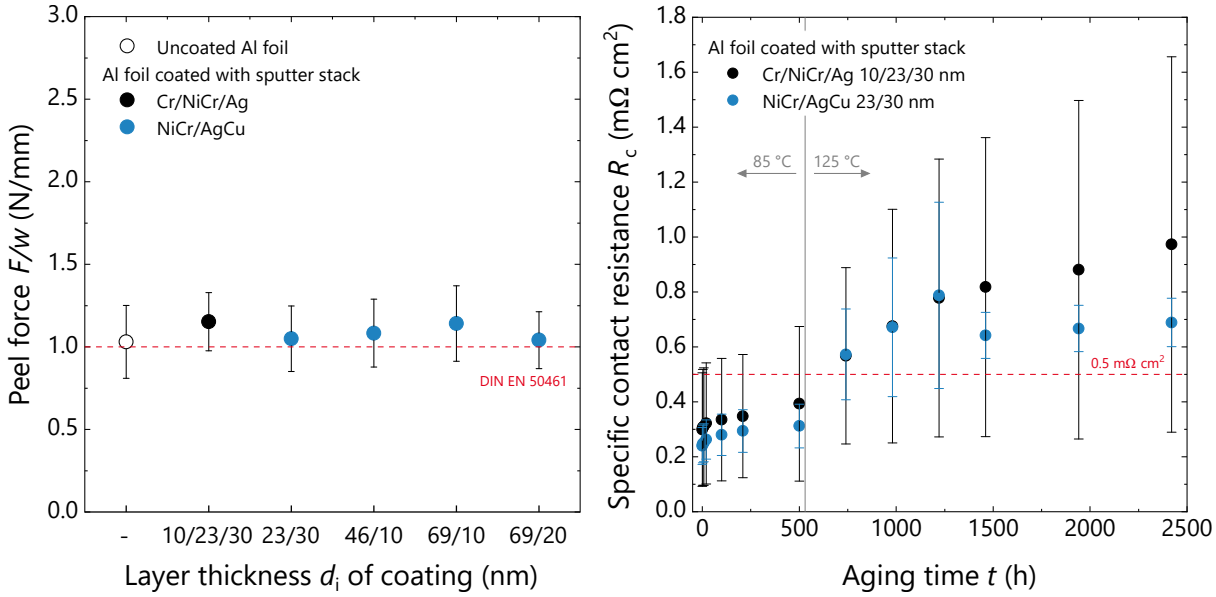

Figure A.24.: Left: Peel force of glued joints on uncoated and sputter-coated Al foil. Each data point represents mean and standard deviation of five 90° peel force measurements according to DIN EN 50461 [174]. Right: Specific contact resistance of glued joints on different sputter stacks on Al foils.

For the tests, a commercially available ECA is used. The sample design is the same as designed for the evaluation of solder joints in this work (*cf.* Section 3.2). As reference, uncoated Al foil is compared to sputter-coated Al foil. In the graph on the left in Figure A.24, the peel force is plotted for different sputter stacks. Regardless of the coating, all samples yield peel forces around 1.2 N/mm; also the joints on uncoated Al. For all combinations, an adhesive failure between ECA and ribbon is observed, identifying this interface to limit these joints.

For the mechanics of the joints, an additional coating of Al does not influence the results. In contrast, an additional coating layer does significantly influence the specific contact resistance of glued joints on Al. The graph on the right in Figure A.24 shows the results. For the uncoated Al foil, no reasonable value could be obtained; the resistance is at leas one order of magnitude higher than the values obtained for sputter-coated Al. Two different sputter stacks are tested (color code), yielding similar results. For 500 h, isothermal aging at 85 °C is conducted, afterwards, the temperature is increased to 125 °C. This results in an increase of R_c, exceeding the threshold value of 0.5 mΩ cm² [180]. For the unaged joints, sputter coating of Al with very thin layer thicknesses < 60 nm is a feasible approach to reduce the contact resistance of glued joints on Al foil.

Glossary

Abbreviations

Acronym	Description
5BB	Five busbar
Al_2O_3	Aluminium oxide
Al-BSF	Aluminium back surface field
ARC	Anti-reflection coating
BB	Busbar
BF	Bright field
BSF	Back surface field
BS	Backsheet
c-Si	crystalline silicon
CTM	Cell-to-module
Cz-Si	Silicon fabricated by the Czochralski process
DF	Dark field
DH	Damp heat
d-Zn	Double zincate process
ECA	Electrically conductive adhesive
EDX	Energy dispersive X-ray
EDXS	Energy dispersive X-ray spectroscopy
EL	Electroluminescence
EVA	Ethylen-vinyl acetat
FEM	Finite element method
FIB	Focused ion beam
FoilMet®	Foil-metallized, registered solar cell concept
HAA(DF)	High-angle annular dark field
IMC	Intermetallic compound
IR	Infrared
ITRPV	International Technology Roadmap for Photovoltaic
LCO	Laser contact opening
LeTID	Light and elevated temperature induced degradation
LFC	Laser fired contact
LID	Light induced degradation

LMB	Laser Metal Bonding
MBB	Multi busbar
MPP	Maximum power point
OCA	Optical contact angle
PECVD	Plasma-enhanced chemical vapour deposition
PERC	Passivated emitter and rear cell
PET	Polyethylene terephthalate
PL	Photoluminescence
psq	pseudo-square
PV	Photovoltaic(s)
PVD	Physical vapor deposition
RoHS	Directive on the restriction of the use of certain hazardous substances in electrical and electronic equipment
RT	Room temperature
SE	Secondary electrons
SEM	Scanning electron microscopy
SHJ	Silicon heterojunction
SnPb	Tin-lead solder
Sn60Pb40	Tin lead solder with $60\,\%_{\text{wt.}}$ Sn and $40\,\%_{\text{wt.}}$ Pb
SP	Screen printing, screen-printed
STC	Standard test conditions
STEM	Scanning transmission electron microscopy
SWCT®	SmartWire Connection Technology, registered technology of Meyer Burger Technology AG
s-Zn	Single zincate process
TC	Temperature cycling
TEM	Transmission electron microscopy
TLM	Transfer-length method
TOPCon	Tunnel-oxide passivated contact
WB	Wetting balance

Symbols

Symbol	Description	Unit
Greek		
α	(Optical) contact angle	$^\circ$
η	Photo conversion efficiency	%
σ	Electrical conductivity	$\Omega\,\text{cm}^{-1}$
τ	Charge carrier lifetime	s
ζ	Surface coverage	%

Symbol	Description	Unit
Latin		
c_i	Concentration of element i	$\%_\mathrm{wt.}$ or $\%_\mathrm{at.}$
CTE	Coefficient of thermal expansion	$10^{-6}\mathrm{K}^{-1}$
d	Thickness	µm
F	Force	N
F/w	Peel force, normalized to contact width w	$\mathrm{N\,mm}^{-1}$
FF	Fill factor	%
I	Current	A
I_sc	Short-circuit current	A
pFF	Pseudo fill factor	%
P_mpp	Power at maximum power point	W
R	Resistance	Ω
$R_\mathrm{p}, R_\mathrm{s}$	Parallel or series resistance (for solar cells)	$\Omega\,\mathrm{cm}^2$
R_c	(Specific) contact resistance	$\mu\Omega\,\mathrm{cm}^2$
t	Time	s
T	Temperature	°C
T_liq	Liquidus temperature	°C
T_m	Melting temperature	°C
T_s	Soldering temperature	°C
T_sol	Solidus temperature	°C
V	Voltage	V
V_oc	Open-circuit voltage	V
x, y	Directions on the surface	cm
z	Depth perpendicular to the surface	µm
Z	Atomic number	
Math symbols		
$\mathcal{O}(x)$	Order of magnitude for values of x	
$[x] = 1$ u	Units of symbol x	
$x \equiv x(r)$	Equal by definition; explicit dependence	
Δx	(Measured) difference of quantity x	
σ_x	Standard deviation on x	

Bibliography

[1] International Energy Agency, "World Energy Model: Documentation," 27.03.2021. [Online]. Available: https://www.iea.org/reports/world-energy-model

[2] Shell International B.V., "Shell Sky Scenario," 27.03.2021. [Online]. Available: https://www.shell.com/energy-and-innovation/the-energy-future/scenarios/shell-scenario-sky.html

[3] United Nations, "The Paris Agreement," 27.03.2021. [Online]. Available: https://unfccc.int/process-and-meetings/the-paris-agreement/the-paris-agreement

[4] S. Philipps, B. Burger, K. Kiefer, C. Kost, R. Preu, S. Nold, J. Rentsch, T. Schlegl, G. Stryi-Hipp, H. Wirth, and W. Warmuth, "Photovoltaics Report 2020: Fraunhofer Institute for Solar Energy Systems (ISE)."

[5] International Renewable Energy Agency, "Trends in Renewable Energy: Statistics Time Series," 27.03.2021. [Online]. Available: https://www.irena.org/Statistics/View-Data-by-Topic/Capacity-and-Generation/Statistics-Time-Series

[6] M. Tao, *Terawatt Solar Photovoltaics*. London: Springer London, 2014.

[7] G. Humpston and D. M. Jacobson, *Principles of soldering*. Materials Park, Ohio: ASM International, 2004.

[8] "Rohstoffpreise," 27.03.2021. [Online]. Available: https://www.finanzen.net/rohstoffe

[9] B. Burger, "Energy Charts," 27.03.2021. [Online]. Available: https://energy-charts.de/

[10] BP p.l.c., "Statistical Review of World Energy," 2020.

[11] ITRPV, "International Technology Roadmap for Photovoltaic (ITRPV): 11th edition, 2019 Results."

[12] M. Green, E. Dunlop, J. Hohl-Ebinger, M. Yoshita, N. Kopidakis, and X. Hao, "Solar cell efficiency tables (version 57)," *Progress in Photovoltaics: Research and Applications*, vol. 29, no. 1, pp. 3–15, 2021.

[13] National Renewable Energy Laboratory, "Best Research-Cell Efficiency Chart," 30.03.2021. [Online]. Available: https://www.nrel.gov/pv/cell-efficiency.html

[14] M. Redlinger, M. Woodhouse, and R. G. Eggert, "The present and future silver cost component in crystalline silicon PV module manufacturing," *Photovoltaics International*, vol. 31, no. 1, pp. 62–74, 2016.

[15] pv magazine, "Silver accounts for 10% of PV module costs," 01.04.2021. [Online]. Available: https://www.pv-magazine.com/2021/03/04/silver-currently-accounts-for-10-of-pv-module-costs/

[16] R. J. Klein Wassink, *Soldering in Electronics*, 2nd ed. Saulgau/Württ: Leuze, 1991.

[17] J. R. Davis, *Aluminum and Aluminum Alloys*. ASM International, 1998.

[18] EUROPÄISCHEs PARLAMENT UND RAT, "RoHS-Richtlinie 2011/65/EU: Beschränkung der Verwendung bestimmter gefährlicher Stoffe in Elektro- und Elektronikgeräten."

[19] D. M. Chapin, C. S. Fuller, and G. L. Pearson, "A New Silicon p–n Junction Photocell for Converting Solar Radiation into Electrical Power," *Journal of Applied Physics*, vol. 25, no. 5, pp. 676–677, 1954.

[20] A. Goetzberger, B. Voss, and J. Knobloch, *Sonnenenergie: Photovoltaik*, 2nd ed. Stuttgart: Teubner, 1997.

[21] M. A. Green, *Solar cells: Operating principles, technology and system applications*. Kensington, NSW: Univ. of New South Wales, 1998.

[22] K. Mertens, *Photovoltaics: Fundamentals, Technology and Practice*. New Jersey: Wiley, 2014.

[23] H.-G. Wagemann and H. Eschrich, *Photovoltaik: Solarstrahlung und Halbleitereigenschaften, Solarzellenkonzepte und Aufgaben*, 2nd ed. Wiesbaden: Vieweg + Teubner, 2010.

[24] A.-E. Becquerel, "Memoire sur les Effets Electriques Produits sous l'Influence des Rayons Solaires," *Comptes Rendus Hebdomadaires des Seances de L'Academie des Sciences*, vol. 9, pp. 561–567, 1839.

[25] A. Einstein, "Über einen die Erzeugung und Verwandlung des Lichts betreffenden heuristischen Gesichtspunkt: Annalen der Physik," *Annalen der Physik*, vol. 322, no. 6, pp. 132–148, 1905.

[26] W. Shockley and H. J. Queisser, "Detailed balance limit of efficiency of p-n junction solar cells," *Journal of Applied Physics*, vol. 32, no. 3, pp. 510–519, 1961.

[27] A. Richter, S. W. Glunz, F. Werner, J. Schmidt, and A. Cuevas, "Improved quantitative description of Auger recombination in crystalline silicon," *Physical Review B*, vol. 86, no. 16, p. 165202, 2012.

[28] O. Höhn, N. Tucher, A. Richter, M. Hermle, and B. Bläsi, "Light scattering at random pyramid textures: Effects beyond geometric optics," in *8th International Conference on Crystalline Silicon Photovoltaics*, ser. AIP Conference Proceedings. Author(s), 2018, p. 030002.

[29] A. Stapf, C. Gondek, E. Kroke, and G. Roewer, "Wafer Cleaning, Etching, and Texturization," in *Handbook of Photovoltaic Silicon*, D. Yang, Ed. Berlin, Heidelberg: Springer Berlin Heidelberg, 2019, pp. 1–48.

[30] M. A. Green, *Third Generation Photovoltaics: Advanced Solar Energy Conversion*. Springer-Verlag, 2003.

[31] P. Saint-Cast, I. Reis, J. Greulich, S. Werner, E. Lohmüller, H. Höffler, J. Haunschild, and R. Preu, "Cz silicon benchmark for p-type PERC solar cells," in *Proceedings of the 32nd European Photovoltaic Solar Energy Conference and Exhibition (EUPVSEC)*, 2016, pp. 1038–1043.

[32] M. A. Green, "The Passivated Emitter and Rear Cell (PERC): From conception to mass production," *Solar Energy Materials and Solar Cells*, vol. 143, pp. 190–197, 2015.

[33] S. W. Glunz, "High-Efficiency Crystalline Silicon Solar Cells," *Advances in Opto-Electronics*, 2007.

[34] J. Mandelkorn and J. H. J. Lamneck, "A new electric field effect in silicon solar cells," *Journal of Applied Physics*, vol. 44, no. 10, pp. 4785–4787, 1973.

[35] M. Rauer, R. Woehl, K. Ruhle, C. Schmiga, M. Hermle, M. Horteis, and D. Biro, "Aluminum Alloying in Local Contact Areas on Dielectrically Passivated Rear Surfaces of Silicon Solar Cells," *Electron Device Letters, IEEE*, vol. 32, no. 7, pp. 916–918, 2011.

[36] A. Lorenz, M. Linse, H. Frintrup, M. Jeitler, A. Mette, M. Lehner, R. Greutmann, H. Brocker, M. König, D. Erath, and F. Clement, "Screen Printed Thick Film Metallization of Silicon Solar Cells - Recent Developments and Future Perspectives: 35th European Photovoltaic Solar Energy Conference and Exhibition," in *Proceedings of the 35th European Photovoltaic Solar Energy Conference and Exhibition (EUPVSEC)*, 2018, pp. 819–824.

[37] A. Lennon, Y. Yao, and S. R. Wenham, "Evolution of metal plating for silicon solar cell metallisation," *Progress in Photovoltaics: Research and Applications*, vol. 21, no. 7, pp. 1454–1468, 2013.

[38] D. Stüwe, D. Mager, D. Biro, and J. G. Korvink, "Inkjet technology for crystalline silicon photovoltaics," *Advanced materials*, vol. 27, no. 4, pp. 599–626, 2015.

[39] M. Pospischil, "A Parallel Dispensing System for an Improved Front Surface Metallization of Silicon Solar Cells," PhD thesis, Albert-Ludwigs-Universität Freiburg im Breisgau, Freiburg i. Br., Germany, 2016.

[40] J. F. Nekarda, M. Graf, O. John, S. Nold, H. Nagel, D. Eberlein, A. Kraft, R. Boehme, A. Streek, and R. Preu, "Status of FolMet technology: How to produce PERC cells more cheaply than Al-BSF cells," *Photovoltaics International*, vol. 32, pp. 57–66, 2016.

[41] J. F. Nekarda, A. Grohe, O. Schultz, and R. Preu, "Aluminum Foil as Back Side Metallization for LFC Cells," in *Proceedings of the 22nd European Photovoltaic Solar Energy Conference and Exhibition (EUPVSEC)*, 2007, pp. 1499–1501.

[42] J. Nekarda, S. Stumpp, L. Gautero, M. Hörteis, A. Grohe, D. Biro, and R. Preu, "LFC on Screen Printed Aluminium Rear Side Metallization," in *Proceedings of the 24th European Photovoltaic Solar Energy Conference and Exhibition (EUPVSEC)*, 2009, pp. 1441–1445.

[43] J. F. Nekarda, M. Graf, A. Rodofili, R. Preu, R. Böhme, and D. Sontag, "Laser-based foil metallization for industrial PERC solar cells," in *Proceedings of the 28th European Photovoltaic Solar Energy Conference and Exhibition (EUPVSEC)*, 2013, pp. 797–799.

[44] M. Graf, J. F. Nekarda, D. Eberlein, N. Woehrle, R. Preu, R. Böhme, and T. Grosse, "Progress in laser-based foil metallization for industrial PERC solar cells," in *Proceedings of the 29th European Photovoltaic Solar Energy Conference and Exhibition (EUPVSEC)*, 2014, pp. 532–535.

[45] M. Graf, J. F. Nekarda, F. L. Togny, A. Streek, R. Böhme, and R. Preu, "Comprehensive Simulation and Acceleration of the Foil-metallization Laser Process," *Energy Procedia*, vol. 77, pp. 694–700, 2015.

[46] O. John, J. Paschen, A. De Rose, B. Steinhauser, G. Emanuel, A. A. Brand, and J. F. Nekarda, "Laser Metal Bonding (LMB) - Low Impact Joining of Thin Aluminum Foil to Silicon and Silicon Nitride Surfaces," in *Procedia CIRP*, Elsevier B.V., Ed., 2020, pp. 863–868.

[47] J. Paschen, G. Emanuel, A. A. Brand, T. Fellmeth, A. De Rose, O. John, and J. F. Nekarda, "FoilMet® - Connect: A new rear metallization upgrade for PERC and other cell concepts," in *AIP Conference Proceedings 2156*. AIP Publishing, 2019, pp. 020 004–1 – 020 004–5.

[48] J. Paschen, "Laser Welding of Very Thin Aluminum Foils for Cost Reduction of Solar Cell Production: to be published," PhD thesis.

[49] E. Schneiderloechner, R. Preu, R. Lüdemann, and S. W. Glunz, "Laser-fired rear contacts for crystalline silicon solar cells," *Progress in Photovoltaics: Research and Applications*, vol. 10, no. 1, pp. 29–34, 2002.

[50] J. Nekarda, M. Graf, A. Rodofili, A. Wolf, and R. Preu, "Laser-based foil rear side metallization for crystalline silicon solar cells," in *Laser Material Processing for Solar Energy*, ser. SPIE Proceedings, E. W. Reutzel, Ed. SPIE, 2012, p. 847307.

[51] L. C. Rendler, "Stress-reduced Wire Interconnection of Silicon Solar Cells: to be published," PhD thesis, Universität des Saarlandes, Saarbrücken, 2021.

[52] J. Govaerts, T. Borgers, P. Manganiello, M. Debucquoy, van der Heide, A., H. Goverde, E. Voroshazi, J. Szlufcik, and J. Poortmans, "Multi-Wire Interconnection for Multi-Busbar Interdigitated Back-Contact Cells: Opportunities and Pitfalls in Cell-Module Co-Design," in *Proceedings of the 33rd European Photovoltaic Solar Energy Conference and Exhibition (EUPVSEC)*, 2017, pp. 262–265.

[53] J. Walter, M. Tranitz, M. Volk, M. Ebert, and U. Eitner, "Multi-wire interconnection of busbar-free solar cells," *Energy Procedia*, vol. 55, pp. 380–388, 2014.

[54] L. C. Rendler, J. Walter, T. Geipel, M. Volk, C. Ebert, and U. Eitner, "Modelling and verification of mechanical stress induced by soldering of wires for multi busbar interconnection," in *Proceedings of the 31st European Photovoltaic Solar Energy Conference and Exhibition (EUPVSEC)*, 2015, pp. 84–88.

[55] J. Walter, L. C. Rendler, C. Ebert, A. Kraft, and U. Eitner, "Solder joint stability study of wire-based interconnection compared to ribbon interconnection," *Energy Procedia*, vol. 124, pp. 515–525, 2017.

[56] E. M. Sachs, J. Serdy, A. M. Gabor, and F. van Mierlo, "Light-capturing interconnect wire for 2% module power gain," in *Proceedings of the 24th European Photovoltaic Solar Energy Conference and Exhibition (EUPVSEC)*, 2009, pp. 3222–3225.

[57] A. De Rose, D. Erath, T. Geipel, A. Kraft, and U. Eitner, "Low-temperature soldering for the interconnection of silicon heterojunction solar cells," in *Proceedings of the 33rd European Photovoltaic Solar Energy Conference and Exhibition (EUPVSEC)*, 2017, pp. 710–714.

[58] A. De Rose, T. Geipel, D. Erath, A. Kraft, and U. Eitner, "Challenges for the interconnection of crystalline silicon heterojunction solar cells," *Photovoltaics International*, vol. 40, pp. 78–86, 2018.

[59] A. De Rose, T. Geipel, D. Eberlein, A. Kraft, and M. Nowottnick, "Interconnection of Silicon Heterojunction Solar Cells by Infrared Soldering - Solder Joint Analysis and Temperature Study," in *Proceedings of the 36th European Photovoltaic Solar Energy Conference and Exhibition (EUPVSEC)*, 2019, pp. 229–234.

[60] T. Geipel, M. Möller, A. Kraft, and U. Eitner, "Comprehensive study of intermetallic compounds in solar cell interconnections including lead-free, low melting point solders," in *Proceedings of the 32nd European Photovoltaic Solar Energy Conference and Exhibition (EUPVSEC)*, 2016, pp. 479–486.

[61] T. Geipel, *Electrically conductive adhesives for photovoltaic modules*, ser. Solar energy and systems research. Stuttgart: Fraunhofer Verlag, 2018.

[62] C. Kaiser, V. Nikitina, T. Geipel, and A. Kraft, "Reduction of ECA amount for the ribbon interconnection of heterojunction solar cells," in *Proceedings of the 37th European Photovoltaic Solar Energy Conference and Exhibition (EU PVSEC)*, 2020, pp. 1086–1090.

[63] S. Hoffmann, T. Geipel, M. Meinert, and A. Kraft, "Analysis of peel and shear forces after temperature cycle tests for electrical conductive adhesives," in *Proceedings of the 33rd European Photovoltaic Solar Energy Conference and Exhibition (EUPVSEC)*, 2017, pp. 183–186.

[64] T. Geipel and U. Eitner, "Electrically conductive adhesives: An emerging interconnection technology for high-efficiency solar modules," *Photovoltaics International*, vol. 11, no. 21, pp. 27–33, 2013.

[65] T. Geipel, M. Meinert, A. Kraft, and U. Eitner, "Optimization of electrically conductive adhesive bonds in photovoltaic modules," *IEEE Journal of Photovoltaics*, vol. 8, no. 4, pp. 1074–1081, 2018.

[66] N. Klasen, P. Romer, A. J. Beinert, and A. Kraft, "FEM Simulation of Deformations in Strings of Shingled Solar Cells Subjected to Mechanical Reliability Testing," in *AIP Conference Proceedings 2156*, vol. 020016. AIP Publishing, 2019, pp. 020 016–1–020 016–11.

[67] N. Klasen, A. Mondon, A. Kraft, and U. Eitner, "Shingled Cell Interconnection: A New Generation of Bifacial PV-Modules," in *7th Workshop on Metallization and Interconnection for Crystalline Silicon Solar Cells*, Konstanz, Germany, 2017.

[68] W. Schmidt and K.-D. Rasch, "New interconnection technology for enhanced module efficiency," *IEEE Transactions on Electron Devices*, vol. 37, no. 2, pp. 355–357, 1990.

[69] D. C. J. Dickson, "Photovoltaic semiconductor apparartus or the like: US 2938938 A," Patent US 2 938 938 A, 1960.

[70] J. Zhao, A. Wang, P. Campbell, and M. A. Green, "22.7% efficient silicon photovoltaic modules with textured front surface," *Electron Devices, IEEE Transactions on*, vol. 46, no. 7, pp. 1495–1497, 1999.

[71] H. Wirth and C. Ferrara, "PV module technology and reliability - status and perspective," *Green*, vol. 2, no. 4, pp. 159–169, 2012.

[72] J. Deubener, G. Helsch, A. Moiseev, and H. Bornhoeft, "Glasses for solar energy conversion systems," *Journal of the European Ceramic Society*, vol. 29, no. 7, pp. 1203–1210, 2009.

[73] J. Schneider, M. Turek, M. Dyrba, I. Baumann, B. Koll, and T. Booz, "Combined effect of light harvesting strings, anti-reflective coating, thin glass, and high ultraviolet transmission encapsulant to reduce optical losses in solar modules," *Progress in Photovoltaics: Research and Applications*, vol. 22, no. 7, pp. 1–8, 2014.

[74] C. Ballif, J. Dicker, D. Borchert, and T. Hofmann, "Solar glass with industrial porous SiO2 antireflection coating: measurements of photovoltaic module properties improvement and modelling of yearly energy yield gain," *Solar Energy Materials and Solar Cells*, vol. 82, no. 3, pp. 331–344, 2004.

[75] J. H. Wohlgemuth, D. Cunningham, J. Shaner, A. Nguyen, S. Ransome, and A. Artigao, "Crystalline silicon photovoltaic modules with anti-reflective coated glass," in *Proceedings of the 31st IEEE Photovoltaic Specialists Conference*, 2005, pp. 1015–1018.

[76] H. Wirth, K.-A. Weiß, and C. Wiesmeier, *Photovoltaic modules: Technology and reliability*. Berlin and Boston: De Gruyter, 2016.

[77] A. J. Beinert, P. Romer, A. Büchler, V. Haueisen, J. Aktaa, and U. Eitner, "Thermomechanical stress analysis of PV module production processes by Raman spectroscopy and FEM simulation," *Energy Procedia*, vol. 124, pp. 464–469, 2017.

[78] S. Krauter, *Solar Electric Power Generation: Modeling of Optical and Thermal Performance, Electrical Yield, Energy Balance, Effect on Reduction of Greenhouse Gas Emissions*. Springer-Verlag, 2006.

[79] International Electrotechnical Commission, "Terrestrial photovoltaic (PV) modules – Design qualification and type approval – Part 2: Test procedures (IEC 61215-2:2016)," Geneva, Switzerland, 2016.

[80] Deutsches Institut für Normung e.V., "Fertigungsverfahren - Begriffe, Einteilung (DIN 8580:2003-09)," Berlin, 2003.

[81] ——, "Schweißen und verwandte Prozesse – Begriffe - Teil 2: Weichlöten, Hartlöten und verwandte Begriffe (DIN ISO 857-2:2005)," 2005.

[82] H. H. Manko, *Solders and Soldering*, 3rd ed. New York, NY: S&P Global, 1992.

[83] K.-M. Lin, Y.-H. Lee, L.-K. Wang, L.-W. Chen, and S.-Y. Yang, "Electroluminescence observation of microcracks growth behavior of crystalline silicon solar modules fabricated by hot-air soldering technology," *International Journal of Modern Physics: Conference Series*, vol. 06, pp. 43–48, 2012.

[84] V. L. Lanin, "Ultrasonic soldering in electronics," *Ultrasonics Sonochemistry*, vol. 8, no. 4, pp. 379–385, 2001.

[85] K. Dusek, D. Busek, A. Petrác, M. Placek, M. Kozak, M. Mohanec, and I. Beshajová Pelikánová, "Comparison of Mechanical Resistance of SnCu and SnBi of Solder Joints," in *40th International Spring Seminar on Electronics Technology (ISSE)*, 2017.

[86] C.-S. Lee, I.-H. Hwang, J.-W. Lee, and J.-C. Lee, "A study on soldering characteristics of laser tabbing system for crystalline silicon photovoltaic module production," *Journal of Mechanical Science and Technology*, vol. 28, no. 8, pp. 3279–3283, 2014.

[87] S. K. Chunduri and M. Schmela, "Market Survey Cell Interconnection Equipment 2017," 17.04.2021. [Online]. Available: http://taiyangnews.info/TaiyangNews_Market%20Survey%20Cell%20Interconnection%20Equipment%202017%20download%20version.pdf

[88] Alonso García, M. C. and J. L. Balenzategui, "Estimation of photovoltaic module yearly temperature and performance based on Nominal Operation Cell Temperature calculations," *Renewable Energy*, vol. 29, no. 12, pp. 1997–2010, 2004.

[89] D. Faiman, "Assessing the outdoor operating temperature of photovoltaic modules," *Progress in Photovoltaics*, vol. 16, no. 4, pp. 307–315, 2008.

[90] R. Bharti, J. Kuitche, and M. G. TamizhMani, "Nominal Operating Cell Temperature (NOCT): Effects of module size, loading and solar spectrum," in *Proceedings of the 34th IEEE Photovoltaic Specialists Conference*, 2009, pp. 1657–1662.

[91] R. A. Bulwith and C. A. Mackay, "Silver Scavenging Inhibition of Some Silver Loaded Solders," *Welding Journal*, vol. 64, no. 3, pp. 86–90, 1985.

[92] P. G. Harris and K. S. Chaggar, "The role of intermetallic compounds in lead–free soldering," *Soldering & Surface Mount Technology*, vol. 10, no. 3, pp. 38–52, 1998.

[93] K. Suganuma, "Advances in lead-free electronics soldering," *Current Opinion in Solid State and Materials Science*, vol. 5, no. 1, pp. 55–64, 2001.

[94] T. Laurila, V. Vuorinen, and J. K. Kivilahti, "Interfacial reactions between lead-free solders and common base materials," *Materials Science and Engineering: R: Reports*, vol. 49, no. 1-2, pp. 1–60, 2005.

[95] I. Szendiuch, "Roadmap for Lead-Free Soldering," in *30st International Spring Seminar on Electronics Technology (ISSE)*, 2007, pp. 527–534.

[96] F. Li, V. Verdingovas, B. Medgyes, and R. Ambat, "Corrosion Reliability of Lead-free Solder Systems Used in Electronics," in *40th International Spring Seminar on Electronics Technology (ISSE)*, 2017.

[97] T. Geipel, D. Eberlein, and A. Kraft, "Lead-free solders for ribbon interconnection of crystalline silicon PERC solar cells with infrared soldering," in *AIP Conference Proceedings 2156*. AIP Publishing, 2019, p. 020015.

[98] International Organization for Standardization, "Soft solder alloys. Chemical compositions and forms (ISO 9453)," 2014.

[99] W. G. Zelley, "Formation of Immersion Zinc Coatings on Aluminum," *Journal of the Electrochemical Society*, vol. 100, no. 7, pp. 328–333, 1953.

[100] H. Baker, *Alloy Phase Diagrams: ASM Handbook*, 3rd ed. ASM International.

[101] K.-N. Tu, *Solder Joint Technology: Materials, Properties, and Reliability*, ser. Springer Series in Materials Science. New York: Springer, 2007, vol. 117.

[102] P. Lambracht, "Materialwissenschaftliche Aspekte bei der Entwicklung bleifreier Lotlegierungen," Dissertation, Technische Universität Darmstadt, Darmstadt, 2002.

[103] S.-W. Chen, C.-C. Lin, and C. Chen, "Determination of the melting and solidification characteristics of solders using differential scanning calorimetry," *Metallurgical and Materials Transactions A*, vol. 29, no. 7, pp. 1965–1972, 1998.

[104] R. Sayyadi and H. Naffakh-Moosavy, "Physical and mechanical properties of synthesized low Ag/lead-free Sn-Ag-Cu-xBi (x = 0, 1, 2.5, 5 wt%) solders," *Materials Science and Engineering: A*, vol. 735, pp. 367–377, 2018.

[105] G. Gottstein, *Materialwissenschaft und Werkstofftechnik*, 4th ed. Springer-Verlag, 2014.

[106] H.-T. Lee, M.-H. Chen, H.-M. Jao, and T.-L. Liao, "Influence of interfacial intermetallic compound on fracture behavior of solder joints," *Materials and Engineering A*, no. 358, pp. 134–141, 2003.

[107] K. G. Lyon, G. L. Salinger, C. A. Swenson, and G. K. White, "Linear thermal expansion measurements on silicon from 6 to 340 K," *Journal of Applied Physics*, vol. 48, no. 3, pp. 865–868, 1977.

[108] R. B. Roberts, "Thermal expansion reference data: silicon 300-850 K," *Journal of Physics D: Applied Physics*, vol. 14, no. 10, p. L163, 1981.

[109] ——, "Thermal expansion reference data: silicon 80-280K," *Journal of Physics D: Applied Physics*, vol. 15, no. 9, p. L119, 1982.

[110] C. Kohn, R. Kübler, M. Krappitz, G. Kleer, I. Reis, M. Retzlaff, D. Erath, and D. Biro, "Influence of the metallization process on the strength of silicon solar cells," in *Proceedings of the 24th European Photovoltaic Solar Energy Conference and Exhibition (EUPVSEC)*, vol. 21, 2009.

[111] L. C. Rendler, A. Kraft, C. Ebert, U. Eitner, and S. Wiese, "Mechanical stress in solar cells with multi busbar interconnection — Parameter study by FEM simulation," in *17th International Conference on Thermal, Mechanical and Multi-Physics Simulation and Experiments in Microelectronics and Microsystems (EuroSimE)*, 2016.

[112] C. Kohn, T. Faber, R. Kübler, J. Beinert, G. Kleer, F. Clement, D. Erath, I. Reis, F. Martin, and A. Müller, "Analyses of warpage effects induced by passivation and electrode coatings in silicon solar cells," in *Proceedings of the 22nd European Photovoltaic Solar Energy Conference and Exhibition (EUPVSEC)*, 2007, pp. 1270–1273.

[113] S. Wiese and F. Kraemer, "Analysis of thermo-mechanical stresses in novel back contact solar modules," in *Electronic System-Integration Technology Conference (ESTC), 2012 4th*, 2012, pp. 1–6.

[114] F. Kraemer and S. Wiese, "Assessment of long term reliability of photovoltaic glass–glass modules vs. glass-back sheet modules subjected to temperature cycles by FE-analysis," *Microelectronics Reliability*, vol. 55, no. 5, pp. 716–721, 2015.

[115] J. Jendrny, W. H. Müller, and H.-J. Albrecht, "Strength and lifetime analysis of SMT solder joints: An exemplary study of the MiniMELF component," in *Proceedings of the Surface Mount International*, 1997, pp. 626–636.

[116] F. Hua, Z. Mei, and J. Glazer, "Eutectic Sn-Bi as an alternative to Pb-free solders," in *Proceedings of 48th Electronic Components and Technology Conference.* IEEE, 1998, pp. 277–283.

[117] W. M. Haynes, Ed., *CRC handbook of chemistry and physics.* CRC Press, 2014.

[118] A. J. Beinert, A. Büchler, P. Romer, V. Haueisen, L. C. Rendler, M. C. Schubert, M. Heinrich, J. Aktaa, and U. Eitner, "Enabling the measurement of thermomechanical stress in solar cells and PV modules by confocal micro-Raman spectroscopy," *Solar Energy Materials and Solar Cells*, vol. 193, pp. 351–360, 2019.

[119] L. C. Rendler, P. Romer, A. J. Beinert, J. Walter, S. Stecklum, A. Kraft, U. Eitner, and S. Wiese, "Thermomechanical stress in solar cells: Contact pad modeling and reliability analysis," *Solar Energy Materials and Solar Cells*, vol. 196, pp. 167–177, 2019.

[120] L. C. Rendler, J. Walter, A. Kraft, C. Ebert, S. Wiese, and U. Eitner, "Ultra-soft wires for direct soldering on finger grids of solar cells," *Energy Procedia*, vol. 124, pp. 478–483, 2017.

[121] Y. Zemen, Prewitz T., T. Geipel, S. Pingel, and J. Berghold, "The impact of yield strength of the interconnector on the internal stress of the solar cell within a module," in *Proceedings of the 25th European Photovoltaic Solar Energy Conference and Exhibition/ 5th World Conference on Energy Conversion*, 2010, pp. 4073–4078.

[122] R. Meier, M. Pander, R. Klengel, S. Dietrich, S. Klengel, M. Ebert, and J. Bagdahn, "Reduction of soldering induced stresses in solar cells by microstructural optimization of copper-ribbons," in *SPIE Solar Energy + Technology*, ser. SPIE Proceedings. SPIE, 2011, pp. 1–13.

[123] M. Mittag, A. Pfreundt, and J. Shahid, "Impact of solar cell dimensions on module power, efficiency and cell-to-module losses," in *30th PV Solar Energy Conference*, 2020.

[124] M. Rauer, "Alloying from Screen-printed Aluminum Pastes for Silicon Solar Cell Applications," PhD thesis, University of Konstanz, Konstanz, Germany, 2012.

[125] T. Campbell, R. K. Kalia, A. Nakano, P. Vashishta, S. Ogata, and S. Rodgers, "Dynamics of Oxidation of Aluminum Nanoclusters using Variable Charge Molecular-Dynamics Simulations on Parallel Computers," *Physical Review Letters*, vol. 82, no. 24, pp. 4866–4869, 1999.

[126] H. T. Zhang, J. C. Feng, P. He, and H. Hackl, "Interfacial microstructure and mechanical properties of aluminium–zinc-coated steel joints made by a modified metal inert gas welding–brazing process," *Mater. Charact.*, vol. 58, no. 7, pp. 588–592, 2007.

[127] K. Miwa, "Flux for aluminum soldering," Patent US3 655 461 A, 1972.

[128] C. Kammer, *Aluminium-Taschenbuch 3*, 17th ed., ser. Praxis Werkstoffe. Berlin: Beuth, 2014.

[129] W. B. Guo, X. S. Leng, J. C. Yan, and Y. M. Tan, "Ultrasonic Soldering Aluminum at Low Temperature," *Welding Journal*, vol. 94, no. 6, pp. 189–195, 2015.

[130] H. von Campe, S. Huber, S. Meyer, S. REIFF, and J. Vietor, "Direct tin-coating of the aluminum rear contact by ultrasonic soldering," in *Proceedings of the 27th European Photovoltaic Solar Energy Conference and Exhibition (EUPVSEC)*, 2012, pp. 1150–1153.

[131] P. Schmitt, D. Eberlein, C. Ebert, M. Tranitz, U. Eitner, and H. Wirth, "Adhesion of Al-metallization in ultra-sonic soldering on the Al-rear side of solar cells," *Energy Procedia*, vol. 38, pp. 380–386, 2013.

[132] C. E. Brittin, "Vacuum brazing of aluminum alloy workpieces," Patent US4 886 449 A, 1989.

[133] W. L. Winterbottom and G. A. Gilmour, "Vacuum brazing of aluminum: Auger studies of wetting and flow characteristics," *Journal of Vacuum Science and Technology*, vol. 13, no. 2, pp. 634–643, 1976.

[134] C. J. Miller, "Aluminum brazing," Patent US3 321 828 A, 1967.

[135] R. R. Ambriz and V. Mayagoitia, "Welding of Aluminum Alloys," in *Recent Trends in Processing and Degradation of Aluminium Alloys*, Z. Ahmad, Ed., 2011.

[136] P. Praveen and P. Yarlagadda, "Meeting challenges in welding of aluminum alloys through pulse gas metal arc welding," *Journal of Materials Processing Technology*, vol. 164-165, pp. 1106–1112, 2005.

[137] C. A. Huntington and T. W. Eagar, "Laser Welding of Aluminum and Aluminum Alloys," *Welding Journal*, vol. 62, no. 4, pp. 105–107, 1983.

[138] S. K. Tiwari, D. K. Shukla, and R. Chandra, "Friction Stir Welding Of Aluminum Alloys: A Review," *International Journal of Mechanical, Aerospace, Industrial and Mechatronics Engineering*, vol. 7, no. 12, pp. 1315–1320, 2013.

[139] M. Li, C. Zhang, D. Wang, L. Zhou, D. Wellmann, and Y. Tian, "Friction Stir Spot Welding of Aluminum and Copper: A Review," *Materials (Basel, Switzerland)*, vol. 13, no. 1, 2019.

[140] R. Rechner, I. Jansen, and E. Beyer, "Influence on the strength and aging resistance of aluminium joints by laser pre-treatment and surface modification," *International Journal of Adhesion and Adhesives*, vol. 30, no. 7, pp. 595–601, 2010.

[141] S. Gheybi Hashemabad, Z. Gu, and T. Ando, "Flux-less direct soldering of aluminum by ultrasonic surface activation," *Journal of Materials Processing Technology*, vol. 233, pp. 135–141, 2016.

[142] M. L. Santella, T. Engstrom, D. Storjohann, and T.-Y. Pan, "Effects of friction stir processing on mechanical properties of the cast aluminum alloys A319 and A356," *Scripta Materialia*, vol. 53, no. 2, pp. 201–206, 2005.

[143] E. H. Hewitson, "Process of Coating Aluminum Surfaces," Patent US1 627 900 A, 1927.

[144] L. Zhao, K. Bobzin, F. Ernst, J. Zwick, J. Roesing, and E. Lugscheider, "Feasibility Study of Brazing Aluminium Alloys Through Pre-Deposition of a Braze Alloy by Cold Spray Process," *Advanced Engineering Materials*, vol. 8, no. 8, pp. 751–753, 2006.

[145] J. Kumm, R. V. Chacko, H. Samadi, P. Hartmann, D. Eberlein, and A. Wolf, "Long-term and Annealing Stable, Solderable PVD Metallization with Optimized Al Diffusion Barrier," *Energy Procedia*, vol. 77, pp. 374–381, 2015.

[146] H. Nagel, M. Kamp, D. Eberlein, A. Kraft, J. Bartsch, M. Glatthaar, and S. W. Glunz, "Enabling Solderability of PVD Al Rear Contacts on High-Efficiency Crystalline Silicon Solar Cells by Wet Chemical Treatment," in *Proceedings of the 32nd European Photovoltaic Solar Energy Conference and Exhibition (EUPVSEC)*, 2016, pp. 48–52.

[147] M. Kamp, J. Bartsch, G. Cimiotti, R. Keding, A. Zogaj, C. Reichel, A. Kalio, M. Glatthaar, and S. W. Glunz, "Zincate processes for silicon solar cell metallization," *Solar Energy Materials and Solar Cells*, vol. 120, pp. 332–338, 2014.

[148] H. Schulte-Huxel, R. Bock, S. Blankemeyer, A. Merkle, and R. Brendel, "Aluminum-Based Mechanical and Electrical Laser Interconnection Process for Module Integration of Silicon Solar Cells," *IEEE Journal of Photovoltaics*, vol. 2, no. 1, pp. 16–21, 2012.

[149] E. Lugscheider and W. Tillmann, "Methods for brazing ceramic and metal-ceramic joints," *Materials and Manufacturing Processes*, vol. 8, no. 2, pp. 219–238, 1993.

[150] W. Hanson, K. Ironside, and J. Fernie, "Active metal brazing of zirconia," *Acta Materialia*, vol. 48, no. 18-19, pp. 4673–4676, 2000.

[151] V. Jung, F. Heinemeyer, and M. Koentges, "Long-term stable encapsulated solder joints on an Al/Ni:V/Ag metallization for silicon solar cells," *Energy Procedia*, vol. 21, pp. 84–91, 2012.

[152] H. G. Bauer and W. Schadt, Eds., *Walzen von Flachprodukten*, ser. MatWerk - Materialwissenschaft und Werkstofftechnik. Berlin: Springer, 2017.

[153] M. Bambach, M. Pietryga, A. Mikloweit, and G. Hirt, "A finite element framework for the evolution of bond strength in joining-by-forming processes," *Journal of Materials Processing Technology*, vol. 214, no. 10, pp. 2156–2168, 2014.

[154] N. Bay, C. Clemensen, O. Juelstorp, and T. Wanheim, "Bond Strength in Cold Roll Bonding," *CIRP Annals*, vol. 34, no. 1, pp. 221–224, 1985.

[155] A. Kraft, "Plated Copper Front Side Metallization on Printed Seed-Layers for Silicon Solar Cells," PhD thesis, Albert-Ludwigs-Universität Freiburg im Breisgau, 2015.

[156] J. Burschik, Y. Shengzhao, N. Bay, K. Crouse, A. De Rose, A. Hoffmann, H. Kühnlein, B. Lee, A. Letize, M. Passig, D. Pysch, M. Sieber, P. Verlinden, and K. Vosteen, "Transition to 4 and 5 BB Designs for Ni/Cu/Ag Plated Cells," *Energy Procedia*, vol. 98, pp. 66–73, 2016.

[157] G. W. Critchlow and D. M. Brewis, "Review of surface pretreatments for aluminium alloys," *International Journal of Adhesion and Adhesives*, vol. 16, no. 4, pp. 255–275, 1996.

[158] K. Azumi, T. Yugiri, M. Seo, and S. Fujimoto, "Double Zincate Pretreatment of Sputter-Deposited Al Films," *Journal of the Electrochemical Society*, vol. 148, no. 6, pp. C433–C438, 2001.

[159] S. Court, C. Ponce de León, J. R. Smith, and F. C. Walsh, "Monitoring of zincate pre-treatment of aluminium prior to electroless nickel plating," *Transactions of the IMF*, vol. 95, no. 2, pp. 97–105, 2017.

[160] M. Hino, K. Murakami, M. Hiramatsu, K. Chen, and Saijo, Atsushi and Kanadani, Teruto, "Effect of Zincate Treatment on Adhesion of Electroless Ni-P Plated Film for 2017 Aluminum Alloy," *Materials Transactions*, vol. 46, no. 10, pp. 2169–2175, 2005.

[161] F. Keller and W. G. Zelley, "Conditioning Aluminum Alloys for Electroplating," *Journal of the Electrochemical Society*, vol. 97, no. 4, pp. 143–151, 1949.

[162] M. Hino, K. Murakami, Y. Mitooka, K. Muraoka, and Furukawa, Ryosuke and Kanadani, Teruto, "Effect of Zincate Treatment on Adhesion of Electroless Ni-P Coating onto Various Aluminum Alloys," *Materials Transactions*, vol. 50, no. 9, pp. 2235–2241, 2009.

[163] SurTec Deutschland GmbH, "SurTec 652 Q: Cyanidfreie Zinkatbeize: Data sheet."

[164] M. Kamp, "Electrochemical process for metallization of novel silicon solar cells," PhD thesis, Albert-Ludwigs-Universität Freiburg im Breisgau, Freiburg i. Br., Germany, 2016.

[165] MacDermid GmbH, "Niklad ELV 808: Blei- und cadmiumfreier Nickelelektrolyt."

[166] S. De Wolf, A. Descoeudres, Z. C. Holman, and C. Ballif, "High-efficiency Silicon Heterojunction Solar Cells: A Review," *Green*, vol. 2, no. 1, pp. 7–24, 2012.

[167] S. Gulkowski and E. Krawczak, "RF/DC Magnetron Sputtering Deposition of Thin Layers for Solar Cell Fabrication," *Coatings*, vol. 10, no. 8, p. 791, 2020.

[168] Deutsches Institut für Normung e.V., "DIN EN 573-3:2019-10, Aluminium and aluminium alloys - Chemical composition and form of wrought products - Part 3: Chemical composition and form of products," Berlin.

[169] C. Kammer, *Aluminium-Taschenbuch*, 16th ed. Berlin: Beuth, 2012.

[170] Y. Yuan and T. R. Lee, "Contact angle and wetting properties," in *Surface science techniques*, G. Bracco and B. Holst, Eds. Springer Berlin Heidelberg, 2013, pp. 3–34.

[171] L. Wilhelmy, "Ueber die Abhängigkeit der Capillaritäts-Constanten des Alkohols von Substanz und Gestalt des benetzten festen Körpers," *Annalen der Physik und Chemie*, vol. 195, no. 6, pp. 177–217, 1863.

[172] MatWeb - Material Property Data, "Eutectic Solder (63Sn-37Pb): ASTM B 32 Grade Sn63," 03.04.2021. [Online]. Available: http://www.matweb.com/search/datasheet_print.aspx?matguid=3a5c8bc670914d588b26ab0b994d88cb

[173] K.-L. L. Chwan-Ying Lee, "Wetting kinetics and the interfacial interaction behavior between electroless Ni-Cu-P and molten solder," *Japanese Journal of Applied Physics*, vol. 33, no. 2684, 1994.

[174] Deutsches Institut für Normung e.V., "Solarzellen - Datenblattangaben und Angaben zum Produkt für kristalline Silicium-Solarzellen (DIN EN 50461:2007-03)," 2007.

[175] International Electrotechnical Commission, "Test methods for electrical materials, printed boards and other interconnection structures and assemblies - Part 2: Test methods for materials for interconnection structures (61189-2: 2006-05)," 2006.

[176] D. B. Williams and C. B. Carter, *Transmission electron microscopy: A textbook for materials science.* New York and New York, NY: Springer and Plenum Press anfangs, 1996.

[177] K. N. Chen, A. Fan, C. S. Tan, and R. Reif, "Contact resistance measurement of bonded copper interconnects for three-dimensional integration technology," *Electron Device Letters, IEEE*, vol. 25, no. 1, pp. 10–12, 2004.

[178] Chern, J. G. J. and W. G. Oldham, "Determining specific contact resistivity from contact end resistance measurements," *IEEE Electron Device Letters*, vol. 5, no. 5, pp. 178–180, 1984.

[179] H. H. Berger, "Contact resistance and contact resistivity," *Journal of the Electrochemical Society*, vol. 119, no. 4, pp. 507–514, 1972.

[180] Y. Zemen, S. C. Schulz, H. Trommler, S. T. Buschhorn, W. Bauhofer, and K. Schulte, "Comparison of new conductive adhesives based on silver and carbon nanotubes for solar cells interconnection," *Solar Energy Materials and Solar Cells*, vol. 109, pp. 155–159, 2013.

[181] International Electrotechnical Commission, "Photovoltaic Devices - Part 1: Measurement of Photovoltaic Current-Voltage Characteristics (60904-1: 2006-09)," 2006.

[182] R. A. Sinton and A. Cuevas, "A quasi-steady state open-circuit voltage method for solar cell characterization," in *Proceedings of the 16th European Photovoltaic Solar Energy Conference and Exhibition (EUPVSEC)*, 2000.

[183] G. Dost, H. Höffler, and J. M. Greulich, "Vignetting in luminescence imaging of solar cells," *Review of Scientific Instruments*, vol. 90, no. 10, p. 103707, 2019.

[184] K. Bedrich, M. Bokalic, M. Bliss, M. Topic, T. R. Betts, and R. Gottschalg, "Electroluminescence Imaging of PV Devices: Advanced Vignetting Calibration," *IEEE Journal of Photovoltaics*, vol. 8, no. 5, pp. 1297–1304, 2018.

[185] International Electrotechnical Commission, "Einvironmental testing - Part 2-2: Tests - Test B: Dry heat (EN 60068-2-2:2007)," 2007.

[186] ——, "International Electrotechnical Vocabulary (IEV): Part 192: Dependability (60050-192:2015)," 2015.

[187] M. Köntges, U. Jahn, K. A. Berger, C. Packard, S. Kurtz, and K. Kato, "Performance and reliability of photovoltaic systems: External final report IEA-PVPS 2014."

[188] A. De Rose, A. Kraft, S. Gledhill, M. T. Ali, T. Kroyer, C. Pscherer, M. Graf, J. F. Nekarda, and U. Eitner, "Solder Interconnection of Aluminum Foil Rear Side Metallization for Passivated Emitter and Rear Solar Cells," in *7th Workshop on Metallization and Interconnection for Crystalline Silicon Solar Cells*, Konstanz, Germany, 2017.

[189] A. De Rose, A. Kraft, U. Eitner, and M. Nowottnick, "Solder Joint Analysis on Coated Aluminum for Silicon Solar Cell Interconnection," in *41st International Spring Seminar on Electronics Technology (ISSE)*, IEEE, Ed. IEEE, 2018, pp. 1–6.

[190] A. Krämer, Z. Liu, K. Karhausen, H. Aretz, M. Teller, and G. Hirt, "Characterizing multi-pass conditions for roll bonding of aluminum alloys," in *Proceedings of the 22nd International Esaform Conference on Material Forming (Esaform 2019)*, ser. AIP Conference Proceedings. AIP Publishing, 2019, p. 050014.

[191] A. Melzner and G. Hirt, "Roll Bonding of Two Materials Using Temperature to Compensate the Material Strength Difference," *Advanced Materials Research*, vol. 966-967, pp. 471–480, 2014.

[192] M. Pietryga, J. Lohmar, and G. Hirt, "A New FE-Model for the Investigation of Bond Formation and Failure in Roll Bonding Processes," *Materials Science Forum*, vol. 854, pp. 152–157, 2016.

[193] A. Mikloweit, M. Bambach, M. Pietryga, and G. Hirt, "Development of a Testing Procedure to Determine the Bond Strength in Joining-by-Forming Processes," *Advanced Materials Research*, vol. 966-967, pp. 481–488, 2014.

[194] C. M. Schlögl, "Walzplattieren von Magnesium-Aluminium-Verbunden," Diploma thesis, Montanuniversität Leoben, Leoben, 2012.

[195] Wickeder Westfalenstahl GmbH (Carina Franken), "Applications for (solderable) Al foils produced by roll-cladding: Private communication," 15.04.2021.

[196] G. Drossel, S. Friedrich, W. Huppatz, C. Kammer, W. Lehnert, O. Liesenberg, W. Mader, M. Paul, A. Rudolf, W. Thate, M. Ullmann, H.-W. Wenglorz, and S. Zeltner, *Aluminium-Taschenbuch 2*, 17th ed., ser. Praxis. Berlin and Wien and Zürich: Beuth Verlag GmbH, 2018.

[197] H.-J. Bargel and G. Schulze, *Werkstoffkunde*. Berlin, Heidelberg: Springer Berlin Heidelberg, 2018.

[198] A. J. Beinert, "Thermomechanical Design Rules for the Development of Photovoltaic Modules: to be published," PhD thesis, Karlsruhe Institute of Technology, 2021.

[199] H. W. Tseng, S. J. Wang, and C. Y. Liu, "Cross-interaction effect in the Ni/Sn/Cu solder joints," in *11th Electronics Packaging Technology Conference, 2009*, IEEE Reliability/CPMT/ED Singapore Chapter, Ed. Piscataway, NJ: IEEE, 2009, pp. 325–330.

[200] S.-E. Jeong, S.-B. Jung, and J.-W. Yoon, "Fast formation of Ni–Sn intermetallic joints using Ni–Sn paste for high-temperature bonding applications," *Journal of Materials Science: Materials in Electronics*, vol. 31, no. 18, pp. 15 048–15 060, 2020.

[201] J. M. Pauls, C. E. Shuck, A. Genç, S. Rouvimov, and A. S. Mukasyan, "In-situ transmission electron microscopy determination of solid-state diffusion in the aluminum-nickel system," *Journal of Solid State Chemistry*, vol. 276, pp. 114–121, 2019.

[202] O. John, "Laser Metal Bonding - Ein neuer Ansatz für die Folienmetallisierung von Solarzellenrückseiten: to be published," PhD thesis, 2021.

[203] A. De Rose, M. Kamp, G. Mikolasch, A. Kraft, and M. Nowottnick, "Adhesion improvement for solder interconnection of wet chemically coated aluminum surfaces," in *AIP Conference Proceedings 2156*, vol. 2156. AIP Publishing, 2019, pp. 020 014–1 – 020 014–10.

[204] A. De Rose, G. Mikolasch, M. Kamp, A. Kraft, and M. Nowottnick, "Microstructure and long-term stability of solder joints on nickel-plated aluminium formed during short soldering times," *RSC Advances*, vol. 10, no. 66, pp. 40 215–40 224, 2020.

[205] David R. Lide, *CRC Handbook of Chemistry and Physics*. Boca Raton, Florida: CRC Press, 2005.

[206] S. P.-S. Lim, M. Z. Ding, J. K. Lin, and V. S. Rao, "Development of fluxless flip chip reflow process for high density flip chip interconnect," in *17th Electronics Packaging and Technology Conference (EPTC)*, IEEE, Ed. Piscataway, NJ: IEEE, 2015, pp. 1–6.

[207] S. J. Wang and C. Y. Liu, "Asymmetrical solder microstructure in Ni/Sn/Cu solder joint," *Scripta Materialia*, vol. 55, no. 4, pp. 347–350, 2006.

[208] A. Kraft, C. Wolf, J. Bartsch, and M. Glatthaar, "Characterization of copper diffusion in silicon solar cells," *Energy Procedia*, vol. 67, pp. 93–100, 2015.

[209] A. Mondon, "Nickel Silicide from Plated Nickel for High Adhesion of Fully Plated Silicon Solar Cell Metallization," PhD thesis, Albert-Ludwigs-Universität Freiburg im Breisgau, 2015.

[210] E. Schneiderlöchner, R. Preu, R. Lüdemann, S. W. Glunz, and G. Willeke, "Laser-fired contacts (LFC)," in *Proceedings of the 17th European Photovoltaic Solar Energy Conference and Exhibition (EUPVSEC)*, 2001, pp. 1303–1306.

[211] J. Zhu, D. Montiel-Chicharro, M. Owen-Bellini, T. Betts, and R. Gottschalg, "The role of EVA encapsulation in the degradation of wafer based PV modules," in *12th Photovoltaic Science, Application and Technology Conference C98 (PVSAT-12)*, 2016.

[212] M. W. Rowell, S. G. Daroczi, D. W. J. Harwood, and A. M. Gabor, "The Effect of Laminate Construction and Temperature Cycling on the Fracture Strength and Performance of Encapsulated Solar Cells," in *Proceedings of the 7th World Conference on Photovoltaic Energy Conversion*. IEEE, 2018, pp. 3927–3931.

[213] M. Owen-Bellini, D. Montiel-Chicharro, J. Zhu, T. R. Betts, and R. Gottschalg, "Influence of Viscoelastic Properties of Encapsulation Materials on the Thermomechanical Behavior of Photovoltaic Modules," *IEEE Journal of Photovoltaics*, vol. 8, no. 1, pp. 183–188, 2018.

[214] I. Zafirovska, M. K. Juhl, J. W. Weber, J. Wong, and T. Trupke, "Detection of Finger Interruptions in Silicon Solar Cells Using Line Scan Photoluminescence Imaging," *IEEE Journal of Photovoltaics*, vol. 7, no. 6, pp. 1496–1502, 2017.

[215] E. Urrejola, K. Peter, H. Plagwitz, and G. Schubert, "Al–Si alloy formation in narrow p-type Si contact areas for rear passivated solar cells," *Journal of Applied Physics*, vol. 107, no. 12, p. 124516, 2010.

[216] ——, "Silicon diffusion in aluminum for rear passivated solar cells," *Applied Physics Letters*, vol. 98, no. 15, p. 153508, 2011.

[217] M. Mittag and M. Ebert, "Systematic PV module optimization with the cell-to-module (CTM) analysis software," *Photovoltaics International*, no. 36, pp. 97–104, 2017.

[218] T. Geipel, M. Moeller, J. Walter, A. Kraft, and U. Eitner, "Intermetallic compounds in solar cell interconnections: Microstructure and growth kinetics," *Solar Energy Materials and Solar Cells*, vol. 159, pp. 370–388, 2017.

[219] T. Kroyer, S. Gledhill, M. T. Ali, and A. De Rose, "Verfahren zum Verbinden zweier Werkstücke mittels Löten und Vorrichtung mit einem ersten und einem zweiten Werkstück, welche mittels eines Lots verbunden sind," Patent DE 10 2019 101 921 A1.

[220] J. Wendt, M. Koehler, and M. Traeger, "Quantifiying the solderability of lead free solder alloys on solar cells using wetting balance analyzer," in *Proceedings of the 26th European Photovoltaic Solar Energy Conference and Exhibition (EUPVSEC)*, 2011, pp. 3298–3301.

[221] M. J. Rizvi, Y. C. Chan, C. Bailey, H. Lu, M. N. Islam, and B. Y. Wu, "Wetting and reaction of Sn-2.8Ag-0.5Cu-1.0Bi solder with Cu and Ni substrates," *Journal of Electronic Materials*, vol. 34, no. 11, pp. 15–22, 2005.

[222] T. Matsumoto and K. Nogi, "Wetting in Soldering and Microelectronics," *Annual Review of Materials Research*, vol. 38, no. 1, pp. 251–273, 2008.

[223] L. M. Lander, L. M. Siewierski, W. J. Brittain, and E. A. Vogler, "A Systematic Comparison of Contact Angle Methods," *Langmuir*, vol. 9, no. 8, pp. 2237–2239, 1993.

[224] T. Takemoto and M. Miyazaki, "Effect of Excess Temperature above Liquidus of Lead-Free Solders on Wetting Time in a Wetting Balance Test," *Materials Transactions*, vol. 42, no. 5, pp. 745–750, 2001.

[225] J. Liang, N. Dariavach, P. Callahan, and D. Shangguan, "Metallurgy and Kinetics of Liquid–Solid Interfacial Reaction during Lead-Free Soldering," *Materials Transactions*, vol. 47, no. 2, pp. 317–325, 2006.

[226] J. Moyer and W. Zhang, "Solder wetting measurement of back contact paste using a wetting balance," in *34th IEEE Photovoltaic Specialists Conference (PVSC)*, IEEE, Ed. IEEE, 2009, pp. 001 838–001 841.

[227] S. Glaser, B. Büttner, S. Hippeli, H. Weinläder, S. Beisel, T. Kroyer, M. Gremmelspacher, T. Rist, B. Lang, and R. Kübler, "Flexibler Randverbund für Vakuumisolierglas-Systeme (VIG-S): Abschlussbericht Forschungsvorhaben 03ET1147, 2016."

[228] W. Qiu, B. Zee, F. J. Foo, and W. Grunewald, "Alternative flip chip sample preparation technique using triple ion beam milling," in *16th Electronics Packaging Technology Conference (EPTC 2014)*. Piscataway, NJ: IEEE, 2014, pp. 587–591.

[229] M. He, Z. Chen, G. Qi, C. C. Wong, and S. G. Mhaisalkar, "Effect of post-reflow cooling rate on intermetallic compound formation between Sn–3.5 Ag solder and Ni–P under bump metallization," *Thin Solid Films*, vol. 462-463, pp. 363–369, 2004.

[230] M. Schaefer, R. A. Fournelle, and J. Liang, "Theory for intermetallic phase growth between cu and liquid Sn-Pb solder based on grain boundary diffusion control," *Journal of Electronic Materials*, vol. 27, no. 11, pp. 1167–1176, 1998.

[231] A.-K. Larsson, L. Stenberg, and S. Lidin, "The superstructure of domain-twinned eta'-Cu6Sn5," *Acta Crystallographica Section B*, vol. 50, no. 6, pp. 636–643, 1994.

[232] K. Nogita and T. Nishimura, "Nickel-stabilized hexagonal (Cu,Ni)6Sn5 in Sn-Cu-Ni lead-free solder alloys," *Scripta Materialia*, vol. 59, no. 2, pp. 191–194, 2008.

[233] Z. L. Li, H. J. Dong, X. G. Song, H. Y. Zhao, H. Tian, J. H. Liu, J. C. Feng, and J. C. Yan, "Homogeneous (Cu, Ni)6Sn5 intermetallic compound joints rapidly formed in asymmetrical Ni/Sn/Cu system using ultrasound-induced transient liquid phase soldering process," *Ultrasonics Sonochemistry*, vol. 42, pp. 403–410, 2018.

[234] C. E. Ho, M. K. Lu, P. T. Lee, Y. H. Huang, and W. L. Chou, "TEM investigation of interfacial microstructure and fracture mode of the Sn-Ag-Cu/Ni joint system," *Materials Science and Engineering: A*, vol. 706, pp. 269–278, 2017.

[235] W. M. Chen, S. C. Yang, M. H. Tsai, and C. R. Kao, "Uncovering the driving force for massive spalling in the Sn–Cu/Ni system," *Scripta Materialia*, vol. 63, no. 1, pp. 47–49, 2010.

[236] S. J. Wang and C. Y. Liu, "Kinetic analysis of the interfacial reactions in Ni/Sn/Cu sandwich structures," *Journal of Electronic Materials*, vol. 35, no. 11, pp. 1955–1960, 2006.

[237] C. R. Brundle, C. A. Evans, and S. Wilson, *Encyclopedia of Materials Charakterization: Sufaces, Interfaces, Thin Films*, 1992.

[238] T. Urban, M. Heimann, A. Schmid, A. Mette, and J. Heitmann, "Analysis of Ohmic Losses Due to Solder and Pressure Interconnection and Related Interface Resistances for Solar Cells," *Proceedings of the Fifth Workshop on Metallization for Crystalline Silicon Solar Cells*, vol. 77, pp. 420–427, 2015.

[239] M. Heimann, R. Bakowskie, M. Köhler, J. Hirsch, M. Junghänel, A. Hussack, and S. Sachert, "Analysis of Different Soldering Failure Modes at Module Level – a Compartive Study," in *Proceedings of the 29th European Photovoltaic Solar Energy Conference and Exhibition (EUPVSEC)*, 2014, pp. 3166–3171.

[240] D. K. Schroder and D. L. Meier, "Solar cell contact resistance - A review," *Electron Devices, IEEE Transactions on*, vol. 31, no. 5, pp. 637–647, 1984.

[241] A. Herguth, G. Schubert, M. Kaes, and G. Hahn, "A New Approach to Prevent the Negative Impact of the Metastable Defect in Boron Doped CZ Silicon Solar Cells," in *Proceedings of the 4th IEEE World Conference on Photovoltaic Energy Conversion*, Institute of Electrical and Electronics Engineers, Ed., 2006, pp. 940–943.

[242] F. Kersten, F. Frühauf, R. Lantzsch, M. Schütze, C. Taubitz, F. Fertig, M. Schaper, and J. W. Müller, "Stability investigations of Cz-PERC modules during damp heat testing and transport: The impact of the boron-oxygen defect," in *15th International Conference on Concentrator Photovoltaic Systems (CPV-15)*, ser. AIP Conference Proceedings, AIP Conference Proceedings, Ed. AIP Publishing, 2019, p. 090001.

[243] SCHLENK Metallfolien GmbH & Co. KG (Thomas Booz), "Applications for (solderable) Al foils produced by roll-cladding: Private communication," 18.03.2021.

[244] SCHLENK Metallfolien GmbH & Co. KG (Fabian Distelrath), "Applications for (solderable) Al foils produced by roll-cladding: Private communication," 18.03.2021.

[245] Hydro Aluminium Rolled Products GmbH (Dr. Günter Schubert), "Applications for (solderable) Al foils: Private communication," 17.03.2021.

[246] J. Nekarda, A. Kraft, O. John, J. Paschen, A. De Rose, S. Stecklum, T. Kroyer, S. Gledhill, H. Nagel, and G. Emanuel, "Industrielle Hochleistungsmodule mit folienmetallisierten Solarzellen; Akronym "Folmet-Modul" : gemeinsamer, öffentlicher Abschlussbericht des Forschungsvorhabens : Projektlaufzeit: 01.04.2016-30.04.2019."

[247] O. John, G. Emanuel, J. Paschen, A. De Rose, B. Steinhauser, A. Brand, and J. Nekarda, "Laser Metal Bonding (LMB) - Low Impact Joining of Thin Aluminum Foil to PERC and TOPCon Rear Side Surfaces," in *47th IEEE Photovoltaic Specialists Conference (PVSC)*. IEEE, 2020, pp. 0063–0066.

[248] J. Nekarda, A. Brand, M. Graf, A. De Rose, and A. Kraft, "Method for producing a photovoltaic solar cell, photovoltaic solar cell and photovoltaic module," Patent US 2021/0 005 773 A1.

[249] J. Paschen, O. John, P. Baliozian, and J. Nekarda, "FoilMet®-Interconnect: Busbarless, ECA- and Solder-Free Aluminum Interconnection for Shingled Modules: tbp." in *Proceedings of the 38th European Photovoltaic Solar Energy Conference and Exhibition (EU PVSEC)*, 2021.

[250] H. Nagel, S. Gledhill, T. Kroyer, D. Eberlein, A. Kraft, T. Fischer, A. Hain, P. Wohlfart, M. Glatthaar, and S. W. Glunz, "Solderable PVD Al Back Contacts for the Module Integration of High-Efficiency c-Si Solar Cells," in *Proceedings of the 37th European Photovoltaic Solar Energy Conference and Exhibition (EU PVSEC)*, 2020, pp. 861–866.

[251] Z. Mei and J. Morris, "Characterization of eutectic Sn-Bi solder joints," *Journal of Electronic Materials*, vol. 21, no. 6, pp. 599–607, 1992.

[252] M. J. Burek, S. Jin, M. C. Leung, Z. Jahed, J. Wu, A. S. Budiman, N. Tamura, M. Kunz, and T. Y. Tsui, "Grain boundary effects on the mechanical properties of bismuth nanostructures," *Acta Materialia*, vol. 59, no. 11, pp. 4709–4718, 2011.

[253] M. Nowottnick and A. Novikov, "Possibilities and Limits of Bismuth Solders," in *Proc. of SMTA International*, 2017, pp. 195–200.

[254] T. Soederstroem, P. Papet, and J. Ufheil, "Smart wire connection technology," in *Proceedings of the 28th European Photovoltaic Solar Energy Conference and Exhibition (EUPVSEC)*, 2013, pp. 495–499.

[255] S. Braun, R. Nissler, C. Ebert, D. Habermann, and G. Hahn, "High Efficiency Multibusbar Solar Cells and Modules," *IEEE Journal of Photovoltaics*, vol. 4, no. 1, pp. 148–153, 2014.

[256] T. Geipel and U. Eitner, "Electrically conductive adhesives: An emerging interconnection technology for high-efficiency solar modules," *Photovoltaics International*, vol. 11, no. 21, pp. 27–33, 2013.

[257] G. Schubert, "Aluminiumfolie in Lebensmittelverpackungen - Funktionen und Grenzen," 27.06.2017. [Online]. Available: https://www.ivlv.org/?news=der-freisinger-abend-im-braeustueberl-weihenstephan-am-27-juni-2017-aluminium-in-lebensmittel

[258] R. N. Lumley, Ed., *Fundamentals of aluminium metallurgy: Production, processing and applications*, ser. Woodhead Publishing series in metals and surface engineering. Cambridge, MA: Woodhead Publishing, 2018.

[259] R. N. Lumley, "Introduction: Aluminium, the Strategic Material," in *Fundamentals of aluminium metallurgy*, ser. Woodhead Publishing series in metals and surface engineering, R. N. Lumley, Ed. Cambridge, MA: Woodhead Publishing, 2018.

[260] Heraeus Electronics (Thilo Happ), "Applications for (solderable) Al foils produced by roll-cladding: Private communication," 29.03.2021.

[261] A. Das, D. Li, D. Williams, and D. Greenwood, "Weldability and shear strength feasibility study for automotive electric vehicle battery tab interconnects," *Journal of the Brazilian Society of Mechanical Sciences and Engineering*, vol. 41, no. 1, 2019.

[262] Hydro Aluminium Rolled Products GmbH, "Aluminium life cycle," 13.04.2021. [Online]. Available: https://www.hydro.com/en-DE/aluminium/about-aluminium/aluminium-life-cycle/

[263] A. Tummalieh, A. Pfreundt, and M. Mittag, "Trend Tracking of Efficiency and CTM Ratio of PV Modules," in *Proceedings of the 37th European Photovoltaic Solar Energy Conference and Exhibition (EU PVSEC)*, 2020, pp. 1091–1095.

[264] P. Sánchez-Friera, F. Ropero, B. Lalaguna, L. J. Caballero, and J. Alonso, "Power Losses in Crystalline Silicon PV Modules due to Cell Interconnection," in *Proceedings of the 23rd European Photovoltaic Solar Energy Conference and Exhibition (EUPVSEC)*, 2008, pp. 2701–2704.

[265] P. Schmitt, D. Eberlein, P. Voos, M. Tranitz, and H. Wirth, "Metallographic preparation of solar cell samples for quality assurance and material evaluation," *Energy Procedia*, vol. 8, pp. 402–408, 2011.

[266] J.-F. Nekarda, M. Hörteis, F. Lottspeich, A. Wolf, and R. Preu, "Comparison of Three Different Metallization Concepts for LFC Cells," in *Proceedings of the 25th European Photovoltaic Solar Energy Conference and Exhibition/ 5th World Conference on Energy Conversion*, 2010.

[267] I. L. Repins, F. Kersten, B. Hallam, K. VanSant, and M. B. Koentopp, "Stabilization of light-induced effects in Si modules for IEC 61215 design qualification," *Progress in Solar Energy 1*, vol. 208, pp. 894–904, 2020.

[268] A. A. Brand, K. Krauß, P. Wild, S. Schörner, S. Gutscher, S. Roder, S. Rein, and J. Nekarda, "Ultrafast In-Line Capable Regeneration Process for Preventing Light Induced Degradation of Boron-Doped p-Type Cz-Silicon Perc Solar Cells," in *Proceedings of the 33rd European Photovoltaic Solar Energy Conference and Exhibition (EUPVSEC)*, 2017, pp. 382–387.

[269] T. Niewelt, J. Schoen, W. Warta, S. W. Glunz, and M. C. Schubert, "Degradation of Crystalline Silicon Due to Boron–Oxygen Defects," *IEEE Journal of Photovoltaics*, vol. 7, no. 1, pp. 383–398, 2017.

List of Figures

List of Tables

List of Publications

Main Author

- **A. De Rose**, G. Mikolasch, M. Kamp, A. Kraft, M. Nowottnick, "Microstructure and long-term stability of solder joints on nickel-plated aluminium formed during short soldering times", RSC Advances, vol. 10, no. 66, pp. 40215-40224, 2020, DOI: 10.1039/D0RA06115H

- **A. De Rose**, M. Kamp, G. Mikolasch, A. Kraft, M. Nowottnick, "Adhesion improvement for solder interconnection of wet chemically coated aluminum surfaces", in AIP Conference Proceedings, vol. 2156, pp. 020014-1-020014-10, 2019, DOI: 10.1063/1.5125879

- **A. De Rose**, T. Geipel, D. Eberlein, A. Kraft, M. Nowottnick, "Interconnection of Silicon Heterojunction Solar Cells by Infrared Soldering - Solder Joint Analysis and Temperature Study", in Proceedings of the 36$^{\text{th}}$ EUPVSEC, pp. 229-234, 2019, Marseille, DOI: 10.4229/EUPVSEC20192019-2CO.11.4

- **A. De Rose**, "Solder Interconnection of Advanced Silicon Solar Cell Concepts", SiliconFOREST, 2019, Falkau, Germany. (Oral presentation)

- **A. De Rose**, A. Kraft, U. Eitner, M. Nowottnick, "Solder Joint Analysis on Coated Aluminum for Silicon Solar Cell Interconnection", in 41$^{\text{st}}$ International Spring Seminar on Electronics Technology (ISSE), IEEE, pp. 1-6, 2018, Zlatibor, DOI: 10.1109/ISSE.2018.8443630

- **A. De Rose**, T. Geipel, D. Erath, A. Kraft, U. Eitner, "Challenges for the interconnection of crystalline silicon heterojunction solar cells", Photovoltaics International, vol. 40, pp. 78-86, 2018

- **A. De Rose**, A. Kraft, S. Gledhill, M. T. Ali, T. Kroyer, C. Pscherer, M. Graf, J. Nekarda, U. Eitner, "Solder interconnection of aluminum foil rear side metallization for passivated emitter and rear solar cells", in 7$^{\text{th}}$ Workshop on Metallization and Interconnection for Crystalline Silicon Solar Cells, 2017, Konstanz, DOI: 10.2139/ssrn.3152428

- **A. De Rose**, D. Erath, T. Geipel, A. Kraft, U. Eitner, "Low-temperature soldering for the interconnection of silicon heterojunction solar cells", in Proceedings of the 33$^{\text{rd}}$ EUPVSEC, pp. 710-714, 2017, Amsterdam, DOI: 10.4229/EUPVSEC20172017-2AV.3.1

Co-Author

- H. Schulte-Huxel, A. Kraft, T. Roessler, **A. De Rose**, Module interconnection technologies, in: Silicon Solar Cell Metallization and Module Technology, ed. by T. Dullweber and L. Tous, The Institution of Engineering and Technology, 2021, *in press*

- N. Klasen, F. Heinz, **A. De Rose**, T. Roessler, A. Kraft, "Root Cause Analysis of Solar Cell Cracks at Shingle Joints", Solar Energy Materials & Solar Cells, submitted

- D. Erath, S. Pingel, R. Khotimah, **A. De Rose**, D. Eberlein, T. Wenzel, S. Roder, A. Lorenz, F. Clement, "Fast Screen Printing and Curing Process for Silicon Heterojunction Solar Cells", in AIP Conference Proceedings, vol. 2367, pp. 020006-1-020006-9, 2021, DOI: 10.1063/5.0056429

- S. Pingel, D. Erath, T. Wenzel, S. Nold, D. Eberlein, **A. De Rose**, S. Tepner, J. Schube, G. Ivanov, E. Terukova, A. Moldovan, A. Lorenz, F. Clement, "Low-temperature Ag-paste screening for silicon heterojunction solar cells and modules", in Proceedings of 37th EUPVSEC, pp. 508-511, 2020, DOI: 10.4229/EUPVSEC20202020-2DV.3.17

- S. Hoffmann, **A. De Rose**, M. Passig, N. Bay, D. Brunner, A. Kraft, "Module Reliability of Solar Cells with Ultra-Thin Plated Metallization for Silver and Nickel Reduction", Poster presentation at 37th EUPVSEC, 2020

- O. John, J. Paschen, **A. De Rose**, B. Steinhauser, G. Emanuel, A. A. Brand, J. Nekarda, "Laser Metal Bonding (LMB) - Low Impact Joining of Thin Aluminum Foil to Silicon and Silicon Nitride Surfaces", in Procedia CIRP, Elsevier B.V., pp. 863-868, 2020, DOI: 10.1016/j.procir.2020.09.109

- O. John, G. Emanual, J. Paschen, **A. De Rose**, B. Steinhauser, A. Brand, J. Nekarda, "Laser Metal Bonding (LMB) - Low Impact Joining of Thin Aluminum Foil to PERC and TOPCon Rear Side Surfaces", in 47th IEEE PVSC, pp. 63-66, 2020, DOI: 10.1109/PVSC45281.2020.9300595

- A.-K. U. Michel, A. Heßler, S. Meyer, J. Pries, Y. Yu, T. Kalix, M. Lewin, J. Hanss, **A. De Rose**, T. W. W. Maß, M. Wuttig, D. N. Chigrin, T. Tauber, "Advanced Optical Programming for Individual Meta-Atoms Beyond the Effective Medium Approach", Adv. Mater., vol, 31, no. 29, 2019, DOI: 10.1002/adma.201901033

- J. Paschen, G. Emanuel, A. A. Brand, T. Fellmeth, **A. De Rose**, O. John, J. F. Nekarda, "FoilMet® - Connect: A new rear metallization upgrade for PERC and other cell concepts", in AIP Conference Proceedings, vol. 2156, pp. 020004-1-020014-5, 2019, DOI: 10.1063/1.5125869

- J. Paschen, G. Emanuel, A. A. Brand, T. Fellmeth, O. John, **A. De Rose**, J. F. Nekarda, "FoilMet® - Connect: a New Rear Metallization Upgrade for PERC and Other Cell Concepts", Poster presentation at 36th EUPVSEC, 2019, Marseille

- J. Burschik, Y. Shengzhao, N. Bay, K. Crouse, **A. De Rose**, A. Hoffmann, H. Kühnlein, B. Lee, A. Letize, M. Passig, D. Pysch, M. Sieber, P. Verlinden, K. Vosteen, "Transition to 4 and 5 BB Designs for Ni/Cu/Ag Plated Cells", Energy Proceedia, vol. 98, pp. 66-73, 2016, DOI: 10.1016/j.egypro.2016.10.082

- D. Pysch, J. Burschik, Y. Shengzhao, N. Bay, K. Crouse, **A. De Rose**, A. Hoffmann, H. Kühnlein, B. Lee, A. Letize, M. Passig, M. Sieber, P. Verlinden, K. Vosteen, "Advantages of transition to four and five busbar front contact grid designs for Ni/Cu/Ag plated silicon solar cells", in Proceedings of the 32nd EUPVSEC, pp. 796-800, 2016, Munich, DOI: 10.4229/EUPVSEC20162016-2AV.3.12

Patents

- T. Kroyer, S. Gledhill, M. T. Ali, **A. De Rose**, "Verfahren zum Verbinden zweier Werkstücke mittels Löten und Vorrichtung mit einem ersten und einem zweiten Werkstück, welche mittels eines Lots verbunden sind", Patent DE 10 2019 101 921 A1.

- J. Nekarda, A. Brand, M. Graf, **A. De Rose**, A. Kraft, "Method for producing a photovoltaic solar cell, photovoltaic solar cell and photovoltaic module", Patent US 2021/0 005 773 A1.

Danksagung

In den letztem Jahren konnte ich die einmalige Erfahrung machen, meine Doktorarbeit in einem unglaublich vielfältigen Themenbereich anzufertigen. Ich habe viel Neues gelernt und möchte mich an dieser Stelle bei all Denjenigen bedanken, die auf die ein oder andere Weise zum Gelingen dieser Arbeit beigetragen haben.

Ein besonderer Dank geht an **Prof. Dr. Mathias Nowottnick**, der mich als externe Doktorandin an der Universität Rostock herzlich aufgenommen und in die Welt der Mikroelektronik eingeführt hat. Trotz der 950 km zwischen Freiburg und Rostock hat der intensive Austausch zu Lötstellen und allem was dazu gehört meine Arbeit sehr bereichert.

Prof. Dr. Stefan Glunz danke ich für die Übernahme der Zweitbetreuung, durch die ich von Beginn meiner Zeit am Fraunhofer ISE Unterstützung bei meiner Arbeit und außerdem spannende Einblicke in die Institutshistorie bekommen habe.

Außerordentliches Vertrauen und eine stetige Bereitschaft zur Unterstützung habe ich von meinem Betreuer **Achim Kraft** am Fraunhofer ISE erfahren. Ich danke für die Hilfe in schwierigen Phasen meiner Promotion, beim gemeinsamen Suchen nach Lösungen und für etliche Meetings. Durch ihn habe ich die Verbindungstechnik der Solarzelle kennen gelernt. Die Kolleg:innen in der Abteilung "Photovoltaische Module" haben mich sehr herzlich am ISE aufgenommen. An dieser Stelle möchte ich auch allen PVMlern für ihre vielseitige Unterstützung danken, insbesondere dem damaligen Team Verbindungstechnik: **Christian, Christina, Dirk, Li, Marco, Nils, Stephan, Torsten** und **Veronika**.

Weiterhin haben eine Vielzahl von ISE Kolleg:innen zum Gelingen dieser Arbeit beigetragen, von denen ich einige hier erwähnen möchte. Dem PV-TEC Charakterisierungsteam (**Alex, Thien Thanh, Fiona, Naila, Johannes H., Johannes G.**) danke ich für etliche *I-V*, EL und PL Messungen, der Lasergruppe (**Oli, Jan P., Martin, Jan N.**) für die Zusammenarbeit im Projekt FolMet-Modul, dem TestLab PV Modules (**Esther, Sandor, Paul, Georg**) für den intensiven Austausch zu PV Modulen und Alterung, dem SHJ-Metallisierungsteam (**Denis, Sebastian**) für spannende Abwechslung und eine super Zusammenarbeit, den **PVMK-Doktorand:innen** für die unterhaltsamen iBBB-Runden, den **Doktorandinnen und TALENTAs**, auch an den anderen Freiburger Fraunhofer-Instituten, für den wertvollen Austausch, sowie weiteren Kolleg:innen am ISE (**Gernot, Jonas H., Jutta, Lina, Saskia, Timo** und den Kolleginnen aus der **ISE-Bibliothek**), die mich bei meiner Arbeit unterstützt haben.

Besonders möchte ich mich außerdem bei **Sophie, Tom, Gabriele** und **Matze** bedanken. Ohne euch wäre meine Arbeit inhaltlich nie so vielfältig geworden. Ich danke euch für die super Zusammenarbeit und die Unterstützung bei der Probenherstellung von

beschichtetem Aluminium, auch über Projektgrenzen hinaus.

In meiner Doktorarbeit wurden etliche Abzugstests und Widerstandsmessungen durchgeführt, sowie metallographische Schliffe erstellt. Dafür möchte ich mich für die tatkräftige experimentelle Unterstützung bei einigen Studenten bedanken: **Karthika, Felix, Manisha, Jonas S., Cristina, Hassan, Ädem, Najwa, Rachid** und **Miriam**.

Im interdisziplinären Themenfeld meiner Arbeit, haben mich wertvolle Kontakte außerhalb des Fraunhofer ISE unterstützt. Ich danke **Günter Schubert** (*Hydro Aluminium*), **Claudia Pscherer, Fabian Distelrath** und **Thomas Booz** (*SCHLENK Metallfolien*), **Brunhilde Kindle-Hasse** (*ROWO Coating*), sowie **Carina Franken** und **Patrick Löffler** (*Wickeder Westfalenstahl*) für die interessanten Gespräche zu Aluminiumfolien, lötbaren Schichten und möglichen Anwendungen.

Weiterhin möchte ich **Dirk S.**, **Andrej. N.** und **Jacob M.** von der Universität Rostock danken. Ihr habt mich sowohl inhaltlich als auch experimentell bei meiner Arbeit unterstützt und mich sehr herzlich in euren Kreis in Rostock aufgenommen.

Meine Dissertation und auch mein Leben in Freiburg wären nicht zu dem geworden was sie jetzt sind, ohne die Samba-Rhythmen von **Brasilikum**. Ein riesiges Dankeschön an die beste Trommelgruppe der Welt! Durch euch habe ich den Samba entdeckt, neue Freunde gefunden und stets einen super Ausgleich zum Wissenschaftsalltag gehabt.

Schließlich wäre meine Promotion ohne die Unterstützung meiner Freunden nicht so gelungen. Egal ob im Süden Deutschlands, im Norden oder ganz im Westen, danke euch allen: **Anton, Anya, Andi, Georg, Hannah, Janina, Nina, Nils, Ully** und **Viki**. Ich bin froh euch zu haben!

Zu guter Letzt danke ich meiner Familie, insbesondere **Timo, Inge** und **Francesco**! Ihr seid immer für mich da; auch wenn uns 450 km trennen, ich kann mich auf euch verlassen. Danke für den Rückhalt in den letzten Jahren und die schönen Momente die wir zusammen erlebt haben. Danke **Jonas**, für deine Liebe, unendliche Geduld und Unterstützung in so vielfältiger Hinsicht!